



# THE UNIVERSITY --- *of* ADELAIDE

## **Investigations of Ultra-High Performance Fibre Reinforced Concrete (UHPFRC) Column**

Chengfeng Fang  
BEng (Civil and Structural Engineering) Hons

Thesis submitted to The University of Adelaide in fulfilment of the requirements for the degree of  
Doctor of Philosophy

The University of Adelaide  
Faculty of Engineering, Computer and Mathematical Sciences  
School of Civil, Environmental and Mining Engineering

Copyright© 2019.

This thesis is dedicated to my parents and people who loved me

# Investigations of Ultra-High Performance Fibre Reinforced Concrete (UHPFRC) Column

By:

Chengfeng Fang

Supervised by:

Mohamed Ali, M.S, *Ph.D.*, *Senior Lecturer*,  
*School of Civil, Environmental & Mining Engineering*,  
*The University of Adelaide*

Abdul H. Sheikh, *Ph.D.*, *Associate Professor*,  
*School of Civil, Environmental & Mining Engineering*,  
*The University of Adelaide*

Thesis submitted in fulfilment of the requirements for the degree of

**Doctor of Philosophy**

School of Civil, Environmental & Mining Engineering

Faculty of Engineering, Computer and Mathematical Sciences

The University of Adelaide

North Terrace, Adelaide, SA 5005, Australia

Tel: +61(8) 8313 1570

Fax: +61(8) 8313 4359

Email: [chengfeng.fang@adelaide.edu.au](mailto:chengfeng.fang@adelaide.edu.au)

Copyright© Chengfeng Fang, October, 2019

# Contents

Abstract.....	i
Statement of Originality .....	iii
Declaration.....	iv
List of Journal Papers Published /Under Review .....	v
ACKNOWLEDGEMENTS.....	vi
<b>CHAPTER 1. Introduction and General Overview .....</b>	<b>1</b>
<b>Objectives and Scope of Research .....</b>	<b>2</b>
<b>Outline of the Thesis .....</b>	<b>3</b>
<b>List of Journal Papers Published /Under Review .....</b>	<b>5</b>
<b>References.....</b>	<b>6</b>
<b>CHAPTER 2. Investigations on Shrinkage Characteristics of Ultrahigh Performance Concrete Reinforced With and Without Steel Fibres .....</b>	<b>9</b>
<b>2.1. Characterizations of Autogenous and drying shrinkage of ultra-high performance concrete (UHPC): An experimental study .....</b>	<b>13</b>
<b>2.1.1. INTRODUCTION.....</b>	<b>14</b>
<b>2.1.2. EXPERIMENTAL PROGRAM.....</b>	<b>16</b>
<b>2.1.2.1. Ingredients used for UHPC mix .....</b>	<b>16</b>
<b>2.1.2.2. Test concepts and methods.....</b>	<b>18</b>
<b>2.1.2.2.1. Compressive strength .....</b>	<b>19</b>
<b>2.1.2.2.2. Flowability and passing ability .....</b>	<b>19</b>
<b>2.1.2.2.3. Exothermic reaction at early curing ages .....</b>	<b>19</b>
<b>2.1.2.2.4. Unit weight and porosity .....</b>	<b>20</b>
<b>2.1.2.2.5. Scanning electron microscopy (SEM) analysis and Energy-dispersive X-ray spectroscopy (EDS) .....</b>	<b>20</b>
<b>2.1.2.2.6. Thermal gravity (TG) analysis .....</b>	<b>21</b>
<b>2.1.3. EFFECT OF BINDER-TO-SAND RATIO ON THE PROPERTIES OF THE UHPCS ...</b>	<b>24</b>
<b>2.1.3.1. Flowability of concrete.....</b>	<b>24</b>
<b>2.1.3.2. Autogenous shrinkage.....</b>	<b>24</b>
<b>2.1.3.3. Free total shrinkage .....</b>	<b>25</b>
<b>2.1.3.4. Assessment of free drying component .....</b>	<b>26</b>
<b>2.1.3.5. Assessment of free drying component .....</b>	<b>28</b>
<b>2.1.3.6. Compressive strength .....</b>	<b>28</b>
<b>2.1.3.7. Unit weight and porosity of the UHPCs.....</b>	<b>29</b>
<b>2.1.3.8. Exothermic reaction at early curing period.....</b>	<b>30</b>

2.1.3.9. Morphological characterization by scanning electron microscopy (SEM) and Energy-dispersive X-ray spectroscopy (EDX) .....	32
2.1.3.10. Results of thermal gravity (TG) analysis .....	35
2.1.3.11. Selection of the mix for further investigations to mitigate autogenous shrinkage .....	36
<b>2.1.4. EFFECTS OF APPLIED TECHNIQUES ON THE PROPERTIES OF THE UHPCS .....</b>	<b>37</b>
2.1.4.1. Flowability .....	37
2.1.4.2. Autogenous shrinkage.....	38
2.1.4.3. Free total shrinkage and assessment of free drying component .....	40
2.1.4.4. Compressive strength .....	43
2.1.4.5. Exothermic reaction at early curing ages: effects of SRA and crushed ice dosage .....	45
2.1.4.6. Unit weight and porosity of the hardened UHPCs.....	46
2.1.4.7. Morphological characterization of the UHPCs .....	48
2.1.4.8. Thermal gravity (TG) analysis.....	52
<b>2.1.5. COMPARISONS AMONG THE THREE TECHNIQUES AND FURTHER SUGGESTIONS FOR UHPC MIX .....</b>	<b>54</b>
<b>2.1.6. CONCLUSIONS .....</b>	<b>55</b>
<b>2.1.7. REFERENCES.....</b>	<b>56</b>
<b>2.2. The Influence of Steel Fibre Properties on the Shrinkage of Ultra-High Performance Fibre Reinforced Concrete .....</b>	<b>70</b>
<b>2.2.1. INTRODUCTION.....</b>	<b>70</b>
<b>2.2.2. EXPERIMENTAL PROGRAM.....</b>	<b>72</b>
2.2.2.1. Materials and Concrete mixtures .....	72
2.2.2.1.1. <i>Ingredients used for the UHPC matrix</i> .....	72
2.2.2.1.2. <i>Steel Fibres</i> .....	73
2.2.2.1.3. <i>Mixing procedure of UHPFRCs</i> .....	74
2.2.2.2. Test methods.....	76
2.2.2.2.1. <i>Measurements of the total- and autogenous- shrinkage</i> .....	76
2.2.2.2.2. <i>Fibre pulled-out for the UHPC matrix</i> .....	77
2.2.2.2.3. <i>Compressive and splitting tensile strength</i> .....	78
<b>2.2.3. RESULTS AND DISCUSSIONS .....</b>	<b>78</b>
2.2.3.1. Slump .....	78
2.2.3.2. Fibre pulled-out test results .....	78
2.2.3.3. Shrinkage characterizations.....	81
2.2.3.3.1. <i>General observations</i> .....	81
2.2.3.3.2. <i>Effect of fibre volume fraction</i> .....	84
2.2.3.3.3. <i>Effect of fibre shape</i> .....	86
2.2.3.3.4. <i>Effect of fibre aspect ratio</i> .....	88

2.2.3.4. Mechanical properties of the UHPFRCs.....	90
2.2.4. CONCLUSIONS AND REMARKS .....	92
2.2.5. ACKNOWLEDGMENTS .....	93
2.2.6. REFERENCES.....	93
<b>CHAPTER 3. Investigations on Ultrahigh Performance Fibre Reinforced Concrete Columns subjected to concentrically and eccentrically axial loads .....</b>	<b>100</b>
<b>3.1. Numerical and Finite-Element Analysis of Short Ultrahigh-Performance Fiber-Reinforced Concrete Columns.....</b>	<b>104</b>
3.1.1. INTRODUCTION.....	105
3.1.2. DEVELOPING NUMERICAL MODELS USING PARTIAL-INTERACTION (PI) ANALYSIS .....	107
3.1.2.1. Fundamental mechanism of the column plastic hinge.....	108
3.1.2.2. Cross-sectional analysis at partial interaction (PI) region .....	113
3.1.2.3. Partial interaction (PI) tension stiffening mechanism .....	115
3.1.2.4. Partial interaction (PI) concrete softening.....	119
3.1.2.5. Load Deflection relationship .....	120
3.1.3. FINITE ELEMENT (FE) MODELLING .....	121
3.1.3.1. Concrete damage plasticity (CDP) model .....	125
3.1.4. COMPARISON BETWEEN THEORETICAL MODEL & TEST RESULTS .....	127
3.1.4.1. Introduction of experimental program .....	127
3.1.4.2. Fundamental material properties.....	130
3.1.4.2.1. Unconfined and confined compressive stress-strain relationships of UHPFRC.....	130
3.1.4.2.2. Tensile characterizations of UHPFRC .....	132
3.1.4.2.3. Local Bond-slip ( $\tau/\delta$ ) relationship.....	133
3.1.5. VALIDATION OF NUMERICAL MODEL AND FINITE ELEMENT MODELLING SIMULATION .....	134
3.1.5.1. Load-deflection relationships.....	134
3.1.5.2. Verification of proposed load-moment (P-M) interaction diagram .....	137
3.1.6. FAILURE MODES .....	139
3.1.7. CONCLUSIONS .....	142
3.1.8. LIST OF NOTATIONS.....	142
3.1.9. ACKNOWLEDGEMENTS.....	148
3.1.10. REFERENCES.....	148
<b>3.2. Experimental and numerical investigation of the slenderness effects regarding ultrahigh performance fibre reinforced concrete column under concentric and eccentric loads .....</b>	<b>153</b>
3.2.1. INTRODUCTION.....	153
3.2.2. EXPERIMENTAL PROGRAM.....	155

3.2.2.1. UHPFRC mixture and mixing process.....	155
3.2.2.2. Material tests for UHPFRC and steel reinforcements.....	156
3.2.2.3. Structural member tests .....	157
3.2.2.3.1. <i>Specimen detail and designation</i> .....	158
3.2.2.3.2. <i>Instrumentation and test setup</i> .....	158
3.2.3. EXPERIMENTAL TEST RESULTS AND OBSERVATION .....	162
3.2.3.1. Load-bearing, moment capacities, and ductility indices .....	162
3.2.3.2. Load-axial strain and lateral deflection relationships .....	165
3.2.3.3. Failure location and damage pattern .....	167
3.2.4. NUMERICAL (FINITE ELEMENT) MODELLING .....	169
3.2.4.1. FE modelling.....	170
3.2.4.2. Theoretical background of CDP model.....	173
3.2.5. COMPARISONS AND DISCUSSIONS .....	176
3.2.5.1. Comparisons of experimental and simulated results .....	176
3.2.5.2. Comparisons of failure mode .....	178
3.2.5.3. Comparisons of load-moment interaction curves .....	183
3.2.6. PARAMETRIC STUDY FOR SLENDERNESS EFFECT.....	184
3.2.7. CONCLUSION .....	190
3.2.8. ACKNOWLEDGEMENTS.....	191
3.2.9. REFERENCE.....	192
<b>CHAPTER 4. Experimental and numerical investigations on concrete filled carbon FRP tube (CFRP-CFFT) columns manufactured with ultra-high-performance fibre reinforced concrete</b> .....	198
<b>Experimental and numerical investigations on concrete filled carbon FRP tube (CFRP-CFFT) columns manufactured with ultra-high-performance fibre reinforced concrete.....</b>	200
<b>4.1. INTRODUCTION.....</b>	201
<b>4.2. EXPERIMENTAL PROGRAM.....</b>	204
4.2.1. UHPFRC mixture and mixing procedure.....	205
4.2.2. FRP tubes fabrication.....	206
4.2.3. Material tests .....	207
4.2.3.1. <i>Uniaxial compression and direct tensile tests on UHPFRC</i> .....	207
4.2.3.2. <i>Flat FRP coupon test</i> .....	208
4.2.3.3. <i>Uniaxial compression tests on actively confined UHPFRC</i> .....	209
4.2.4. Structural member tests .....	213
4.2.4.1. <i>Specimen detail</i> .....	213
4.2.4.2. <i>Instrumentation</i> .....	214
4.2.4.3. <i>Testing procedure</i> .....	218

<b>4.3. COLUMN TEST RESULTS AND OBSERVATIONS.....</b>	<b>219</b>
4.3.1. Load bearing and flexural moment capacities and corresponding deflections .....	219
4.3.2. Failure Mode and location .....	221
<b>4.4. FINITE-ELEMENT (FE) MODELLING .....</b>	<b>223</b>
4.4.1. FE modelling the CFRP-CFFT UHPFRC primary members .....	223
4.4.2. Modelling of the CFRP-CFFT UHPFRC columns .....	226
4.4.3. Modelling of the CFRP-CFFT UHPFRC beam .....	227
4.4.4. Concrete failure model .....	230
4.4.5. FRP failure model .....	233
<b>4.5. VALIDATIONS OF FE MODEL.....</b>	<b>238</b>
4.5.1. Comparisons of experimental and simulated results .....	238
4.5.2. Comparisons of damage pattern regarding CFRP tube.....	241
4.5.3. Comparisons of failure mode regarding UHPFRC.....	244
4.5.4. Comparisons of load-moment interaction curves .....	247
<b>4.6. CONCLUSIONS .....</b>	<b>248</b>
<b>4.7. ACKNOWLEDGMENTS .....</b>	<b>249</b>
<b>4.8. REFERENCES.....</b>	<b>250</b>
<b>CHAPTER 5. Conclusions and Future Work .....</b>	<b>256</b>
<b>5.1. INTRODUCTION.....</b>	<b>256</b>
<b>5.2. INVESTIGATIONS IN SHRINKAGE CHARACTERISTICS OF UHPC .....</b>	<b>257</b>
<b>5.3. INVESTIGATIONS OF THE EFFECTS OF STEEL FIBRES ON THE SHRINKAGE OF UHPFRC.....</b>	<b>258</b>
<b>5.4. NUMERICAL AND FE MODELLING OF SHORT UHPFRC COLUMNS .....</b>	<b>259</b>
<b>5.5. EXPERIMENTAL AND NUMERICAL INVESTIGATIONS SLENDER UHPFRC COLUMNS AND THE CORRESPONDING EFFECTS OF SLENDERNESS .....</b>	<b>260</b>
<b>5.6. EXPERIMENTAL AND NUMERICAL INVESTIGATIONS ON CFRP-CFFT UHPFRC COLUMNS .....</b>	<b>261</b>
<b>5.7. SCOPE FOR FUTURE WORK .....</b>	<b>262</b>
<b>5.8. SUMMARY .....</b>	<b>263</b>
<b>APPENDIX I. Published paper.....</b>	<b>264</b>



# Abstract

Ultra-high-performance concrete (UHPC) has attracted significant attention in recent decades due to its superior compressive strength and exceptional durability, while concerns have been raised due to the fact that inherent brittleness of concrete resulted in an explosive failure of UHPC. To extend the applications of UHPC in engineering design and construction, incorporating randomly distributed steel fibres into UHPC concrete matrix has been considered as one of the effective methods to enhance the ductility of the material. This is due to the fibre bridging effects preventing the propagation of the crack thereby to enhance the ductility and compressive and tensile strengths of the material. Therefore, the ultra-high performance fibre reinforced concrete (UHPFRC) has a great potential to bring a step-change in the way of infrastructure are designed and constructed.

The main objectives and findings of this paper are detailed as follows:

- (1) To study the long-term shrinkage mechanisms of UHPC with and without steel fibres, a series of experiments was conducted to achieve the optimal mixtures with the autogenous and drying shrinkage mitigated.
- (2) To investigate the structural responses of axial members (both UHPFRC short and slender columns) subjected to a concentric or eccentric load, the optimal UHPFRC mixture was then utilized to manufacture the test specimens for experimental investigations.
- (3) A generic mechanic-based partial-interaction (PI) approach that used to simulate the conventional concrete members (flexural and axial members) is suitably modified based on the material properties of UHPFRC to accurately simulate the structural responses of the short UHPRC columns under eccentric loading conditions.
- (4) Finite element analysis (FEA) is carried on in conjunction with a concrete damage plasticity (CDP) model to simulate the structural behaviours and damage patterns of both UHPFRC short and slender columns subjected to a concentric or eccentric load. An extended study is also conducted based on the clarified finite element (FE) model to investigate the slenderness effects regarding the structural response of the slender columns.
- (5) An experimental program is undertaken to investigate the structural performances of the concrete-filled carbon FRP tube (CFRP-CFFT) columns manufactured with ultra-high-performance fibre reinforced concrete (UHPFRC). Furthermore, finite element (FE) analysis incorporating CDP and Hashin's damage model is then conducted to simulate both

the structural response of CFRP-CFFT UHPFRC columns as well as the corresponding damage patterns of CFRP tubes and concrete.

The proposed load-moment ( $P$ - $M$ ) interaction envelopes regarding UHPFRC short and slender columns as well as CFRP-CFFT UHPFRC column generated in these studies accurately predict the structural behaviours of columns subjected to axial loads with different eccentricities. Hence, these  $P$ - $M$  envelopes can serve as foundations for promoting design guideline of the UHPFRC columns in the future.

# Statement of Originality

I, **Chengfeng Fang**, hereby certify that this work contains no material which has been accepted for the award of any other degree or diploma in my name, in any university or other tertiary institution and, to the best of my knowledge and belief, contains no material previously published or written by another person, except where due reference has been made in the text. In addition, I certify that no part of this work will, in the future, be used in a submission in my name, for any other degree or diploma in any university or other tertiary institution without the prior approval of the University of Adelaide and where applicable, any partner institution responsible for the joint award of this degree.

I give consent to this copy of my thesis when deposited in the University Library, being made available for loan and photocopying, subject to the provisions of the Copyright Act 1968.

The author acknowledges that copyright of published works contained within this thesis resides with the copyright holder(s) of those works.

I also give permission for the digital version of my thesis to be made available on the web, via the University's digital research repository, the Library Search and also through web search engines, unless permission has been granted by the University to restrict access for a period of time.

\_\_\_\_\_  
Chengfeng Fang

\_\_\_\_\_07/10/2019\_\_\_\_\_  
Date

# Declaration

I, **Chengfeng Fang**, certify that this work contains no material which has been accepted for the award of any other degree or diploma in my name, in any university or other tertiary institution and, to the best of my knowledge and belief, contains no material previously published or written by another person, except where due reference has been made in the text. In addition, I certify that no part of this work will, in the future, be used in a submission in my name, for any other degree or diploma in any university or other tertiary institution without the prior approval of the University of Adelaide and where applicable, any partner institution responsible for the joint-award of this degree.

I acknowledge that copyright of published works contained within this thesis resides with the copyright holder(s) of those works.

I also give permission for the digital version of my thesis to be made available on the web, via the University's digital research repository, the Library Search and also through web search engines, unless permission has been granted by the University to restrict access for a period of time.

I acknowledge the support I have received for my research through the provision of an Australian Government Research Training Program Scholarship.

\_\_\_\_\_  
Chengfeng Fang

\_\_\_\_\_  
07/10/2019

\_\_\_\_\_  
Date

### **List of Journal Papers Published /Under Review**

Xie, T., Fang, C., Mohamad Ali, M.S. and Visintin, P. 2018. Characterizations of autogenous and drying shrinkage of ultra-high performance concrete (UHPC): An experimental study. *Cement and Concrete Composites*, 91: 156-173.

Fang, C., Mohamad Ali, M.S., Xie, T., Visintin, P., Sheikh, A.H. 2019. Effects of Steel Fibres on Shrinkage Characterizations of Ultra-High Performance Fibre Reinforced Concrete. Submitted on *Construction and building materials* (under review).

Fang, C., Mohamad Ali, M.S., Sheikh, A.H. and Singh, M. 2019. Numerical and Finite-Element Analysis of Short Ultrahigh-Performance Fiber-Reinforced Concrete Columns. *Journal of Structural Engineering*. 2019 Aug 9;145(10):04019111.

Fang C, Mohamad Ali, M.S., Sheikh, A.H. 2019. Experimental and numerical investigations on concrete filled carbon FRP tube (CFRP-CFFT) columns manufactured with ultra-high-performance fibre reinforced concrete. Submitted on *Composite structures* (under review).

# ACKNOWLEDGEMENTS

Firstly, I would like to express my sincere gratitude to my supervisors, Dr Mohamed Ali Mohamed Sadakkathulla and A/Prof Abdul Sheikh for their supervisions and continuous support of my Ph.D study, for their patience, motivation and immense knowledge. Their guidance helped me in all the time of research and writing of this thesis.

I would also like to thank A/Prof Phillip Visintin for his valuable advises and suggestions during my Ph.D study. I also thank Messrs. Jon Ayoub, Dale Hodson, Simon Golding and Ian Ogier, for their technical assistance with the experimental work and their impressive craftsmanship for all test configurations they made.

I am very grateful to my fellow research students and staffs: Dr Tianyu Xie, Dr Can Wang, Dr Lei Gu, Dr Exequiel Sepúlveda, Dr Ching-Tai Ng (Alex), Miss Jessica Bohorquez Arevalo, Yue Chen, Carman Yeung, Messrs, Alex Sturm, Linh A. Le, Juan Allen, Michael Crisp, Xuân Hồng Đỗ, Kiet Wong, Xinkai Hao, Shahin Mahdi, Dat Phan, Yu Nie, Ziyang Weng, Ming sun for their friendships. I also thank Master Shi Jie Wen's guidance for my life is also gratefully acknowledged. Special thanks are given to Dr. Tianyu Xie for his support with the insightful comments and encouragement during these four years.

Last but not the least, I would like to thank my family: my parents, Songhua Fang, Lifang Wang and to my brother Tianxiang Fang and my grandmother Shaohua Zhao for their unconditional love and spiritual support.

THIS PAGE HAS BEEN LEFT INTENTIONALLY BLANK

## **CHAPTER 1. Introduction and General Overview**

Concrete, is one of the most frequently used construction materials worldwide. Due to its extensive application in construction of infrastructures, commercial buildings and bridges, its usage worldwide is dramatically increasing to cater for the intensified urbanization and civilization. However, the brittleness and limitations in both compressive and tensile strengths and material durability of the conventional concrete limits its application to fulfil requirements of the high-performance based designs where a high ductility, corrosion resistance, and a high impact or seismic resistance are warranted.

Due to rapid advancements in concrete technology, a specially formulated cement based composite characterised by a very high compressive strength ( $f_c' = 240$  MPa) and a low water to binder ratio was first developed by Yudenfreund et al (1972), and this new concrete was called ultra-high performance concrete (UHPC). Further improvements in binder properties was promoted by applying autoclaving at a temperature of  $250^\circ\text{C}$  and a pressure of 50 MPa, which resulted in a compressive strength of 510 MPa with zero-porosity (Roy et al. 1972). Investigations conducted to analyse the microstructure of UHPC indicate that the particle spaces between cement and ultra-fine particles have been densely packed through a series of chemical reactions, which resulted in high compressive strength generally more than 150 MPa associate with very high flexural strength in the range of 60 to 70 MPa.

Although UHPC exhibits considerably high compressive strength, the inherent brittleness of concrete results in an explosive failure. To overcome this shortcoming, very high strength steel fibres (with a volume fraction from 1% to 3% of concrete) were incorporated to the UHPC matrix and this was termed as ultra-high-performance fibre reinforced concrete (UHPRFC).



This UHPFRC is usually made from cementitious materials such as Portland cement, silica fume, finely graded quartz sand, high range water reducer, water, and a small amount of discrete non-mantellic and metallic fibres for overcoming the brittleness of ultra-high performance concrete (UHPC). UHPFRC is characterised by its superior mechanical properties (with compressive strength greater than 150MPa and ductile tensile strength characteristics), exceptional ductility, high durability and high corrosion resistance due to low water permeability and low porosity. Therefore, these material characteristics make UHPFRC highly suitable for high-performance based designs in modern constructions.

Due to its exceptional material characteristics, it is envisaged that replacing conventional concrete by the UHPFRC in the design of heavily loaded columns of high-rise structures, bridges and infrastructures allows a significant reduction in both dimensions of structural members, construction period, building footprints and life-cycle costs. Nevertheless, the underlying mechanisms and effects of steel fibres regarding shrinkage characteristics for UHPC and UHPFRC have not been fully addressed from the previous research. Moreover, limited investigations were conducted to explore the structural behaviours of short and slender UHPFRC columns reinforced by steel rebars under axial loads, and hence it is a necessary to develop rational analytical procedures along with studying the underlying structural mechanism for analysing and predicting the behaviours of UHPFRC columns.

## **Objectives and Scope of Research**

There are six major objectives of research carried out for this thesis work. The details are as follows:

1. To contribute to the existing knowledge base on UHPFRC by using only locally available materials with conventional mixing and curing methods to manufacture UHPC mixture.
2. To further adjust the proportions of ingredients of the UHPC mixture to reduce the usage of cement without compromising its compressive strength. This will lead to economical and optimal UHPFRC mix design.
3. To reduce the magnitude of shrinkage strains and also will yield an optimal mixture design, differing the binder to sand ratios, adding shrinkage reducing agent (SRA), and replacing water in ambient temperature by ice water were adopted to the original UHPC mixture.
4. To study the shrinkage mechanism of both UHPC and UHPFRC in detail, and the influences of fibre properties on the shrinkage behaviour of concrete were also explored to develop mix design procedures and the formulation and code practice of UHPFRC.
5. To develop rational analytical procedures and finite element analyse (FEA) to investigate the structural response of UHPFRC columns.
6. Experimental and numerical investigations are conducted for analysing the structural behaviours as well as the failure mechanisms of concrete filled carbon fibre reinforced polymer tube (CFRP-CFFT) columns manufactured with UHPFRC.

### **Outline of the Thesis**

This thesis is organised into five major chapters. Chapter 1 provides background information of this thesis along with major research objectives and intended significant outcomes. It is worth noting that Chapters 2 to 4 deal with the major research investigations of this thesis work and these are organised as a collection of manuscripts and journal papers, which were either published or submitted for review. A brief description of chapter 2-5 is given as follows:

Chapter 2 describes the experimental works conducted to systematically investigate the shrinkage characteristics of UHPC and UHPFRC and the corresponding underlying mechanism. The mix design recipe used for this work follows closely the investigations carried out by Sobuz et al. (2016) at the University of Adelaide. Different techniques such as differing the binder to sand ratios, adding shrinkage reducing agent (SRA), and replacing normal tap water with chilled water were investigated to study the effects on both drying and autogenous shrinkage strains. Moreover, experimental observations and variation of shrinkage strains were interpreted with characterization tests such as scanning electron microscopy (SEM) and thermal gravity (TG) analysis. The influence of varying the fibre properties such as fibre aspect ratios, fibre dosage, fibre type, and hybridization of steel fibres with blended micro straight and hook end fibres on both total and autogenous shrinkage behaviours were also investigated. Manuscripts of two journal papers form the core of this chapter. It is worth noting that whilst the first paper has already been published in the journal of Cement and Concrete Composite (Elsevier), and the second paper is under review by Construction and Building Materials (Elsevier).

Chapter 3 deals with the research work carried out to investigate the structural behaviours of both short and slender UHPFRC columns. In this chapter, a numerical model is developed by suitably modifying a structural mechanics based approach developed at the University of Adelaide by Visintin et al. (2013), these developed models aim to simulate accurately the structural responses such as axial load VS deflection relationships of both short and slender UHPFRC columns subjected to either concentric or eccentric axial loads. Additionally, these models were compared and validated against the test results obtained from an experimental study on short and slender UHPFRC columns conducted earlier at the University of Adelaide by (Singh et al. 2015 and Douglas et al. 2015). Furthermore, finite element analysis (FEA) was

conducted for both short and slender columns to simulate their structural responses and the corresponding concrete damaged patterns. These numerical models were compared and validated against experimental results, and then another procedure is developed to generate axial load-moment interaction envelopes with high accuracy. This chapter consists of a journal paper published in the Journal of Structural Engineering (ASCE) for the short UHPFRC column and the work pertaining to slender column is presented as a separate sub-chapter.

In Chapter 4, structural investigations related to UHPFRC columns made with concrete filled carbon fibre reinforced polymer tube (CFRP-CFFT) are described in detail. Both material and structural testing were conducted to study the structural behaviour of CFRP-CFFT UHPFRC columns under either concentrically or eccentrically axial loads. Subsequently, the obtained material properties from testing were then used as a fundamental input for conducting finite element analysis for simulating the behaviours of these CFRP-CFFT columns. This chapter consists of a journal paper under review for possible publication by the Composite Structures (Elsevier).

Chapter 5 is the concluding part of this thesis where the major findings and achievements of this thesis work are summarised. It also suggests areas of research that needs future investigations.

### **List of Journal Papers Published /Under Review**

[1] T. Xie, C. Fang, M.S. Mohamad Ali, and P. Visintin. "Characterizations of autogenous and drying shrinkage of ultra-high performance concrete (UHPC): An experimental study." *Cement and Concrete Composites* 91 (2018): 156-173.

[2] C. Fang, M.S. Mohamed Ali, and P. Visintin, T. Xie. “Effects of Steel Fibres on Shrinkage Characterizations of Ultra-High Performance Fibre Reinforced Concrete.” Submitted to Construction and building materials (under review).

[3] Fang C, Mohamed Ali MS, Sheikh AH, Singh M. “Numerical and Finite-Element Analysis of Short Ultrahigh-Performance Fiber-Reinforced Concrete Columns.” Journal of Structural Engineering. 2019 Aug 9;145(10):04019111.

[4] Fang C, Mohamed Ali MS, Sheikh AH. “Experimental and numerical investigations on concrete filled carbon FRP tube (CFRP-CFFT) columns manufactured with ultra-high-performance fibre reinforced concrete.” Submitted to Composite structures (under review).

## References

Yudenfreund, M., Odler, I., Brunauer, S. (1972) Hardened portland cement pastes of low porosity I. Materials and experimental methods, Cement Concrete Research. 2 (3) 313-330.

Roy, D.M., Gouda, G.R., A. Bobrowsky. (1972) Very high strength cement pastes prepared by hot pressing and other high pressure techniques, Cement Concrete Research. 2 (3) 349-366.

Sobuz, H. R., Oehlers, D. J., Visintin, P., Hasan, N. M. S., Hoque, M. I., and Akid, A. S. M. (2017). "Flow and Strength Characteristics of Ultra-high Performance Fiber Reinforced Concrete: Influence of Fiber Type and Volume-fraction." Journal of Civil Engineering and Construction, 6(1), 15.

Visintin, P., D. J. Oehlers, M. Haskett, and C. Wu. (2013). “Mechanics based hinge analysis for reinforced concrete columns.” Journal of Structural Engineering. 139 (11): 1973–1980.

Singh, M. Mohamed Ali, M.S. and Sheikh, A.H. (2015). “Structural behaviour of ultra-high performance fibre reinforced concrete columns subjected to eccentric loading”, IABSE Conference – Structural Engineering: Providing Solutions to Global Challenges, Zürich, Switzerland: International Association for Bridge and Structural Engineering.

Douglas B, Fairweather A, Jolly A, Reid C. (2015). “Investigation into the behaviour of UHPFRC in slender columns”. University of Adelaide. Adelaide. Australia.

**THIS PAGE HAS BEEN LEFT INTENTIONALLY BLANK**

## **CHAPTER 2. Investigations on Shrinkage Characteristics of Ultrahigh Performance Concrete Reinforced With and Without Steel Fibres**

### **Introduction**

This chapter presents a series of the experimental investigations regarding long-term shrinkage characteristics of ultra-high performance concrete (UHPC) reinforced with and without steel fibres. This chapter consist of manuscripts of two international journal articles.

The first paper contained in this chapter namely “Characterizations of autogenous and drying shrinkage of ultra-high performance concrete (UHPC): An experimental study” Reports tests conducted on ten batches of concrete prisms that aims to investigate the efficiency of techniques such as differing the binder to sand ratios, adding shrinkage reducing agent (SRA), and replacing normal tap water with chilled water. These measures are expected to reduce the magnitudes of both drying shrinkage and autogenous shrinkage strains. Scanning electron microscopy (SEM) and thermal gravity (TG) analysis were also conducted to interpret the underlying mechanism governing both autogenous and drying shrinkages.

In the second paper entitled “The Influence of Steel Fibre Properties on the Shrinkage of Ultra-High Performance Fibre Reinforced Concrete”, the influences of the fibre aspect ratios, fibre dosage, fibre type, and hybridization of steel fibres with blended micro straight and hook end fibres were studied on magnitudes of both total and autogenous shrinkage strains. Direct pull-out tests were also conducted on steel fibres-concrete interface to establish the bond-slip relationships to assist in explaining the mechanism behind the autogenous shrinkage strains.



## List of manuscripts

1. Xie, T., Fang, C., Mohamad Ali, M.S. and Visintin, P. 2018. Characterizations of autogenous and drying shrinkage of ultra-high performance concrete (UHPC): An experimental study. *Cement and Concrete Composites* 91: 156-173.
2. Fang, C., Mohamed Ali, M.S., Xie, T., Visintin, P. 2019. The Influence of Steel Fibre Properties on the Shrinkage of Ultra-High Performance Fibre Reinforced Concrete. *Construction and building materials*. Submitted on 6<sup>th</sup> August 2019–(under review)

# Statement of Authorship

Title of Paper	CHARACTERIZATIONS OF AUTOGENOUS AND DRYING SHRINKAGE OF ULTRA-HIGH PERFORMANCE CONCRETE (UHPC): AN EXPERIMENTAL STUDY		
Publication Status	<input checked="" type="checkbox"/> Published	<input type="checkbox"/> Accepted for Publication	
	<input type="checkbox"/> Submitted for Publication	<input type="checkbox"/> Unpublished and Unsubmitted work written in manuscript style	
Publication Details	Xie, T., Fang, C., Ali, M. M., & Visintin, P. (2018). Characterizations of autogenous and drying shrinkage of ultra-high performance concrete (UHPC): An experimental study. <i>Cement and Concrete Composites</i> , 91, 156-173.		

## Principal Author

Name of Principal Author (Candidate)	Tianyu Xie		
Contribution to the Paper	Designing concept, conducting experiments, analysing of data, drafting manuscript		
Overall percentage (%)	40		
Certification:	This paper reports on original research I conducted during the period of my Higher Degree by Research candidature and is not subject to any obligations or contractual agreements with a third party that would constrain its inclusion in this thesis. I am the primary author of this paper.		
Signature		Date	12/02/2019


## Co-Author Contributions

By signing the Statement of Authorship, each author certifies that:

- i. the candidate's stated contribution to the publication is accurate (as detailed above);
- ii. permission is granted for the candidate to include the publication in the thesis; and
- iii. the sum of all co-author contributions is equal to 100% less the candidate's stated contribution.

Name of Co-Author	Chengfeng Fang		
Contribution to the Paper	Designing concept, conducting experiments, analysing of data, drafting manuscript (20%)		
Signature		Date	12/02/2019

Name of Co-Author	Dr Mohamed Ali Sadakkathulla		
Contribution to the Paper	Designing concept, analysing of data, revising manuscript (20%)		
Signature		Date	12/02/2019

Name of Co-Author	Associate Professor Phillip Visintin		
Contribution to the Paper	Designing concept, analysing of data, revising manuscript (20%)		
Signature		Date	12/02/2019

Please cut and paste additional co-author panels here as required.

## **2.1. Characterizations of Autogenous and drying shrinkage of ultra-high performance concrete (UHPC): An experimental study**

Xie, T.<sup>1</sup>, Fang, C.<sup>1</sup>, Mohamed Ali, M.S.<sup>1</sup>, \*Visintin, P.<sup>1</sup>

<sup>1</sup>School of Civil, Environmental and Mining Engineering, The University of Adelaide, SA  
5005, Australia

### **ABSTRACT:**

Due to the high content of binder and low water to cement ratio, ultra-high performance concrete (UHPC), exhibits higher levels of autogenous shrinkage compared to ordinary concrete. This shrinkage has been shown to lead to a reduction in strength over time as a result of the formation of thermal and shrinkage cracks. Aiming to mitigate the negative impacts associated with shrinkage, the efficacy of three different techniques to reduce the impact of shrinkage are investigated, namely: reducing the binder content; incorporating high levels of shrinkage reducing admixture; and using crushed ice to partially replace mixing water. The effects of these techniques are experimentally investigated and the underlying mechanisms of the actions are characterized. It is found that autogenous shrinkage predominates the overall shrinkage of UHPC and that the three techniques can effectively reduce shrinkage without significantly compromising its mechanical strength. The results also suggest, that from the perspective of reducing shrinkage: the optimal binder-to-sand ratio is in the range of 1 - 1.1; the optimal dosage rate of shrinkage reducing admixture is 1%; and replacing of mixing water by crushed ice up to 50% by weight has also induced a significant reduction in shrinkage.

**Keywords:** Ultra-high performance concrete (UHPC); Autogenous shrinkage; free total shrinkage; compressive strength; microstructure; hydration

### **2.1.1. INTRODUCTION**

Ultra-high performance concrete (UHPC) is characterized by very high compressive strength and superior durability (Mosaberpanah and Eren 2016; Shi et al. 2015; Singh et al. 2017; Wang et al. 2015; Yoo and Banthia 2016). These characteristics are typically achieved using mix designs with high quantities of binder (cement and silica fume) and low water to cement ratios (in the order of 0.2 or less). As a result, partially hydrated binder is often present within the mortar resulting in an increase in autogenous shrinkage (Wu et al. 2017; Youssef 2013) up to an order of magnitude greater than that of conventional concrete (Park et al. 2014; Soliman and Nehdi 2011; Soliman and Nehdi 2014; Yalçınkaya and Yazıcı 2017; Yoo et al. 2013; Yoo et al. 2014). Hence total shrinkage strains in UHPC (including both the autogenous- and drying-shrinkage) are expected to be higher than conventional concrete. This is significant as high early age shrinkage strains may result in early age cracking (Şahmaran et al. 2009; Sobuz et al. 2016; Wang et al. 2015; Yoo et al. 2014; Yoo et al. 2014); and if containing fibers, a reduction in strength over time due to the restraint provided by fibers (Soliman and Nehdi 2014; Yoo et al. 2017; Yoo et al. 2014; Yoo et al. 2014).

The importance of quantifying shrinkage strains has led to a number of recent studies aimed at understanding the underlying mechanisms governing autogenous shrinkage of UHPC and its impact on performance. For example, experimental programs conducted by Yoo et al. (Yoo et al. 2018; Yoo et al. 2018; Yoo et al. 2014) and Şahmaran et al. (Şahmaran et al. 2015; Şahmaran et al. 2009; Sahmaran et al. 2009) systematically examined the effects of mixing proportion, curing condition, geometry and specimen restraint on autogenous shrinkage of UHPC specimens. Research has also identified several means for reducing both the magnitude of shrinkage strains, as well as the time over which they develop. For example, Rößler et al. (Rößler et al. 2014) have shown that by curing at a temperature of 20 °C, a reduction of 85%

in autogenous shrinkage strains is possible compared to those obtained under at 90 °C heat curing. Alternatively (Dudziak and Mechtcherine 2008; Jensen 2013) have shown that it is possible to reduce drying shrinkage via the inclusion of moisture retaining superabsorbent polymers into the mix. These release water over time, replacing that lost due to hydration and drying, resulting in a reduction of shrinkage strains of up to 75%. The effects of shrinkage reducing admixtures on the autogenous shrinkage of UHPC have been investigated by (Koh et al. 2011; Soliman and Nehdi 2014; Yoo et al. 2015).

In this paper a standard UHPC mix which has been widely investigated at both the material (Sobuz et al. 2016; Sobuz et al. 2017; Visintin et al. 2018) and member levels (Singh et al. 2017; Sturm et al. 2018; Visintin et al. 2018) is taken as a baseline, and simple means for improving its dimensional stability is investigated. Approaches considered in this study include:

- The use of iced water in the mix design to lower concrete temperature and hence reduce the potential for autogenous shrinkage and temperature induced deformations (Smith 2001).
- Varying mix design proportions to identify the beneficial restraining influence of (fine) aggregate, and the presence of unhydrated binders that may act as a filler providing additional dimensional stability.
- Varying mix design proportions to identify the reduction in autogenous shrinkage due to a reduction in cementitious binder content.
- The use of high dosages of conventional shrinkage reducing admixtures to physically reduce shrinkage by reducing the surface tension in the concrete pore water.

For each approach investigated a range of material and characterization tests are conducted to determine the relative effectiveness of each approach, as well as the underlying mechanism of action. It is envisaged that this work will assist in allowing concrete technologists to decide on the most appropriate means for achieving the desired reduction in shrinkage.

In the remainder of the paper the characteristics and constituents of the UHPC materials investigated are first described. This is followed by a description of the experimental method and tests conducted; finally, the change in autogenous and drying shrinkage achieved by each approach is presented as well as a discussion of the mechanism of action.

## **2.1.2. EXPERIMENTAL PROGRAM**

### **2.1.2.1. Ingredients used for UHPC mix**

Two types of cementitious binder were used, namely sulphate resisting cement and silica fume. The sulphate resisting cement, which contains 3-8% gypsum by weight, has a 28-day compressive strength of 60 MPa and a 28-day mortar shrinkage strain of 650 (microstrain) as determined through the tests performed as per AS 2350. 11 (Australian Standard 2006) and AS 2350. 13 (Australian Standard 2006), respectively. The undensified silica has a bulk density of 635 kg/m<sup>3</sup> and has a silicon dioxide (SiO<sub>2</sub>) content over 89.6 %. A natural washed river sand with a maximum nominal grain size of 0.4 mm was used as the fine aggregate for all UHPC mixes. A third generation high range water reducer with an added retarder was added to each UHPC during the mixing. For the purpose of further minimizing shrinkage, a shrinkage reducing admixture (SRA), which meets and exceeds all requirements of Australian Standard 1478.1-2000 (Australian Standard 2000) as special purpose admixture type (SN), was added to the UHPC mix with different dosages. As an alternative to the use of an SRA, aiming to prevent the generation of a large amount of heat and therefore thermally and chemically induced plastic shrinkage cracks, the use of crushed ice to partially replace mixing water is also examined.

A total of ten batches of UHPC mortar were manufactured. The first five batches of UHPCs designated as U- series were prepared using the same water-to-binder (*w/b*) ratio but with different binder-to-sand (*b/s*) ratios. A UHPC mix with a *b/s* ratio of 1.266 and *w/b* ratio of

0.152, which was identified as optimal using the same raw materials in the previous study (Sobuz et al. 2016), was used as the reference mix design. Note that the water content from the chemical admixtures (i.e. 20% in SRA and 70% in SP) has been included in the calculation of the water-to-binder ratio for each mix. In the first stage of testing, the compressive strengths and total shrinkage strains of five batches of UHPC with varying  $b/s$  ratio were measured. The mix with the overall best performance was then taken for the second stage of testing. This stage included: the addition of SRA to three mixes in dosages of SRA-to-cement weight ratio of 1, 2 or 3% (designated as SRA series) or the addition of crushed ice (designated as Ice series) was incorporated into the remaining two UHPC mixes as a partial replacement of water by a weight ratio of 25 or 50%. The proportions of all mixes are given in Table 2-1-1. For manufacturing UHPCs, all the dry materials, including sand and binders were initially mixed in an 80 L capacity rotating pan mixer with fixed blades for approximately 5 minutes. Following the dry mixing, water, crushed ice, superplasticizer and SRA, were subsequently added to the mixer and the mixing was continued until the concrete started to flow.

Table 2-1-1. Mix proportion of the UHPCs

Mix	Cement (wr)	Silica fume (wr)	Sand (wr)	water (wr)	Crushed ice (wr)	SRA <sup>1</sup> (wr)	SP <sup>2</sup> (wr)	$w/b$	$b/s$	Paste weight fraction	Mixing water weight fraction
U-0.8	0.632	0.168	1.000	0.104			0.024	0.152	0.800	0.480	0.063
U-0.9	0.711	0.189	1.000	0.117			0.027	0.152	0.900	0.509	0.067
U-1.0/SRA-0/Ice-0	0.790	0.210	1.000	0.130			0.030	0.152	1.000	0.535	0.070
U-1.1	0.869	0.231	1.000	0.143			0.033	0.152	1.100	0.559	0.073
U-1.266	1.000	0.266	1.000	0.165			0.038	0.152	1.266	0.593	0.078
SRA-1	0.790	0.210	1.000	0.129		0.008	0.030	0.152	1.000	0.535	0.070
SRA-2	0.790	0.210	1.000	0.127		0.016	0.030	0.152	1.000	0.535	0.070
SRA-3	0.790	0.210	1.000	0.126		0.024	0.030	0.152	1.000	0.535	0.070
Ice-25/75	0.790	0.210	1.000	0.098	0.033		0.030	0.152	1.000	0.535	0.070
Ice-50/50	0.790	0.210	1.000	0.065	0.065		0.030	0.152	1.000	0.535	0.070

1. Containing 20% water; 2. Containing 70% water



### 2.1.2.2. Test concepts and methods

To assess the effectiveness of each approach in reducing shrinkage, standard shrinkage tests were performed according to Australian Standard 2350.13 (Australian Standard 2006) over a period of 180 days when subjected to constant environmental conditions (25 °C and humidity < 50%).

To monitor the total shrinkage properties of UHPCs, square prism specimens which were 75 mm wide, and 285 mm long (shown in Fig.2-1-1 (a)) were regularly monitored to measure the change in length. To provide an indication of the drying shrinkage relative to the total observed shrinkage, autogenous shrinkage was determined from the length change of the prisms in Fig. 2-1-1(b) which were carefully sealed with water-proof aluminum tape to prevent the moisture loss to the environment.



(a)

(b)

Figure 2-1-1. Shrinkage test specimens: a) sealed prism for autogenous shrinkage measurement; b) unsealed prism for free total shrinkage measurements

It is known that the evolution of autogenous shrinkage of cementitious composite is strongly related to the time when the paste develops a ‘stable’ solid skeleton to transfer tensile stress, which is defined as ‘time-zero’ for autogenous shrinkage measurement. In the present study,

the final setting time obtained from calorimetry curve was adopted as the ‘time-zero’ where autogenous shrinkage initiated in according to ASTM C1698-09 (ASTM 2009) and the studies reported previously (Darquennes et al. 2011; Mechtcherine et al. 2014).

To further characterize the materials tested, and in order to identify the mechanisms controlling the change in shrinkage, a series of further material and characterization tests were undertaken as follows:

#### ***2.1.2.2.1. Compressive strength***

The compressive strengths ( $f'_c$ ) of the UHPCs at different concrete ages were obtained through axial compression tests, performed on cylinders (100 mm diameter × 200 mm height) in accordance with Australian Standard (Standard Australia 2014).

#### ***2.1.2.2.2. Flowability and passing ability***

The rheological properties of each mix was assessed through a slump flow test performed in accordance with ASTM standard C143/C143M (ASTM International 2000) and a flow-table test according to ASTM C1621 (ASTM International 2009) including the use of a J-ring to assess passing ability around reinforcement.

#### ***2.1.2.2.3. Exothermic reaction at early curing ages***

Heat generated as a result of the exothermic reaction associated with cement hydration accelerates the autogenous shrinkage of the concrete (Kadri and Duval 2009; Langan et al.

2002) and may result in the formation of micro-cracks (Aitcin 1999; Kim et al. 2011; Lura et al. 2003). To examine the exothermic reaction of the UHPCs, a thermal sensor was embedded at the center of a 100 mm cubic specimen. The ambient room temperature and internal concrete temperature was also continuously recorded monitored for a period of three days, after which no significant change in temperature occurred.

#### ***2.1.2.2.4. Unit weight and porosity***

The unit weight of the hardened UHPCs was obtained by weighing concrete cylinders (100 mm diameter ×200 mm height) 90 days after casting, such that the hydration reaction can be considered to be complete. The porosity of each series of the UHPC was quantified by measuring the volume of pore space voids in disc specimens of 150 mm diameter and 50 mm thickness through tests performed in accordance with ASTM C642-13 (ASTM International 2013) using a hot water bath. Measurements of porosity were taken because porosity of concrete is an essential indicator associated with not only the mechanical strength but also the durability characteristics of the concrete.

#### ***2.1.2.2.5. Scanning electron microscopy (SEM) analysis and Energy-dispersive X-ray spectroscopy (EDS)***

Scanning electron microscopy (SEM) characterization was performed to evaluate the microstructure of the UHPC matrix and hence assist in identifying the: unreacted binder component, homogeneity of the matrix, and pores and cracks seen in the microstructure of the matrix. Energy-dispersive X-ray spectroscopy (EDS) analysis was also conducted to identify any change in the hydration products resulting from the shrinkage reduction methods applied.

#### **2.1.2.2.6. Thermal gravity (TG) analysis**

Thermal gravity (TG) analysis was undertaken to estimate the degree of hydration of the UHPC 90-days after casting. The analysis was undertaken to assess both the non-evaporable water content and the calcium hydroxide ( $\text{Ca}(\text{OH})_2$ ) content. These approaches have been commonly applied cementitious mortar, for example see (Bentz 2005; Chen and Wu 2013; Maltais and Marchand 1997).

TG analysis was conducted using METTLER TOLEDO TGA testing machine, for each mix a sample weighing 2.5 kg was oven-dried at 105 °C for 24 hours to remove the evaporable water, and the sample was then pulverized to a size of < 45µm. About 20 µg of this sample was placed in a ceramic crucible and heated in the furnace from ambient temperature to 900 °C in a nitrogen atmosphere at a rate of 10 °C/min to determine the weight loss of matrix due to decomposition of the hydration products.

##### **2.1.2.2.6.1. Non-evaporable water content**

The amount of hydration products and the degree of hydration ( $D_h$ ) of UHPC is obtained by determining the non-evaporable water content ( $W_{ne}$ ) using loss-on-ignition (LOI) method. Cementitious paste is commonly used for this test as the non-evaporable water content is present due to the reactive cementitious binders only, and the degree of hydration is strongly correlated with the  $w/b$  ratio of the cementitious paste (Huang et al. 2017; Lam et al. 2000; Yio et al. 2014). The effects of coarse and fine aggregates on hydration are usually ignored due to their inertness. It is worth noting that in this study cement mortar was used instead of cement paste as the: pore diameter, paste-to aggregate interfacial transition zone (ITZ), distribution of aggregate and the mixing efficiency are all affected by the aggregate content, and hence their

effects on hydration cannot be neglected. The LOIs of the UHPC mortar were estimated using the LOIs of cementitious powder without moisture damage and considering the LOIs of the sand (Bentz 2005; Chen and Wu 2013; Maltais and Marchand 1997).

Previous studies by Lam et al. and Wong et al. (Lam et al. 2000; Wong and Buenfeld 2009) have shown that absolute hydration of 1g anhydrous cement can produce approximately 0.23g of non-evaporable water and this non-evaporable water content-to-cement ratio ( $W_{ne0}/C_0$ ) of 0.23g/g was applied as the reference value to determine the degree of hydration of the UHPCs in the following calculations for  $D_h$ .

To calculate  $D_h$ , the  $LOI_{raw}$  of the raw cementitious powder, silica fume and sand are firstly calculated using:

$$LOI_{raw} = \frac{(W_{d-raw} - W_{i-raw})}{W_{i-raw}} \quad (2-1)$$

where  $W_{d-raw}$  is the dry weight of the as-received raw material, and  $W_{i-raw}$  is the ignited weight of the as-received raw material after TG test. These  $LOI_{raw}$  values are required to correct the calculations of non-evaporable water content ( $W_{ne}$ ) as follows:

$$W_{ne} = [W_{d-U} - W_{i-U} * (1 + \sum LOI_{raw})] \quad (2-2)$$

where  $W_{d-u}$  is the dry weight of the UHPC mortar sample,  $W_{i-u}$  is the ignited weight of the UHPC mortar sample after TG test and  $\sum LOI_{raw}$  is the total ignited weight of the as-received raw materials, including sand cement and silica fume. The effective residual cementitious binder content ( $C_{eff}$ ) is calculated by

$$C_{eff} = \left[ W_{i-U} * \left( 1 - \frac{\sum LOI_{raw}}{W_{ne0}/C_0} \right) \right] \quad (2-3)$$

Finally, the degree of hydration of UHPC ( $D_h$ ) is defined as the function of  $W_{ne}$ , effective residual cementitious binder content ( $C_{eff}$ ) and the reference value of the non-evaporable water content-to-cement ratio ( $W_{ne0}/C_0$ ), as given in Eq. (2-4):

$$D_h(\%) = \frac{W_{ne}/C_{eff}}{W_{ne0}/C_0} \times 100 \quad (2-4)$$

The loss of the non-evaporable water that is chemically bonded in hydration products can be determined by calculating the difference in weights between at 100°C and 700 °C from TG. This temperature interval is selected to avoid the interference due to the water evaporation at 100 °C and de-carbonation of calcium carbonate (CaCO<sub>3</sub>) of the composite when the temperature overs 700 °C (Vedalakshmi et al. 2003).

#### 2.1.2.2.6.2. Calcium hydroxide (Ca(OH)<sub>2</sub>) content

A fully hydrated cementitious-silica fume material usually consists of dicalcium silicate (C<sub>2</sub>S) and tricalcium silicates (C<sub>3</sub>S) (Brunauer and Kantro 1964; Hasanzadeh et al. 2016; Newman et al. 2005). The formations of these calcium silicates (C<sub>n</sub>S) consume around 20-25 % by weight of the water in the mix and produce 20-25 % by weight of the calcium hydroxide (Ca(OH)<sub>2</sub>). Therefore, the degree of hydration of the UHPC can also be assessed by the Ca(OH)<sub>2</sub> content in the concrete. The amount of Ca(OH)<sub>2</sub> products can be determined by calculating the drop in weight of the sample within 400 to 450 °C during TG tests (Dweck et al. 2000; Vedalakshmi et al. 2003), which indicates the decomposition of Ca(OH)<sub>2</sub> in the hydration products.

In the remainder of the paper the effectiveness of each shrinkage reduction approach including 1) reducing binder usage; 2) using SRA; 3) partially reducing mixing water with crushed ice will be presented and the mechanism of their action explored using the characterization tests above.

### 2.1.3. EFFECT OF BINDER-TO-SAND RATIO ON THE PROPERTIES OF THE UHPCS

#### 2.1.3.1. Flowability of concrete

Table 2-1-2 presents the results of slump flow and flow-table tests of the UHPC specimens, from which it can be inferred that the flow- and passing ability of the UHPC generally increased with an increase in the  $b/s$  ratio. This can be attributed to the fact that the increased  $b/s$  ratio in the UHPC mix resulted in an increased volume of paste that covered the surface of the fine aggregates leading to the reduction in friction between the sand particles in the fresh UHPC (Hermida et al. 2009).

Table 2-1-2. Influence of binder-to-sand ratio on rheological properties of fresh UHPCs

Specimen	$b/s$ ratio	Slump (mm)	Flow table (mm)	J-ring (mm)
U-0.8	0.8	165	375	412
U-0.9	0.9	240	440	451
U-1.0	1	235	425	443
U-1.1	1.1	250	430	455
U-1.266	1.266	250	470	506

#### 2.1.3.2. Autogenous shrinkage

The autogenous shrinkage strains ( $\epsilon_a$ ) plotted in Fig. 2-1-2 for each mix with a different  $b/s$  ratio, were measured using the sealed prisms shown in Fig. 2-1-1(b). These values can be seen to decrease with an increase in  $b/s$  ratio. Further it is also observed that for all mixes, regardless of the variation in  $b/s$ , the autogenous shrinkage began to plateau 42 days after casting, indicating the completion of hydration. At the concrete age of 42 days, the  $\epsilon_a$  of U-1.266 was up to 35% lower than those of the companion specimens. Furthermore, the UHPC prepared using a higher  $b/s$  ratio (i.e. U-1.1 and -1.266 series) exhibited a lower rate of autogenous shrinkage gain which can be inferred by the reduced slope of the curves.

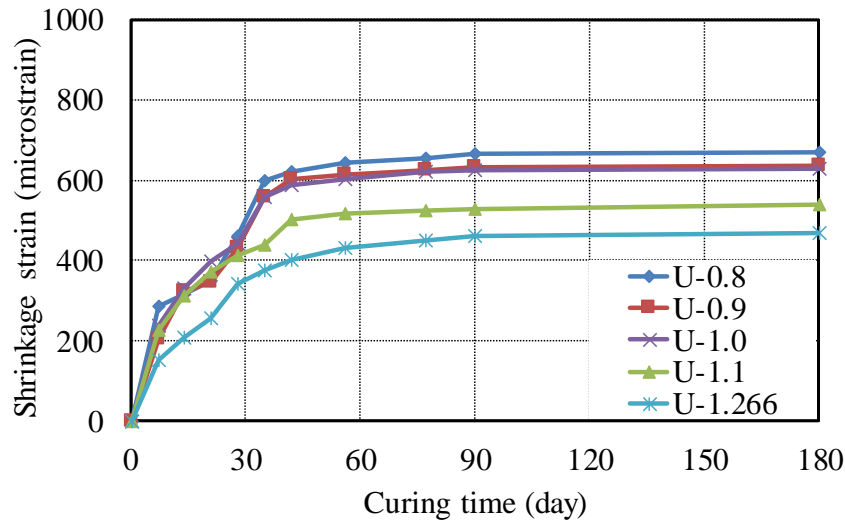


Figure 2-1-2. Effect of binder-to-sand ratio on autogenous shrinkage

Moreover, when comparing the autogenous shrinkage strains in Fig. 2-1-2 with those expected from conventional concrete (e.g. (Bentur et al. 2001; Zhang et al. 2003)) for a given age (i.e. concrete age of 28 days), the autogenous shrinkage of UHPCs (>400 microstrain) are significantly higher than those of the conventional normal- and high- strength concrete (< 150 microstrain). This difference is because the increased binder and reduced mixing water in UHPC means it tends to undergo a more rapid self-desiccation than conventional concrete and potentially to form more micro-cracks as further shown and discussed in Section 2.3.9.

### 2.1.3.3. Free total shrinkage

Figure 2-1-3 illustrates the effect of  $b/s$  ratio on free total shrinkage measured using the unsealed prisms shown in Figure 2-1-1 (a). Similar to the results of the autogenous shrinkage tests, the free total shrinkage strains ( $\epsilon_t$ ) of the UHPC specimens generally decreased with an increase in  $b/s$  ratio for a given concrete age. Unlike the autogenous shrinkage tests, where the shrinkage deformations stabilized at 42 days, it is observed that the free total shrinkage increased in all five mixes continued up to the concrete age of 90 days. This is due to the



continuous drying of the UHPCs, which is associated with loss of moisture from the concrete to the environment and is in contrast to the significant slowing of autogenous shrinkage after 42 days as a result of the decreased rate of hydration.

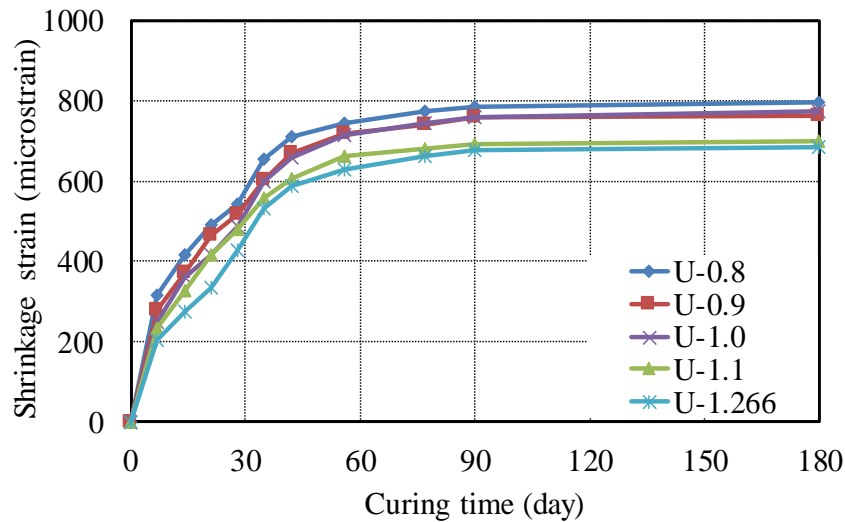


Figure 2-1-3. Effect of binder-to-sand ratio on free total shrinkage

#### 2.1.3.4. Assessment of free drying component

The free drying shrinkage component of the UHPCs can be estimated and assessed by the difference between the free total (solid line) and autogenous (dashed line) shrinkage properties shown in Fig. 2-1-4 (a) to (e). It is evident from the Fig. 2-1-4 that at the early curing ages (i.e. before the concrete age of 7 days), the difference between the free total and autogenous shrinkage of each UHPC series was negligible. The difference between the  $\epsilon_a$  and  $\epsilon_t$  of each series increased up to 110% with an increase in the  $b/s$  ratio from 0.8 to 1.266 at the concrete age of 180 days. Note that although the  $w/b$  ratio for a UHPC mix is low, with adequate mixing energy the moisture (including water and superplasticizer) can be evenly distributed to form a high paste volume (Russell and Graybeal 2013; Schießl et al. 2007). This suggests that more moisture was able to diffuse from the UHPC for mixes with a higher paste volume owing to the higher  $b/s$  ratio, as reported in Table 2-1-1, and the observation is in consistent with previous research (Ma et al. 2004; Shen et al. 2016; Soliman and Nehdi 2013). In addition, as

illustrated in Fig. 2-1-4 (a) and (b), the drying shrinkage component of each specimen was significantly lower than the corresponding autogenous shrinkage at each given concrete age, indicating that the autogenous shrinkage predominates the overall free total shrinkage of UHPCs.

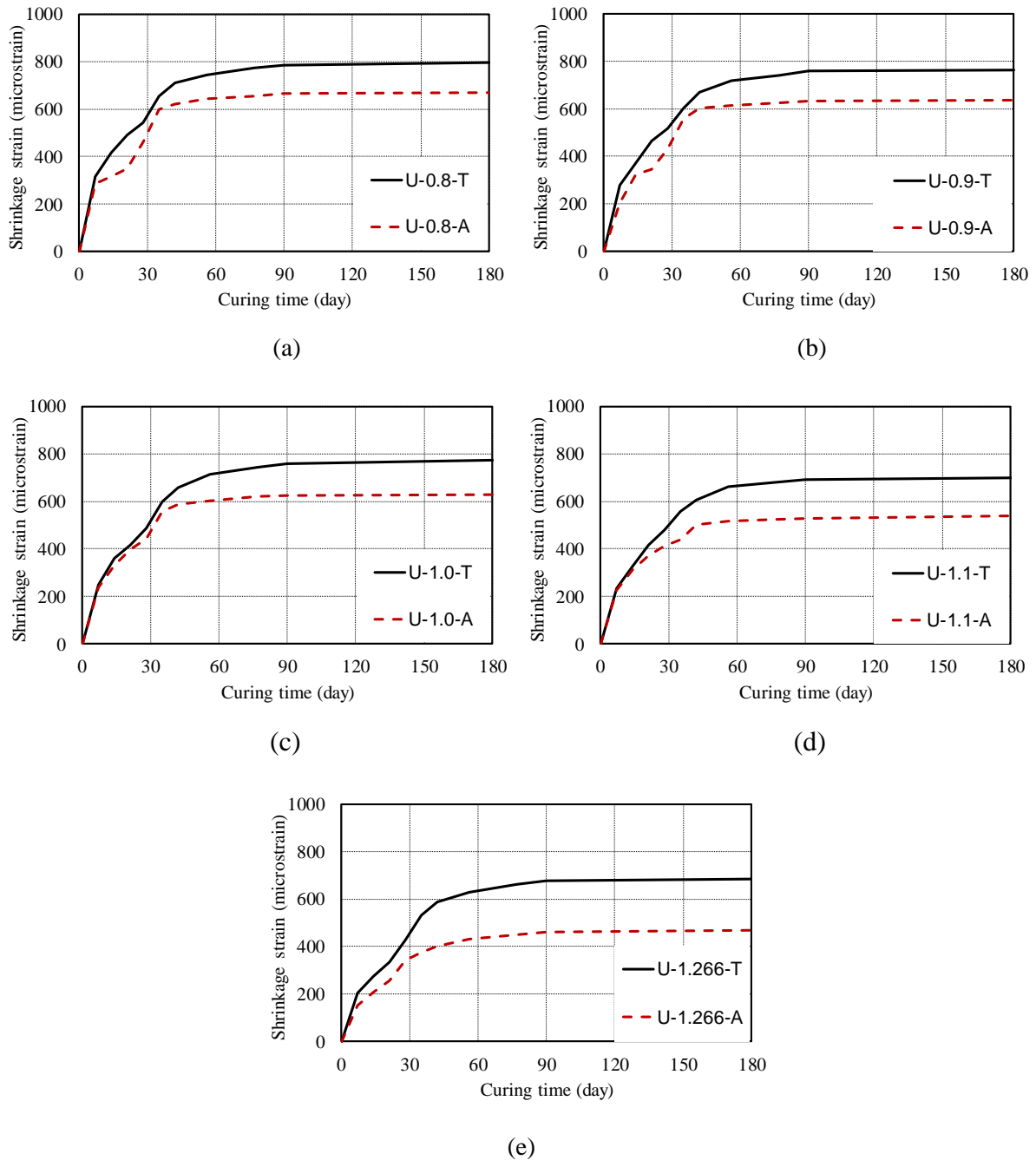


Figure 2-1-4. Effect of binder-to-sand ratio on free drying component: a) U-0.8; b) U-0.9; c) U-1.0; d) U-1.1; (e) U-1.266

### 2.1.3.5. Assessment of free drying component

The free drying shrinkage component of the UHPCs can be estimated and assessed by the difference between the free total (solid line) and autogenous (dashed line) shrinkage properties shown in Fig. 2-1-4 (a) to (e). It is evident from the Fig. 2-1-4 that at the early curing ages (i.e. before the concrete age of 7 days), the difference between the free total and autogenous shrinkage of each UHPC series was negligible. The difference between the  $\varepsilon_a$  and  $\varepsilon_t$  of each series increased up to 110% with an increase in the  $b/s$  ratio from 0.8 to 1.266 at the concrete age of 180 days. Note that although the  $w/b$  ratio for a UHPC mix is low, with adequate mixing energy the moisture (including water and superplasticizer) can be evenly distributed to form a high paste volume (Russell and Graybeal 2013; Schießl et al. 2007). This suggests that more moisture was able to diffuse from the UHPC for mixes with a higher paste volume owing to the higher  $b/s$  ratio, as reported in Table 2-1-1, and the observation is in consistent with previous research (Ma et al. 2004; Shen et al. 2016; Soliman and Nehdi 2013). In addition, as illustrated in Fig. 2-1-4 (a) and (b), the drying shrinkage component of each specimen was significantly lower than the corresponding autogenous shrinkage at each given concrete age, indicating that the autogenous shrinkage predominates the overall free total shrinkage of UHPCs.

### 2.1.3.6. Compressive strength

The effect of  $b/s$  ratio on  $f'_c$  is shown in Fig. 2-1-5. It is observed that the U-1.266 series developed a lower compressive strength than the other four companion mixes for a given age. The reduction in strength associated with the reduction in fine aggregate could be a result of the mechanism of stress transfer within the concrete as per the well-known theory for conventional mortars (Reddy and Gupta 2008). That is the transfer of normal force in a mortar is largely due to the interaction of sand to sand interfaces. For the UHPC with a lower  $w/b$  ratio,

its compressive strength is not predominated by failures of cementitious paste but by adhesive failures between aggregates and cementitious materials (Jun et al. 2004; Park et al. 2008). The presence of excessive unhydrated cementitious materials in the UHPC series with higher binder content weakened the interfacial transition zones (ITZs) between the fine aggregate and binder, which led to the observed reduction in compressive strength. It is also worth noting in Fig. 2-1-5 that, all these five UHPC series experienced reduction (up to 5.3%) in their compressive strengths within the curing age from 90 to 180 days, as shown in Fig. 2-1-5 (b). This reduction in the  $f'_c$  was caused by the formation of internal micro cracks (discussed further in section 2.3.9) as a consequence of the increased shrinkage of the concrete (Sobuz et al. 2016). The above observations indicate that the most appropriate  $b/s$  ratio for UHPC should be within 1 to 1.1 to achieve adequate aggregate interaction without compromising the  $f'_c$ .

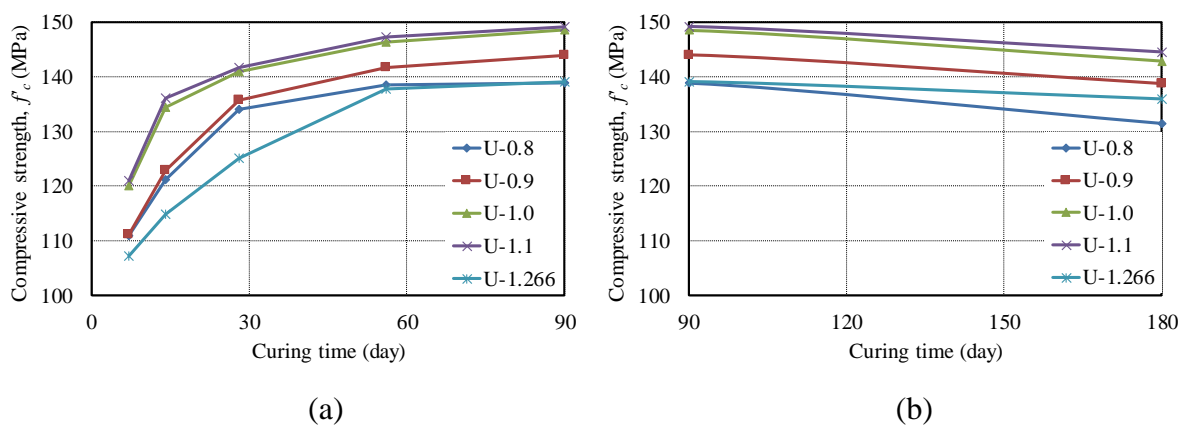


Figure 2-1-5. Effect of binder-to-sand ratio on compressive strength: (a) curing time from 0 to 90 day; (b) curing time from 90 to 180 day

### 2.1.3.7. Unit weight and porosity of the UHPCs

Figure 2-1-6 shows the effect of  $b/s$  ratio on the unit weight and porosity of the hardened UHPCs measured at the concrete age of 28 days. It is observed that the unit weight of the UHPC increased with an increase in  $b/s$  ratio due to the higher unit weight of the cementitious materials (approximate  $3500 \text{ kg/m}^3$ ) compared to that of the sand (approximate  $2000 \text{ kg/m}^3$ ).

The porosity of the UHPC also decreased approximately 10 % with an increase in  $b/s$  ratio from 0.8 to 1.266. This reduction in porosity may be attributed to the increased amount of residual unhydrated binder which fills the pore spaces. The reduction in binder also reduces the total amount of porous ITZs around the sand particles (Brough and Atkinson 2000; Scrivener et al. 2004).

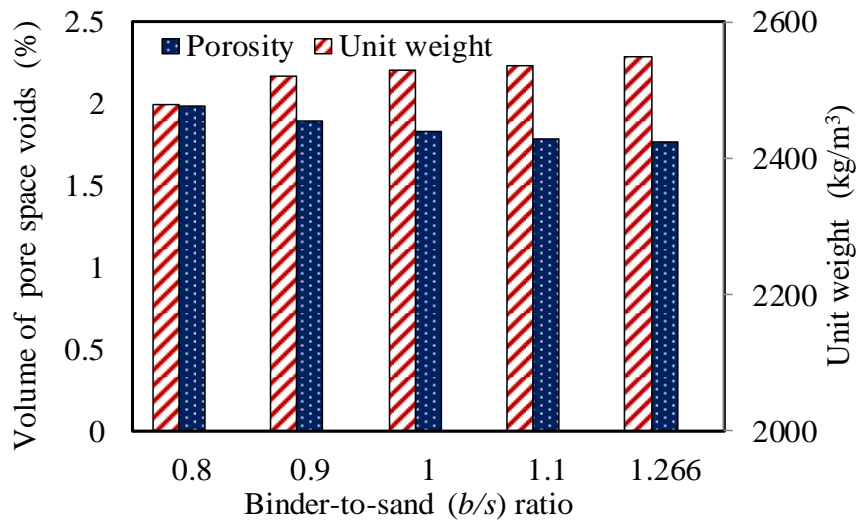


Figure 2-1-6. Effects of binder-to-sand ratio on unit weight and porosity of hardened UHPCs

### 2.1.3.8. Exothermic reaction at early curing period

Figure 2-1-7 illustrates the variations of internal temperature of the five different specimens with the curing time. It is worth noting that the temperature measured at the center of each UHPC series was normalized by the corresponding ambient temperature in order to remove its influence. From the calorimetry curves in Fig. 2-1-7, it can be observed that a decrease in  $b/s$  ratio led to an increase in the magnitude of the peak temperature measured at the center of the sample, with the maximum magnitude of change being approximately 10%. The increase in temperature with a reduction in  $b/s$  indicates that the UHPC with a lower  $b/s$  ratio had a higher degree of exothermic reaction and generated more heat as the consequence of a higher degree of reaction. This is due to the residual unhydrated binders in the UHPC with a higher  $b/s$  which act to fill the pores and voids and absorbed water to their surface, which hindered the level and

rate of hydration in the concrete (Yu et al. 2014). These facts can be further verified using the TG analysis and SEM characterizations presented in the following sections. The above observation indicates that the UHPC prepared using a lower  $b/s$  ratio underwent a more significant chemical reaction process, which consumed more raw materials and achieved a higher degree of hydration. Therefore, UHPC prepared using a lower  $b/s$  ratio tended to have a more significant autogenous shrinkage at the early curing stage, which can be inferred from the curves in Fig. 2-1-2.

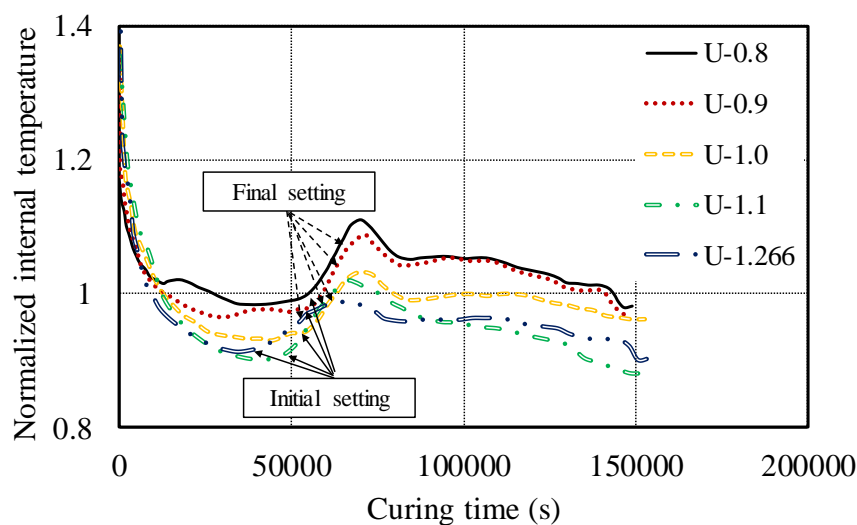


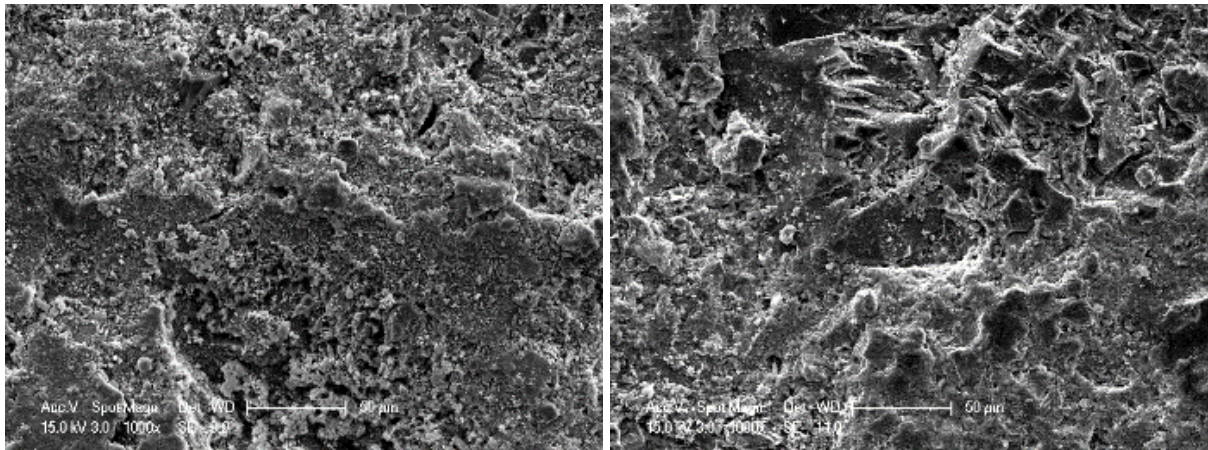
Figure 2-1-7. Effect of binder-to-sand ratio on variations of the internal temperature with curing time

The initial and final setting times of each mix can be identified as the first trough and the end point of the linear ascending branch on the calorimetry curves in Fig. 2-1-7. These points were also affected by the  $b/s$  ratio, in which the initial and final setting time of the UHPC were delayed by approximately 4 hours when the highest quantity of aggregate was considered. This could be explained by the fact that the increased amount of aggregates hindered the contact between water and binder which led to a longer induction period (referred to the initial gentle trough stage) and resulted in this later setting of the concrete (Jennings and Pratt 1979; Odler 1998).

### **2.1.3.9. Morphological characterization by scanning electron microscopy (SEM) and Energy-dispersive X-ray spectroscopy (EDX)**

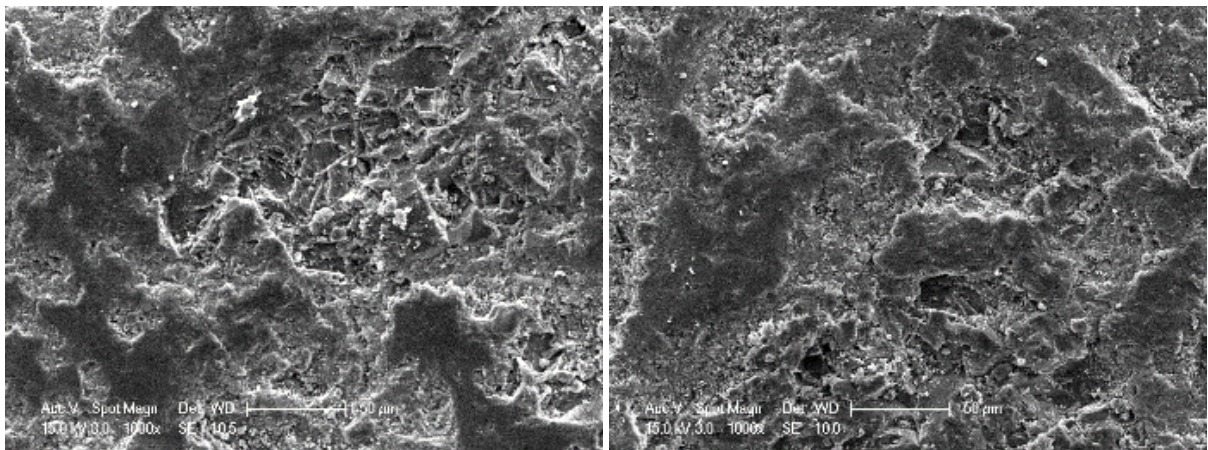
The scanning electron microscopy (SEM) micrographs were evaluated to investigate the effect of  $b/s$  ratio on the microstructure of the UHPCs, as depicted in Figs. 2-1-8 and 2-1-9 at different magnifications. It is evident from the SEM micrographs at 1000 $\times$  magnification that the increased volume of cementitious paste (at higher  $b/s$  ratio) led to a much denser microstructure as a result of the reduction in volume fraction of the porous aggregate-paste ITZs. This fact also caused by the micro-filler effect offered by unreacted cementitious binders. Moreover, as shown on the SEM micrographs at 10000 $\times$  magnification, a large amount of ettringite ( $3\text{CaO}\cdot\text{Al}_2\text{O}_3\cdot 3\text{CaSO}_4\cdot 32\text{H}_2\text{O}$ ) and calcium hydroxide (C-H) were observed and characterized using EDX spectroscopy in the microstructure of the UHPC prepared using the lower  $b/s$  ratio (i.e. U-0.8, and -0.9). This is because the increased porosity in the concrete provided the space for the growth of ettringite and C-H crystals owing to their expansive nature (Mehta 1973). For the UHPC prepared using a relatively higher  $b/s$  ratio (i.e. U-1.0, -1.1 and -1.266), a larger amount of unreacted cementitious materials were detected, as indicated in Fig. 2-1-9. Ettringite and C-H crystals were rarely observed in the matrix of U-1.0, -1.1 and -1.266 series owing to the increased denseness and reduced pore space in their matrix shown in Fig. 2-1-8. The presence of these unreacted binders may restrain the shrinkage of the matrix contributing to the reduction in autogenous- and drying- shrinkage shown in Figs. 2-1-2 and 2-1-3. The presence of the unreacted binder is also a clear indication of the decreased degree of hydration in the UHPC prepared using a higher  $b/s$  ratio. It is worth mentioning that the observed increased pore space in UHPC adversely affected the drying shrinkage of the concrete, which seemingly contradicts to the observations reported in the literature (Han and Lytton 1995). The possible explanation is that the expansion resulting from the abundance of crystalline ettringite and C-H in the pores and cracks was more significant than the drying shrinkage of the concrete (Mehta

1973; Yan et al. 2004). To verify the deduction on the decrease in mechanical strength of UHPC after a long-term curing, Fig. 2-1-10 illustrates a representative SEM micrograph of U-1.1 series with the indications of the micro-cracks that were induced by thermal and autogenous shrinkage.



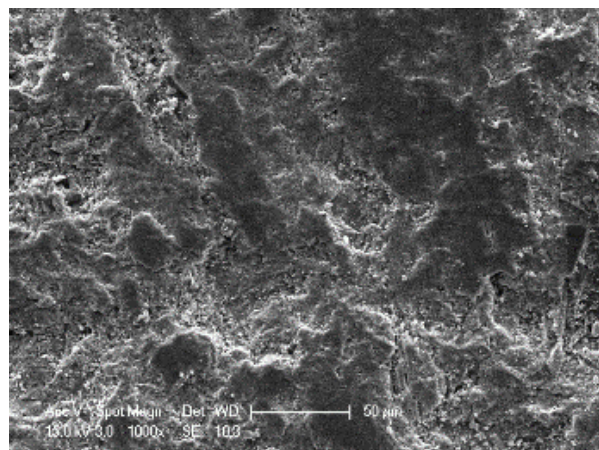
(a)

(b)



(c)

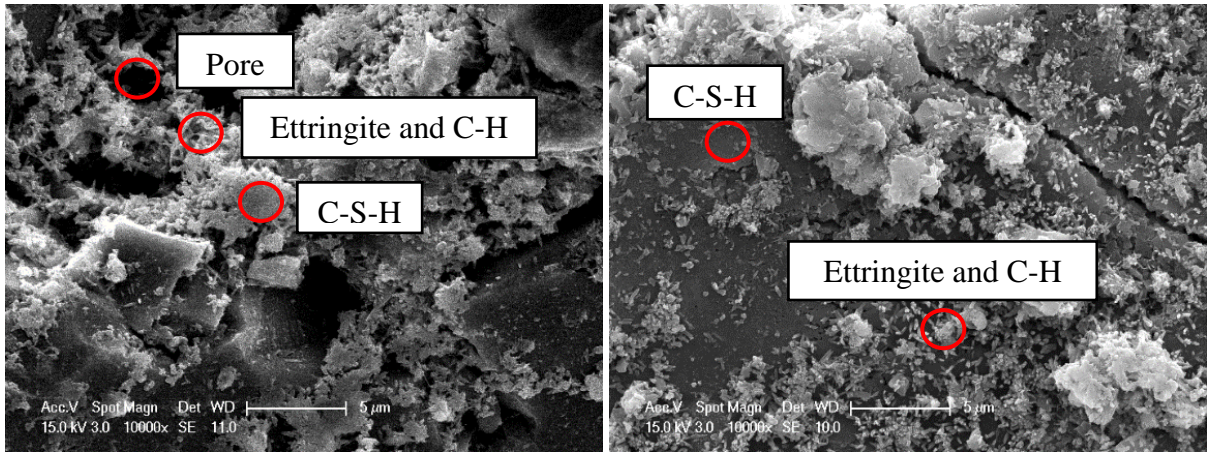
(d)





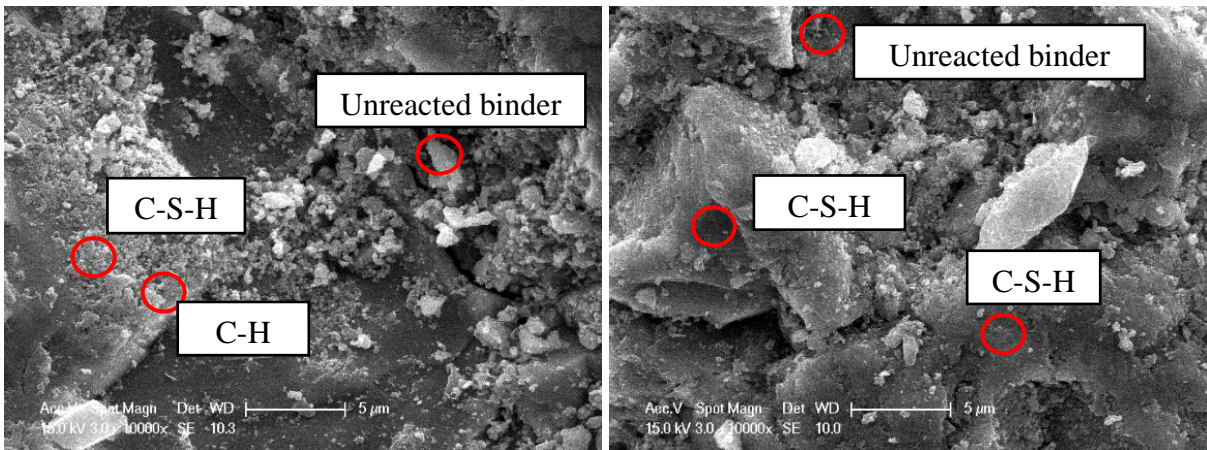
(e)

Figure 2-1-8. SEM images of the fracture surface of the UHPCs (1000× magnification): a) U-0.8; b) U-0.9; c) U-1.0; d) U-1.1; e) U-1.266



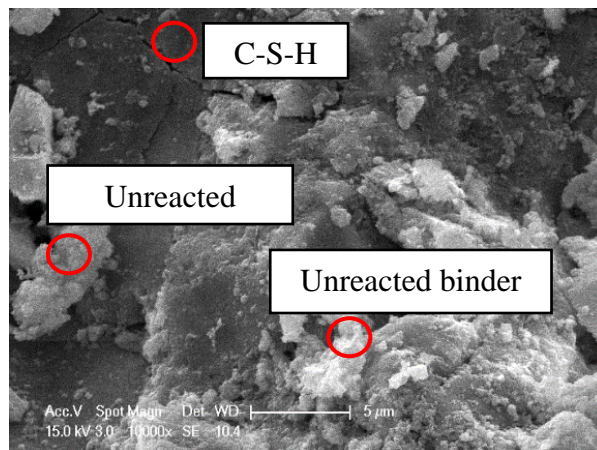
(a)

(b)



(c)

(d)



(e)

Figure 2-1-9. SEM images of the fracture surface of the UHPCs (10000× magnification): a) U-0.8; b) U-0.9; c) U-1.0; d) U-1.1; e) U-1.266

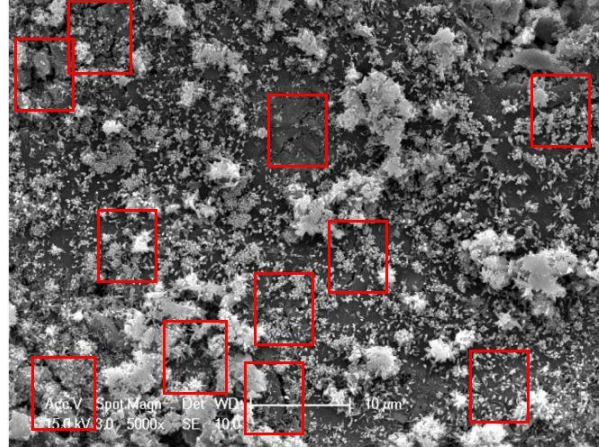


Figure 2-1-10. Observed shrinkage induced micro-cracks in the micro-structure of the UHPC

#### 2.1.3.10. Results of thermal gravity (TG) analysis

The TGA curves of the comparing UHPCs are shown in Fig. 2-1-11 and the effect of binder to sand ratio on the degree of hydration and C-H content are shown in Fig. 2-1-12. It should be noted that the paste weight fraction factor for each specimen series, as given in Table 2-1-1, was considered in the calculations of the chemically bonded water and C-H content of the paste that is the actual materials for hydration. In general, except for U-0.8 series, the calculated degree of hydration and the C-H content decreased with an increase in the  $b/s$  ratio (i.e. up to approximately 18% lower). While the  $w/b$  ratio remained the same for the mixes being compared, the UHPC prepared using a higher  $b/s$  underwent a lower degree of hydration and hence contained less hydration products. This further confirmed the previously observed less significant autogenous shrinkage for the UHPC prepared using a lower  $b/s$  ratio.

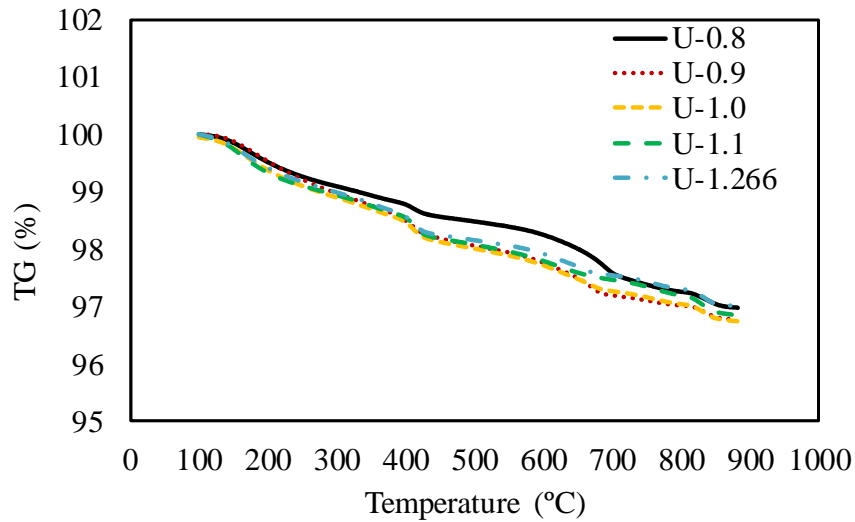


Figure 2-1-11. TG analysis for U-0.8, -0.9, -1.0, -1.1, and -1.266 UHPC series

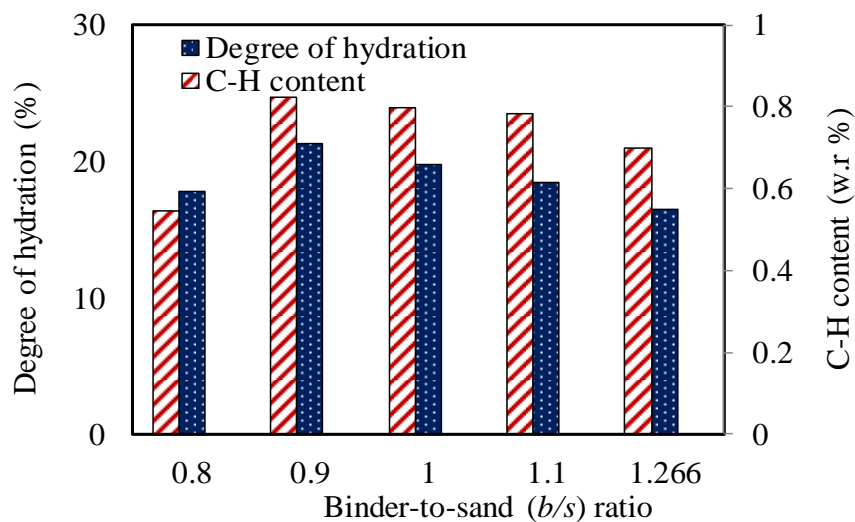


Figure 2-1-12. Effect of binder-to-sand ratio on degree of hydration and C-H content

### 2.1.3.11. Selection of the mix for further investigations to migrate autogenous shrinkage

A comprehensive study of the experimental results of among U-0.8, -0.9, -1.0 -1.1 and -1.266 UHPC series led to the selection of the mix design of U-1.0 as the mix for further investigation. These investigations include: the incorporation of shrinkage reducing admixture (SRA) and the used crushed ice to partially replace mixing water. Mix designs for the second stage of this work are shown in Table 2-1-3.

Table 2-1-3. Effect of SRA content on rheological properties of fresh UHPCs

Specimen	<i>b/s</i> ratio	SRA content (%)	Slump (mm)	Flow table (mm)	J-ring (mm)
SRA-0	1	0	235	425	443
SRA-1	1	1	280	512	529
SRA-2	1	2	Full	579	568
SRA-3	1	3	Full	560	585

## 2.1.4. EFFECTS OF APPLIED TECHNIQUES ON THE PROPERTIES OF THE UHPCS

### 2.1.4.1. Flowability

#### 2.1.4.1.1. Effect of shrinkage reducing admixture (SRA) content

For the flow test results reported in Table 2-1-3, it can be seen that the UHPC series prepared with a higher SRA content exhibited better flowability and passing ability. This is due to the higher liquid content (i.e. 80% of the organic liquid component in SRA) in the UHPC mix with a higher SRA content that provides better lubrication, resulting in a better rheology of the UHPC.

#### 2.1.4.1.2. Effect of crushed ice dosage

The flow test results presented in Table 2-1-4 indicate that that the replacement of water with crushed ice had negligible impact on the flowability and passing ability of the UHPC as the added crush ice completely melted after sufficient mixing. The temperature of the mixing water was recorded immediately prior to adding to the mixer. For mixes without using crushed ice the water temperature was found to be the same as the ambient temperature (i.e. 25 °C) while for water with crushed ice the temperature was found to be 2.6°C and 1.2°C at 25% and 50% replacement ratio (by weight) respectively. The incorporations of crushed ice in a UHPC mix

are expected to reduce the internal temperature of the specimens and hence lessen the potential formations of thermal cracks.

Table 2-1-4. Effect of crushed ice dosage on rheological properties of fresh UHPCs

Specimen	<i>b/s</i> ratio	Crushed ice dosage (%)	Slump (mm)	flow table (mm)	J-ring (mm)
Ice-0	1	0	235	425	443
Ice-25/75	1	25	240	418	456
Ice-50/50	1	50	235	431	462

### 2.1.4.2. Autogenous shrinkage

#### 2.1.4.2.1. Effect of shrinkage reducing admixture (SRA) content

Figure 2-1-13 shows the effects of SRA contents on the autogenous shrinkage of the UHPC. It can be seen that the  $\epsilon_a$  of the UHPC decreased significantly with an increasing SRA content (up to approximately 69% for UHPC at age of 90 days). It is also observed that the SRA started reducing the autogenous shrinkage right after the initial casting of the UHPC. As stated by Collepardi et al., Folliard et al. (Collepardi et al. 2005; Folliard and Berke 1997) and Lura et al. (Lura et al. 2003), SRA incorporation eases the surface tension in the capillary pores of the concrete and subsequently reduces the drying- and autogenous- shrinkage of the concrete. The reduction in autogenous shrinkage with incorporation of SRA seen in the present study is also in reasonable agreement with those reported by studies on UHPC mortar. For example, Su et al. (Anshuang et al. 2017) reported an up to 95% reduction in autogenous shrinkage with 2% SRA dosage at 7 days (compared to 65.6 % as reported in the present study) and an approximated 61% reduction in autogenous shrinkage with 2% SRA dosage at 160 days was observed by Soliman and Nehdi (Soliman and Nehdi 2014) (compared to 57.8% as reported in the present study). In addition, the comparison of the efficacy of using SRA on autogenous

shrinkage between UHPC and conventional cementitious mortar (i.e. as reported in (Bentz et al. 2001)) suggests the nearly the same performance of SRA to reduce autogenous shrinkage at a given dosage of SRA.

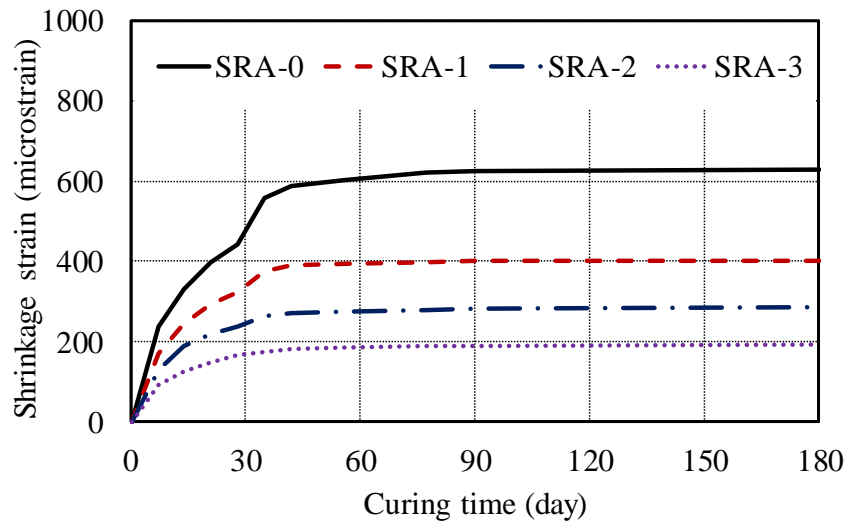


Figure 2-1-13. Effect of SRA content on autogenous shrinkage properties

#### 2.1.4.2.2. Effect of crushed ice dosage

The effect of crushed ice on the autogenous shrinkage of the UHPCs is depicted in Fig. 2-1-14. At each given curing age, the UHPC manufactured using a higher crushed ice exhibited a lower  $\epsilon_a$  (up to approximately 19 % at concrete age of 180 days). This observation is expected as the internal temperature of UHPC decreased with the incorporation of crushed ice, which led to the deceleration of the rate of hydration of the concrete and hence reduced autogenous shrinkage.

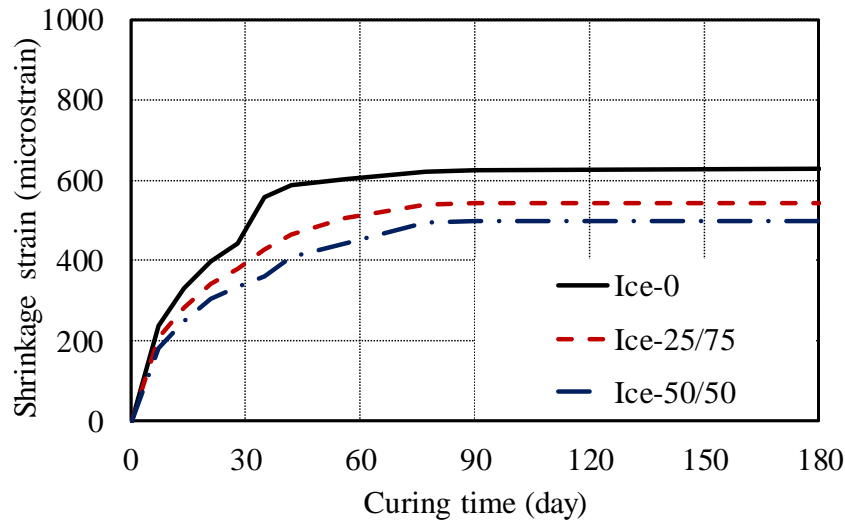


Figure 2-1-14. Effect of crushed ice dosage on autogenous shrinkage properties

### 2.1.4.3. Free total shrinkage and assessment of free drying component

#### 2.1.4.3.1. Effect of shrinkage reducing admixture (SRA) content

The effect of SRA content on the free total shrinkage of the UHPC is illustrated in Fig. 2-1-15, where it can be seen that the UHPC prepared using a higher content of SRA exhibited a lower  $\epsilon_t$ . Fig. 2-1-16 (a) to (c) illustrate the comparisons between the free total shrinkage and the autogenous shrinkage at all curing ages of each of the four comparing UHPC series, in which the difference between the free total shrinkage and the autogenous shrinkage of each UHPC series yields approximately the free drying shrinkage component of the concrete. It is observed that the UHPC prepared using a higher SRA content developed a lower drying shrinkage than their counterparts with lower SRA contents. This observation is consistent with the findings of previous studies by Yoo et al. (Yoo et al. 2013; Yoo et al. 2014) and suggests that the SRA is particularly effective to mitigate the free drying shrinkage of the UHPC through reducing the surface tension in the capillary pores of the concrete during the drying process.

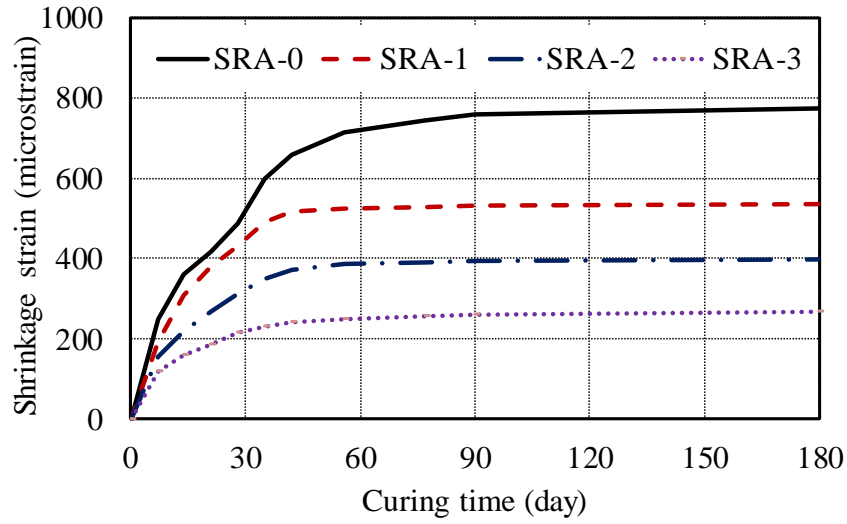


Figure 2-1-15. Effect of SRA content on total shrinkage

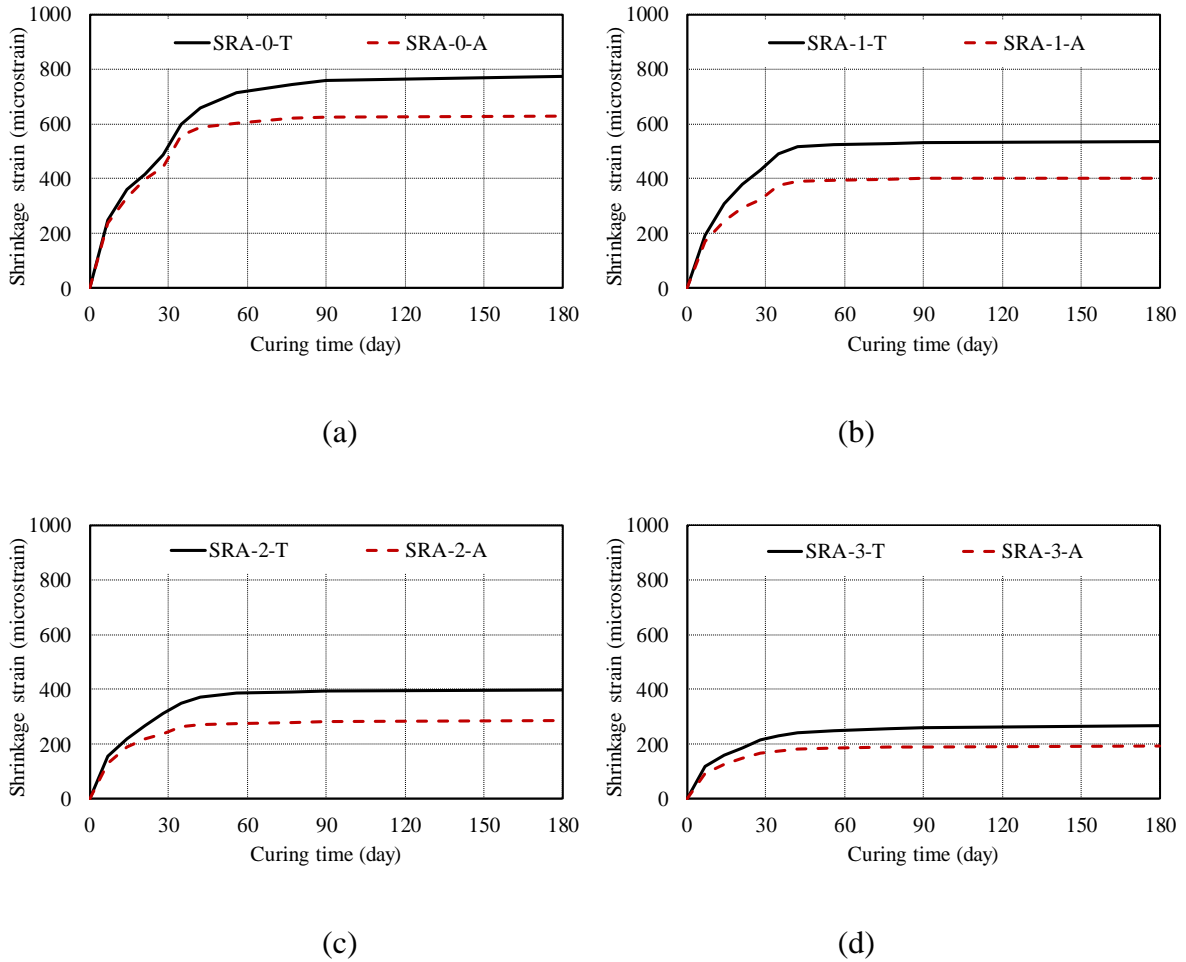


Figure 2-1-16. Effect of SRA content on free drying component: (a) SRA=0%; (b) SRA=1%; (c) SRA=2%; (d) SRA=3%



### 2.1.4.3.2. Effect of crushed ice

The  $\varepsilon_t$  of the UHPC series with different crushed ice dosages were also periodically measured up to the concrete age of 180 days and illustrated in Fig. 2-1-17 as the corresponding values of the  $\varepsilon_r$  and  $\varepsilon_a$  are also shown in Fig. 2-1-18. It is observed that the  $\varepsilon_t$  of the UHPC decreased with an increase in crushed ice dosage whereas the replacement of mixing water with crushed ice led to no impact on the free drying shrinkage property of the concrete. This is observed because the drying shrinkage only depends on the moisture movement out of the concrete.

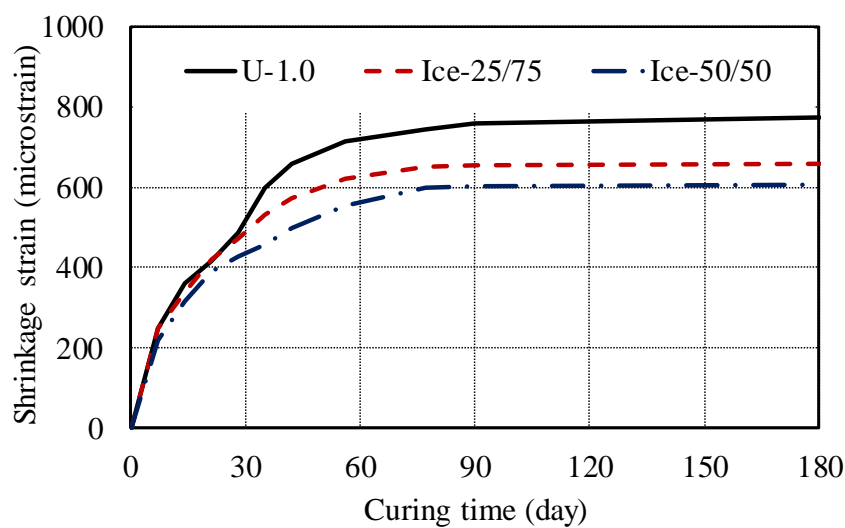
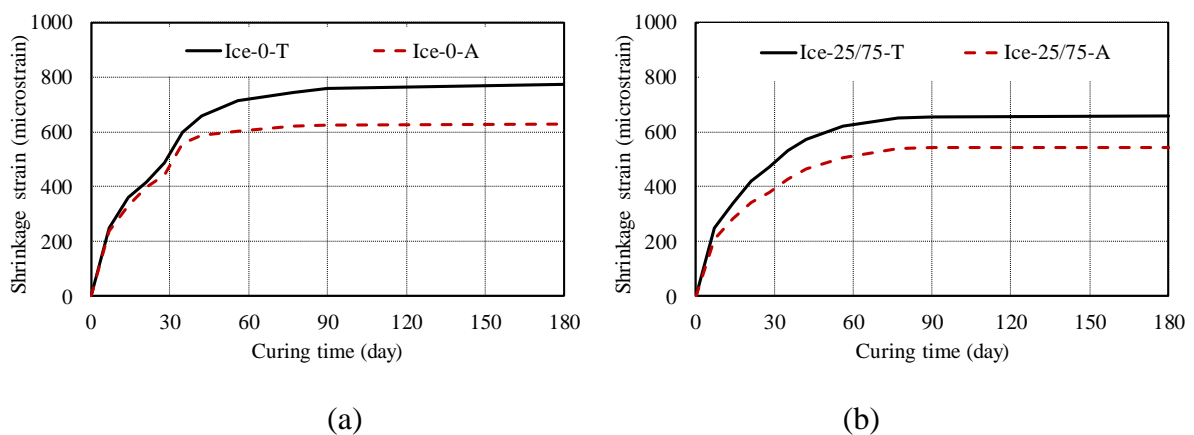
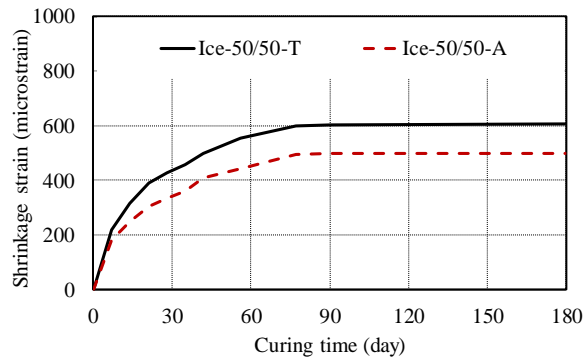


Figure 2-1-17. Effect of crushed ice dosage on total shrinkage





(c)

Figure 2-1-18. Effect of ice replaced water ratio on free drying shrinkage: (a) Ice = 0%; (b) Ice = 25%; (c) Ice = 50%

#### 2.1.4.4. Compressive strength

##### 2.1.4.4.1. Effect of shrinkage reducing admixture (SRA) content

The effect of SRA content on  $f'_c$  at all curing time are illustrated in Fig. 2-1-19. For each given concrete age,  $f'_c$  decreased significantly with an increase in the SRA dosage (up to 21.5 % decrease in  $f'_c$  at 90 days with SRA content of 3%), which is in agreement with those reported in the previous studies on UHPCs (Soliman and Nehdi 2011; Yoo et al. 2013). It is also worth noting that the mixes incorporating SRA exhibited no compressive strength losses ( $\Delta f'_c$ ) for the concrete age ranging between 90 to 180 days. This finding further validates the hypothesis of Sobuz et al. (Sobuz et al. 2016) that the reduction in strength of UHPC over time is due to the formation of micro-shrinkage cracks.

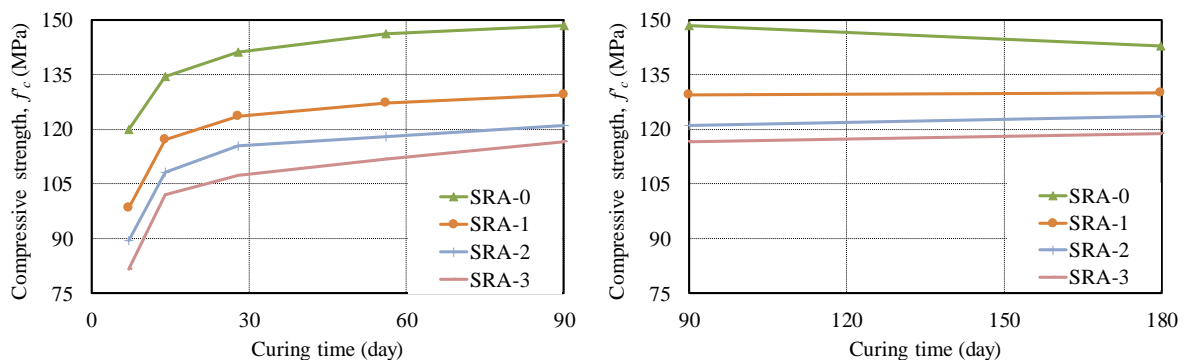


Figure 2-1-19. Effect of SRA content on compressive strength: (a) curing time from 0 to 90 day; (b) curing time from 90 to 180 day

#### 2.1.4.4.2. *Effect of crushed ice dosage*

Figure 2-1-20 illustrates the variations of  $f'_c$  with curing time of the UHPCs manufactured using different crushed ice replacement ratios. For a given concrete age, the U-25/75 and -50/50 series, which were prepared with crushed ice, developed a lower  $f'_c$  than the corresponding UHPC without crushed ice (up to 8 % reduction when replacing 50% of water by crushed ice), whereas there was only a slight difference in  $f'_c$  between U-25/75 and -50/50 series. This is likely due to the small difference in temperature between mix U-25/75 and -50/50 compared to the control without ice. Moreover, as shown in Fig. 2-1-20, U-25/75 and -50/50 UHPC series all exhibited insignificant strength losses (< 1%) between concrete age between 90 and 180 days compared to that seen in U-1.0. This can be explained by the fact that less thermal and plastic shrinkage cracks formed during the exothermic reaction stage, due to the reduction in the heat generation by the incorporation of crushed ice at the early curing stage (i.e. within 72 hours after casting). This will be shown in the calorimetry curves of these UHPC series are presented and their effects are discussed in the following sections. This finding indicates that the simple replacement of a proportion of the mixing water with ice may be all that is required to mitigate the excessive shrinkage strains which causes a reduction in strength of UHPC over time.

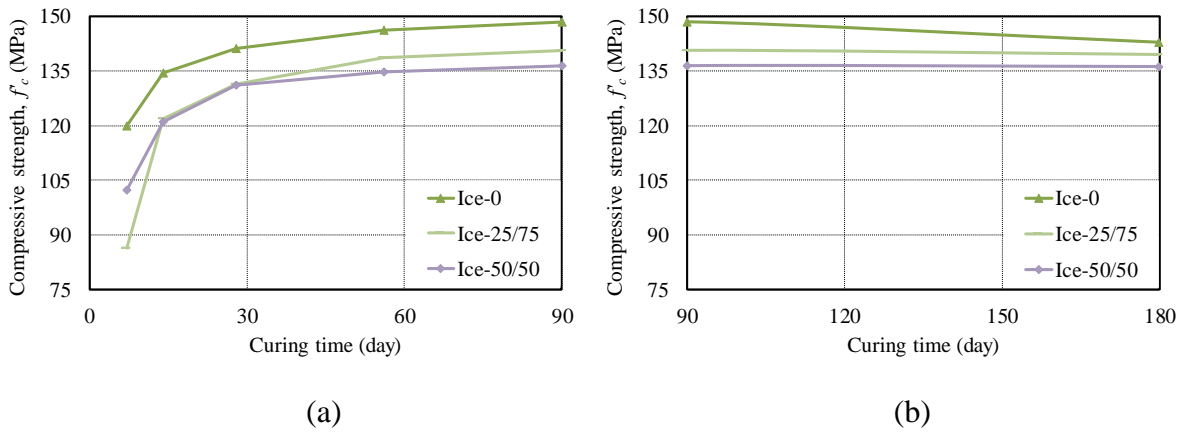


Figure 2-1-20. Effect of ice replaced water ratio on compressive strength: (a) curing time from 0 to 90 day; (b) curing time from 90 to 180 day

#### 2.1.4.5. Exothermic reaction at early curing ages: effects of SRA and crushed ice dosage

The effects of SRA content and crushed ice dosage on the internal temperature of the UHPC are depicted in Figs. 2-1-21 and 2-1-22, respectively. As can be seen from both figures, the incorporation of SRA or replaced mixing water by crushed ice in the UHPC mix can significantly delay the initial and final setting time and reduce the magnitude of peak temperature, which indicates a lower degree of hydration. It is also observed that the strength development period (referred to the width of the hump of the temperature history curve) was increased by using SRA or replacing mixing water with crushed ice. This indicates that the UHPC mixed with SRA or crushed ice could experience a slightly slower strength gain within the very early age (i.e. 72 hours) due to the decelerated reaction rate.

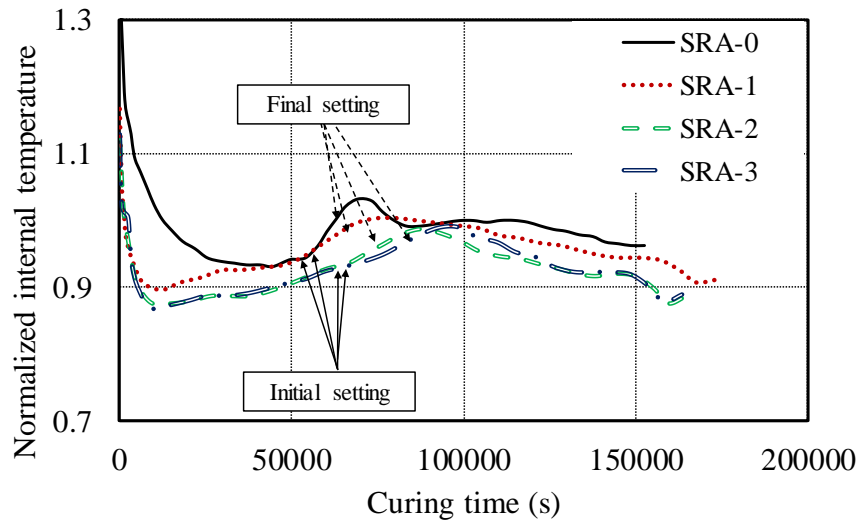


Figure 2-1-21. Effect of SRA content on variations of the internal temperature with curing time

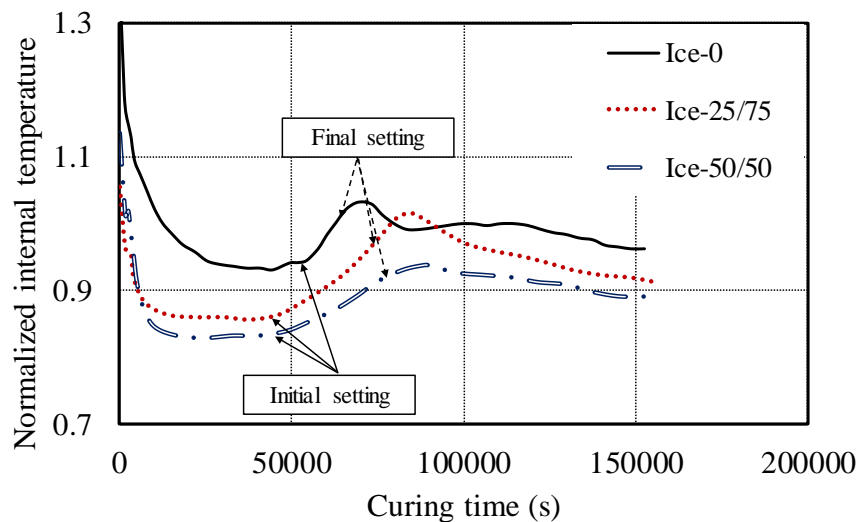


Figure 2-1-22. Effect of ice replaced mixing water ratio on variations of the internal temperature with curing time

#### 2.1.4.6. Unit weight and porosity of the hardened UHPCs

As illustrated in Fig. 2-1-23, it is observed that the SRA content has marginal effect on the unit weight of the hardened UHPC, however it did lead to an increase in the volume of pore space. This was as expected as SRA, which is a type of organic substance (mainly chemically stable

ethanol derivatives) (Shlonimskaya et al. 2014), is inert to during hydration and thus causes formation of additional pores in the UHPCs.

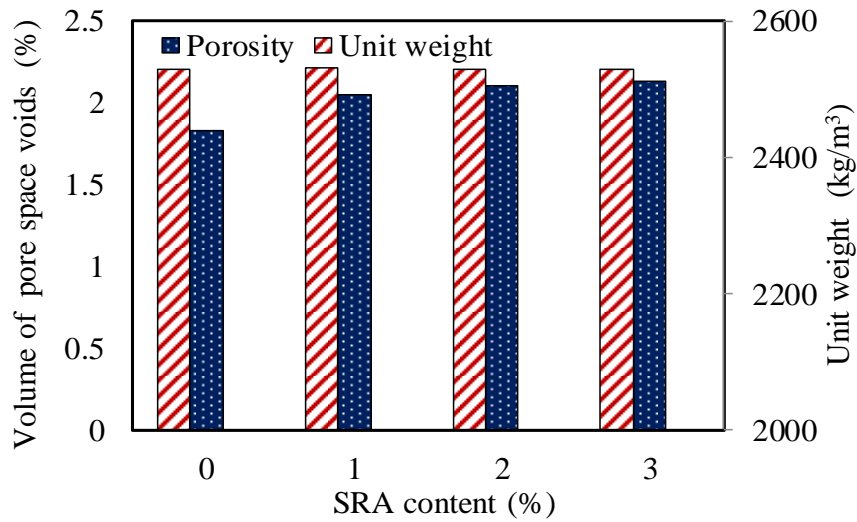


Figure 2-1-23. Effects of ice replaced water ratio on unit weight and porosity of hardened UHPCs

The test results of the unit weight and porosity of the hardened UHPCs shown in Fig. 2-1-24 suggest that partially replacing the mixing water by crushed ice resulted had no significant effect on the unit weight of the concrete. However, a slight increase in the porosity of the UHPC with an increase in the crushed ice dosage was observed due to the decreased reaction rate. This is because the lower temperature caused amount of unreacted raw materials (i.e. water and binder) to remain in the structure of the matrix. The gradual evaporation of the residual water subsequently led to the increased porosity of the concrete.

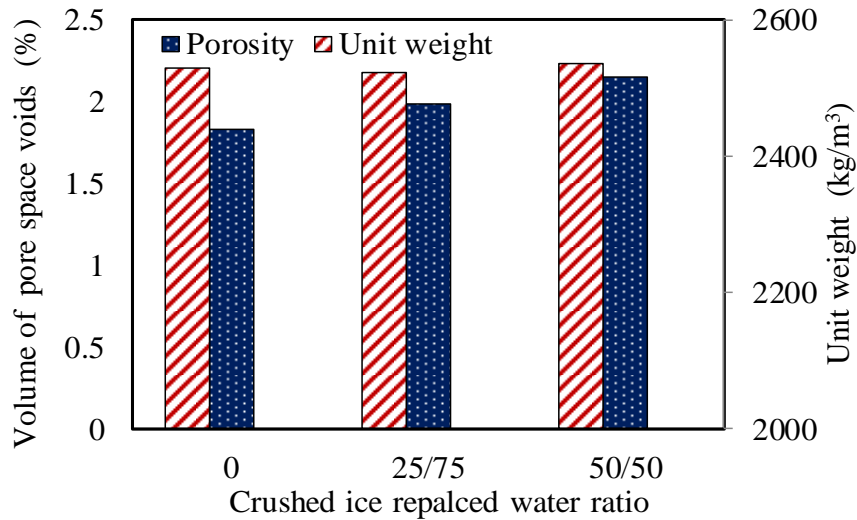
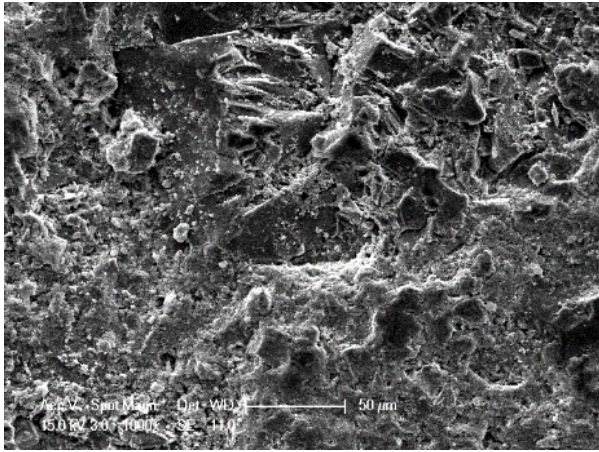


Figure 2-1-24. Effects of SRA content on unit weight and porosity of hardened UHPCs

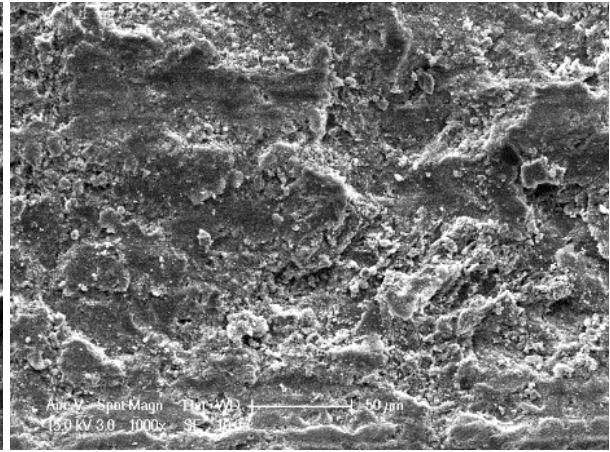
### 2.1.4.7. Morphological characterization of the UHPCs

#### 2.1.4.7.1. Effect of SRA content

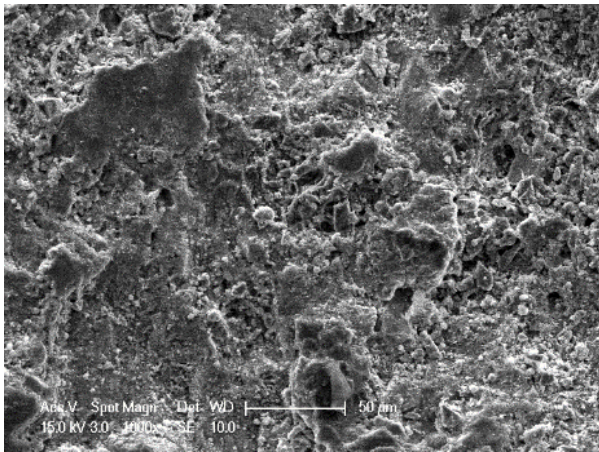
Figures. 2-1-25 and 2-1-26 illustrated the SEM micrographs of the fracture surface of SRA -0, -1, -2 and -3 UHPCs with different magnifications. The comparisons among these micrographs at the lower magnification (i.e. 1000×) suggest that the increased SRA content in the UHPC mix led to increased porosity of the concrete, which is in agreement with the findings from the porosity test mentioned earlier. For the SEM micrographs at the higher magnification (i.e. 10000×), an increased amount of unhydrated binder and ettringite were observed, which indicated lower degree of hydration and increased pore space in the concrete. As discussed previously, this arises because the SRA does not participate in the hydration process but rather acts to slow the hydration process by reducing the contact between the water and binder. In addition, based on the porosity tests results and SEM micrograph, the increased porosity of the UHPC with SRA incorporation might be another potential explanation for the reduction in the autogenous shrinkage of the concrete, where the presence of pores limited the space for the autogenous shrinkage of the matrix for a given content of aggregate in the mix.



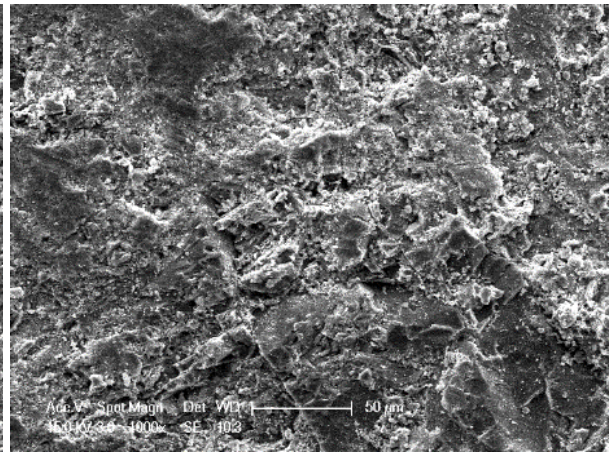
(a)



(b)

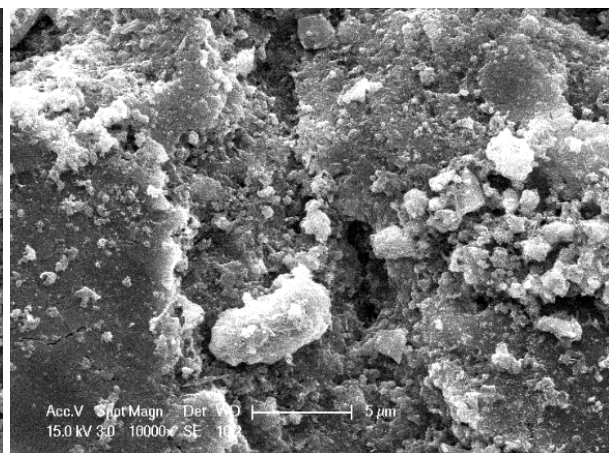
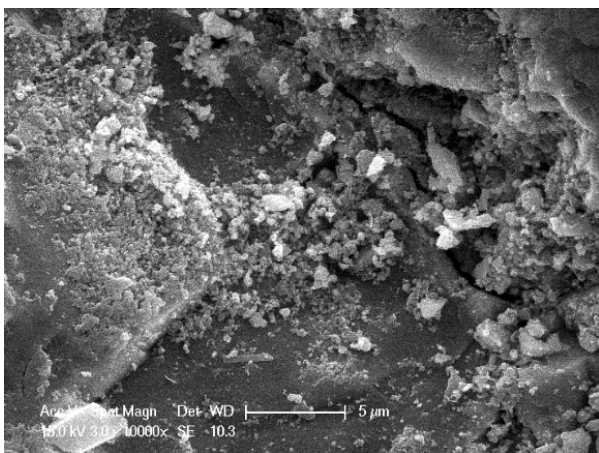


(c)



(d)

Figure 2-1-25. SEM images of the fracture surface of the UHPCs (1000× magnification): a) SRA-0; b) SRA-1; c) SRA-2; d) SRA-3





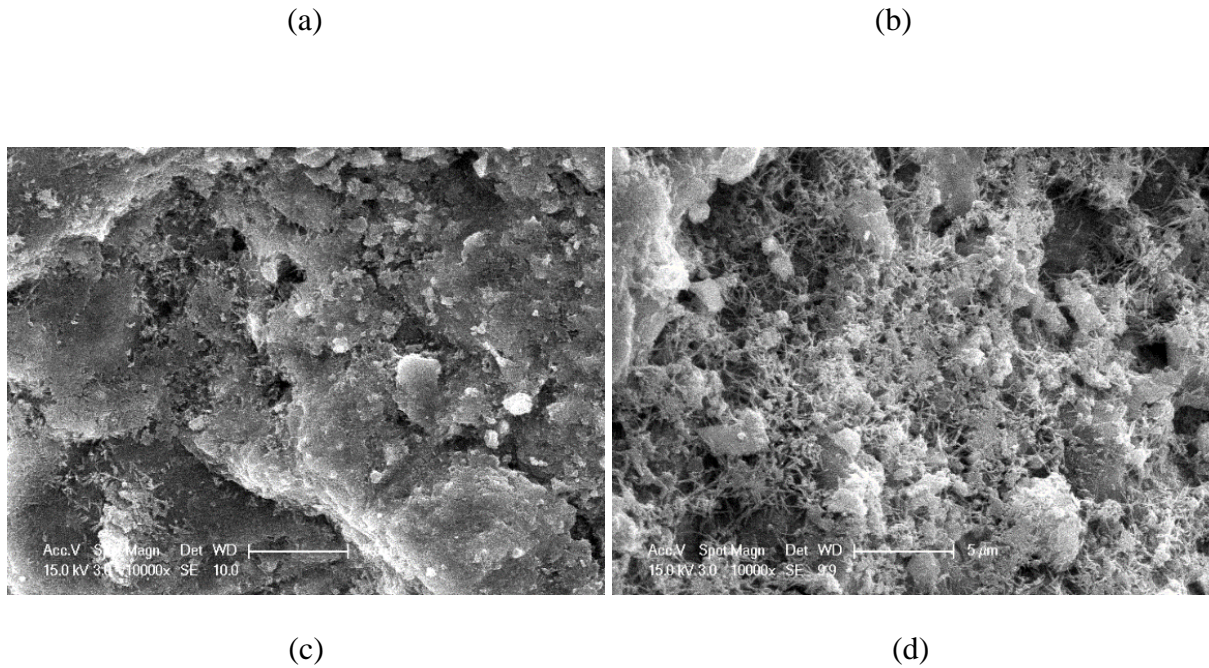
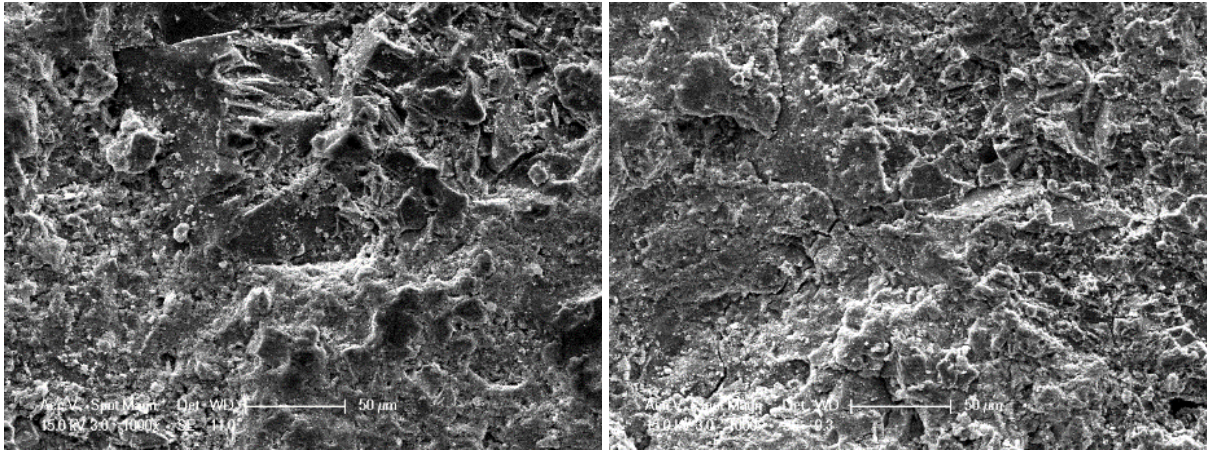


Figure 2-1-26. SEM images of the fracture surface of the UHPCs (10000× magnification): a) SRA-0; b) SRA-1; c) SRA-2; d) SRA-3

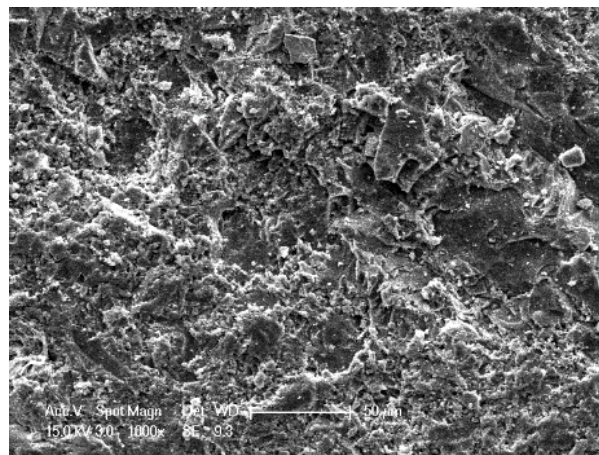
#### 2.1.4.7.2. Effect of crushed ice dosage

Figures. 2-1-27 and 2-1-28 show SEM micrographs of the fracture surface of Ice -0, -25/75, and -50/50 UHPCs at the different magnifications. From SEM micrographs of these UHPC series at the lower magnification (i.e. 1000×), the denseness of the UHPC is observed to decrease with an increase in the crushed ice dosage, indicating an increase in porosity. The comparisons of the SEM micrographs at the higher magnification (i.e. 10000×) show the increased amount of unhydrated binder and ettringite, which suggest the lower degree of hydration and increased pore space for the UHPC prepared using a higher crushed ice replaced water ratio. The increased porosity, formation of ettringite in the concrete and the reduced heat of hydration together explain the mechanism by which the replacement of mixing water with crushed ice reduces self-desiccation.



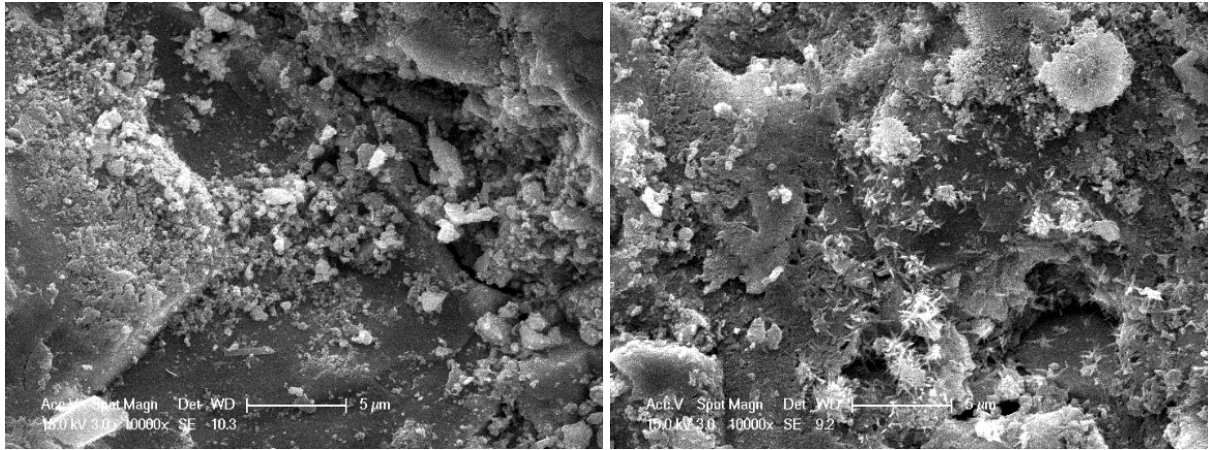
(a)

(b)



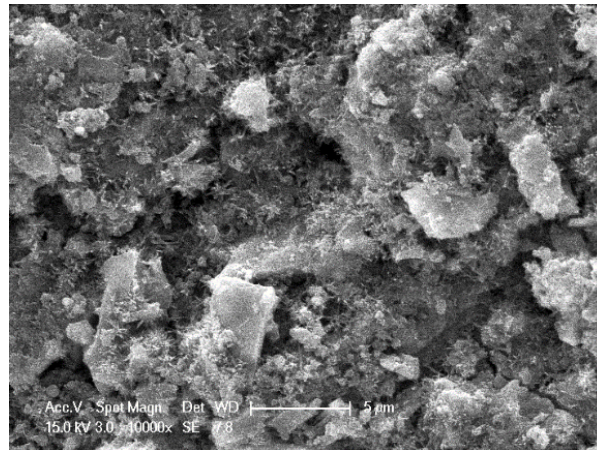
(c)

Figure 2-1-27. SEM images of the fracture surface of the UHPCs (1000× magnification): (a) Ice = 0%; (b) Ice = 25%; (c) Ice = 50%



(a)

(b)



(c)

Figure 2-1-28. SEM images of the fracture surface of the UHPCs (10000× magnification): (a) Ice = 0%; (b) Ice = 25%; (c) Ice = 50%

#### 2.1.4.8. Thermal gravity (TG) analysis

The TGA curves of SRA -0,-1, -2 and -3 UHPC series and Ice -0, -25/75, and -50/50 UHPC series are shown in Figs. 2-1-29 and 2-1-30 respectively and the degree of hydration of these UHPCs at their hardened stage are shown in Figs. 2-1-31 and 2-1-32 in conjunction with the calculated C-H contents. It is evident from Fig. 2-1-31 that the increased SRA content generally lowered the degree of hydration of the UHPCs (i.e. up to around 20%). An even more

pronounced reduction in the degree of hydration (i.e. up to approximately 95%) was observed for the UHPC using a higher crushed ice replaced dosage. These characterizations further confirm that using SRA or replacing mixing water by crushed ice can efficiently reduce the shrinkage of UHPC due to chemical reaction.

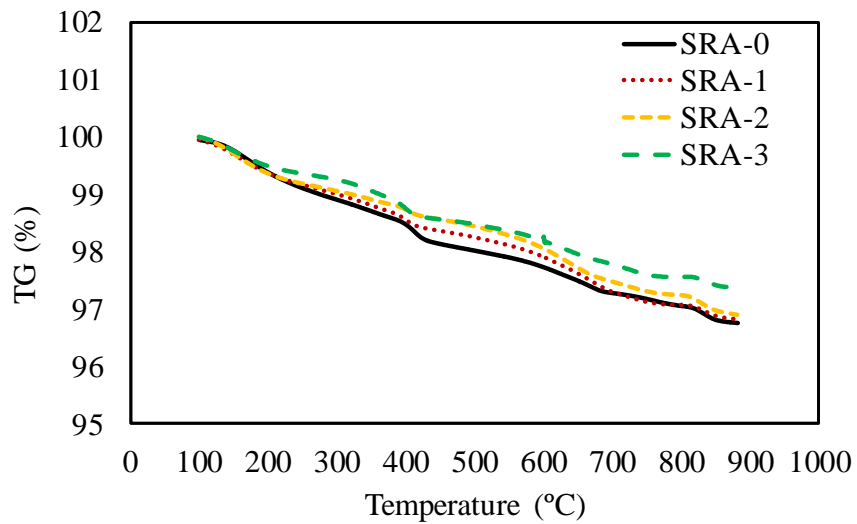


Figure 2-1-29. TG analysis for SRA -0,-1, -2 and -3 UHPC series.

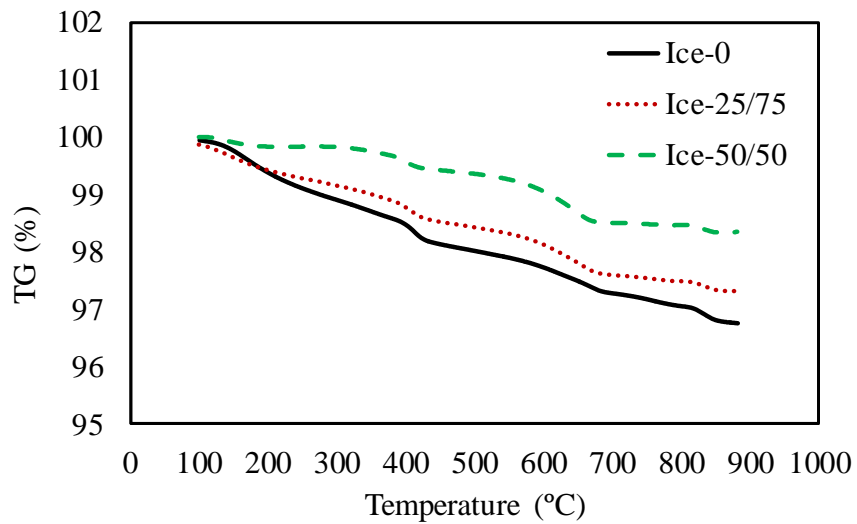


Figure 2-1-30. TG analysis Ice = 0%, Ice = 25% and Ice = 50% UHPC series

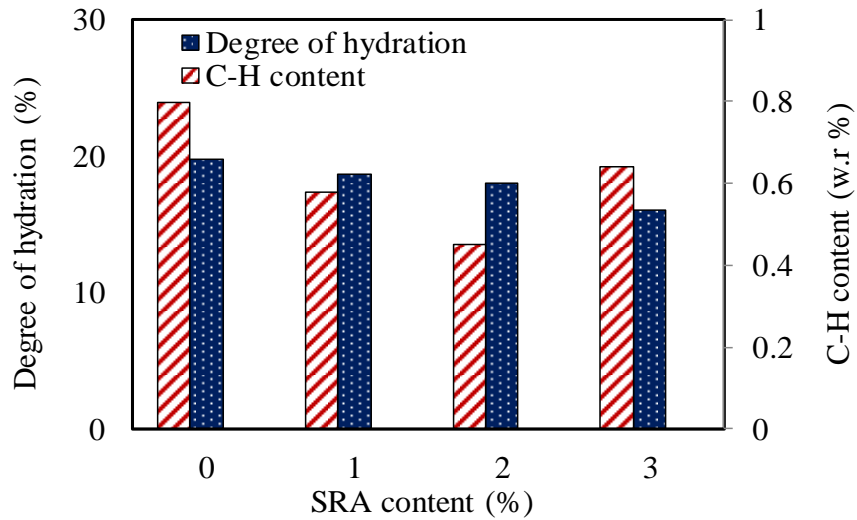


Figure 2-1-31. Effect of SRA content on degree of hydration and C-H content

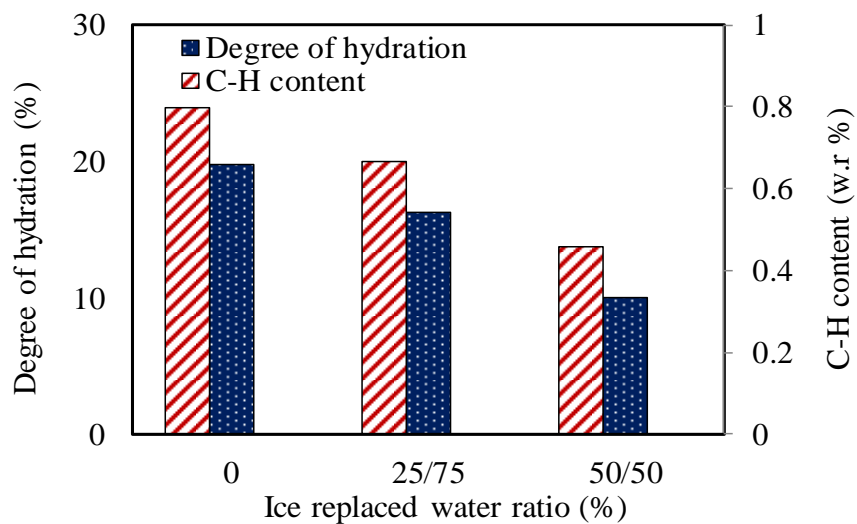


Figure 2-1-32. Effect of ice replaced water ratio on degree of hydration and C-H content

### 2.1.5. COMPARISONS AMONG THE THREE TECHNIQUES AND FURTHER SUGGESTIONS FOR UHPC MIX

To compare the effectiveness of the three techniques used in the present study to mitigate shrinkage of the UHPCs, the key findings of each test are summarized in Table 2-1-5. To make a valid comparison, the test results of each UHPC series are compared with the reference mix, U-1.0 series. It can be seen from Table 2-1-5 that compared to U-1 series, both U-1.1 and 1.266

had significantly lower 90-day autogenous- and total- shrinkage strains and a marked  $\Delta f'_c$  at 90 days. All five U-series of UHPCs experienced strength drop after 90 days. Incorporation of SRA and partially replaced of mixing water in UHPC mix by crushed ice can both led to the reduction in autogenous- and total- shrinkage of the concrete, hence minimizing the compressive strength loss ( $\Delta f'_c$ ) after long term. While the use of SRA is more efficient in reducing shrinkage and the associated reduction in strength over time than replaced mixing water by ice, the low cost and simplicity of using ice has significant benefits. However, it is also noted that the application of either of the technique causes a reduction the maximum compressive strength achieved. Therefore, from this study, it can be concluded that the best mix for reducing the impact of shrinkage without significant  $\Delta f'_c$  in the long-term will be 1) SRA-1 using 1% SRA dosage and 2) Ice-50/50 prepared using crushed ice dosage of 50%.

Table 2-1-5. Effects of nominated techniques on shrinkage and other properties of the UHPCs

Specimen	Change in autogenous shrinkage strain at 90 days	Change in total shrinkage strain at 90 days	Change in $f'_c$ at 90 days	$\Delta f'_c$ between 90 and 180 days
U-0.8	6.4%	3.3%	-6.5%	-5.3%
U-0.9	0.8%	-0.2%	-3.0%	-3.6%
U-1.0/SRA-0/Ice-0	0.0%	0.0%	0.0%	-3.8%
U-1.1	-15.7%	-8.6%	0.5%	-3.9%
U-1.266	-26.3%	-10.9%	-6.3%	-2.3%
SRA-1	-36.1%	-30.0%	-12.9%	0.6%
SRA-2	-69.6%	-47.9%	-18.5%	2.0%
SRA-3	-55.0%	-65.7%	-21.5%	1.8%
Ice-25/75	-13.5%	-13.7%	-5.3%	-0.8%
Ice-50/50	-20.7%	-20.4%	-8.1%	-0.2%

## 2.1.6. CONCLUSIONS

The following major inferences can be made from the results of the present study to investigate the effects of  $b/s$  ratio, SRA content and crushed ice dosage on the shrinkage properties of the UHPC:

- Autogenous shrinkage of the UHPC decreases with an increase in the  $b/s$  ratio due to the more significant shrinkage restraint provided by the residual binders in the UHPC prepared with a higher  $b/s$  ratio.
- An increase in the  $b/s$  ratio in the UHPC mix leads to a decrease in the porosity of the concrete. For UHPC prepared using a lower  $b/s$  ratio, the abundance of crystalline ettringite and C-H seen in the pores and cracks in the concrete minimized the drying shrinkage of the concrete
- An optimal  $b/s$  ratio will be 1 - 1.1 for a typical UHPC mix to minimize the shrinkage effect without significantly comprising  $f'_c$ .
- The autogenous shrinkage has more significant effect than the drying shrinkage on total shrinkage of the UHPCs.
- The porosity and the amount of unreacted binder, which are related to the degree of hydration of the concrete, are the two influential factors on the shrinkage properties of UHPCs.
- SRA is not only able to reduce the drying shrinkage but also the autogenous shrinkage (i.e. up to 55% at 90 days with 3% of SRA dosage) of UHPCs
- The replacement of half of the mixing water by crushed ice in a UHPC mix can reduce the autogenous shrinkage of the UHPC up to 22% and has nearly no effect on the drying shrinkage properties of the UHPCs. This technique is cost-effective and relatively practical to apply in any cast in-situ or pre-casting scenarios.

### 2.1.7. REFERENCES

Aitcin, P. "17 AUTOGENOUS SHRINKAGE MEASUREMENT." *Proc., Autogenous shrinkage of concrete: proceedings of the international workshop, organised by JCI (Japan Concrete Institute), Hiroshima, June 13-14, 1998*, Taylor & Francis, 257.

- Anshuang, S., Ling, Q., Shoujie, Z., Jiayang, Z., and Zhaoyu, L. (2017). "Effects of Shrinkage Reducing Agent and Expansive Admixture on the Volume Deformation of Ultrahigh Performance Concrete." *Advances in Materials Science and Engineering*, 2017.
- ASTM, A. (2009). "C1698-09 Standard test method for autogenous strain of cement paste and mortar." *ASTM International, West Conshohocken, PA*.
- ASTM International (2000). "ASTM C143 / C143M - 00, Standard Test Method for Slump of Hydraulic Cement Concrete." *ASTM International, West Conshohocken*.
- ASTM International (2009). "ASTM C1621/C1621M-09 Standard Test Method for Passing Ability of Self-Consolidating Concrete by J-Ring." *ASTM International, West Conshohocken*.
- ASTM International (2013). "ASTM C642 - 13. Standard Test Method for Density, Absorption, and Voids in Hardened Concrete." *ASTM International, West Conshohocken*.
- Australian Standard (2000). "AS 1478.1-2000. Chemical admixtures for concrete, mortar and grout Admixtures for concrete." *Standards Australia, Sydney*.
- Australian Standard (2006). "AS/NZS 2350.11. Methods for testing Portland, blended and masonry cements." *Standards Australia, Sydney*.
- Australian Standard (2006). "AS/NZS 2350.13. Methods for testing Portland, blended and masonry cements – determination of drying shrinkage of cement mortars." *Standards Australia, Sydney*.
- Bentur, A., Igarashi, S.-i., and Kovler, K. (2001). "Prevention of autogenous shrinkage in high-strength concrete by internal curing using wet lightweight aggregates." *Cement and concrete research*, 31(11), 1587-1591.
- Bentz, D., Geiker, M. R., and Hansen, K. K. (2001). "Shrinkage-reducing admixtures and early-age desiccation in cement pastes and mortars." *Cement and concrete research*, 31(7), 1075-1085.



- Bentz, D. P. "Capitalizing on self-desiccation for autogenous distribution of chemical admixtures." *Proc., Lund University*, Citeseer.
- Brough, A., and Atkinson, A. (2000). "Automated identification of the aggregate–paste interfacial transition zone in mortars of silica sand with Portland or alkali-activated slag cement paste." *Cement and Concrete Research*, 30(6), 849-854.
- Brunauer, S., and Kantro, D. (1964). "The Hydration of Tricalcium Silicate and  $\beta$  Dicalcium Silicate from 5 C to 50 C." *The Chemistry of Cement*, 1, 287.
- Chen, X., and Wu, S. (2013). "Influence of water-to-cement ratio and curing period on pore structure of cement mortar." *Construction and Building Materials*, 38, 804-812.
- Colleparidi, M., Borsoi, A., Colleparidi, S., Olagot, J. J. O., and Troli, R. (2005). "Effects of shrinkage reducing admixture in shrinkage compensating concrete under non-wet curing conditions." *Cement and Concrete Composites*, 27(6), 704-708.
- Darquennes, A., Staquet, S., and Espion, B. (2011). "Determination of time-zero and its effect on autogenous deformation evolution." *European journal of environmental and civil engineering*, 15(7), 1017-1029.
- Dudziak, L., and Mechtcherine, V. "Mitigation of volume changes of ultra-high performance concrete (UHPC) by using super absorbent polymers." *Proc., Proceedings of the 2nd international symposium on ultra high performance concrete. Kassel University Press, Kassel*, 425-432.
- Dweck, J., Buchler, P. M., Coelho, A. C. V., and Cartledge, F. K. (2000). "Hydration of a Portland cement blended with calcium carbonate." *Thermochimica Acta*, 346(1), 105-113.
- Folliard, K. J., and Berke, N. S. (1997). "Properties of high-performance concrete containing shrinkage-reducing admixture." *Cement and Concrete Research*, 27(9), 1357-1364.

- Han, M. Y., and Lytton, R. L. (1995). "Theoretical prediction of drying shrinkage of concrete." *Journal of materials in civil engineering*, 7(4), 204-207.
- Hasanzadeh, B., Liu, F., and Sun, Z. (2016). "Monitoring hydration of UHPC and conventional paste by quantitative analysis on Raman patterns." *Construction and Building Materials*, 114, 208-214.
- Hermida, G., Moranville, M., and Flatt, R. (2009). "The Role of Paste Volume on Performance of Concrete." *Special Publication*, 261, 201-214.
- Huang, W., Kazemi-Kamyab, H., Sun, W., and Scrivener, K. (2017). "Effect of cement substitution by limestone on the hydration and microstructural development of ultra-high performance concrete (UHPC)." *Cement and Concrete Composites*, 77, 86-101.
- Jennings, H., and Pratt, P. (1979). "An experimental argument for the existence of a protective membrane surrounding Portland cement during the induction period." *Cement and Concrete Research*, 9(4), 501-506.
- Jensen, O. M. (2013). "Use of superabsorbent polymers in concrete." *Concrete international*, 35(1), 48-52.
- Jun, P. J., Tae, K. S., Sung, R. G., Wook, K. S., and Hwa, L. J. "The effect of material factors on the compressive strength of ultra-high strength Steel Fiber Reinforced Cementitious Composites." *Proc., Proceedings of the Korea Concrete Institute Conference*, Korea Concrete Institute.
- Kadri, E.-H., and Duval, R. (2009). "Hydration heat kinetics of concrete with silica fume." *Construction and Building Materials*, 23(11), 3388-3392.
- Kim, G.-Y., Lee, E.-B., Nam, J.-S., and Koo, K.-M. (2011). "Analysis of hydration heat and autogenous shrinkage of high-strength mass concrete." *Magazine of Concrete Research*, 63(5), 377-389.

- Koh, K., Ryu, G., Kang, S., Park, J., and Kim, S. (2011). "Shrinkage properties of ultra-high performance concrete (UHPC)." *Advanced Science Letters*, 4(3), 948-952.
- Lam, L., Wong, Y., and Poon, C. (2000). "Degree of hydration and gel/space ratio of high-volume fly ash/cement systems." *Cement and Concrete Research*, 30(5), 747-756.
- Langan, B., Weng, K., and Ward, M. (2002). "Effect of silica fume and fly ash on heat of hydration of Portland cement." *Cement and Concrete research*, 32(7), 1045-1051.
- Lura, P., Jensen, O. M., and van Breugel, K. (2003). "Autogenous shrinkage in high-performance cement paste: an evaluation of basic mechanisms." *Cement and Concrete Research*, 33(2), 223-232.
- Ma, J., Orgass, M., Dehn, F., Schmidt, D., and Tue, N. "Comparative investigations on ultra-high performance concrete with and without coarse aggregates." *Proc., Proceedings of international symposium on ultra high performance concrete, Germany*, 205-212.
- Maltais, Y., and Marchand, J. (1997). "Influence of curing temperature on cement hydration and mechanical strength development of fly ash mortars." *Cement and concrete research*, 27(7), 1009-1020.
- Mechtcherine, V., Gorges, M., Schroefl, C., Assmann, A., Brameshuber, W., Ribeiro, A. n. B., Cusson, D., Custódio, J., da Silva, E. F., and Ichimiya, K. (2014). "Effect of internal curing by using superabsorbent polymers (SAP) on autogenous shrinkage and other properties of a high-performance fine-grained concrete: results of a RILEM round-robin test." *Materials and structures*, 47(3), 541-562.
- Mehta, P. K. (1973). "Mechanism of expansion associated with ettringite formation." *Cement and Concrete Research*, 3(1), 1-6.
- Mosaberpanah, M. A., and Eren, O. (2016). "Relationship between 28-days Compressive Strength and Compression Toughness Factor of Ultra High Performance Concrete Using Design of Experiments." *Procedia Engineering*, 145, 1565-1571.

- Newman, S. P., Clifford, S. J., Coveney, P. V., Gupta, V., Blanchard, J. D., Serafin, F., Ben-Amotz, D., and Diamond, S. (2005). "Anomalous fluorescence in near-infrared Raman spectroscopy of cementitious materials." *Cement and concrete research*, 35(8), 1620-1628.
- Odler, I. (1998). "Hydration, setting and hardening of Portland cement." *Lea's chemistry of cement and concrete*, 4, 241-297.
- Park, J.-J., Yoo, D.-Y., Kim, S.-W., and Yoon, Y.-S. (2014). "Benefits of using expansive and shrinkage-reducing agents in UHPC for volume stability." *Magazine of Concrete Research*, 66(14), 745-750.
- Park, J. J., Kang, S. T., Koh, K. T., and Kim, S. W. "Influence of the ingredients on the compressive strength of UHPC as a fundamental study to optimize the mixing proportion." *Proc., Proceedings of the international symposium on ultra-high performance concrete, structural materials and engineering series*, 105-112.
- Reddy, B. V., and Gupta, A. (2008). "Influence of sand grading on the characteristics of mortars and soil-cement block masonry." *Construction and Building Materials*, 22(8), 1614-1623.
- Rößler, C., Bui, D.-D., and Ludwig, H.-M. (2014). "Rice husk ash as both pozzolanic admixture and internal curing agent in ultra-high performance concrete." *Cement and Concrete Composites*, 53, 270-278.
- Russell, H. G., and Graybeal, B. A. (2013). "Ultra-high performance concrete: A state-of-the-art report for the bridge community."
- Şahmaran, M., Al-Emam, M., Yıldırım, G., Şimşek, Y. E., Erdem, T. K., and Lachemi, M. (2015). "High-early-strength ductile cementitious composites with characteristics of low early-age shrinkage for repair of infrastructures." *Materials and Structures*, 48(5), 1389-1403.

- Şahmaran, M., Lachemi, M., Hossain, K. M., and Li, V. C. (2009). "Internal curing of engineered cementitious composites for prevention of early age autogenous shrinkage cracking." *Cement and Concrete Research*, 39(10), 893-901.
- Sahmaran, M., Lachemi, M., Hossain, K. M., Ranade, R., and Li, V. C. (2009). "Influence of aggregate type and size on ductility and mechanical properties of engineered cementitious composites." *Materials Journal*, 106(3), 308-316.
- Schießl, P., Mazanec, O., and Lowke, D. (2007). "SCC and UHPC—effect of mixing technology on fresh concrete properties." *Advances in Construction Materials 2007*, Springer, 513-522.
- Scrivener, K. L., Crumbie, A. K., and Laugesen, P. (2004). "The interfacial transition zone (ITZ) between cement paste and aggregate in concrete." *Interface Science*, 12(4), 411-421.
- Shen, W., Li, X., Gan, G., Cao, L., Li, C., and Bai, J. (2016). "Experimental investigation on shrinkage and water desorption of the paste in high performance concrete." *Construction and Building Materials*, 114, 618-624.
- Shi, C., Wu, Z., Xiao, J., Wang, D., Huang, Z., and Fang, Z. (2015). "A review on ultra high performance concrete: Part I. Raw materials and mixture design." *Construction and Building Materials*, 101, 741-751.
- Shlonimskaya, N., Biernacki, J. J., Kayello, H. M., and Visco, D. P. (2014). "An Application of Computer-Aided Molecular Design (CAMD) Using the Signature Molecular Descriptor—Part 2. Evaluating Newly Identified Surface Tension-Reducing Substances for Potential Use as Shrinkage-Reducing Admixtures." *Journal of the American Ceramic Society*, 97(2), 378-385.

- Singh, M., Sheikh, A., Ali, M. M., Visintin, P., and Griffith, M. (2017). "Experimental and numerical study of the flexural behaviour of ultra-high performance fibre reinforced concrete beams." *Construction and Building Materials*, 138, 12-25.
- Smith, B. G. (2001). "Durability of silica fume concrete exposed to chloride in hot climates." *Journal of materials in civil engineering*, 13(1), 41-48.
- Sobuz, H., Visintin, P., Ali, M. M., Singh, M., Griffith, M., and Sheikh, A. (2016). "Manufacturing ultra-high performance concrete utilising conventional materials and production methods." *Construction and Building Materials*, 111, 251-261.
- Sobuz, H. R., Oehlers, D. J., Visintin, P., Hasan, N. M. S., Hoque, M. I., and Akid, A. S. M. (2017). "Flow and Strength Characteristics of Ultra-high Performance Fiber Reinforced Concrete: Influence of Fiber Type and Volume-fraction." *Journal of Civil Engineering and Construction*, 6(1), 15.
- Soliman, A., and Nehdi, M. (2011). "Effect of drying conditions on autogenous shrinkage in ultra-high performance concrete at early-age." *Materials and structures*, 44(5), 879-899.
- Soliman, A., and Nehdi, M. (2013). "Effect of partially hydrated cementitious materials and superabsorbent polymer on early-age shrinkage of UHPC." *Construction and Building Materials*, 41, 270-275.
- Soliman, A., and Nehdi, M. (2014). "Effects of shrinkage reducing admixture and wollastonite microfiber on early-age behavior of ultra-high performance concrete." *Cement and Concrete Composites*, 46, 81-89.
- Standard Australia (2014). "AS 1012.9:2014. Methods of testing concrete Compressive strength tests - Concrete, mortar and grout specimens. ." *Standards Australia, Sydney*.

- Sturm, A. B., Visintin, P., Ferris, K., and Oehlers, D. J. (2018). "A new testing approach for extracting the shear friction material properties of ultra-high performance fibre reinforced concrete." *ASCE Journal of Materials in Civil Engineering*.
- Vedalakshmi, R., Raj, A. S., Srinivasan, S., and Babu, K. G. (2003). "Quantification of hydrated cement products of blended cements in low and medium strength concrete using TG and DTA technique." *Thermochimica Acta*, 407(1), 49-60.
- Visintin, P., Ali, M. M., Xie, T., and Sturm, A. B. (2018). "Experimental investigation of moment redistribution in ultra-high performance fibre reinforced concrete beams." *Construction and Building Materials*, 166, 433-444.
- Visintin, P., Sturm, A. B., Ali, M. M., and Oehlers, D. J. (2018). "Blending Macro and Micro Fibres to Enhance the Serviceability Behaviour of UHPFRC." *Australian Journal of Civil Engineering*.
- Wang, D., Shi, C., Wu, Z., Xiao, J., Huang, Z., and Fang, Z. (2015). "A review on ultra high performance concrete: Part II. Hydration, microstructure and properties." *Construction and Building Materials*, 96, 368-377.
- Wong, H., and Buenfeld, N. (2009). "Determining the water–cement ratio, cement content, water content and degree of hydration of hardened cement paste: Method development and validation on paste samples." *Cement and Concrete Research*, 39(10), 957-965.
- Wu, L., Farzadnia, N., Shi, C., Zhang, Z., and Wang, H. (2017). "Autogenous shrinkage of high performance concrete: a review." *Construction and Building Materials*, 149, 62-75.
- Yalçınkaya, Ç., and Yazıcı, H. (2017). "Effects of ambient temperature and relative humidity on early-age shrinkage of UHPC with high-volume mineral admixtures." *Construction and Building Materials*, 144, 252-259.

- Yan, P., Zheng, F., Peng, J., and Qin, X. (2004). "Relationship between delayed ettringite formation and delayed expansion in massive shrinkage-compensating concrete." *Cement and Concrete Composites*, 26(6), 687-693.
- Yio, M., Phelan, J., Wong, H., and Buenfeld, N. (2014). "Determining the slag fraction, water/binder ratio and degree of hydration in hardened cement pastes." *Cement and Concrete Research*, 56, 171-181.
- Yoo, D.-Y., and Banthia, N. (2016). "Mechanical properties of ultra-high-performance fiber-reinforced concrete: A review." *Cement and Concrete Composites*, 73, 267-280.
- Yoo, D.-Y., Banthia, N., and Yoon, Y.-S. (2015). "Effectiveness of shrinkage-reducing admixture in reducing autogenous shrinkage stress of ultra-high-performance fiber-reinforced concrete." *Cement and Concrete Composites*, 64, 27-36.
- Yoo, D.-Y., Banthia, N., and Yoon, Y.-S. (2017). "Ultra-High-Performance Fiber-Reinforced Concrete: Shrinkage Strain Development at Early Ages and Potential for Cracking." *Journal of Testing and Evaluation*, 45(6), 2061-2070.
- Yoo, D.-Y., Banthia, N., and Yoon, Y.-S. (2018). "Geometrical and boundary condition effects on restrained shrinkage behavior of UHPFRC slabs." *KSCE Journal of Civil Engineering*, 22(1), 185-195.
- Yoo, D.-Y., Kang, S.-T., Lee, J.-H., and Yoon, Y.-S. (2013). "Effect of shrinkage reducing admixture on tensile and flexural behaviors of UHPFRC considering fiber distribution characteristics." *Cement and Concrete Research*, 54, 180-190.
- Yoo, D.-Y., Kim, M.-J., Kim, S., Ryu, G.-S., and Koh, K.-T. (2018). "Effects of mix proportion and curing condition on shrinkage behavior of HPRCCs with silica fume and blast furnace slag." *Construction and Building Materials*, 166(1), 241-256.



- Yoo, D.-Y., Min, K.-H., Lee, J.-H., and Yoon, Y.-S. (2014). "Shrinkage and cracking of restrained ultra-high-performance fiber-reinforced concrete slabs at early age." *Construction and Building Materials*, 73, 357-365.
- Yoo, D.-Y., Park, J.-J., Kim, S.-W., and Yoon, Y.-S. (2014). "Influence of reinforcing bar type on autogenous shrinkage stress and bond behavior of ultra high performance fiber reinforced concrete." *Cement and Concrete Composites*, 48, 150-161.
- Yoo, D.-Y., Park, J.-J., Kim, S.-W., and Yoon, Y.-S. (2014). "Influence of ring size on the restrained shrinkage behavior of ultra high performance fiber reinforced concrete." *Materials and structures*, 47(7), 1161-1174.
- Youssef, D. (2013). "The Use of Lightweight Sand for Internal Curing and Its Effect on Performance of HPC Used for Concrete Infrastructures." Université de Sherbrooke.
- Yu, R., Spiesz, P., and Brouwers, H. (2014). "Effect of nano-silica on the hydration and microstructure development of Ultra-High Performance Concrete (UHPC) with a low binder amount." *Construction and Building Materials*, 65, 140-150.
- Zhang, M., Tam, C., and Leow, M. (2003). "Effect of water-to-cementitious materials ratio and silica fume on the autogenous shrinkage of concrete." *Cement and Concrete Research*, 33(10), 1687-1694.

THIS PAGE HAS BEEN LEFT INTENTIONALLY BLANK

# Statement of Authorship

Title of Paper	The influence of steel fibre properties on the shrinkage of ultra-high performance fibre reinforced concrete
Publication Status	<input type="checkbox"/> Published <input type="checkbox"/> Accepted for Publication <input checked="" type="checkbox"/> Submitted for Publication <input type="checkbox"/> Unpublished and Unsubmitted work written in manuscript style
Publication Details	Fang, C., Mohamed Ali, M. S., Xie, T., Visintin, P., & Sheikh, A. H. (2019). The influence of steel fibre properties on the shrinkage of ultra-high performance fibre reinforced concrete. Submitted to Construction and Building Materials.

## Principal Author

Name of Principal Author (Candidate)	Chengfeng Fang		
Contribution to the Paper	Designing concept, conducting experiments, analysing of data, drafting manuscript		
Overall percentage (%)	30		
Certification:	This paper reports on original research I conducted during the period of my Higher Degree by Research candidature and is not subject to any obligations or contractual agreements with a third party that would constrain its inclusion in this thesis. I am the primary author of this paper.		
Signature		Date	06/08/2019

## Co-Author Contributions

By signing the Statement of Authorship, each author certifies that:

- i. the candidate's stated contribution to the publication is accurate (as detailed above);
- ii. permission is granted for the candidate to include the publication in the thesis; and
- iii. the sum of all co-author contributions is equal to 100% less the candidate's stated contribution.

Name of Co-Author	Dr Mohamed Ali Sadakkathulla		
Contribution to the Paper	Designing concept, analysing of data, revising manuscript (20%)		
Signature		Date	06/08/2019

Name of Co-Author	Tianyu Xie		
Contribution to the Paper	Designing concept, conducting experiments, analysing of data, drafting manuscript (20%)		

Signature		Date	06/08/2019
-----------	--	------	------------

Name of Co-Author	Associate Professor Phillip Visintin		
Contribution to the Paper	Designing concept, analysing of data, revising manuscript (20%)		
Signature		Date	06/08/2019

Name of Co-Author	Associate Professor Abdul H. Sheikh		
Contribution to the Paper	Designing concept (10%)		
Signature		Date	06/08/2019

Please cut and paste additional co-author panels here as required.

## **2.2. The Influence of Steel Fibre Properties on the Shrinkage of Ultra-High Performance Fibre Reinforced Concrete**

Fang, C. <sup>1</sup>, Mohamed Ali, M.S. <sup>1</sup>, Xie, T. <sup>1</sup>, Visintin, P. <sup>1</sup>, Sheikh, A.H. <sup>1</sup>

<sup>1</sup>School of Civil, Environmental and Mining Engineering, The University of Adelaide, SA  
5005, Australia

### **ABSTRACT:**

In this study, the effects of fibre volume fraction, fibre type, and aspect ratio on various shrinkages of the ultra-high performance fibre reinforced concretes (UHPFRCs) were experimentally investigated. Single fibre pull-out tests were conducted and the corresponding results were incorporated to explore the underlying mechanism governing the magnitudes of both autogenous and drying shrinkages. In general, the presence of randomly distributed steel fibres was found to reduce both the total and autogenous shrinkage, and more specifically, an increase in fibre volume fraction or fibre aspect ratio results in significant mitigation in both total and autogenous shrinkages. Hook-end fibres were found to be more effective in restraining autogenous shrinkage compared to straight fibres and consequently blended fibre mixes that include straight fibres were less effective at restraining shrinkage than only hooked-end fibres.

**Keywords:** ultra-high performance fibre reinforced concrete (UHPFRC); steel fibres; autogenous shrinkage; free total shrinkage; fibre pull-out load-slip relationship.

### **2.2.1. INTRODUCTION**

The exceptional durability of ultra-high performance concrete (UHPC) will bring about a step-change in the way structures and infrastructures are planned, managed, and maintained, while

its outstanding mechanical properties will fundamentally change how structural engineers approach reinforced concrete design. The great potential of UHPC has largely been demonstrated by favourable early-age compressive and tensile strengths. Further, the excellent ductility and durability of UHPC at a structural level observed in instantaneous tests on members has led to the suggestion that UHPC members can be constructed with reduced quantities of the traditional reinforcement (Fang et al. 2019; Krahl et al. 2018; Ngo et al. 2017; Song et al. 2018; Xie et al. 2019).

The excellent mechanical and durability characteristics exhibited by UHPC can be attributed predominately to the low water by binder ( $w-b$ ) ratio used to produce this type of concrete. The low water content results in reduced drying shrinkage of UHPC in the long-term but causes a severe autogenous shrinkage when compared to normal strength concrete (NSC) (Koh et al. 2011; Shi et al. 2015; Wang et al. 2015; Xie et al. 2018). In order to address this shortcoming, attempts have been made to reduce shrinkage by adding additional steel fibres to the UHPC matrix. Investigations of the short- and long-term shrinkage of UHPFRCs, including autogenous shrinkage (Yoo et al. 2015; Yoo et al. 2014), drying shrinkage (Park et al. 2013) and restrained shrinkage (Yoo et al. 2014; Yoo et al. 2014) have mostly been conducted by Yoo et al, with a smaller number of studies by others (e.g. (Garas et al. 2009; Meng and Khayat 2018; Meng et al. 2018; Soliman and Nehdi 2012; Soliman and Nehdi 2014; Soliman and Nehdi 2013)). It is worth noting that in these studies a single type of hooked end steel fibre was incorporated into the UHPC matrix with a typical fibre volume fraction of 2% for studying autogenous- and drying- shrinkage, respectively (e.g. Yoo et al. (Yoo et al. 2013) and Garas et al. (Garas et al. 2009)). Further, the only investigation found to date that monitors the variations in autogenous shrinkage of UHPFRCs by varying fibre types, fibre dosages, and proportions of different fibre blends is that conducted by Meng and Khayat (Meng and Khayat 2018). In this study, it was found that autogenous shrinkage of the UHPC mixture was decreased by more

than 60% with an increase in fibre content of straight fibres from 0% to 5% by volume. Furthermore, the inclusion of 0.5% PVA fibres as well as 1% of hooked end steel fibres significantly reduced the autogenous shrinkage and enhanced the tensile strength as well as fracture energy of specimens when compared with the specimens having 2% of straight steel fibres only. A further increase in the fibre content of hooked end fibre resulted in reductions in flexural and tensile strengths of UHPFRC, and this was mainly due to the fibre agglomeration during the mixing process.

From the preceding discussions, it can be inferred that there is a lack of investigation to explore the influence on fibre type, fibre aspect ratios and volume fraction of the fibres regarding on the shrinkage mechanism of UHPFRC; therefore there is a need to extract the influence of fibre properties on the shrinkage behaviour which is necessary for both the development of mix design procedures and the formulation and code practice for a new formulated concrete, such as UHPFRC. The primary objective of the present study is to experimentally quantify the effects of fibre aspect ratios, fibre dosage, fibre type, and hybridization of steel fibres with micro straight and hook end fibres blended, on the shrinkage behaviour of UHPFRC.

## **2.2.2. EXPERIMENTAL PROGRAM**

### **2.2.2.1. Materials and Concrete mixtures**

#### ***2.2.2.1.1. Ingredients used for the UHPC matrix***

A single UHPC mixture recipe based on the work by Sobuz et al. (Sobuz et al. 2016) at the University of Adelaide was used to prepare the concrete matrix of the UHPFRCs (the detailed mixture proportions are summarized in Table 2-2-1). The blended binder consists of sulphate

resisting cement and undensified silica fume and a detailed description of the chemical composition of both binders can be found in Sobuz et al. (Sobuz et al. 2016). A well-graded natural washed river sand with a nominal maximum size of 4 mm and a fineness modulus of 2.34 was used as the only aggregate in the mixture. To enhance the workability, a high range water reduced agent with an added retarder (which meets the requirements of AS1478.1-2000 (Australian Standard 2000)), was used as the superplasticizers (SP) for all mixes at a constant SP to binder ratio of 0.06.

#### **2.2.2.1.2. Steel Fibres**

Four different types of steel fibres, as illustrated in Fig. 2-2-1, were added to the concrete mixture. The manufacturer reported properties of each fibre type are provided in Table 2-2-2. Three of these four fibres (type H1, H2, and H3) are macro-fibres of hooked end shape and with different nominal diameters and lengths, whereas the fourth (type S) is a straight micro-fibre. A total of 12 UHPFRC mixes were prepared with steel fibres to investigate the effects of fibre type, fibre volume fraction, the aspect ratio of fibre and the hybridization of steel fibres with micro straight and hook end fibres blended on the mechanical and shrinkage properties of UHPFRCs. Specifically, mixture 1 is the reference mixture without steel fibres, and the mixture 2-12 were manufactured with different types of fibre with volume fractions of 1.5%, 2%, and 2.5%, and it is worth noting that straight and hooked end fibres blended with a proportion of 1:1 with a total volume fraction of 2% were added into the mixture 9. To quantify the total fibre reinforcement, a reinforcing index (*RI*) used as a measurement in the previous studies (Ou et al. 2011; Xie and Ozbakkaloglu 2015) was adopted in the present study to investigate its influence regarding shrinkages and the corresponding definition is defined as follow:



$$RI = V_f \% \times \frac{l_f}{d_f} \quad (1)$$

in which  $V_f$  % is the total fibre volume fraction as a percentage, and  $l_f$  and  $d_f$  are the length and nominal diameter of the fibre, respectively. For the UHPFRC containing blended fibres the  $RI$  is determined by calculating the volumetric average  $RI$  of each fibre.

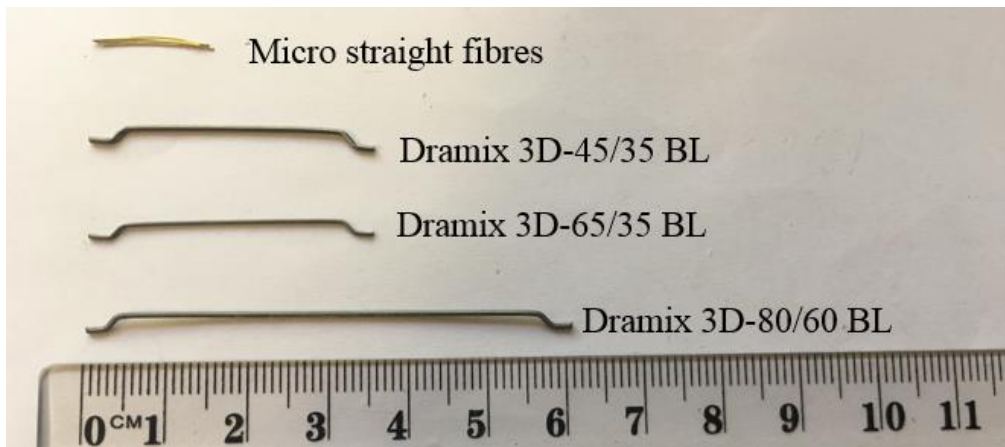


Figure. 2-2-1 Steel fibres used in the UHPFRCs.

#### 2.2.2.1.3. *Mixing procedure of UHPFRCs*

To prepare the UHPFRC mixtures, all the dry components, including binder and sand were mixed in a rotating pan mixer with 80 L capacity for five minutes. Following this, the liquid constituents (water and superplasticizer) were added and mixing was continued until the desired slump flow of the matrix was achieved. Finally, the discrete steel fibres were added before mixing for a few more minutes to ensure a uniform distribution of the fibres.

Table. 2-2-1 Mix proportion, physical-and mechanical-properties of the UHPFRCs.

Mix No.	Designation	Mix proportion (kg/m <sup>3</sup> )						Fibre volume fraction	Description of fibre	Fibre reinforcing index ( <i>RI</i> )	Slump (mm)	28-d $f_{st}$ (MPa)	28-d $f'_c$ (MPa)	180-d $f'_c$ (MPa)
		Sulfate resisting cement	Silica fume	Sand	Water	SP	Fibre							
M1	Ref						0	0.0%	-	0.00	255	6.1	128.3	126.8
M2	H1-0.015						0.155	1.5%	Dramix 3D-45/35 BL	0.68	230	14.1	129.1	134.9
M3	H2-0.015						0.155	1.5%	Dramix 3D-65/35 BG	0.98	210	14.4	133.7	137.1
M4	H3-0.015						0.155	1.5%	Dramix 3D-80/60 BG	1.20	195	14.8	141.8	144.4
M5	S-0.02						0.207	2.0%	Micro straight fibres	1.30	215	13.6	122.6	126.8
M6	H1-0.02						0.207	2.0%	Dramix 3D-45/35 BL	0.90	205	12.4	147.2	151.4
M7	H2-0.02	0.79	0.21	1.00	0.12	0.06	0.207	2.0%	Dramix 3D-65/35 BG	1.30	210	11.8	133.7	138.2
M8	H3-0.02						0.207	2.0%	Dramix 3D-80/60 BG	1.60	170	13.9	137.3	139.7
M9	50H2/50S-0.02						0.207	2.0%	Blended fibres (50% & 50%) (Straight & Dramix 3D- 65/35 BG)	1.30	205	12.0	133.9	137.9
M10	H1-0.025						0.259	2.5%	Dramix 3D-45/35 BL	1.13	155	10.7	139.8	142.6
M11	H2-0.025						0.259	2.5%	Dramix 3D-65/35 BG	1.63	125	11.9	125.8	130.3
M12	H3-0.025						0.259	2.5%	Dramix 3D-80/60 BG	2.00	145	13.0	127.6	131.0

Table. 2-2-2 Manufacturer-reported details of steel fibres

Fibre type	Designation	Diameter, $d_f$ (mm)	Length, $l_f$ (mm)	Aspect ratio, ( $l_f/d_f$ )	Yield tensile strength, $f_t$ (MPa)	Young's modulus, $E_c$ (MPa)	Fibre shape
Micro fibres	S	0.2	13	65	2850	210000	Straight
Dramix 3D-45/35 BL	H1	0.75	35	45	1225	210000	Hooked end
Dramix 3D-65/35 BG	H2	0.55	36	65	1345	210000	Hooked end
Dramix 3D-80/60 BG	H3	0.75	60	80	1225	210000	Hooked end

## 2.2.2.2. Test methods

### 2.2.2.2.1. Measurements of the total- and autogenous- shrinkage

The total- and autogenous- shrinkage was determined using prismatic specimens which were 75 mm x 75 mm in cross-section and 285 mm long (Fig. 2-2-2). Specimens used for measuring the autogenous shrinkage were carefully sealed with waterproofed aluminium tape to prevent diffusion of moisture from the concrete into the surrounding environment (Fig. 2-2-2(a)), while specimens used for measuring the total shrinkage were exposed to the surrounding environment (Fig. 2-2-2(b)). The change in length of each specimen was regularly monitored up to the concrete age of 180 days with the ‘time-zero’ for autogenous and total shrinkage measurement taken as the final setting time of the matrix conforming to ASTM C1698-09 (ASTM 2009) and in accordance with previous studies (Darquennes et al. 2011; Mechtcherine et al. 2014). All the total shrinkage and autogenous- shrinkage specimens were stored in an environmental chamber that was maintained at a constant 25 °C (77 °F) temperature and a relative humidity of 50% for the entire duration of testing.



(a)



(b)

Figure. 2-2-2 Shrinkage test specimens: a) sealed prism for autogenous shrinkage measurement; b) unsealed prism for free total shrinkage measurements

#### 2.2.2.2.2. Fibre pulled-out for the UHPC matrix

In order to explore the underlying mechanism governing the effect of fibres on the different shrinkage components of UHPFRC, the interaction between the steel fibres and the UHPC matrix was quantified by the load-slip ( $P-\delta$ ) relationships derived by processing the test results from single fibre pull-out tests. As can be seen in Fig. 2-2-3, semi dog-bone shaped specimens were used, in which the fibre was embedded concentrically in the matrix with an embedded length equal to half the length of the fibre perpendicular to the concrete face. Three identical specimens were used for each test series. Details the test specimens and the test set-up are shown in Figs. 2-2-3 (a) and (b). All the pull-out test were conducted under a displacement-control with a rate of 1 mm/min.

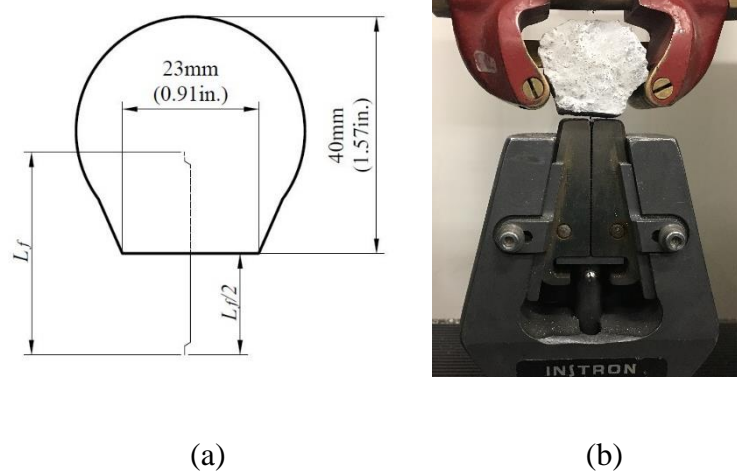


Figure. 2-2-3. Single fibre pull-out test: a) specimen details; b) set-up.

### **2.2.2.2.3. Compressive and splitting tensile strength**

To obtain the compressive strength ( $f'_c$ ) of the UHPFRCs at the age of 28 days and 180 days, compression tests were conducted on cylinder specimens with a 100 mm diameter and 200 mm as per ASTM standard C39/C39 M-05 (ASTM International 2005 ). The splitting tensile strength ( $f_{st}$ ) tests were performed on cylinder specimens with a 100 mm diameter and 200 mm height according to ASTM standard C496/C496 M-04 (ASTM International 2004) at a concrete age of 28 days only.

## **2.2.3. RESULTS AND DISCUSSIONS**

### **2.2.3.1. Slump**

Table 2-2-1 summarises the slump values measured for fresh UHPFRC. Comparisons between different UHPFRC mixtures show that the workability of UHPC is generally reduced with an increase in a volume fraction of steel fibres, and specifically, the slump of the concrete reduced up to 23.5% with the incorporation of 1.5% of steel fibres by volume. Subsequently, a further increase in fibre volume fraction leads to a further reduction in the slump of the UHPC, particularly; the slump of mixture 11 is nearly 49% of the slump of reference mixture due to the fibre bridging effects. As listed in Table 2-2-1, for the mixture with a given fibre volume fraction, the UHPC mixture with the largest fibre aspect ratio (e.g. Dramix 3D-80/60) exhibited the low slump values compared to companion specimens.

### **2.2.3.2. Fibre pulled-out test results**

A typical failure mode of fibre pull-out test is shown in Fig. 2-2-4 with the corresponding representative load-slip relationship shown in Fig. 2-2-5. Note that due to the limitations of testing facilities, the pull-out tests of type S fibres from the matrix were not successfully conducted. Therefore, the pull-out load-slip behaviour of this type of fibre has been approximated as that tested by Qi et al. (Qi et al. 2018) on exactly the same type of straight micro-fibre (from the same supplier with  $l_f=13$  mm,  $d_f=0.2$  mm ) which was pulled-out from a UHPC matrix of cubic strength  $f'_c=151.5$  MPa, which is similar to that reported in this study.



Figure. 2-2-4 Typical failure mode of fibre pull-out test.

It can be observed from Fig. 2-2-5 that the pull-out load-slip relationship of the straight fibre from the matrix is comprised of three distinct phases: the initial linear ascending branch (a linear relationship with a full bonding between matrix and reinforcement), a small transition region between the end of elastic stage and the peak load (debonding occurred while the friction

providing residual strength) and finally the nearly exponentially descending branch (pull-out with kinetic friction) (Qi et al. 2018). Unlike the behaviour of the straight micro-fibre, the pull-out load-slip curves of all the three hooked end fibres exhibit five major parts: the initial linear ascending proportion (a linear relationship with a full bonding between matrix and reinforcement), a small proportion of transition region between the end of elastic stage and the peak load (deformed pull-out with kinetic friction and mechanical anchorage); stress relaxation at the beginning of the descending region (deformed pull-out stage with kinetic friction and mechanical anchorage), a strain hardening stage (deformed pull-out due to kinetic friction and mechanical anchorage), and finally the gradually descending branch (straight pull-out with kinetic friction). To investigate the underlying mechanism governing the effects of fibres on the shrinkage properties of the UHPFRCs, only the static friction component (the ascending branch of each curve presented in Fig. 2-2-5) on the pull-out load-slip curve is considered.

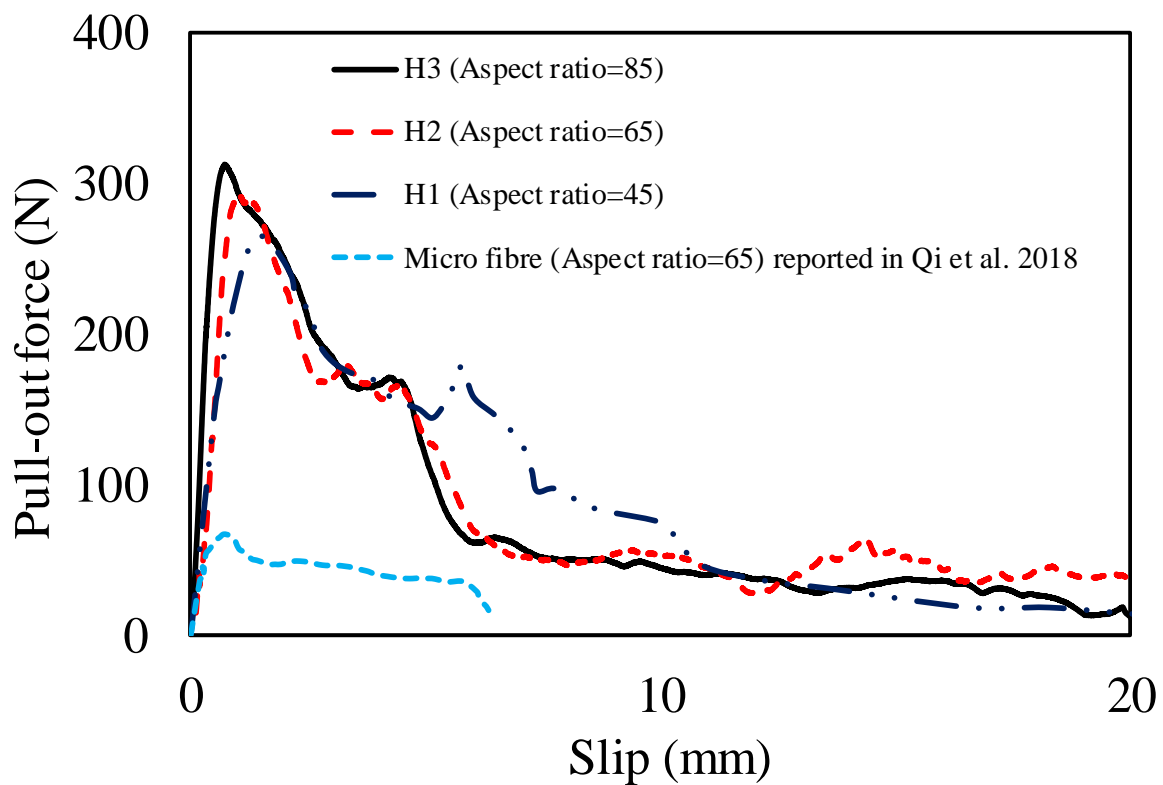


Figure. 2-2-5 Fibre pull-out force- slip relationships.

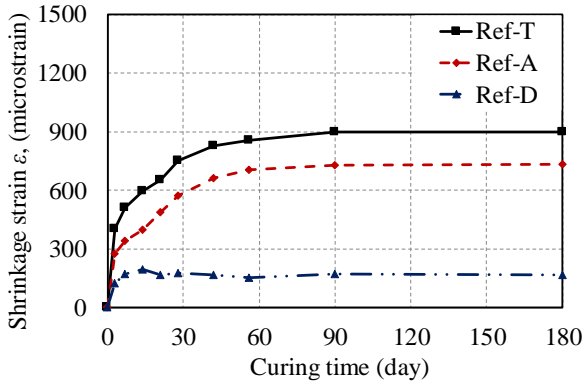
As shown in Fig. 2-2-5, for a given pull-out force within the static friction region, fibre type H3, which has the highest aspect ratio suffered a slightly lower slip compared to those developed by the hooked end fibres with lower aspect ratios. This implies that the fibre with a higher aspect ratio is more effective to resist the tensile stress exerted on the matrix. Moreover, it is also observed that due to the anchorage provided by their hooked ends, each of the H series of fibres induced a lower slip than the straight fibre for a given pull-out force within the static friction phase.

### **2.2.3.3. Shrinkage characterizations**

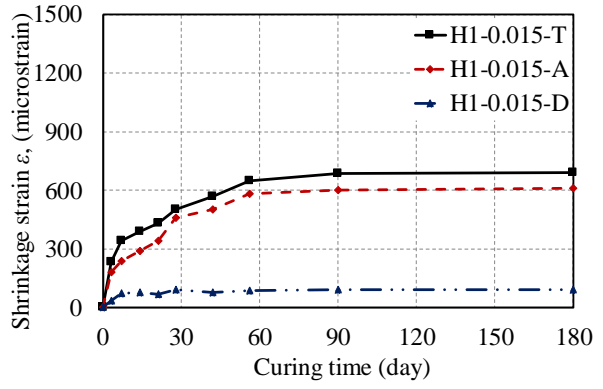
#### **2.2.3.3.1. General observations**

Figures 2-2-6 (a) to (l) show the shrinkage characterizations, including the measured total shrinkage strain, autogenous shrinkage strain and also the calculated free drying shrinkage magnitudes for all test series. Note that the free drying shrinkage strain ( $\epsilon_{sh-D}$ ) values were estimated by subtracting the autogenous (red dashed line) shrinkage strain ( $\epsilon_{sh-A}$ ) from the free total (black solid line) shrinkage strain ( $\epsilon_{sh-T}$ ) for concrete age up to 180 days for all specimen series. It can be observed from Fig.2-2-6. that for all the mixtures, the increase in  $\epsilon_{sh}$  values with time exhibits a similar pattern over a long term, but the magnitudes of shrinkage strain were significantly affected by the fibre volume fraction, type of fibres and aspect ratio of the fibres.

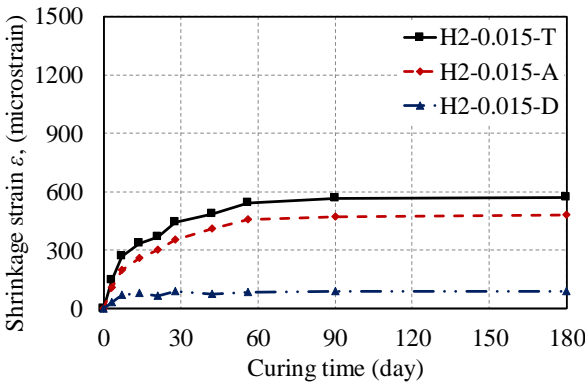




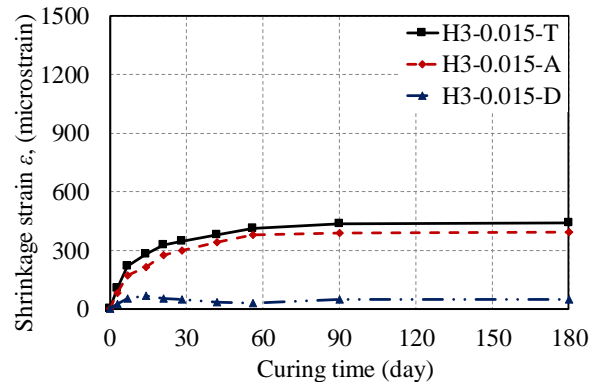
(a)



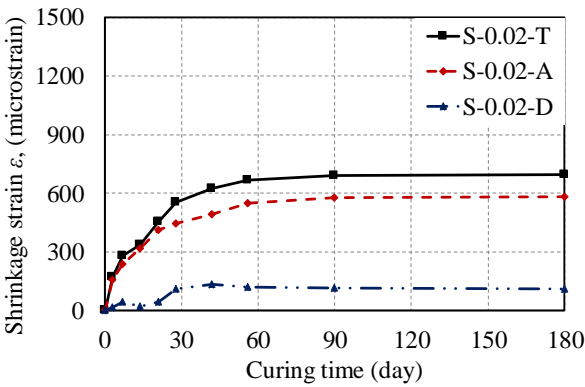
(b)



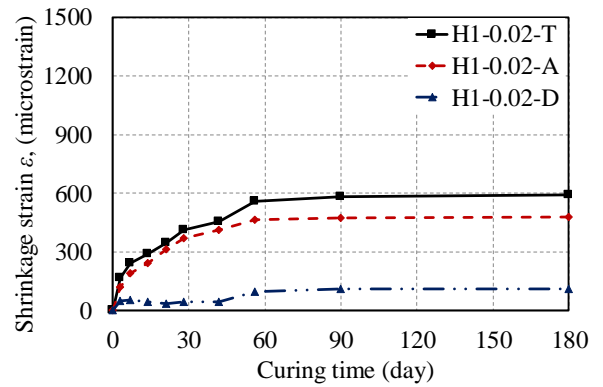
(c)



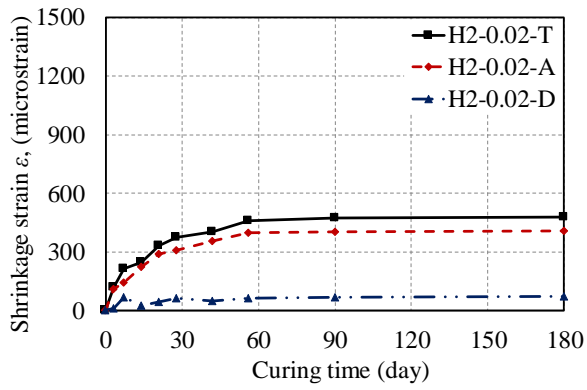
(d)



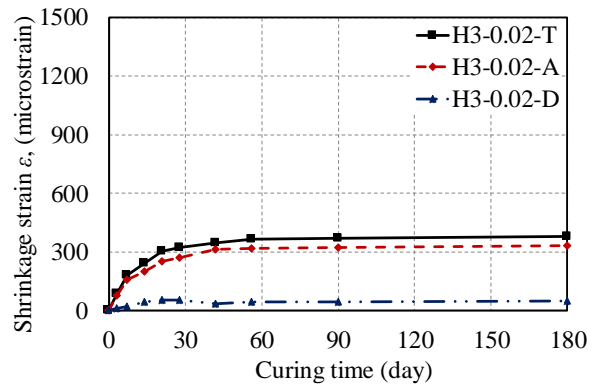
(e)



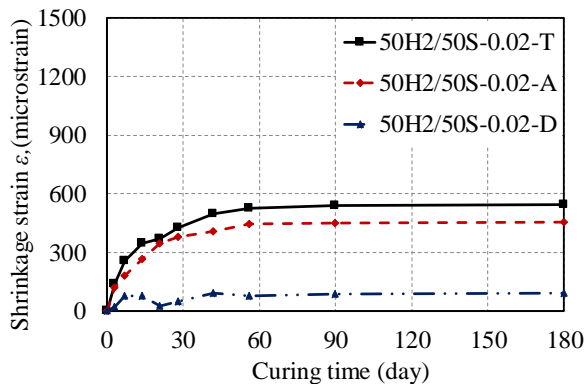
(f)



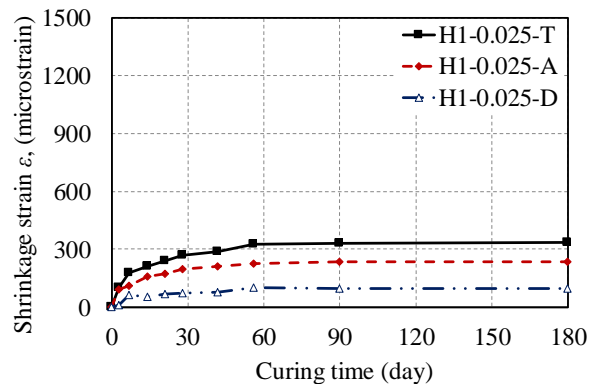
(g)



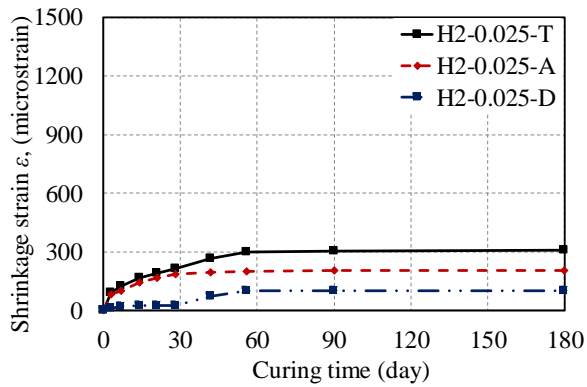
(h)



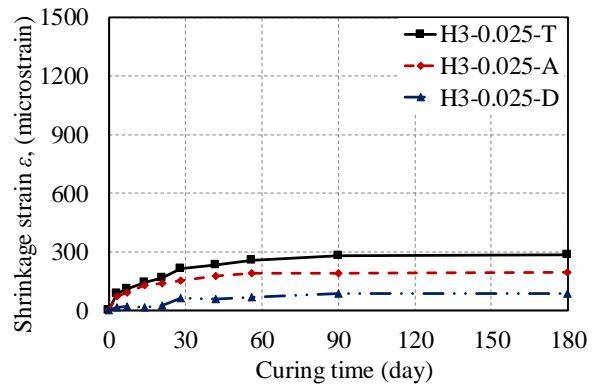
(i)



(j)



(k)



(l)

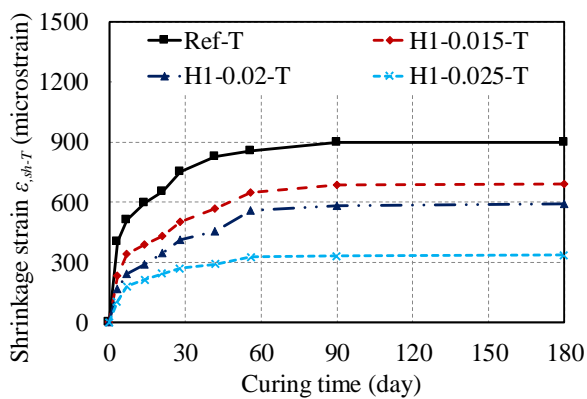
Figure. 2-2-6 Shrinkage characterization of the UHPFRCs: a) Ref series; b) H1-0.015 series; c) H2-0.015 series; d) H3-0.015 series; e) S-0.02 series; f) H1-0.02 series; g) H2-0.02 series; h) H3-0.02 series; i) 50H2/50S-0.02 series; j) H1-0.025 series; k) H2-0.025 series; l) H3-0.025 series.

It is observed from Fig. 2-2-6 (a-1) that the substantial part of  $\varepsilon_{,sh-T}$  is due to  $\varepsilon_{,sh-A}$  (range from 80-95%) and the remainder of the shrinkage strain is due to  $\varepsilon_{,sh-D}$  which is attributed to the low moisture diffusion from the matrix. Moreover, the higher values of  $\varepsilon_{,sh-A}$  can be explained by the fact that a high binder content contributes to a very high degree of hydration of cement and the pozzolanic reaction of silica fume, and hence it led to a significant self-desiccation of the concrete matrix. These findings were also reported by the previous investigations (Xie et al. 2018). Moreover, the reduction in drying shrinkage can be attributed to the disruption of the interconnection of pores by fibres, reducing the amount of water present in the capillary pores (Lei and Cao 2011). The steel fibres also restrain the autogenous shrinkage due to the bond between the fibres and matrix, as they provide friction to resist against the effects of self-desiccation of the concrete (Mangat and Azari 1984). This inference generally agrees well with those reported in the studies conducted on UHPFRCs or FRCs in which the presence of discrete, rigid metallic fibres in the concrete matrix is shown to reduce drying- and autogenous-shrinkage (Lei and Cao 2011; Mangat and Azari 1984; Meng and Khayat 2018; Ullah 2017). The effects of the various fibre parameters on the shrinkage phenomenon are discussed in the following sections.

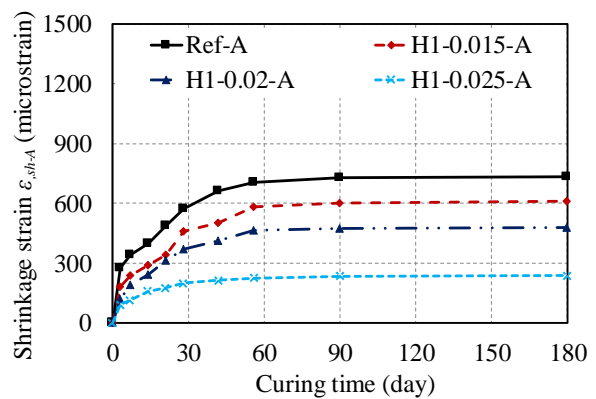
#### ***2.2.3.3.2. Effect of fibre volume fraction***

The effect of fibre volume fraction on shrinkage can be studied by comparing the shrinkage measurements at a given concrete curing age of the companion concrete series produced using the same type of fibre but with different fibre volume fractions (as illustrated in Fig. 2-2-7 (a) to (f)). Generally, an increase in the fibre volume fraction significantly reduce magnitudes of both  $\varepsilon_{,sh-A}$  and  $\varepsilon_{,sh-T}$ , and it is worth mentioning that with additional 1.5% of steel fibres, the values of  $\varepsilon_{,sh-T}$  in 180 days were reduced by 23.2% - 56.5% compared to the reference mixture,

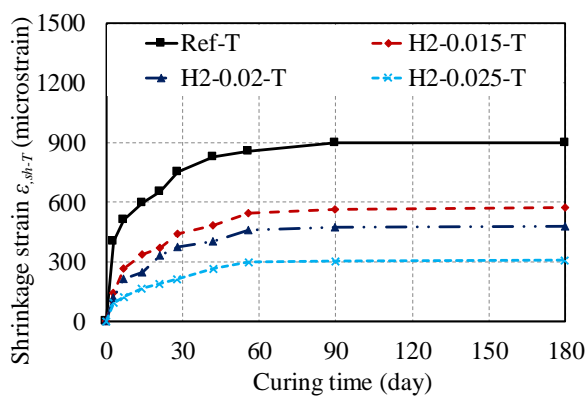
as presented in Fig. 2-2-7 (a),(c), and (e). Furthermore, the total shrinkage strain values  $\epsilon_{,sh-T}$  were slightly reduced with an increase in fibre volume fraction from 1.5% to 2%; for instance, comparisons between specimens H1-0.015-T and H1-0.02-T presented a 14.8% of reduction in total shrinkage, as shown in Fig. 2-2-7 (a). A further increase of 0.5% of fibre volume fraction from 2% to 2.5% causes the values of  $\epsilon_{,sh-A}$  and  $\epsilon_{,sh-T}$  of all specimens to drop by approximately 300 and 200 micro strains, respectively. It is also observed that the inclusions of 2.5% of steel fibres by volume in the UHPC matrix resulted in an approximately 67% reduction in total shrinkage and over 70% reduction in autogenous shrinkage compared to that of the reference mixture, as shown in Fig. 2-2-7(a) and (b).



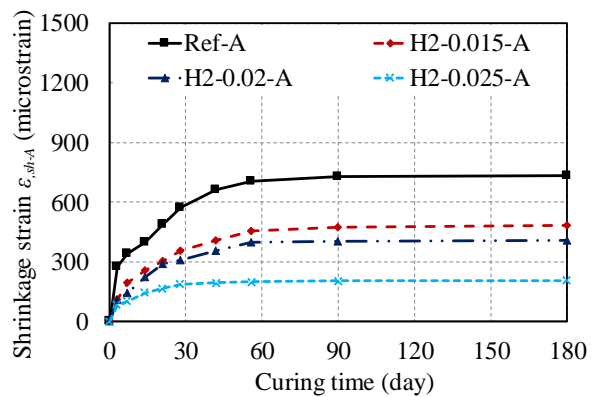
(a)



(b)



(c)



(d)

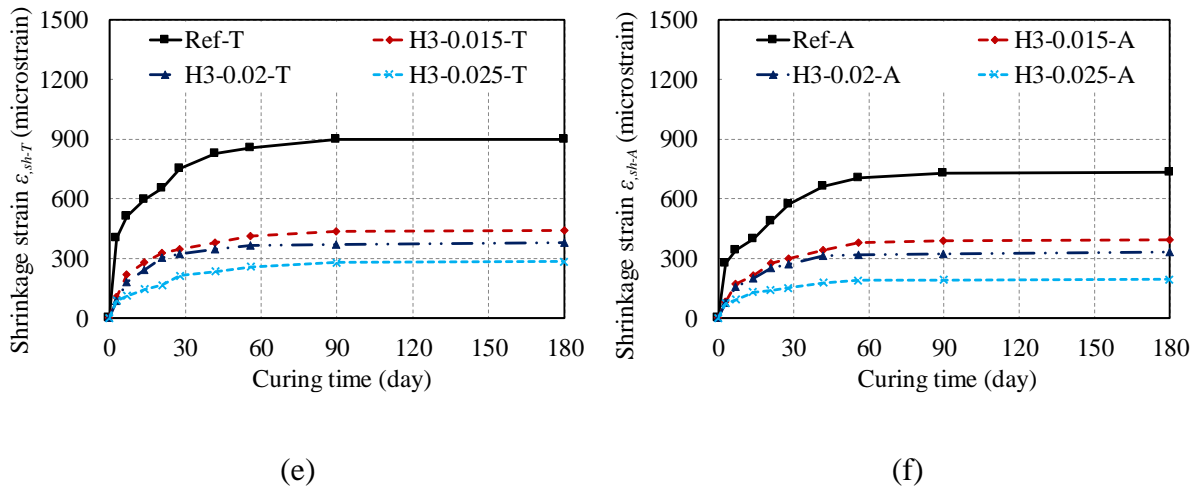


Figure. 2-2-7 Effect of fibre volume fraction on: a) total shrinkage-H1 series; b) autogenous shrinkage-H1 series; c) total shrinkage-H2 series; d) autogenous shrinkage-H2 series; e) total shrinkage-H3 series; f) autogenous shrinkage-H3 series.

It can also be deduced from Fig. 2-2-6 that generally, an increase in fibre volume slightly reduces drying shrinkage. This can be explained by the fact that the steel fibres in the UHPC matrix act as a skeleton for the concrete matrix along with the fine aggregate to provide increased dimensional stability. Moreover, the reduction in all categories of shrinkage with increased fibre content can also be attributed to the higher elastic modulus of the fibres, as well as the higher strength-to-size ratio of the fibres (Ullah 2017).

### 2.2.3.3.3. Effect of fibre shape

Figures 2-2-8 (a) and (b) shows the effect of fibre shape on the total and autogenous shrinkage of the UHPFRCs. It is worth mentioning that the comparisons were made for the shrinkage properties of the concrete produced using the fibres with the same aspect ratio (i.e. S and H2 both have an aspect ratio of 65), with the same volume fraction (i.e.  $V_f = 2.0\%$ ), and with different shapes (i.e. straight, hooked end or blended straight and hooked end). These

comparisons shown in the figures 2-2-8 (a) and (b) suggest that the hooked fibres were more effective than the straight fibres to reduce both the total- and autogenous- shrinkage of the UHPFRCs. For instance, the incorporations of S series of fibres reduced the total shrinkage by around 23% and the autogenous shrinkage by 35%, while the addition of H2 hooked end fibres resulted in a corresponding of 47% reduction in total shrinkage and 55% reduction in autogenous shrinkage. Although the straight micro-fibres may be more evenly distributed than the hooked end fibres in the matrix, the larger reduction in shrinkage with the addition of a hooked end is attributed to the enhanced bond between the fibres and the matrix (see Fig. 2-2-5).

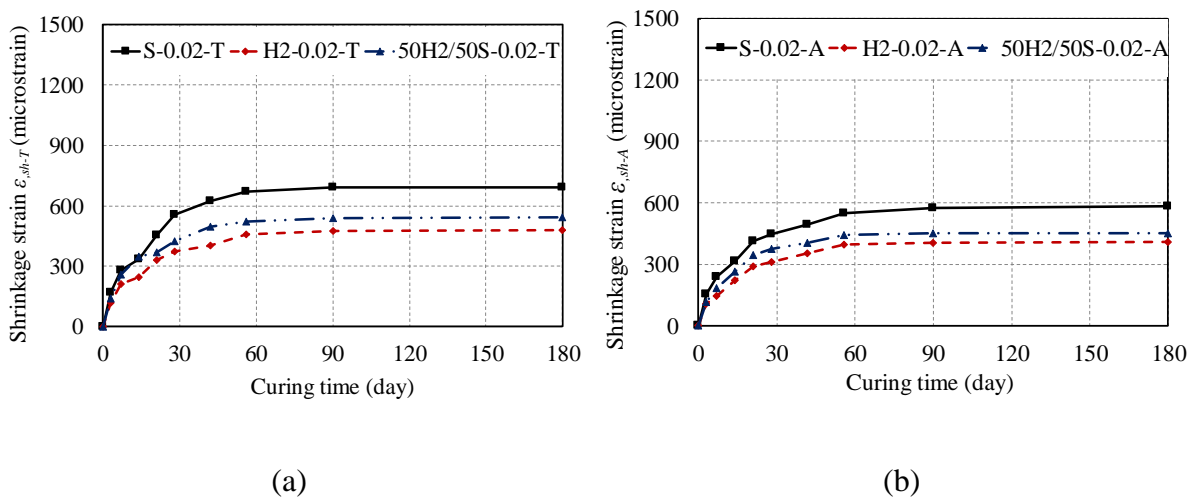


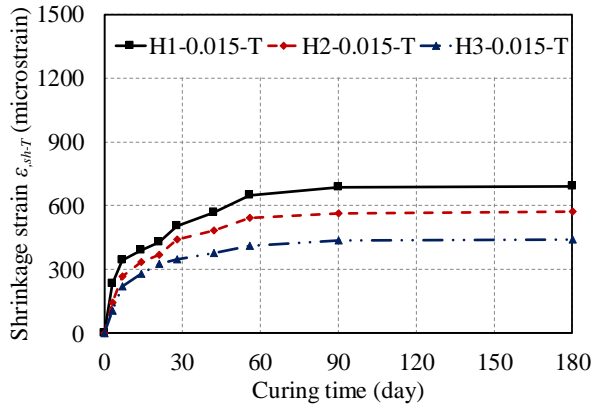
Figure. 2-2-8 Effect of fibre shape on: a) total shrinkage; b) autogenous shrinkage.

It can also be seen from Figures. 2-2-6 (e) to (h) that the effect of fibre shape on the drying shrinkage component exhibited at a similar trend to the total and autogenous shrinkages, where hooked end fibres performed better than the straight- and the blended fibres in reducing the drying shrinkage strain of the concrete. Compared with specimens with only a single type of

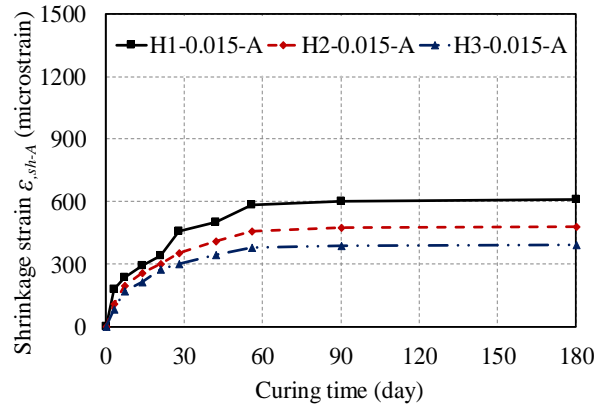
fibre, the blending of fibres resulted in a moderate reduction (up to 49%) in the autogenous shrinkages and a 39% of reduction in drying shrinkage of the UHPFRCs.

#### **2.2.3.3.4. Effect of fibre aspect ratio**

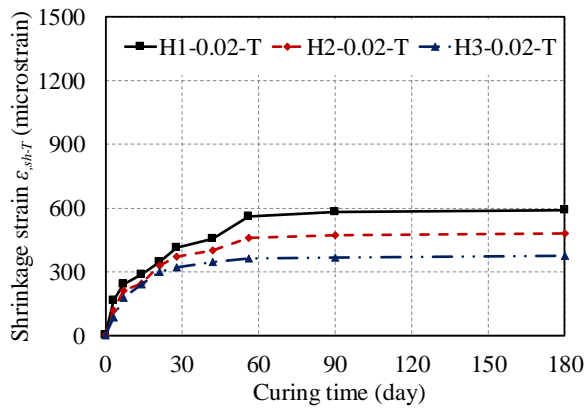
Figures 2-2-9 (a) to (f) present the effect of fibre aspect ratio on the shrinkage characterizations at different fibre volume fractions (i.e.  $V_f = 1.5, 2, \text{ or } 2.5\%$ ). It is evident from the figure that for the same fibre dosage, the use of H3 type of fibre, which has the highest aspect ratio among all the three types of hooked end fibres, resulted in a lower total- and autogenous- shrinkage of the UHPFRCs. In addition, it is shown in Fig. 2-2-6 that the drying shrinkage component of the UHPFRCs was also influenced by the fibre aspect ratio, where in general, at a given fibre volume and for a given age, the calculated drying shrinkage strain of the UHPFRCs decreased with an increase in the fibre aspect ratio. As confirmed by the fibre pull-out test results in section, this is attributed to a higher interfacial bond force for fibres with a higher aspect ratio (Qi et al. 2018). Note that H1 and H2 types of fibres have the same length but different diameters; H1 and H3 type of fibres have identical diameters but different lengths. Hence, based on the reported data above, it is suggested that the fibre length ( $l_f$ ) mainly predominate the reductions in total shrinkage ( $\epsilon_{sh-T}$ ), whereas the diameter of fibres is less significant in restraining the shrinkages. This can be attributed to the build-up of stress due to the bond between the fibres and matrix that occurred mostly along the length of fibres. Note that within the current range of the aspect ratios of the selected fibres (i.e. 45 to 80), the aspect ratio of the fibre is not as influential as the volume fraction or the shape of fibre presents on the shrinkage properties of the UHPFRCs.



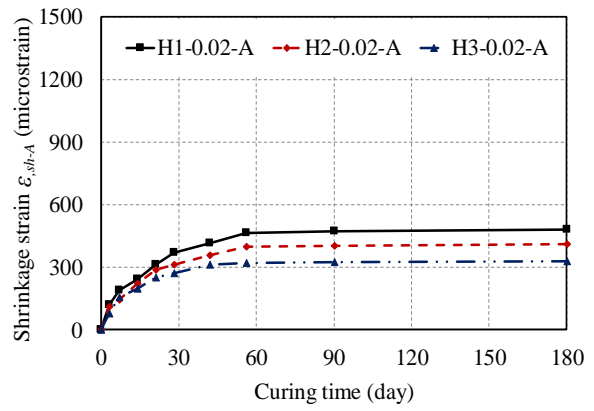
(a)



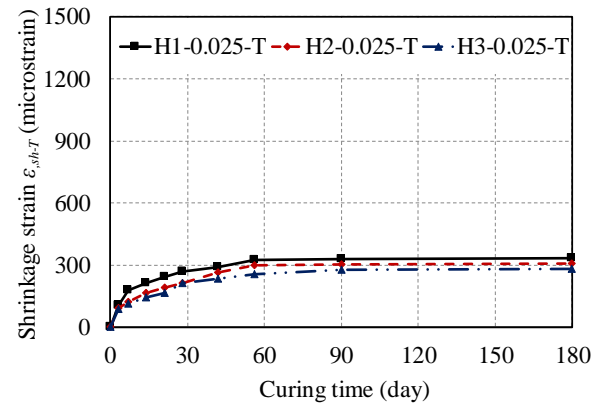
(b)



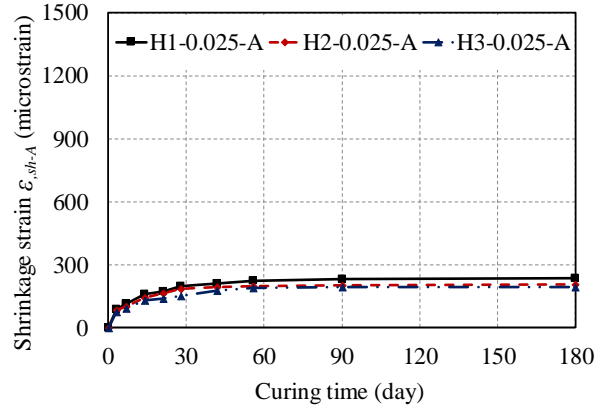
(c)



(d)



(e)



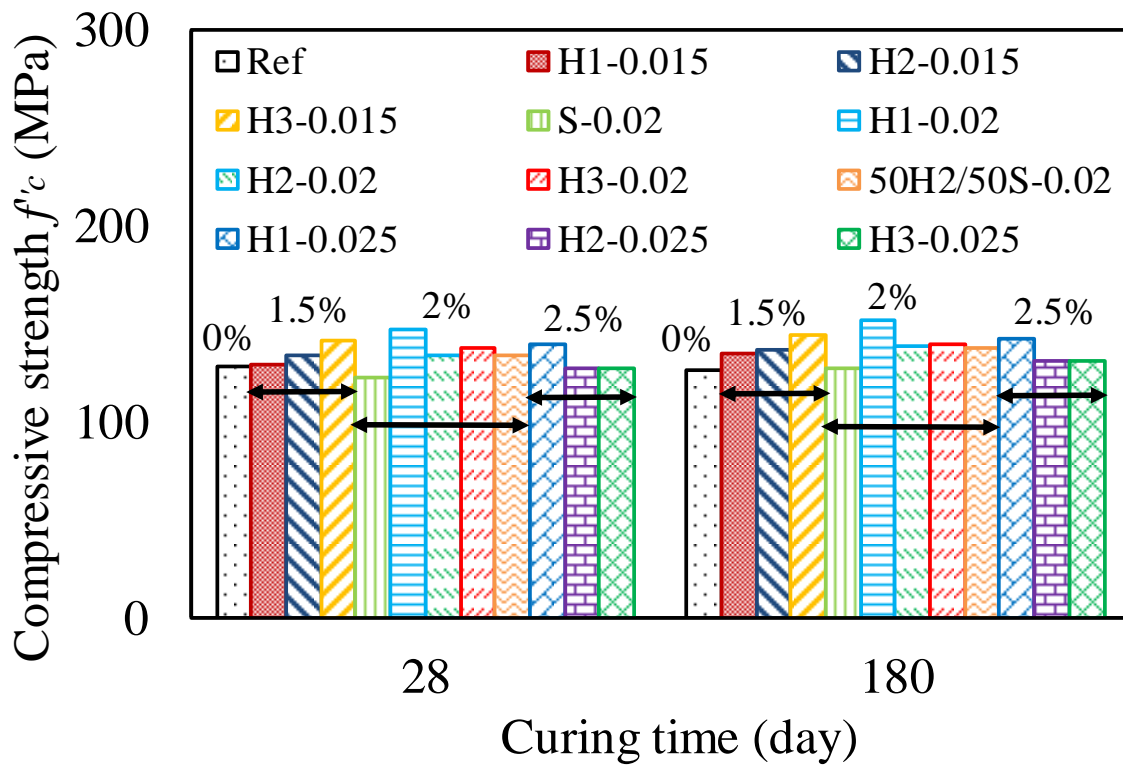
(f)

Figure. 2-2-9 Effect of fibre aspect ratio on: a) total shrinkage ( $V_f=1.5\%$ ); b) autogenous shrinkage ( $V_f=1.5\%$ ); c) total shrinkage ( $V_f=2.0\%$ ); d) autogenous shrinkage ( $V_f=2.0\%$ ); e) total shrinkage ( $V_f=2.5\%$ ); c) autogenous shrinkage ( $V_f=2.5\%$ ).

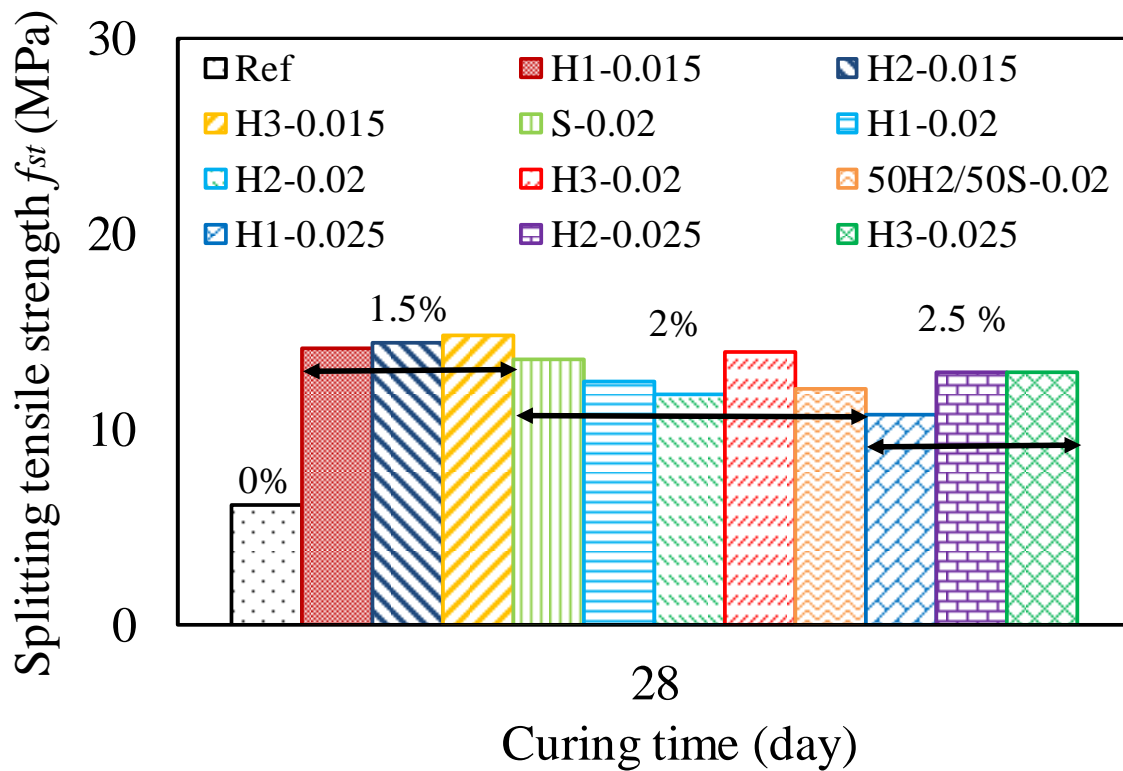


#### **2.2.3.4. Mechanical properties of the UHPFRCs**

Figures. 2-2-10 (a) and (b) graphically show the compressive and splitting tensile strengths of the UHPFRCs for a given specific testing age and these mechanical properties are also reported in Table 2-2-1. As can be seen from Fig. 2-2-10 (a), the incorporations of steel fibres into the UHPC matrix generally resulted in insignificant changes in their compressive strength for all concrete ages. This observation is in a good agreement with the findings reported in the previous studies on FRCs (Bhargava et al. 2006; Nataraja et al. 1999). There was also a slight reduction in compressive strength between the curing age of 28 and 180 days of the reference series without fibres. As explained in the previous studies on UHPCs and UHPFRCs (Sobuz et al. 2016; Xie et al. 2018), this reduction in mechanical strength was caused by the shrinkage induced cracks in the specimens. For the UHPFRC series with steel fibres, their compressive strength increased slightly between the concrete curing age of 28 and 180 days and no reduction in their compressive strength were occurred owing to the inclusion of fibres, which prevents the formations of the shrinkage, induced micro-cracks.



(a)



(b)

Figure. 2-2-10 Mechanical properties of the UHPFRCs: a) compressive strength; b) splitting tensile strength.

For the splitting tensile strength of the concretes measured at 28 days, it can be seen from Fig. 2-2-10 (b) that the inclusion of discrete steel fibres in the UHPC matrix significantly improves the tensile properties of the concrete because the fibres provide an internal confining effect by bridging the tensile cracks (Visintin and Oehlers 2018; Visintin et al. 2018). It can be seen from Fig. 2-2-10 (b) that regardless of the geometry of the fibres, the UHPFRC with 1.5 % of fibres (by volume fraction) exhibited a higher splitting tensile strength when compared to at the corresponding UHPFRC with a higher volume fraction (i.e. 2% or 2.5%) and the UHPFRCs with 2 and 2.5% had nearly identical  $f_{st}$  value. This may be due to the fact that at the fibre volume fraction of 1.5%, the fibres could be distributed more evenly in the matrix, and hence an effective enhancement the splitting tensile strength. It can also be seen from Table 2-2-1 and Fig. 2-2-10 (b), that for a given fibre volume fraction, the UHPFRC series with a higher fibre reinforcing index (which indicates a higher internal confining effect offered by the steel fibres) generally exhibited a slightly higher  $f_{st}$ .

#### **2.2.4. CONCLUSIONS AND REMARKS**

The following major conclusions can be drawn based on the results of the present study to investigate the effect of steel fibre on the shrinkage properties of the UHPFRCs:

1. At the initial static friction stage, the pull-out test results of a single fibre from a UHPC matrix suggests that the fibre with hooked ends and a higher aspect ratio leads to higher pull-out force for a given slip.
2. Incorporation of discrete steel fibres into a UHPC matrix can significantly reduce the total- and autogenous- shrinkage, this is mainly due to the bond stress between the fibres and matrix resisting the self-desiccation of the matrix.

3. An increase in fibre volume fraction leads to a reduction both the total and autogenous shrinkage magnitudes.
4. For a given aspect ratio, steel fibres with hooked ends are more efficient than the straight micro-fibres in reducing the total and autogenous shrinkage values of the UHPFRCs. The use of blended hooked end and straight fibres leads to only a marginal reduction in the shrinkage.
5. The use of fibres with a higher aspect ratio in a UHPFRC mix can reduce the total- and autogenous shrinkage of the UHPFRCs. However, the aspect ratio of the fibre is not as influential as the volume fraction and the shape of fibre on the long-term shrinkage properties of the UHPFRCs.
6. The inclusion of fibre in a UHPC matrix significantly improves its splitting tensile strength, whereas only a minor increase in the compressive strength of the concrete is attained. In addition, the optimal fibre volume fraction improves the tensile strength of the concrete is 1.5%.

#### **2.2.5. ACKNOWLEDGMENTS**

The first and fourth authors would like to thank the Australian Research Training Program (RTP) for financial support.

#### **2.2.6. REFERENCES**

ASTM, A. (2009). "C1698-09 Standard test method for autogenous strain of cement paste and mortar." *ASTM International, West Conshohocken, PA.*

- ASTM International (2004). "ASTM C496/C496M-04. Standard Test Method for Splitting Tensile Strength of Cylindrical Concrete Specimens." *ASTM International, West Conshohocken*.
- ASTM International (2005 ). "ASTM C39/C39M-05. tandard Test Method for Compressive Strength of Cylindrical Concrete Specimens." *ASTM International, West Conshohocken*.
- Australian Standard (2000). "AS 1478.1-2000. Chemical admixtures for concrete, mortar and grout Admixtures for concrete." *Standards Australia, Sydeny*.
- Bhargava, P., Sharma, U. K., and Kaushik, S. K. (2006). "Compressive stress-strain behavior of small scale steel fibre reinforced high strength concrete cylinders." *Journal of advanced concrete technology*, 4(1), 109-121.
- Darquennes, A., Staquet, S., and Espion, B. (2011). "Determination of time-zero and its effect on autogenous deformation evolution." *European journal of environmental and civil engineering*, 15(7), 1017-1029.
- Fang, C., Mohamed Ali, M., Sheikh, A., and Singh, M. (2019). "Numerical and Finite-Element Analysis of Short Ultrahigh-Performance Fiber Reinforced Concrete Columns." *ASCE Journal of Structural Engineering*.
- Garas, V. Y., Kahn, L. F., and Kurtis, K. E. (2009). "Short-term tensile creep and shrinkage of ultra-high performance concrete." *Cement and Concrete Composites*, 31(3), 147-152.
- Koh, K., Ryu, G., Kang, S., Park, J., and Kim, S. (2011). "Shrinkage properties of ultra-high performance concrete (UHPC)." *Advanced Science Letters*, 4(3), 948-952.
- Krahl, P. A., Gidrão, G. d. M. S., and Carrazedo, R. (2018). "Compressive behavior of UHPFRC under quasi-static and seismic strain rates considering the effect of fiber content." *Construction and Building Materials*, 188, 633-644.

- Lei, Y. B., and Cao, X. J. "Study on thermal dilation coefficient of fiber concrete at early stage." *Proc., Applied Mechanics and Materials*, Trans Tech Publ, 777-781.
- Mangat, P., and Azari, M. M. (1984). "A theory for the free shrinkage of steel fibre reinforced cement matrices." *Journal of materials science*, 19(7), 2183-2194.
- Mechtcherine, V., Gorges, M., Schroefl, C., Assmann, A., Brameshuber, W., Ribeiro, A. n. B., Cusson, D., Custódio, J., da Silva, E. F., and Ichimiya, K. (2014). "Effect of internal curing by using superabsorbent polymers (SAP) on autogenous shrinkage and other properties of a high-performance fine-grained concrete: results of a RILEM round-robin test." *Materials and structures*, 47(3), 541-562.
- Meng, W., and Khayat, K. H. (2018). "Effect of hybrid fibers on fresh properties, mechanical properties, and autogenous shrinkage of cost-effective UHPC." *Journal of Materials in Civil Engineering*, 30(4), 04018030.
- Meng, W., Samaranayake, V., and Khayat, K. H. (2018). "Factorial Design and Optimization of Ultra-High-Performance Concrete with Lightweight Sand." *ACI Materials Journal*, 115(1).
- Nataraja, M., Dhang, N., and Gupta, A. (1999). "Stress–strain curves for steel-fiber reinforced concrete under compression." *Cement and concrete composites*, 21(5-6), 383-390.
- Ngo, T. T., Park, J. K., Pyo, S., and Kim, D. J. (2017). "Shear resistance of ultra-high-performance fiber-reinforced concrete." *Construction and Building Materials*, 151, 246-257.
- Ou, Y.-C., Tsai, M.-S., Liu, K.-Y., and Chang, K.-C. (2011). "Compressive behavior of steel-fiber-reinforced concrete with a high reinforcing index." *Journal of Materials in Civil Engineering*, 24(2), 207-215.

- Park, J.-J., Yoo, D.-Y., Kim, S.-W., and Yoon, Y.-S. (2013). "Drying shrinkage cracking characteristics of ultra-high-performance fibre reinforced concrete with expansive and shrinkage reducing agents." *Magazine of concrete research*, 65(4), 248-256.
- Qi, J., Wu, Z., Ma, Z. J., and Wang, J. (2018). "Pullout behavior of straight and hooked-end steel fibers in UHPC matrix with various embedded angles." *Construction and Building Materials*, 191, 764-774.
- Shi, C., Wu, Z., Xiao, J., Wang, D., Huang, Z., and Fang, Z. (2015). "A review on ultra high performance concrete: Part I. Raw materials and mixture design." *Construction and Building Materials*, 101, 741-751.
- Sobuz, H., Visintin, P., Ali, M. M., Singh, M., Griffith, M., and Sheikh, A. (2016). "Manufacturing ultra-high performance concrete utilising conventional materials and production methods." *Construction and Building Materials*, 111, 251-261.
- Soliman, A., and Nehdi, M. (2012). "Early-Age Shrinkage of Ultra-High-Performance Concrete under Drying/Wetting Cycles and Submerged Conditions." *ACI Materials Journal*, 109(2).
- Soliman, A., and Nehdi, M. (2014). "Effects of shrinkage reducing admixture and wollastonite microfiber on early-age behavior of ultra-high performance concrete." *Cement and Concrete Composites*, 46, 81-89.
- Soliman, A. M., and Nehdi, M. L. (2013). "Self-Restraining Shrinkage Ultra-High-Performance Concrete: Mechanisms and Evidence." *ACI Materials Journal*, 110(4).
- Song, Q., Yu, R., Shui, Z., Wang, X., Rao, S., and Lin, Z. (2018). "Optimization of fibre orientation and distribution for a sustainable Ultra-High Performance Fibre Reinforced Concrete (UHPRFC): Experiments and mechanism analysis." *Construction and building materials*, 169, 8-19.

- Ullah, F. (2017). "Early age autogenous shrinkage and long-term drying shrinkage of fibre reinforced concrete."
- Visintin, P., and Oehlers, D. J. (2018). "Fundamental mechanics that govern the flexural behaviour of reinforced concrete beams with fibre-reinforced concrete." *Advances in Structural Engineering*, 21(7), 1088-1102.
- Visintin, P., Sturm, A. B., Ali, M. M., and Oehlers, D. J. (2018). "Blending Macro and Micro Fibres to Enhance the Serviceability Behaviour of UHPFRC." *Australian Journal of Civil Engineering*.
- Wang, D., Shi, C., Wu, Z., Xiao, J., Huang, Z., and Fang, Z. (2015). "A review on ultra high performance concrete: Part II. Hydration, microstructure and properties." *Construction and Building Materials*, 96, 368-377.
- Xie, T., Fang, C., Ali, M. M., and Visintin, P. (2018). "Characterizations of autogenous and drying shrinkage of ultra-high performance concrete (UHPC): An experimental study." *Cement and Concrete Composites*, 91, 156-173.
- Xie, T., Mohamed Ali, M. S., Elchalakani, M., and Moya, D. (2019). "Experimental and Analytical Study of Ultra-High Performance Fibre Reinforced Concrete Curved Beams." *ASCE Journal of Structural Engineering*.
- Xie, T., and Ozbakkaloglu, T. (2015). "Behavior of steel fiber-reinforced high-strength concrete-filled FRP tube columns under axial compression." *Engineering Structures*, 90, 158-171.
- Yoo, D.-Y., Banthia, N., and Yoon, Y.-S. (2015). "Effectiveness of shrinkage-reducing admixture in reducing autogenous shrinkage stress of ultra-high-performance fiber-reinforced concrete." *Cement and Concrete Composites*, 64, 27-36.



- Yoo, D.-Y., Min, K.-H., Lee, J.-H., and Yoon, Y.-S. (2014). "Shrinkage and cracking of restrained ultra-high-performance fiber-reinforced concrete slabs at early age." *Construction and Building Materials*, 73, 357-365.
- Yoo, D.-Y., Park, J.-J., Kim, S.-W., and Yoon, Y.-S. (2013). "Early age setting, shrinkage and tensile characteristics of ultra high performance fiber reinforced concrete." *Construction and Building Materials*, 41, 427-438.
- Yoo, D.-Y., Park, J.-J., Kim, S.-W., and Yoon, Y.-S. (2014). "Influence of reinforcing bar type on autogenous shrinkage stress and bond behavior of ultra high performance fiber reinforced concrete." *Cement and Concrete Composites*, 48, 150-161.
- Yoo, D.-Y., Park, J.-J., Kim, S.-W., and Yoon, Y.-S. (2014). "Influence of ring size on the restrained shrinkage behavior of ultra high performance fiber reinforced concrete." *Materials and structures*, 47(7), 1161-1174.

THIS PAGE HAS BEEN LEFT INTENTIONALLY BLANK

## **CHAPTER 3. Investigations on Ultrahigh Performance Fibre Reinforced Concrete Columns subjected to concentrically and eccentrically axial loads**

### **Introduction**

This chapter presents a series of analytical and numerical work performed to investigate the structural responses and failure modes of both short and slender UHPFRC columns. This chapter is presented as a compilation of a published manuscript of short UHPFRC columns and a conventional thesis chapter on slender UHPFRC columns.

In the first paper entitled “Numerical and Finite-Element Analysis of Short Ultra-high-Performance Fiber-Reinforced Concrete Columns”, an analytical approach was developed based on the moment-rotation ( $M/\theta$ ) approach incorporating the partial-interaction (PI) mechanism using material properties of both concrete and reinforcements as inputs. The models successfully simulated the structural responses such as load-axial deflection ( $P-\delta_{axial}$ ) and load-middle height deflection ( $P-\delta_{mid}$ ) relationships of the short UHPFRC columns when they are either subjected to concentric or eccentric axial loads.

In the sub-chapter entitled “Experimental and numerical investigation of the slenderness effects regarding ultrahigh performance fibre reinforced concrete column under concentric and eccentric loads”, finite element (FE) models were developed by incorporating a novel concrete damage plasticity (CDP) model. The numerical models were then further applied to conduct an extensive parametric study for investigating the influences of slenderness on the structural responses of the slender UHPFRC columns.

## **List of manuscripts**

1. Fang, C., M. S. Mohamed Ali, A. H. Sheikh, and M. Singh. 2019. Numerical and Finite-Element Analysis of Short Ultrahigh-Performance Fiber-Reinforced Concrete Columns. *Journal of Structural Engineering* 145, no. 10 (2019): 04019111.
2. Sub-chapter “Experimental and numerical investigation of the slenderness effects regarding ultrahigh performance fibre reinforced concrete column under concentric and eccentric loads”

# Statement of Authorship

Title of Paper	Numerical and finite element analysis of short ultra-high performance fiber reinforced concrete columns
Publication Status	<input checked="" type="checkbox"/> Published <input type="checkbox"/> Accepted for Publication <input type="checkbox"/> Submitted for Publication <input type="checkbox"/> Unpublished and Unsubmitted work written in manuscript style
Publication Details	Fang C, Mohamed Ali MS, Sheikh AH, Singh M. Numerical and Finite-Element Analysis of Short Ultrahigh-Performance Fiber-Reinforced Concrete columns. Journal of Structure Engineering. 2019 Aug 9; 145(10): 04019111.

## Principal Author

Name of Principal Author (Candidate)	Chengfeng Fang				
Contribution to the Paper	Performed analysis on all samples, interpreted data, wrote manuscript and acted as corresponding author.				
Overall percentage (%)	90%				
Certification:	This paper reports on original research I conducted during the period of my Higher Degree by Research candidature and is not subject to any obligations or contractual agreements with a third party that would constrain its inclusion in this thesis. I am the primary author of this paper.				
Signature	<table border="1" style="width: 100%;"> <tr> <td style="width: 80%;"></td> <td style="width: 20%;">Date</td> </tr> <tr> <td></td> <td>4/10/2019</td> </tr> </table>		Date		4/10/2019
	Date				
	4/10/2019				

## Co-Author Contributions

By signing the Statement of Authorship, each author certifies that:

- i. the candidate's stated contribution to the publication is accurate (as detailed above);
- ii. permission is granted for the candidate to include the publication in the thesis; and
- iii. the sum of all co-author contributions is equal to 100% less the candidate's stated contribution.

Name of Co-Author	Mohamed Ali Mohamed sadakkathulla				
Contribution to the Paper	Supervised development of numerical modelling, helped in data interpretation and manuscript evaluation				
Signature	<table border="1" style="width: 100%;"> <tr> <td style="width: 80%;"></td> <td style="width: 20%;">Date</td> </tr> <tr> <td></td> <td>4/10/2019</td> </tr> </table>		Date		4/10/2019
	Date				
	4/10/2019				

Name of Co-Author	Abdul Hamid Sheikh				
Contribution to the Paper	Supervised development of finite element simulation, helped in data interpretation and manuscript evaluation				
Signature	<table border="1" style="width: 100%;"> <tr> <td style="width: 80%;"></td> <td style="width: 20%;">Date</td> </tr> <tr> <td></td> <td>4/10/2019</td> </tr> </table>		Date		4/10/2019
	Date				
	4/10/2019				

Name of Co-Author	Manpreet Singh		
Contribution to the Paper	Provide data and information about the experimental program		
Signature	/	Date	4/10/2019

### 3.1. Numerical and Finite-Element Analysis of Short Ultrahigh-Performance Fiber-Reinforced Concrete Columns

Fang, C.<sup>1</sup>, Mohamed Ali, M.S.<sup>1</sup>, Sheikh, A.H.<sup>1</sup>, Singh, M.<sup>1</sup>

<sup>1</sup>School of Civil, Environmental and Mining Engineering, The University of Adelaide, SA  
5005, Australia

#### ABSTRACT:

This paper describes the development of numerical and finite element (FE) models in investigating the behaviors of short ultra-high performance fiber reinforced concrete (UHPFRC) columns under concentric or eccentric loading conditions. A generic mechanic-based partial interaction (PI) approach that is applicable to both flexural and axial members manufactured by conventional fiber reinforced concrete has been suitably modified to analyze the structural response of the short UHPFRC columns. Moreover, finite element (FE) modelling was also conducted to study the behaviors of the UHPFRC members subjected to different loading conditions. Both models aim to generate load-axial deflection ( $P-\delta_{axial}$ ) or load-middle height deflection ( $P-\delta_{mid}$ ) relationships for concentrically or eccentrically loaded columns, as well as a load-middle span deflection ( $P-\delta_{mid}$ ) relationship for a beam subjected to three-point bending. Simulated results display an excellent agreement with test results, and it can accurately predict the structural response of the UHPFRC columns. To aid in the development of a design guideline for the short UHPFRC columns, a load-moment ( $P-M$ ) interaction envelope generated by the numerical model is proposed and it shows a good correlation to the experimental results.

**Keywords:** Ultra-high performance fiber reinforced concrete (UHPFRC); Short column; Partial interaction analysis (PI); Finite element analysis (FEA);

### **3.1.1. INTRODUCTION**

Ultra-high performance fiber reinforced concrete (UHPFRC) is a novel construction material, which is produced using a fine granular mixture, and exhibits enhanced mechanical strength, durability, ductile tensile behaviors and high damage resistance due to of the confining effect offered by the inner steel fibers in the homogenous cementitious based matrix (Hosinieh et al. 2015; Yoo and Banthia 2016; Yoo and Yoon 2016; Visintin et al. 2018a). Because of its superior material characteristics, the use of UHPFRC can significantly reduce the structural member size, shorten the construction period, and lower their life cycle costs (Yoo and Yoon 2016). The recent research on UHPFRC mostly focuses on investigating the behaviors of structural members manufactured using UHPFRC, such as beams (Baby et al. 2014; Singh et al. 2017; Dagenais and Massicotte 2017; Sturm et al. 2018) and columns (Steven and Empelmann 2014; Hosinieh et al. 2015; Singh et al. 2015; Shin et al. 2017; Shin et al. 2018), and these studies indicate that using UHPFRC as construction material can significantly enhance the shear, axial load carrying, and flexural moment capacities of the structures.

To date, a number of studies have been carried out to investigate the structural performance of UHPFRC structural members, for instance columns under the uniaxial compression protocol (Steven and Empelmann 2014; Hosinieh et al. 2015; Shin et al. 2017; Shin et al. 2018), and their experimental results showed that the structures produced using UHPFRC exhibited higher load carrying capacity and improved ductility, in which no catastrophic collapses of the entire structure were observed. Pure axial loading tests on short UHPFRC columns with square cross-sections were conducted by Hosinieh et al. (2015), and Shin et al. (2017) and their test results indicated that the increasing volumetric ratio or reducing spacing of the transverse reinforcement for a given configuration results in a pronounced increases in the axial load carrying capacities and ductility index of the UHPFRC short columns. They also observed that



for a given value of transverse reinforcement spacing, the configurations of reinforcement affected both post-peak strength decay and the toughness of the short UHPFRC columns, where the column with a high steel reinforcement ratio withstood a larger axial load at post-peak stage compared to that of the column with a low steel reinforcement ratio, which allows a high energy absorption and robustness. A series of uniaxial compression tests on UHPFRC columns with circular cross-sections and reinforced by spiral reinforcements were conducted by Shin et al. (2018), and experimental results demonstrated that over 80% of axial load capacity was maintained with the presence of the transverse reinforcements (e.g. 3-5.1%) until the axial strain attained to 0.02. Steven and Empelmann (2014) conducted experimental investigations to study the behavior of rectangular UHPFRC columns subjected to concentric or eccentric loads with eccentricities ranging from 5 mm to 75 mm, and hence derived an empirical expression to predict the load carrying capacity of UHPFRC columns. Based on the above literature review, it recognized that most of the existing studies have investigated the behavior of concentrically loaded UHPFRC columns experimentally, with few reported analytical procedure with strong physical senses to fully describe the underlying mechanism. To fill this research gap, this study primarily aims to develop a rational procedure to analyze the short UHPFRC column to generate individual load-displacement relationship and the load-moment interaction envelope, and hence to initiate the design guidelines of the UHPFRC columns and this further promotes the utilization of UHPFRC for construction.

To achieve this objective, firstly, a step-by-step procedure is developed by suitably modifying the classical structural mechanical-based model, namely, the moment-rotation ( $M/\theta$ ) approach, that has been successfully applied to simulate the axial behavior of conventional reinforced concrete columns (Visintin et al. 2013) and flexural behaviors of FRP-plate reinforced beams (Mohamed et al. 2008) and fiber-reinforced concrete beams (Visintin and Oehlers 2018;

Visintin et al. 2018b). In this study, this generic approach is further extended to simulate UHPFRC short columns by incorporating the effects of steel fibers in the UHPFRC (i.e. tensile strain hardening). Furthermore, aiming to more accurately predict the performance of the eccentrically loaded short UHPFRC columns, the active confinement effects induced by the transverse reinforcements cannot be neglected and need to be properly considered in the analytical approaches. Existing confinement models (Razvi and Saatcioglu 1999) pertaining to high strength concrete (HSC) with steel stirrups were verified based on the specific actively-confined test results of UHPFRC and hence adopted in the proposed numerical model to simulate the stress-strain relationship of the UHPFRC confined by stirrups. In addition to the mechanic-based model, a detailed finite element (FE) analysis is also undertaken to incorporate a purposely developed concrete damage plasticity (CDP) model into a commercially available FE software ABAQUS to simulate the behaviors observed experimentally in UHPFRC column tests. Both models are then compared and validated against experimental results published in previous studies (Steven and Empelmann 2014; Singh et al. 2015), wherein these columns were subjected to the concentric or eccentric loads.

### **3.1.2. DEVELOPING NUMERICAL MODELS USING PARTIAL-INTERACTION (PI) ANALYSIS**

The structural response of a short UHPFRC column under eccentric loading condition can be referred to the following stages:

- (1) Stage 1-pre-cracking stage. A conventional sectional analysis that assumes a full-interaction between reinforcements and adjacent UHPFRC was adopted to generate the ( $M$ - $\theta$ ) relationship of the section.
- (2) Stage 2- post-cracking stage. An increase in flexural bending ( $M$ ) initiates and gradually enlarges tensile cracks at the surface of the columns. Here full-interaction based analysis is

not able to capture this localized behavior, whereas a partial interaction (PI) analysis considering the tension stiffening mechanism well accommodate the relationships between slips ( $\Delta$ ) and forces ( $P_{rb}$ ) in tensile reinforcement into the displacement-based moment rotation ( $M/\theta$ ) approach to obtain the ( $M-\theta$ ) relationship of the column section at the post-cracking stage.

- (3) Stage 3-formation of plastic hinge. Post-cracking stage is then followed by the formation of plastic hinge with the occurrence of the concrete softening (i.e. due to the concrete crushing under compression) and the development of compression wedge also accompanies with gradually yielding of tensile reinforcements. To obtain ( $M-\theta$ ) relationship of the columns in this phase, a size-dependent approach was adopted to quantify the concrete-to-concrete sliding mechanism occurred at the sliding interfaces.

The details of the formation of plastic hinge, segmental approach, and partial interaction (PI) mechanisms, including tension stiffening and concrete softening were described in the following sections.

### **3.1.2.1. Fundamental mechanism of the column plastic hinge**

A displacement-based partial-interaction moment-rotation ( $M/\theta$ ) approach for simulating the structural behaviors of the eccentrically loaded UHPFRC short column after the pre-cracking stage is illustrated in Fig.3-1-1. This technique successfully reproduced the load-lateral deflection ( $P-\delta_{mid}$ ) relationships of conventional RC columns subjected to eccentric load (Visintin et al. 2013) from serviceability to the structural failure, and has been further extended to fiber-reinforced concrete (FRC) flexural member with considering the crack bridging effects (Visintin and Oehlers 2018; Sturm et al. 2018; Xie et al. 2018). Figure 3-1-1 (a) depicts the conceptual model of PI tension stiffening mechanism on the short UHPFRC column at the post-cracking stage. Initially, an increase in flexural bending moment ( $M$ ) induced by eccentric axial

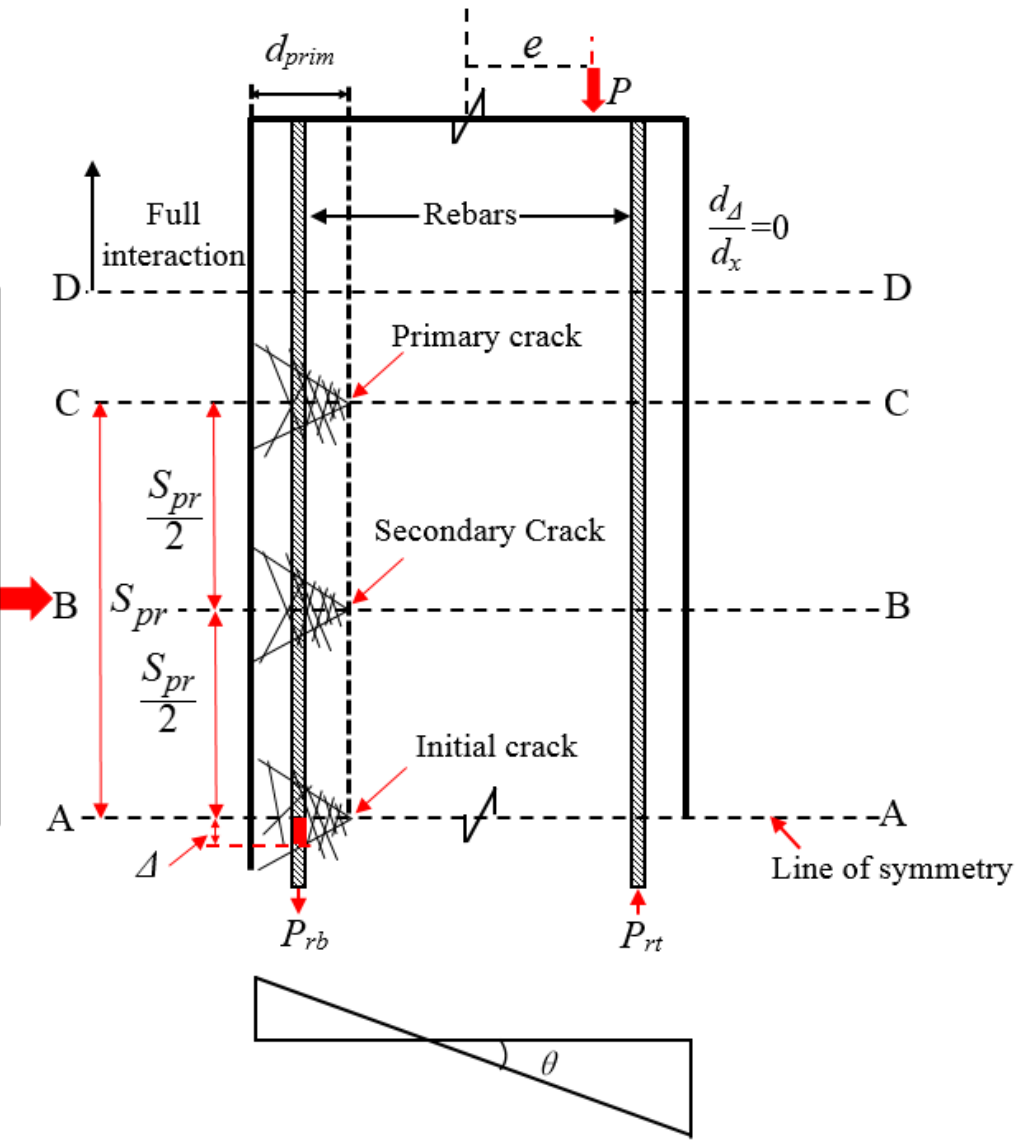
load ( $P$ ) resulted in the formation of the initial crack at the section AA that located at the middle height of the column. Right after the concrete tensile cracking, a slip ( $\Delta$ ) between tensile rebar and surrounding concrete prism with a width of ( $d_{prism}$ ) also affected the force in tensile rebar ( $P_{rb}$ ) at the initial crack section (AA). Specifically, to model the tension stiffening mechanism and hence to accommodate its effect on  $M-\theta$  relationship of the section, a shooting method is applied whose details are described in the later section. Furthermore, the widening of the tensile cracks with increasing moment leads to a subsequent increase in the discrete rotation ( $\theta$ ) of the short column and consequently affects the moment-rotation ( $M-\theta$ ) relationships of the UHPFRC columns after pre-cracking stage. With increasing in bending moment ( $M$ ) along the short column, a primary crack (at section CC in Fig. 3-1-1) occurred adjacent to the initial crack, where the distance between the primary crack and initial crack is defined as a crack spacing ( $S_{pr}$ ), as also shown in Fig. 3-1-1 (a). A secondary crack (at section BB on Fig. 3-1-1), which is ideally located at the middle between initial and primary cracks, is subsequently formed with further increasing applied load. Hence, in the analysis provided in the remainder of the paper, column region AA-DD is identified as a partial interaction zone and the region above the section DD is defined as the full interaction (FI) zone.

With a large discrete rotation ( $\theta$ ) attained, concrete softening initiates at the compressive region of the section owing to the reason that strain in the compression zone exceeds the corresponding strain at the peak compression stress of the UHPFRC, in which this softening region can be idealized as the compressive wedge ( $L_w$ ) as presented in Fig. 3-1-1 (b). The mechanics-based hinge analysis (Visintin et al. 2013) including the PI tension stiffening mechanism and PI concrete softening mechanism accurately quantified the discrete rotation of the column at the plastic hinge stage and hence obtained the load-lateral deflection relationship at the plastic

hinge region of the columns. To simulate the behavior of an eccentrically loaded short column using the mechanics-based hinge analysis, the following assumptions were made:

1. The Euler-Bernoulli principle of plane sections remaining plane was applied for the sectional analysis in all loading stages the columns (Visintin et al. 2013).
2. It assumes a constant moment (i.e.  $M = P \times e$ ) acting along the column and;
3. Premature buckling caused by the secondary moment effect is neglected

- Crack formation following a sequence of initial crack (A-A), primary crack (C-C), and secondary crack (B-B).
- Analysis of single crack segment A-A and C-C (without crack at section B-B) refer to Fig. 3-1-3 (a).
- Analysis of multiple crack segments A-A and C-C (with crack at section B-B) refer to Fig. 3-1-3 (b).



(a)  
111



Figure 3-1-1. Schematic diagram of UHPFRC short column under an eccentric load: (a) post-cracking stage; (b) plastic hinge formation

### 3.1.2.2. Cross-sectional analysis at partial interaction (PI) region

The displacement-based moment rotation ( $M/\theta$ ) approach is a direct application of Euler-Bernoulli theorem of plane section accommodating with the stress-strain relationships for both UHPFRC and reinforcements to determine the internal moment within the cross-section of the column. Generally, the failure of an eccentrically loaded column can be categorized into two modes depending on the magnitude of the eccentricity: (1) failed by concrete compressive softening when the column loaded at zero or a small eccentricity, and (2) failed by flexural bending when the column loaded at a large eccentricity. Fig. 3-1-2 (a) and (b) graphically shows the mechanisms governing the two failure modes of the eccentrically loaded UHPFRC short columns, respectively. For a short column loaded at a small eccentricity showed in Fig. 3-1-2 (a), the strain profile indicates that the neutral axis of column locates outside of the column cross-section and entire cross-section is fully under compression. For this case, the softening of the UHPFRC causes the relative slippage along the concrete-to-concrete interface and determines the friction force of UHPFRC. The total rotation ( $\theta$ ) of the column is affected by the concrete softening after the formation of the compression wedge. It is note that the shear friction mechanism is size-dependent and can be accurately modelled using the size-dependent approach developed by Chen et.al (2014).

The second strain profile of column hinge shown in Fig. 3-1-2 (b) presents the mechanisms governing the failure of UHPFRC columns loaded with a relatively large eccentricity ( $e$ ), and the performance of the column is predominated by the flexural bending moment ( $M$ ) induced by the eccentric loads rather than the applied load ( $P$ ). By inputting the material properties into the PI based sectional analysis, the location of the neutral axis can be easily found and hence



the  $M-\theta$  relationship of the section be obtained at all loading stages. Note that in the PI based analysis the effect of tension stiffening mechanism should be considered, and this can be simply achieved by using the force ( $P_{rb}$ ) based on the relative slip ( $\Delta$ ) between reinforcement and adjacent concrete.

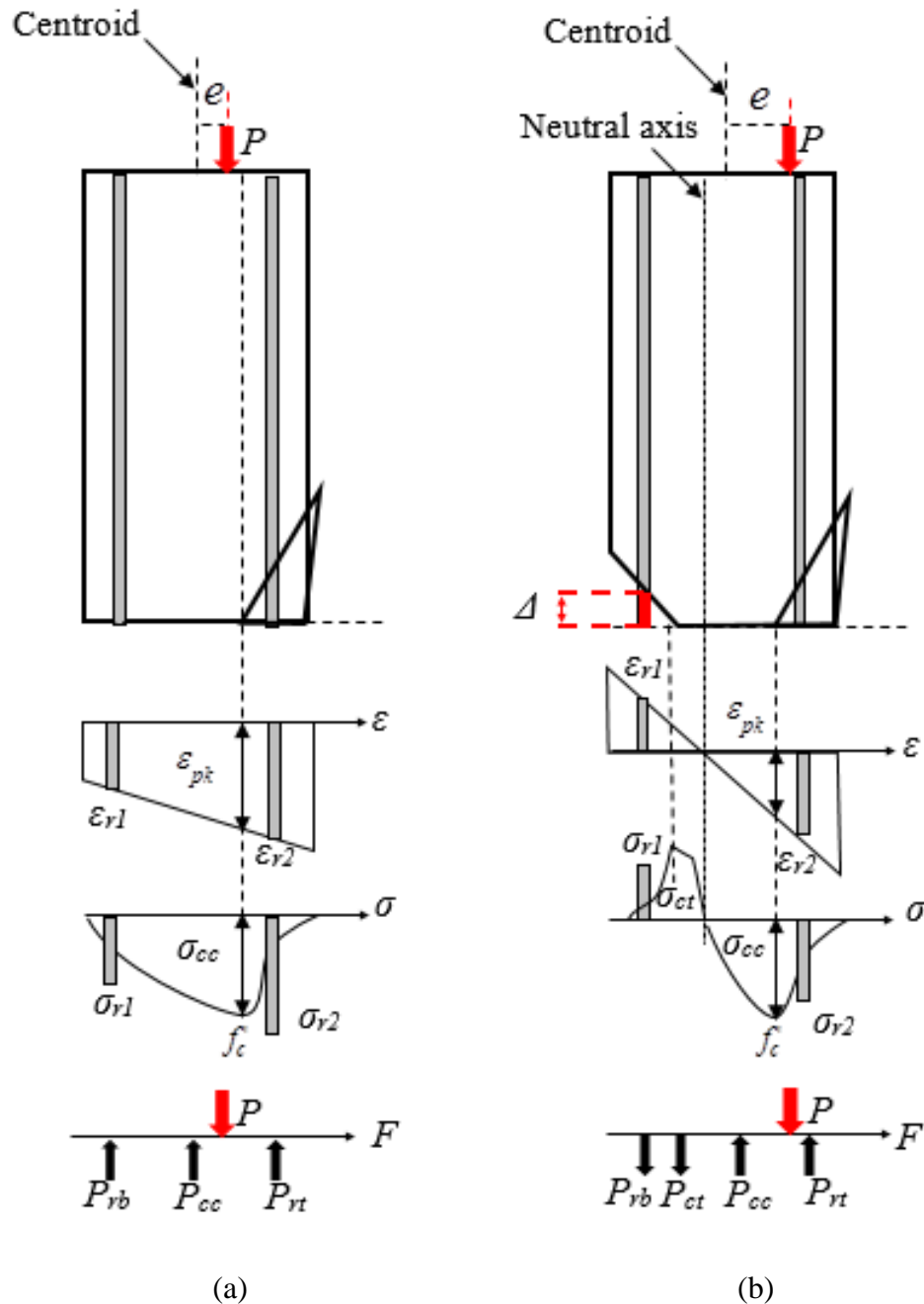


Figure 3-1-2. Cross-section profiles for: (a) the column loaded at a small eccentricity; (b) the column loaded at a large eccentricity

### 3.1.2.3. Partial interaction (PI) tension stiffening mechanism

Tension stiffening mechanism presented in Fig. 3-1-3 is an essential component for quantifying the actual performance of the eccentrically loaded columns at the plastic hinge region. A shooting method for tension stiffening numerical analysis to attain a force-slip ( $P_{rb}-\Delta$ ) relationship and the detailed modelling procedure are schematically shown in Fig. 3-1-4 and Fig. 3-1-5, respectively. As presented in Fig. 3-1-3 (a), the area of a tensile reinforcement is  $A_{bar}$ , and the cross-section of the surrounding concrete is idealized as a square prism with the cross-sectional area of  $A_c$ . With the formation of the initial tensile crack at section AA, both residual tensile force in fibers ( $P_{fib}$ ) and force in tensile rebar ( $P_{rb}$ ) resist against the widening of the initial crack. The slip distribution shown in Fig. 3-1-3 (a) indicates that the maximum slip ( $\Delta$ ) occurred at the initial crack section AA and gradually decreases along the PI region until it reaches zero, and hence it results in a transfer of stress from the reinforcement to concrete through the bond. Furthermore, the full interaction boundary conditions are defined when both distribution of ( $\Delta$ ) and ( $d\Delta/dx$ ) tend to zero at the same location, which in turns to determine the crack spacing ( $S_{pr}$ ) and force-slip ( $P_{rb}-\Delta$ ) relationship. The partial-interaction tension-stiffening numerical mechanism for multiple cracks as reported in the previous studies (Mohamed et al. 2008; Shukri et al. 2016; Visintin and Oehlers 2018) is illustrated in Fig. 3-1-3 (b). For modelling the case of multiple cracks using the shooting method, its boundary condition is defined as that the distribution of ( $\Delta$ ) reaches to zero at the location of ( $S_{pr}/2$ ) from the initial crack. This hence redefines the  $P_{rb}-\Delta$  response at the hinge section for generating the  $M-\theta$  relationships of the columns.

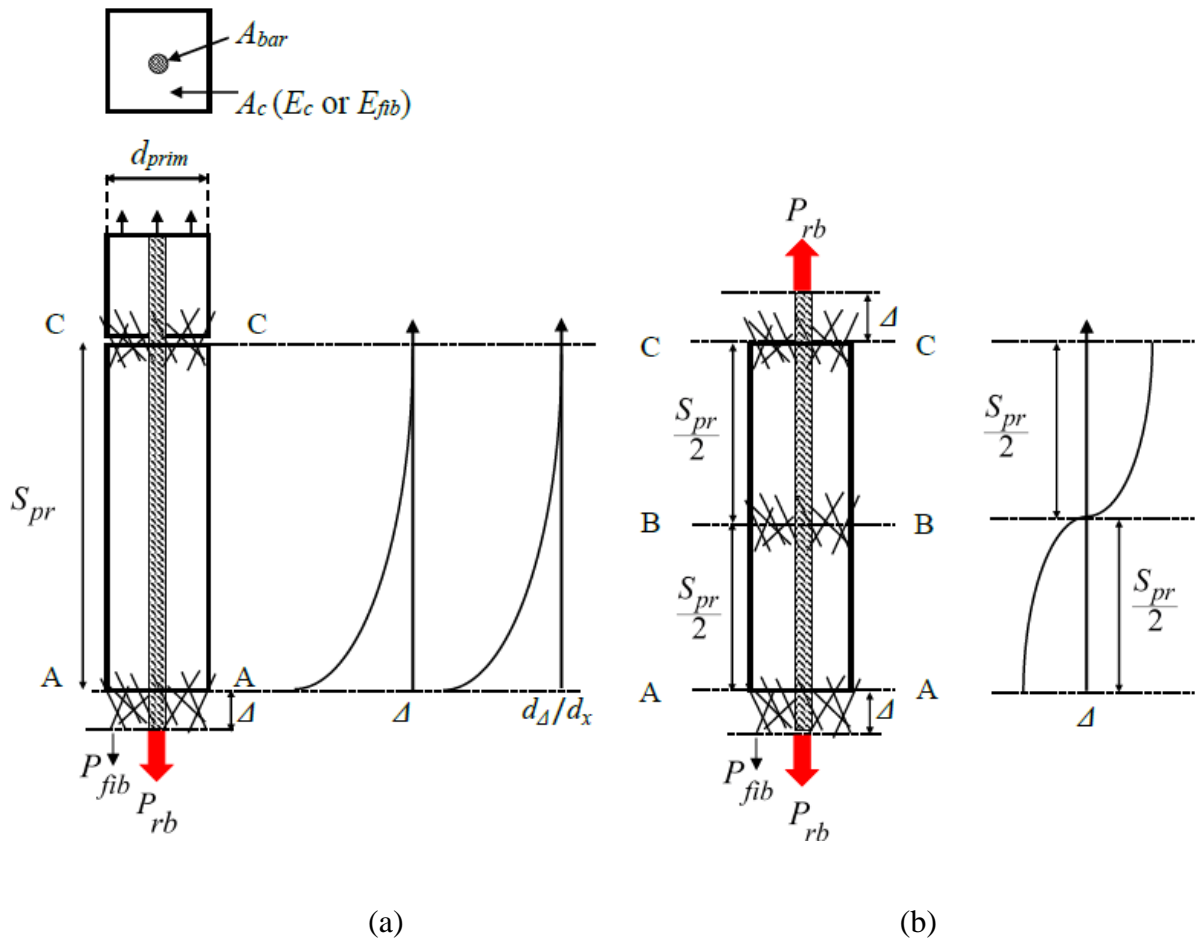


Figure 3-1-3. Partial interaction tension-stiffening mechanisms: (a) tension stiffening with a single crack; (b) tension stiffening with multiple cracks.

As presented in Fig. 3-1-4, the concrete prism is divided into multiple segments with a very short element length ( $L_e$ ) to determine the variation in reinforcement slip and the distribution of strain in the reinforcement and the concrete. Followed that, impose a slip ( $\Delta_l$ ) as the initial value for the slip ( $\Delta$ ) with the maximum value of ( $W_{cr}/2$ ) which is the half of the maximum crack length (Visintin and Oehlers 2018). The corresponding force in UHPFRC due to fiber bridging effect is identified as ( $P_{fib}$ ), which is derived from the relationship between tensile stress ( $\sigma_i$ ) and the half crack width ( $W_{cr}/2$ ). As presented in both Fig. 3-1-4 and Fig. 3-1-5, the force of the tensile reinforcement at the crack face ( $P_{rb}$ ) is initially guessed as the average of

the low boundary ( $P_{rl}$ ) and high boundary ( $P_{ru}$ ), and corresponding strain in the reinforcement ( $\epsilon_{bl}$ ) and concrete ( $\epsilon_{cl}$ ) can be obtained, as presented in Fig. 3-1-5. Hence, the slip strain of the first concrete segment  $(d_{\Delta}/d_x)_1$  which is the algebraic difference of the strain magnitudes between the reinforcement and concrete ( $\epsilon_{bl} - \epsilon_{cl}$ ) is determined. The corresponding differential slip ( $\delta\Delta_l$ ) between concrete and reinforcement in the segment 1 is obtained by integrating the slip strain  $(d_{\Delta}/d_x)_1$  along the segmental length ( $L_e$ ). The bond force in the first element ( $B_1$ ) can be calculated from the known bond slip ( $\tau-\Delta$ ) properties and the contact perimeter ( $L_{per}$ ) of the rebar. This procedure is repeated for element 2 with the tensile force in reinforcement determined as  $(P_{rb} - B_1)$  and the force in concrete determined as  $(P_c + B_1)$ . The slip of the tensile reinforcement at the second segment ( $\Delta_2$ ) is obtained by subtracting  $\delta\Delta_l$  from the initial slip ( $\Delta_1$ ), and corresponding bond force ( $B_2$ ) in element 2 can therefore be determined, as shown in Fig. 3-1-4. A flow chart is given in Fig. 3-1-5 to show the details of applying this shooting method to obtain the  $P_{rb}-\Delta_l$  relationship and the additional information of describing this shooting method can be found in (Visintin and Oehlers 2018). This analysis can then be repeated successively for subsequent elements to yield the  $P_{rb}$  needed to produce a given slip ( $\Delta_l$ ) until the full-interaction boundary conditions are satisfied, where both slip ( $\Delta$ ) and slip strain  $(d_{\Delta}/d_x)$  values in the segment tend to zero. Consequently, this defines the minimum distance from the initial crack face to the primary cracks may form, namely initial crack spacing ( $S_{pr}$ ). Similarly, the same shooting method was applied to conduct the PI tension stiffening analysis for the case of the multiple cracking, and one boundary condition, which the slip ( $\Delta$ ) equals to zero at the location of  $(S_{pr}/2)$  from the initial crack, is required.

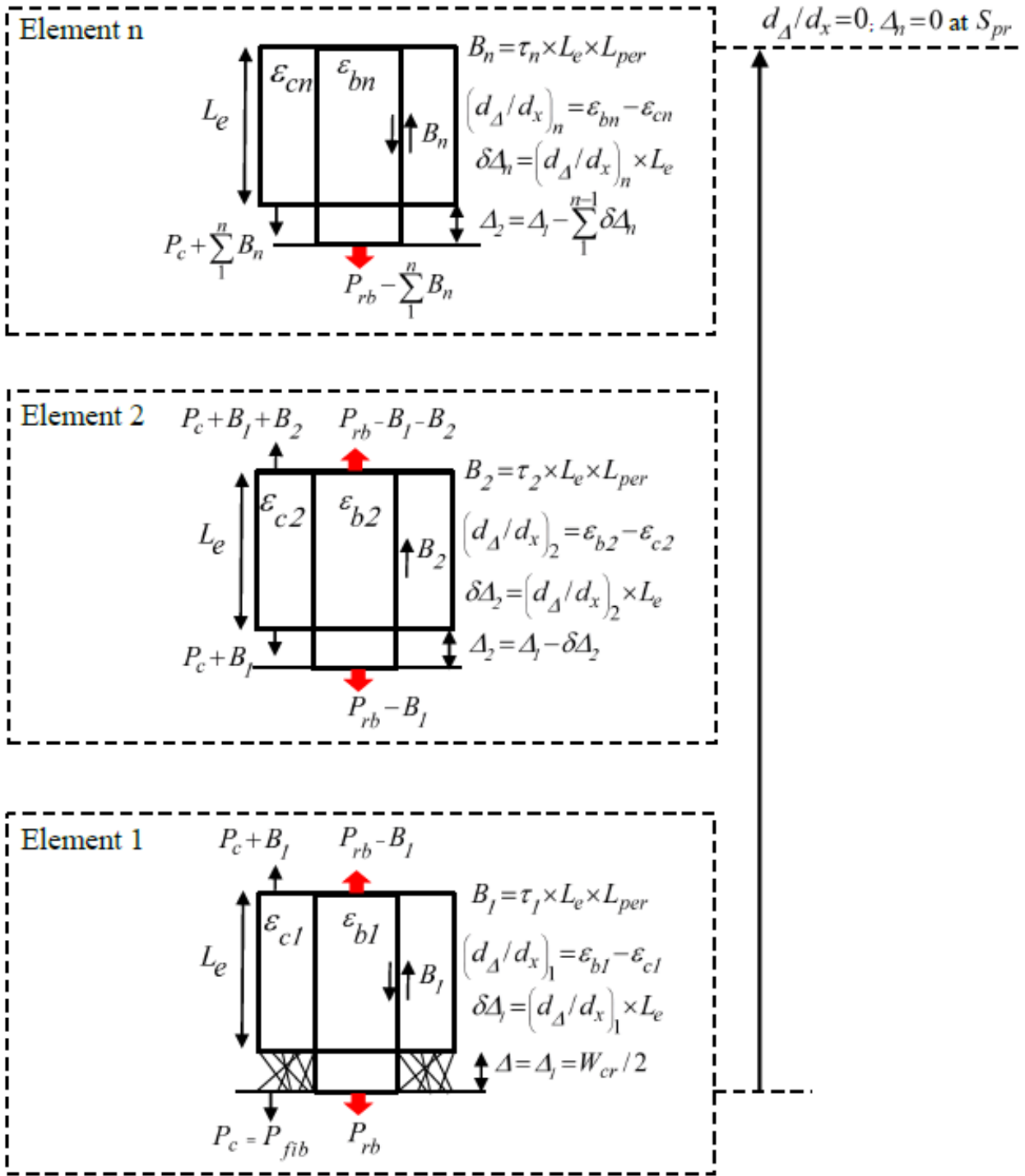


Figure 3-1-1. Shooting method for tension stiffening numerical analysis

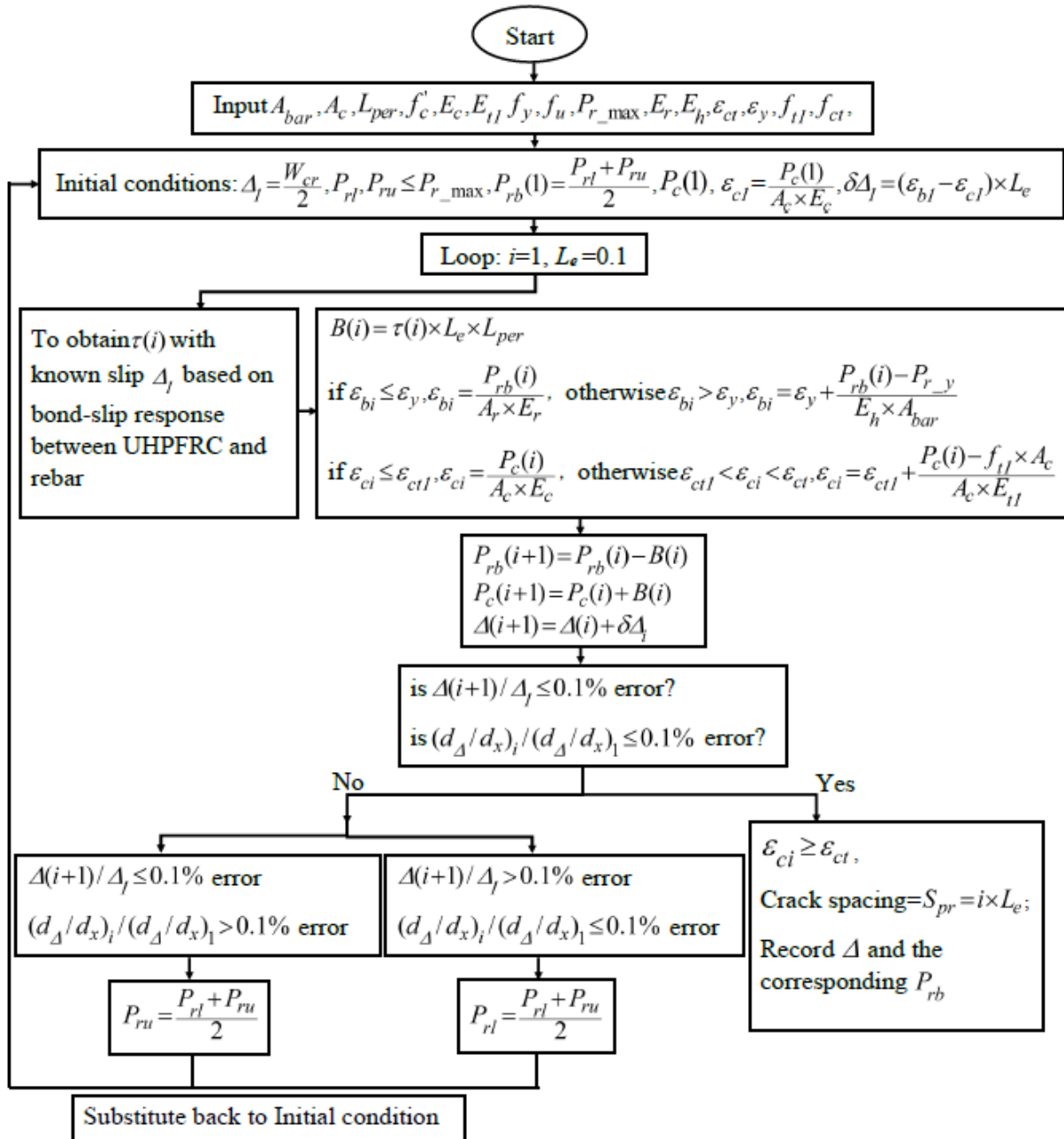


Figure 3-1-5. Modelling procedure to determine the ( $P_{rb} - \Delta$ ) relationship

### 3.1.2.4. Partial interaction (PI) concrete softening

When the compressive strain in conventional concrete exceeds the strain corresponding to the peak stress, concrete starts crushing and a sliding wedge starts to form in the PI compression region. It is known that compressive stress-strain ( $\sigma - \epsilon$ ) relationship for plain concrete comprised by two branches, including an ascending branch up to the peak strength that depends

entirely on the material deformations and a descending branch that is associated with PI sliding along the concrete to the concrete interface of the softening wedge (Zhang et al. 2014). A generic size-dependent  $\sigma$ - $\varepsilon$  relationship based on the results of standard cylinder tests as proposed in Chen et al. (2014) which encompassed the ascending branch dependent on the length of the specimens and the descending branch dominated by the shear friction mechanism along the sliding wedge. This approach which has been successfully applied to conventional concrete (Chen et al. 2014) and has been further extended to steel fiber concrete (FRC) by Visintin and Oehlers (2018) accommodating the wedge restrained by fibers in a flexural analysis, is therefore applied in the segmental analysis of current study to derive the stress in the PI sliding wedge.

$$\varepsilon_{def} = (\varepsilon_{test} - \varepsilon_{mat}) \frac{200}{L_{def}} + \varepsilon_{mat} \quad (1)$$

where  $\varepsilon_{mat}$  is the material strain corresponding to the strain at peak stress;  $\varepsilon_{test}$  is the total strain based on standard compression test using a 200 mm cylinder;  $L_{def}$  is the deformation length which is also a half of the cracking space ( $S_{pr}/2$ ) determined from the partial interaction (PI) tension stiffening mechanism in mm.

### 3.1.2.5. Load Deflection relationship

Having FI, PI tension stiffening and PI concrete softening mechanisms integrated, sectional internal moment corresponding to varying  $\theta$  can be calculated, and hence the completed  $M$ - $\theta$  relationship of individual short UHPFRC column can be determined. Excluding the secondary moment effect due to buckling in simulating the load-middle height deflection ( $P$ - $\delta_{mid}$ ) relationship of the deflected column depicted in Fig. 3-1-6 (a), the distributions of the flexural moment and curvature along the half column are presented in Fig. 3-1-6 (b) and (c), respectively. To note that, moment distribution along the half of the column is constant without

considering the second moment effects, whereas the distribution of curvature is non-linear at the hinge region due to the extra rotation induced by the concrete softening (Visintin et al. 2013). Subsequently, the distribution of rotation along the column shown in Fig. 3-1-6 (d) is obtained by integrating the curvature ( $\chi$ ) from the middle height of the column ( $L/2$ ) to the top of the column. Similarly, having obtained the  $M-\theta$  relationship of the short column it is a matter of integrating the distribution of rotation from the middle height of the column to the top of the column to determine the lateral deflection  $\delta_{mid}$  as shown in Fig. 3-1-6 (e).

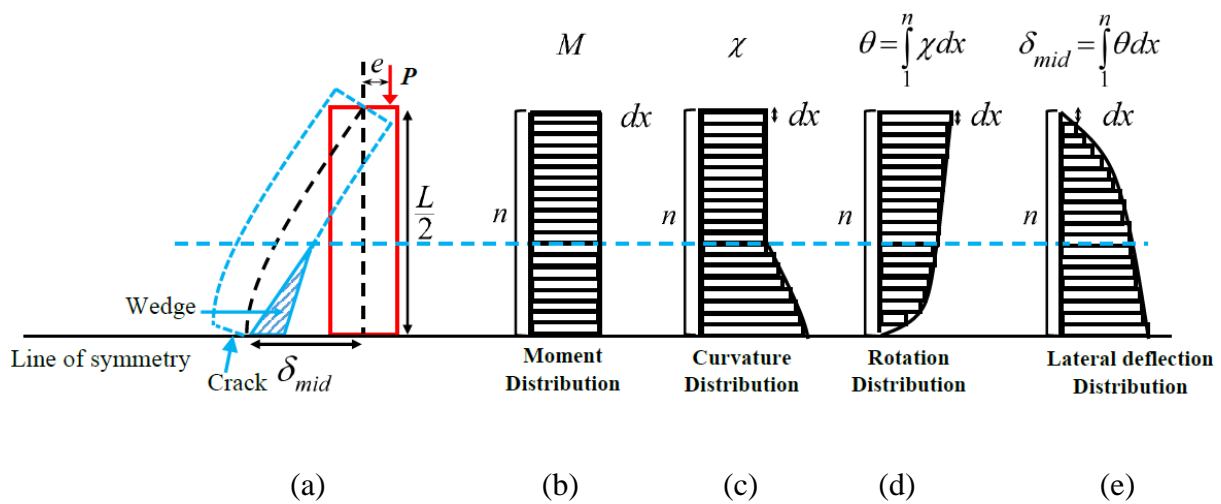


Figure 3-1-6. Schematic diagram for deriving lateral deflection of the short UHPFRC column: (a) deflected short UHPFRC column, (b) moment distribution for the column; (c) curvature distribution for the column; (d) rotation distribution for the column; (e) lateral deflection distribution for the column

### 3.1.3. FINITE ELEMENT (FE) MODELLING

Detailed 3D finite element models are developed to predict the behaviors of concentrically and eccentrically loaded short UHPFRC columns. The finite element (FE) models are first applied for the simulation of column specimens tested in this study and the experimental results are utilized to validate the numerical results predicted by the FE models. This has demonstrated a



very good performance of the numerical model. With this confidence, the FE model is adopted to produce additional results for different eccentricities. It is to be noted that a beam under three point bending is also modelled as such a specimen is tested to get the pure bending capacity of the specimen (with no axial load), which needed for completing the load-moment interaction diagram. In order to have a reliable modelling of these structures, a well-regarded commercially available finite element code ABAQUS is used in this study. The concrete is modelled with 3D hexahedral solid elements having 8 nodes (C3D8R) where the element formulation is based on the reduced integration technique. The steel reinforcements are modelled with truss elements in 3D space with 2 nodes (T3D2). The steel reinforcements (truss elements) are embedded within the concrete (solid elements) that imposed a perfect bonding between these two materials. However, a slip between them is expected in reality, which is incorporated indirectly through the tension stiffening feature of the concrete damage plasticity (CDP) model, which is the most advanced material model provided by ABAQUS for simulating normal strength concrete. Thus, this model may not provide reliable results if it is applied directly without any adjustment to UHPFRC as experienced by the authors (Singh et al. 2016; Singh et al. 2017). Based on that, the problem is addressed by adjusting some parameters such as biaxial ratio and dilation angle. The essential technical details of the model (CDP) are provided in the following section. For the steel reinforcements, the elasto-plastic material model with steel hardening and softening is employed.

Fig. 3-1-7 shows the FE model of one of the four column specimens and a beam specimen. Steel caps consisting of a rectangular flat plate (length: 500 mm, breadth: 350 mm, thickness: 65 mm) and a square ring (length: 165 mm, thickness: 45 mm) used at the two ends of a column are modelled with 3D elements (C3D8R) using elasto-plastic material model, as shown in Fig. 3-1-7 (a) and (b). This is similarly followed for the two additional steel plates (length: 250 mm,

breadth: 100 mm, thickness: 50 mm) used at the two ends of the columns for the application of loading. It is to be noted that the breadth of the loading plate (100 mm) is aligned with the length of the steel cap (500 mm). All translational displacements of the nodes laying on the 250 mm long central line at the top surface of the upper loading plate are restrained, as shown in Fig. 3-1-7(b). This is similarly applied to the lower loading plate at its lower surface except the vertical displacement to allow vertical upward movement. The vertical displacement of these nodes having a single value is imposed and increased gradually with a steady rate (0.15 mm/min) using a reference point along with the multi-point coupling constrain to load the column in the form of displacement control. The above procedure is applicable for the concentrically loaded case while the positions of these restraining and loading lines are simply moved from the central line for the eccentrically loaded scenarios. The contact between the steel cap and the column is ensured by using the surface to surface contact (Standard) algorithm provided by ABAQUS where a hard contact is provided for the normal displacement and sliding contact for the tangential displacements with a friction coefficient of 0.1. A tie contact is used to connect the loading plate with the steel cap.

Three loading plates used for the beam are having same size of the loading plate used for the columns where the length of these plates (250 mm) is oriented along the breadth of the beam. The same surface to surface contact (Standard) is used between the beam and loading plates. The displacements of the 250 mm long central line nodes at the bottom surface of the two supporting plate are fully restrained. The vertically downward displacement of the central loading plate having a single value is imposed and increased gradually with a steady rate (0.15 mm/min) using a reference point along with the multi-point coupling constrain to load the beam. A convergence study for the mesh size is conducted to assure a stable converged solution and

it is found that an element size of 15 mm is adequate which is consistently used in all cases, as shown in Fig. 3-1-7 (a) to (c).

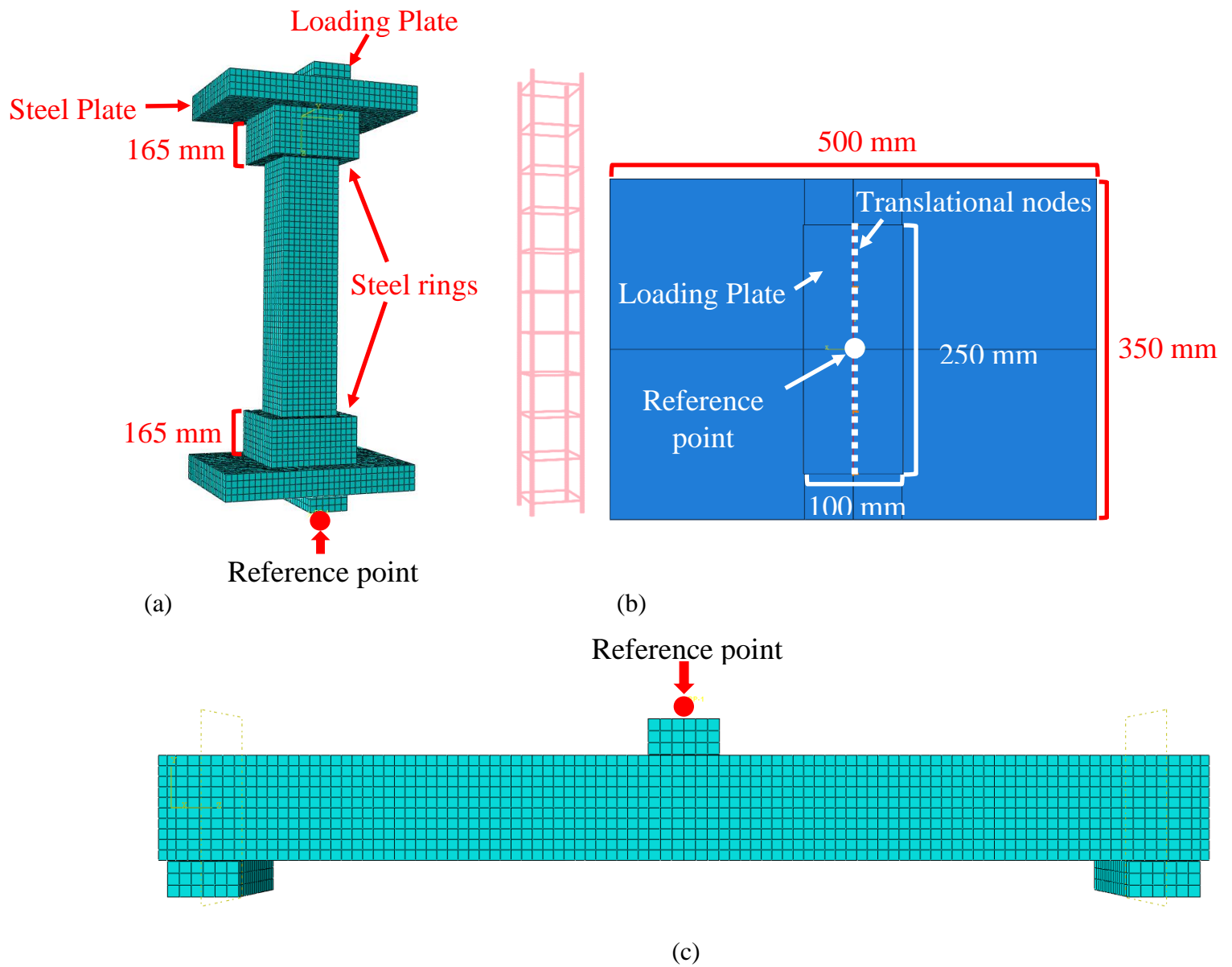


Figure 3-1-7. FE simulations: (a) UHPFRC concentrically and eccentrically loaded short column; (b) Details for steel cap, steel loading plate, and reference point; (c) UHPFRC beam with three points bending setup

### 3.1.3.1. Concrete damage plasticity (CDP) model

In this study, the inelastic responses of concrete material in Concrete damage plasticity (CDP) model is represented by a plasticity-based continuum damage model that encompassed the elasto-plastic responses under tension and compression, and this model is in conjunction with an inputted scalar/isotropic damage parameter. Two equivalent plastic strains obtained from the elasto-plastic responses are associated with failure mechanism under compression and tension, and hence govern the envelope of the yield surface (Lubliner et al. 1989). To this end, the uniaxial ( $\sigma$ - $\varepsilon$ ) responses of concrete in compression or tension are required to either represent the formation of micro-cracks in tension or characterize the plastic response in compression. In order to have a non-associated flow rule, a plastic potential is used to accommodate with the yield function, and five additional parameters are required to determine the yield function and plastic potential:

$$F = \frac{1}{1-\alpha} \left( \bar{q} - 3\alpha \bar{p} + \beta(\tilde{\varepsilon}^{pl}) \langle \hat{\sigma}_{\max} \rangle - \gamma \langle -\hat{\sigma}_{\max} \rangle \right) - \bar{\sigma}_c(\tilde{\varepsilon}^{pl}) \leq 0 \quad (2)$$

$$G = \sqrt{(\xi \sigma_{t0} \tan \varphi)^2 + \bar{q}^2} - \bar{p} \tan \varphi \quad (3)$$

$$\alpha = \frac{\sigma_{bo} - \sigma_{co}}{2\sigma_{bo} - \sigma_{co}}; \quad 0 \leq \alpha \leq 0.5 \quad (4)$$

$$\beta(\tilde{\varepsilon}^{pl}) = \frac{\bar{\sigma}_c(\tilde{\varepsilon}^{pl})}{\bar{\sigma}_t(\tilde{\varepsilon}^{pl})} (1-\alpha) - (1+\alpha) \quad (5)$$

$$\gamma = \frac{3(1-k_c)}{2k_c - 1} \quad (6)$$

where  $\alpha$  and  $\gamma$  are material dependent constants,  $\bar{q}$  is the effective von Mises equivalent stress,  $\bar{p}$  is the hydrostatic pressure based on effective stresses,  $\hat{\sigma}_{\max}$  is the maximum principal effective stress;  $\bar{\sigma}_c(\tilde{\varepsilon}^{pl})$ ,  $\bar{\sigma}_t(\tilde{\varepsilon}^{pl})$  are functions of equivalent plastic strain  $\tilde{\varepsilon}^{pl}$ , representing

effective cohesive stresses under compressive and tensile stresses.  $G$  is the flow potential follows a Drucker Prager hyperbolic function;  $\xi$  is a potential eccentricity parameter for describing the rate of the function approaches the asymptote;  $\sigma_{t0}$  is the uniaxial tensile stress;  $\varphi$  is the dilation angle obtained from the measurement from the  $p$ - $q$  plane under high confining pressure; To characterize the shape of the yield surface, two critical parameters are required: (1)  $\sigma_{bo} / \sigma_{co}$  ratio of the initial biaxial compressive strength and the initial uniaxial compressive strength, and (2) a parameter  $k_c$  is the ratio between the distances from the hydrostatic axis to tensile and compressive meridians. In this study, the value of  $\sigma_{bo} / \sigma_{co}$  is taken as 1.05 for UHPFRC instead of 1.16 that is usually taken for normal strength concrete (Singh et al. 2017). Similarly, the value of the dilation angle  $\varphi$  is taken as  $35^\circ$  (Singh et al. 2016) for UHPFRC instead of  $30^\circ$  which is normally applied for conventional concrete.

As presented in Fig. 3-1-8, completed uniaxial  $\sigma$ - $\varepsilon$  curves of conventional concrete generated from cylinder compression and direct tensile tests, and both inelastic strain ( $\varepsilon_c^{in}$ ) and cracking strain ( $\varepsilon_t^{ck}$ ) are determined by subtracting the elastic components ( $\varepsilon_{0c}^{el}$  and  $\varepsilon_t^{el}$ ) from the total strain ( $\varepsilon_c$  and  $\varepsilon_t$ ), respectively.

$$\varepsilon_c^{in} = \varepsilon_c - \varepsilon_{0c}^{el} = \varepsilon_c - \sigma_c / E_0 \quad (7)$$

$$\varepsilon_t^{ck} = \varepsilon_t - \varepsilon_t^{el} = \varepsilon_t - \sigma_t / E_0 \quad (8)$$

where  $E_0$  is the undamaged elastic modulus of concrete. With this, the aforementioned equivalent plastic strains ( $\tilde{\varepsilon}_c^{pl}$  and  $\tilde{\varepsilon}_t^{pl}$ ) determining the failure mechanism of the yield function can be derived as follow:

$$\tilde{\varepsilon}_c^{pl} = \varepsilon_c^{in} - \frac{d_c}{(1-d_c)} \frac{\sigma_c}{E_0} \quad (9)$$

$$\tilde{\varepsilon}_t^{pl} = \varepsilon_t^{ck} - \frac{d_t}{(1-d_t)} \frac{\sigma_t}{E_0} \quad (10)$$

Damage parameters ( $d_c$  and  $d_t$ ) are utilized to characterize the level of degradation in the material stiffness, ranging from 0 to 1 for describing an undamaged and fully damaged states, respectively. The damage parameters are determined utilizing the concepts Birtel et al. (2006) and Mahmud et al (2013) of as follows:

$$d_c = 1 - \left[ \frac{\frac{\sigma_c}{E_0}}{0.2\varepsilon_c^{in} + \frac{\sigma_c}{E_0}} \right] \quad (11)$$

$$d_t = 1 - \frac{\sigma_t}{f_t} \quad (12)$$

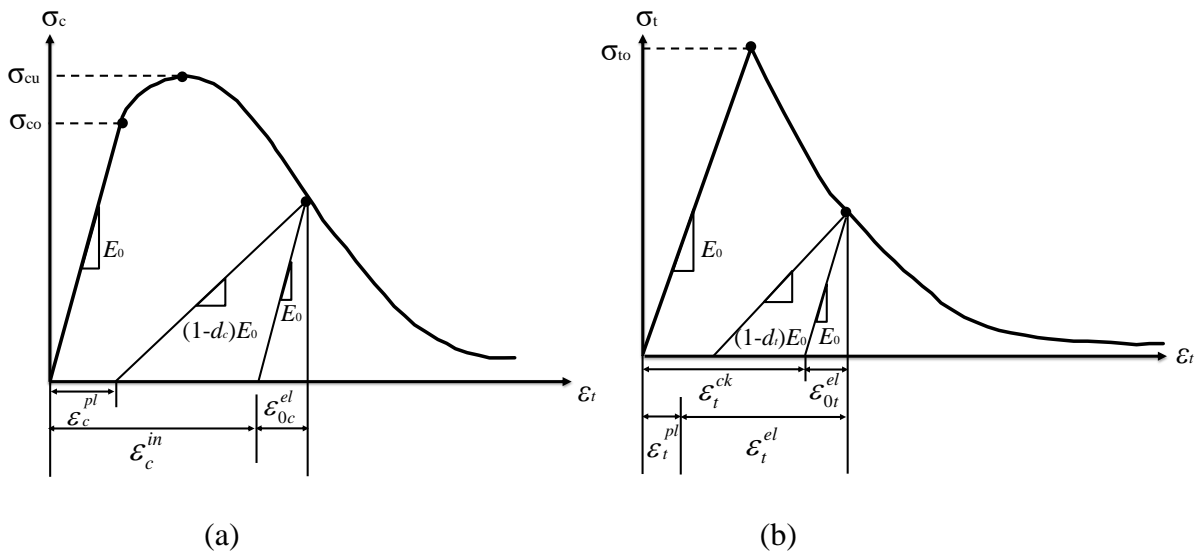


Figure 3-1-8. Defining: (a) compressive behavior; (b) tension stiffening

### 3.1.4. COMPARISON BETWEEN THEORETICAL MODEL & TEST RESULTS

#### 3.1.4.1. Introduction of experimental program

As shown in Fig. 3-1-9 (a), there are 4 reinforced UHPFRC columns with a square cross-section

of 150 mm x 150 mm and 900 mm in height, and all columns are reinforced by 4 longitudinal steel reinforcements with a diameter of 16mm and a yield stress of 500 MPa. A clean concrete cover of 20mm measured from the edge of reinforcements to the edge of columns was applied to all cross sections. Transverse reinforcements with a diameter of 6mm were placed in the columns with a constant stirrup spacing of 85 mm. One column was subjected to pure axial load and three other columns were subjected to eccentric loads with eccentricities of 35, 50, or 80 mm, respectively. Besides that, a UHPFRC member was casted as a beam with the same cross-section and stirrup arrangement as those of the companion columns but a longer span of 1350 mm, as shown in Fig. 3-1-9 (b). This UHPFRC beam was tested under a simply-support condition and further subjected to three-point flexural bending induced by the concentrated point load at the mid-span of the beam. All UHPFRC columns were tested using a universal testing machine (Amsler, Schaffhouse, Switzerland) with a maximum capacity of 5000 kN, and the UHPFRC beam was tested by using Avery universal testing machine with a capacity of 1000 kN. For both concentrically and eccentrically loaded columns, the local contraction and elongation of the column were measured by linear variable differential transducers (i.e. LVDT-1 and LVDT-3), respectively, and the global displacements of the short columns were captured by LVDT-2 and LVDT-4. Additionally, the lateral displacements at the middle region including the middle height of the column and 200 mm above and below the mid height were measured by LVDTs 5-7. As the experimental setup of beam is exhibited in Fig. 3-1-9 (b), LVDTs 1-3 were used to measure the deflection at the middle span of the beam, and LVDTs 4 and 5 were used to measure the tensile crack opening at tensile surface of the beam. For LVDT 6 and 7, they were placed close to the upper surface of the beam and used to measure the contractions due to the hinge rotation.

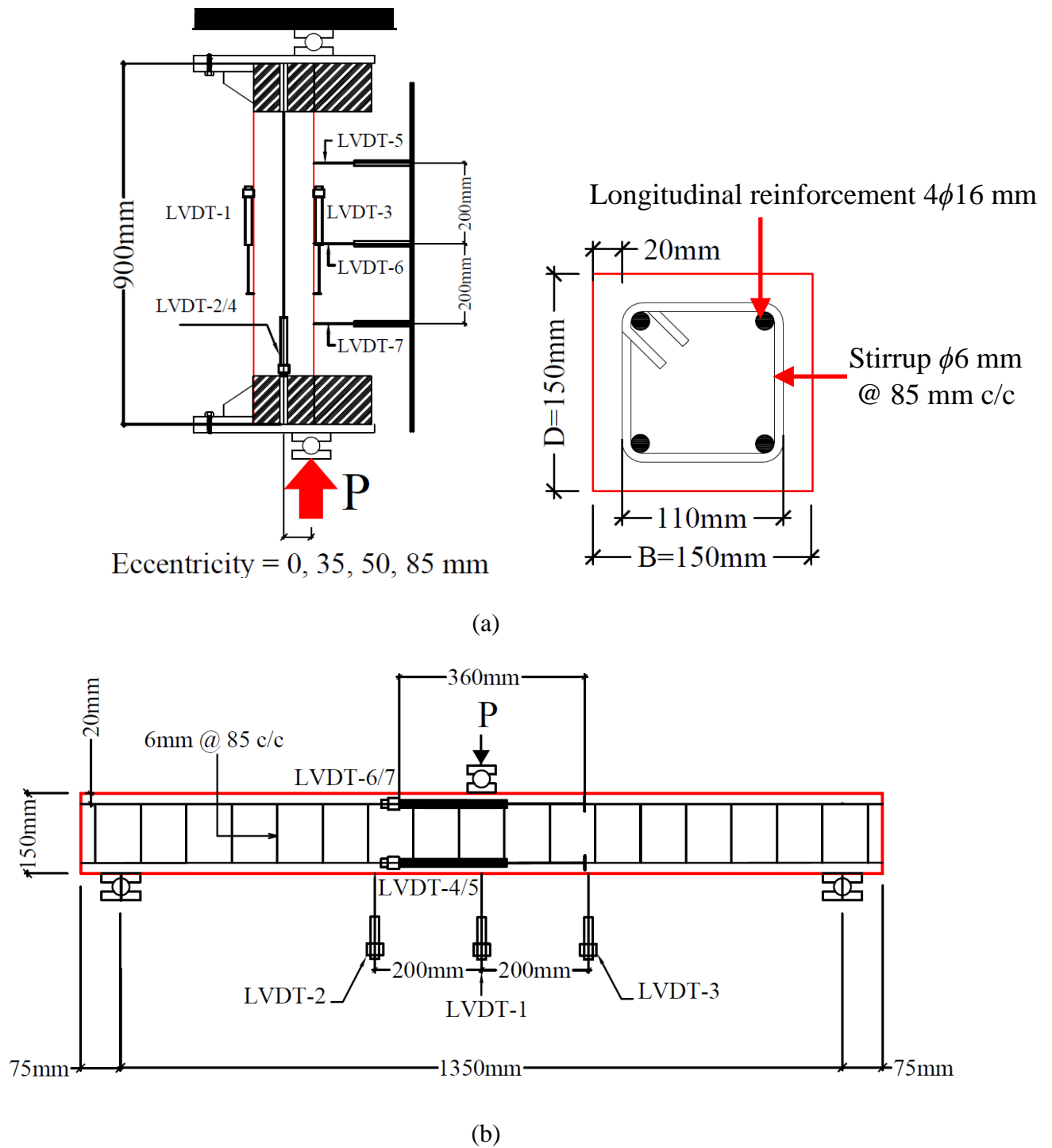


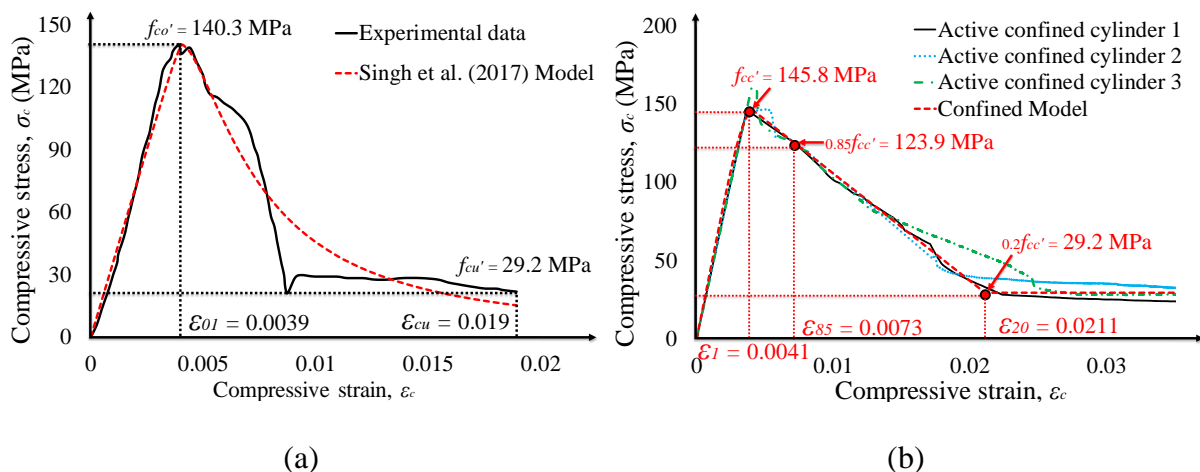
Figure 3-1-9. Instrumentation setup and member geometry details: (a) concentric and eccentric loaded column; (b) three-point flexural bending tests performed on UHPFRC beam

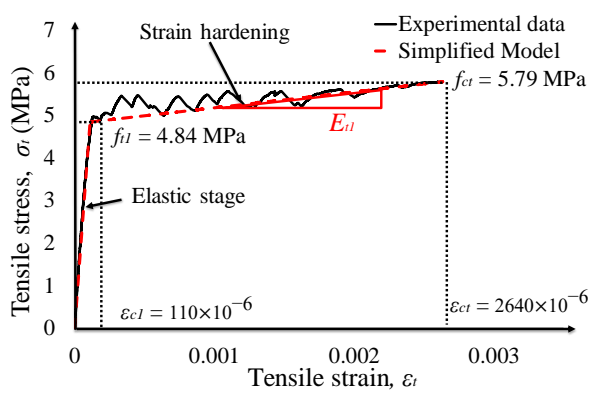


### 3.1.4.2. Fundamental material properties

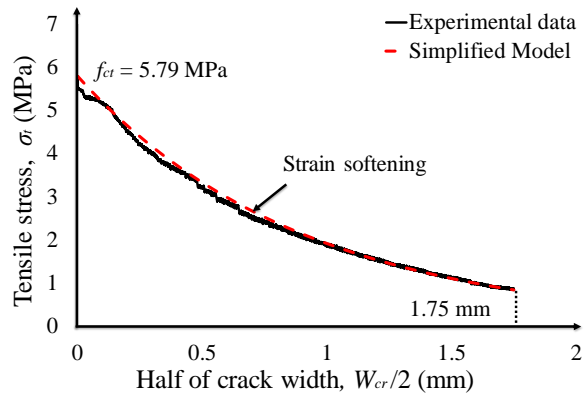
#### 3.1.4.2.1. Unconfined and confined compressive stress-strain relationships of UHPFRC

Material constitutive relationship can be represented using material model presented in this section and is used to input into both the numerical approaches. The compressive stress-strain relationship of UHPFRC can be reproduced using the model developed by Singh et al. (2017) to incorporate with the numerical modelling. As can be seen in Fig. 3-1-10 (a), there is a high agreement between the experimental result and the modelling result. For improving the accuracy of the model, the confining effects on the core concrete inside the stirrups were considered and an actively confinement model for high strength concrete established by Razvi and Saatcioglu (1999) validated using the UHPFRC experimental results was directly applied to represent its stress-strain relationship. In testing the behavior of UHPFRC under triaxial load, compression tests were conducted on UHPFRC cylinders with a diameter of 62.5 mm and a height of 120 mm. A uniform lateral confinement stress of ( $f_l = 4.5$  MPa) was acting on all cylinders by using Hoek cell to reproduce the confinement pressure induced by the transverse reinforcements. Fig. 3-1-10 (b) shows the comparisons between experimental and model results and indicate that a good prediction of the triaxial behavior of the UHPFRC using the model. Summary of parameters of the confined UHPFRC calculated by using Razvi and Saatcioglu (1999) model is presented in Table 3-1-1.

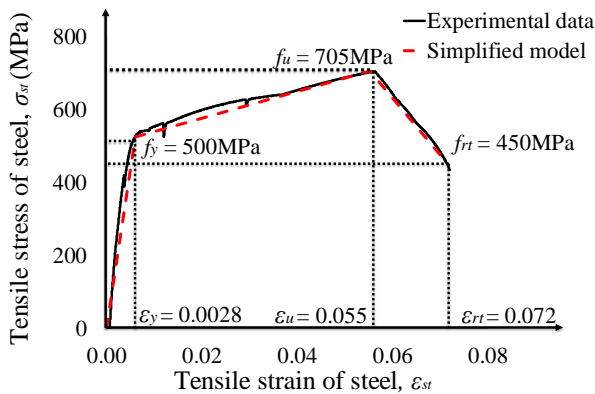




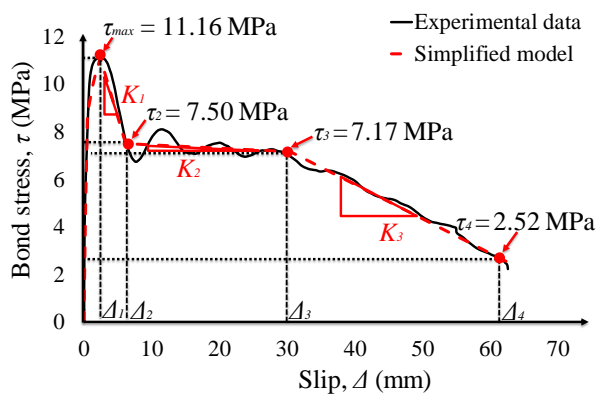
(c)



(d)



(e)



(f)

Figure 3-1-10. Material properties of UHPFRC: (a) compressive stress-strain responses for unconfined UHPFRC; (b) compressive stress-strain response for confined UHPFRC with lateral confine pressure of 4.5 MPa; (c) tensile characterizations of UHPFRC; (d) tensile stress and crack opening response; (e) tensile stress-strain response for steel reinforcement; (f) proposed bond-slip model between UHPFRC and reinforcement

Table 3-1-1. Summary of parameters of confined UHPFRC calculated using Razvi's model

Parameter	Value
Given material properties	
$f_{co}'$ (Mpa)	140.3
$s$ (mm)	85.0
$b_c$ (mm)	98.0
$d_s$ (mm)	6.0
$q$	2.0
$\alpha$	90.0
$s_l$ (mm)	82.0

### Coefficients and lateral confined pressure

$k_2$	0.176
$\rho_c$	0.007
$f_s$ (Mpa)	663.4
$f_t$ (Mpa)	4.504
$f_{te}$ (Mpa)	0.0793
$k_1$	6.970
$f_{cc}'$ (Mpa)	145.8

### Ductility of confined Concrete and descending branch

$\varepsilon_1$	0.0041
$\varepsilon_{01}$	0.0039
$k_3$	0.2852
$\varepsilon_{085}$	0.0052
$k_4$	1.3268
$\varepsilon_{85}$	0.0073
$K$	0.0394

---

#### 3.1.4.2.2. Tensile characterizations of UHPFRC

Tensile characterization of UHPFRC, including its stress-strain relationship prior cracking, strain hardening and post-peak stress-crack opening relationship are defined using Eq. (13), which are established based on the idealized modelling approach with three different phases as proposed by Wille et al. (2014) and simplified based on experimental tested results reported in Singh et al. (2015), as presented in Fig. 3-1-10 (c) and (d):

$$\sigma_t = \begin{cases} E_{ct} \varepsilon_{ct} & (0 \leq \varepsilon_{ct} \leq \varepsilon_{cc}) \\ f_{t1} + E_{t1} (\varepsilon_{ct} - \varepsilon_{t1}) & (\varepsilon_{cc} \leq \varepsilon_{ct} \leq \varepsilon_{soft}) \\ \alpha_1 e^{-\beta_1 (W_{cr}/2)} & (W_{cr}/2 \leq 1.75mm) \end{cases} \quad (13)$$

where  $\sigma_t$  is the tensile stress in MPa;  $\varepsilon_{ct}$  is the total tensile strain;  $E_{ct}$  is the elastic modulus of UHPFRC in 44000 Mpa;  $\varepsilon_{cc}$  is the strain prior strain hardening ( $\varepsilon_{cc} = 110 \times 10^{-6}$ );  $f_{t1}$  is the maximum tensile stress of UHPFRC within elastic range ( $f_{t1} = 4.84$  MPa);  $E_{t1}$  is the modulus for the tensile strain hardening stage ( $E_{t1} = 373.67$  MPa);  $\varepsilon_{soft}$  is the strain corresponding to the

peak stress of 5.79 MPa prior the crack opening stage ( $\varepsilon_{soft} = 2640 \times 10^{-6}$ );  $\alpha_1$  and  $\beta_1$  are constant coefficients of descending curve ( $\alpha_1 = 5.794$ ,  $\beta_1 = -1.098$ ).

### 3.1.4.2.3. Local Bond-slip ( $\tau/\delta$ ) relationship

The experimentally generated material characteristic of steel reinforcements used for the local slip-bond test and subsequently a simplified stress-strain relationship used for the both numerical models are presented in Fig. 3-1-10 (e). Local bond-slip ( $\tau-\Delta$ ) relationship is required as a fundamental input for the shooting method when calculating the cracked spacing and model the tension stiffening behavior in concrete prism, and experimental local bond slip ( $\tau-\Delta$ ) relationship can be obtained from the direct pullout tests conducted by University of Adelaide. For the direct pullout tests, the steel rebar which has the same diameter and material properties as the longitudinal reinforcements used in the UHPFRC columns was embedded in a block of UHPFRC concrete with an embedment depth of 240 mm. The displacements of the reinforcing bar at the top and bottom of the specimen were recorded along with the corresponding force by the Avery machine. As presented in Fig. 3-1-10 (f), a polyline local  $\tau-\Delta$  relationship defined using the general expressions in Eqs. (14) and (15):

$$\tau_{\max} = \alpha_2 \sqrt{f_c'} \quad (14)$$

$$\sigma_t = \begin{cases} \tau_{\max} \left(\frac{\Delta}{\Delta_1}\right)^{\beta_2} & (0 \leq \Delta \leq \Delta_1) \\ k_1 \Delta + b_1 & (\Delta_1 \leq \Delta \leq \Delta_2) \\ k_2 \Delta + b_2 & (\Delta_2 \leq \Delta \leq \Delta_3) \\ k_3 \Delta + b_3 & (\Delta_3 \leq \Delta \leq \Delta_4) \end{cases} \quad (15)$$

where  $\tau_{\max}$  is the peak bond stress in MPa, and  $\delta_1$  (in mm) is the corresponding local slip of the peak bond stress.  $\alpha_2$  and  $\beta_2$  are empirical coefficients fitting the experimental result,  $\alpha_2 =$

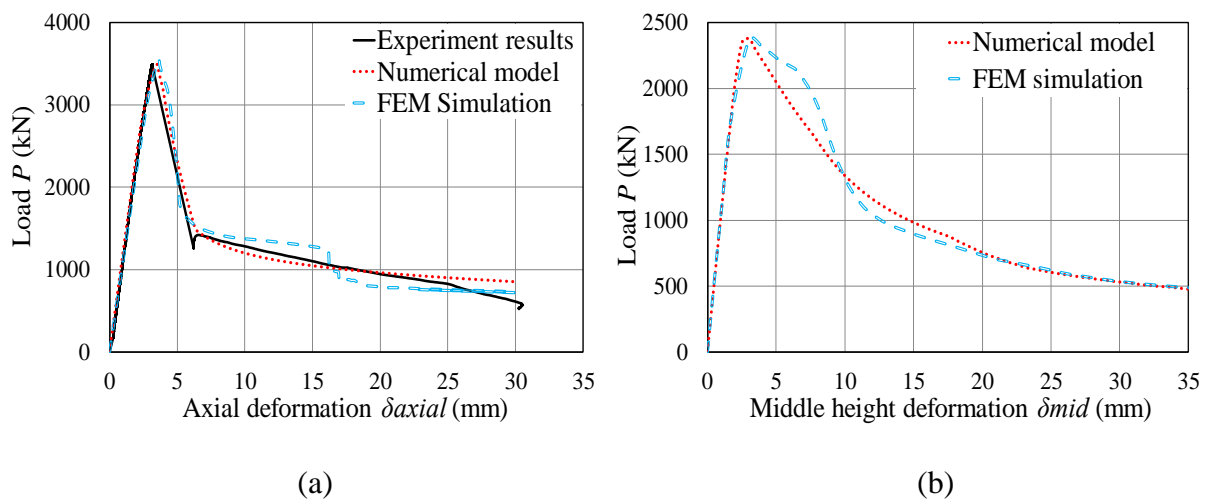
0.91 and  $\beta_2 = 0.2$  for UHPC with a steel fiber content of 2.25%.  $k_1, k_2, k_3$  and  $b_1, b_2, b_3$  are the slopes and y-intersections, respectively, for describing linear descending bond-slip ( $\tau-\Delta$ ) relationship after peak load, in which  $k_1 = -0.97$ ,  $k_2 = -0.01$ ,  $k_3 = -0.15$ , and  $b_1 = 13.47$ ,  $b_2 = 7.56$ ,  $b_3 = 11.50$ .  $\Delta_1, \Delta_2, \Delta_3, \Delta_4$  are slips within different stages of the bond-slip ( $\tau/\delta$ ) relationship, where  $\Delta_1 = 2.4$  mm,  $\Delta_2 = 6.16$  mm,  $\Delta_3 = 30.00$  mm,  $\Delta_4 = 62.65$  mm.

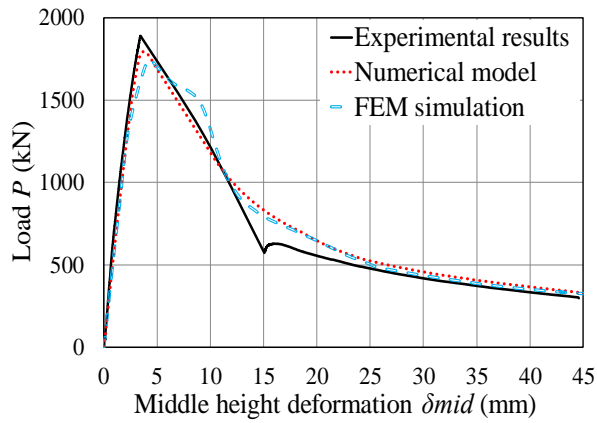
### 3.1.5. VALIDATION OF NUMERICAL MODEL AND FINITE ELEMENT MODELLING SIMULATION

#### 3.1.5.1. Load-deflection relationships

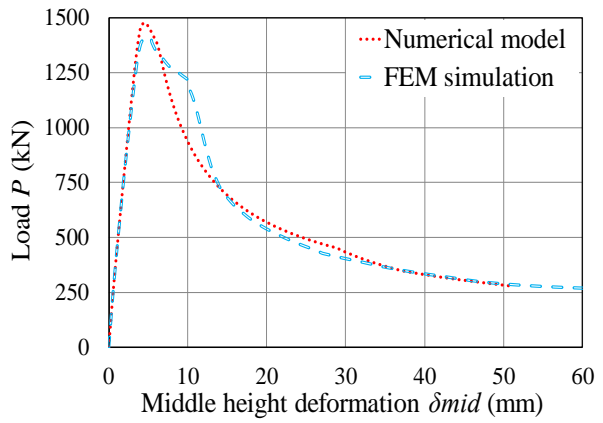
Load-axial deflection ( $P-\delta_{axial}$ ) relationships of the concentrically loaded columns obtained from experiments, numerical and FE models are presented in Fig. 3-1-11 (a), and load-mid height deflection ( $P-\delta_{mid}$ ) relationships of eccentrically loaded columns generated from both experiments and models are shown in Fig. 3-1-11 (b)-(g). For the beam subjected to three-point bending, the load-mid span deflection ( $P-\delta_{mid}$ ) relationships can be observed in Fig. 3-1-11(h). It is worth highlighting that, the numerical model and FE model well-predict the ( $P-\delta_{axial}$ ) and ( $P-\delta_{mid}$ ) relationships of the UHPFRC short columns subjected to with eccentricity of 0 mm, 35 mm, 50 mm and 85 mm. Figure 3-1-11 (b), (d) and (g) present the numerical model and FE model predicted ( $P-\delta_{mid}$ ) relationships of UHPC column subjected to load eccentricities of 20 mm, 45 mm, and 100 mm, in which these eccentricities were not studied experimentally but their effects on  $P-\delta_{mid}$  relationships of UHPFRC short columns were numerically investigated and help to complete the load-moment interaction envelop presented later in this study. For UHPFRC beam shown in Fig. 3-1-11 (h), the proposed PI based model provides an appropriate prediction for the load-mid span deflection ( $P-\delta_{mid}$ ) relationship, and it slightly underestimates the load for the simply supported beam at the post-peak stage. This could be attributed to the

edge effect of friction and bond stress between steel fibers and concrete along the concrete wedge sliding planes in the reality, where the friction provided residual force along the concrete softening zone and fiber prevent the crack propagation and hence restrain the rotation and middle-span displacement at the hinge region. Experimental, numerical, and finite element modelling results pertaining to the peak load and corresponding deflections including  $\delta_{axial}$ , and  $\delta_{mid}$  are summarized in Table 3-1-2, and it is worth noting that the errors of predictions regarding the peak load ( $P_p$ ) are less than 9%. The results presented in Fig. 3-1-11 and Table 3-1-2 show the well correlations between PI based numerical model and FE simulation, which indicates the applicability and accuracy of the proposed numerical, and FE models for predicting the  $P$ - $\delta_{mid}$  relationships of short UHPFRC columns. In order to show the generic nature of the proposed mechanics based model and the FEM model, additional experimental results from a different affliction were adopted as benchmarks for them, in which the experimental program was reported in details in Steven and Empelmann (2014) and the corresponding results are illustrated in Fig. 3-1-12.

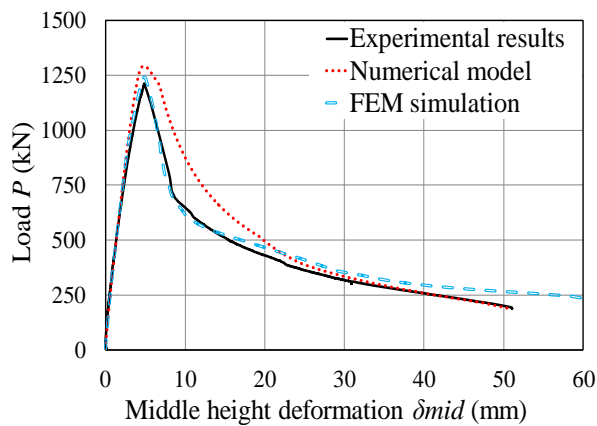




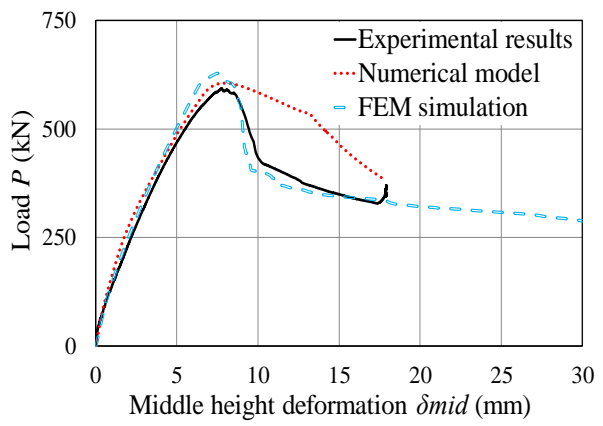
(c)



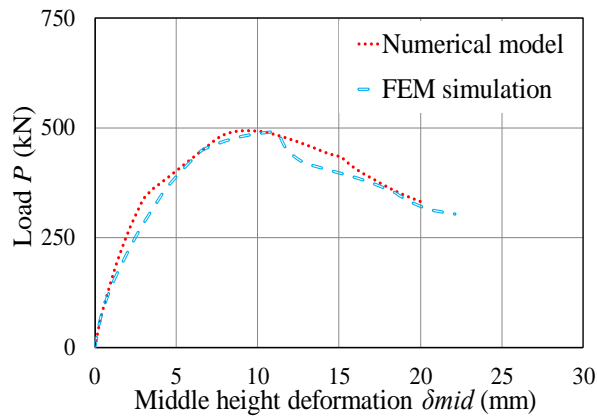
(d)



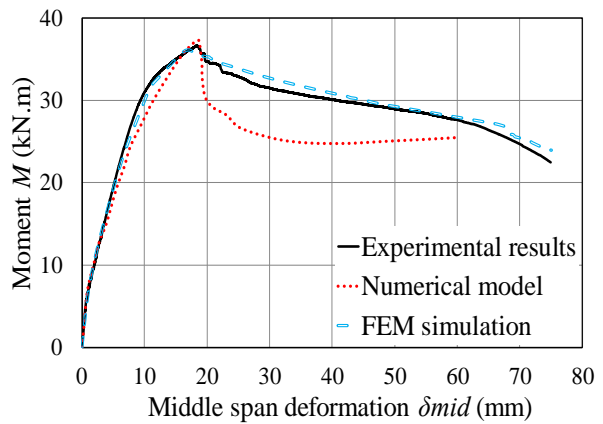
(e)



(f)



(g)



(h)

Figure 3-1-10. Comparisons among experimental results, analytical and numerical models for UHPFRC columns loaded with different eccentricities: (a) concentrate; (b) eccentricity = 20 mm; (c) eccentricity = 35 mm; (d) eccentricity = 45 mm; (e) eccentricity = 50 mm; (f) eccentricity = 85 mm; (g) eccentricity = 100mm; (h) UHPFRC beam

Table 3-1-2. Comparisons among of experimental, numerical, and numerical simulation results

Eccentricity (mm)	Experimental		Numerical		FEM	
	$P_p$ (kN)	$\delta_p$ (mm)	$P_p$ (kN)	$\delta_p$ (mm)	$P_p$ (kN)	$\delta_p$ (mm)
0	3490.86	3.16	3489.66	3.53	3541.48	3.59
20	-	-	2378.36	3.04	2369.43	3.02
35	1890.16	3.43	1793.87	3.75	1735.83	4.05
45	-	-	1476.10	4.56	1409.58	5.18
50	1212.72	4.87	1292.52	4.86	1241.23	4.93
85	593.91	7.77	605.50	8.00	627.82	7.55
100	-	-	493.10	9.32	489.73	10.8
Pure bending	108.57	18.32	110.51	18.54	106.99	17.00

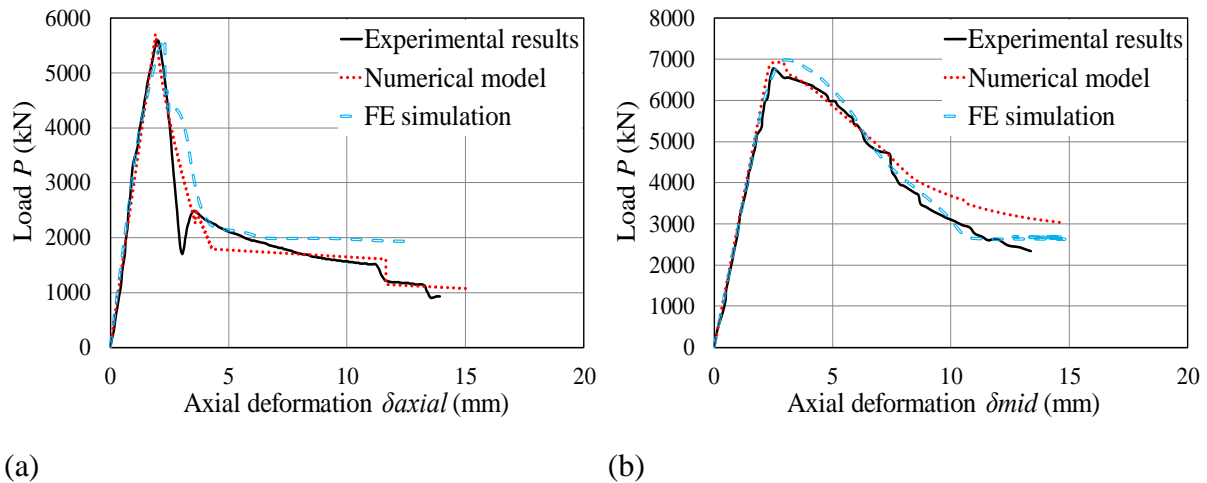


Figure 3-1-12. Comparisons among experimental results, analytical and numerical models for UHPFRC columns conducted by Steven and Empelmann (2014): (a) column S3; (b) column SE 2

### 3.1.5.2. Verification of proposed load-moment (P-M) interaction diagram

Integrating results of the numerical models for short UHPFRC columns loaded with eccentricities from 0 to 100 mm and the UHPFRC beam, a complete load-moment ( $P$ - $M$ ) interaction envelope was plotted in conjunction with actual the experimental results, as presented in Fig. 3-1-13. The comparisons shown in the figure suggest a good agreement



between experimental and theoretical results as the experimental results of the columns loaded with eccentricities of 0 and 85 mm and the pure bending case closely match with the curve developed numerically. Whilst the model well-simulates the axial load of the columns loaded with eccentricities of 35 mm and 50 mm, it slightly underestimates and overestimates the flexural moments, respectively, as shown in Fig. 3-1-13. A potential explanation of the differences between the numerical and experimental results is the fiber distributions and density in the column specimens were slightly different to those of the material tested specimens, and this also influence the load carrying capacities ( $P_P$ ) of the short columns due to the fiber bridging effects, and hence enlarge in the difference at the moment ( $M$ ) when using  $P_P$  to multiply the constant eccentricities. Further comparisons of the bending moment of short columns reveal that the eccentricity of 45 mm led to the largest moment acting on the short UHPFRC columns, and it can be deduced that the loading eccentricity for the columns cause the balance failure of the column ranges from 35 mm to 45 mm.

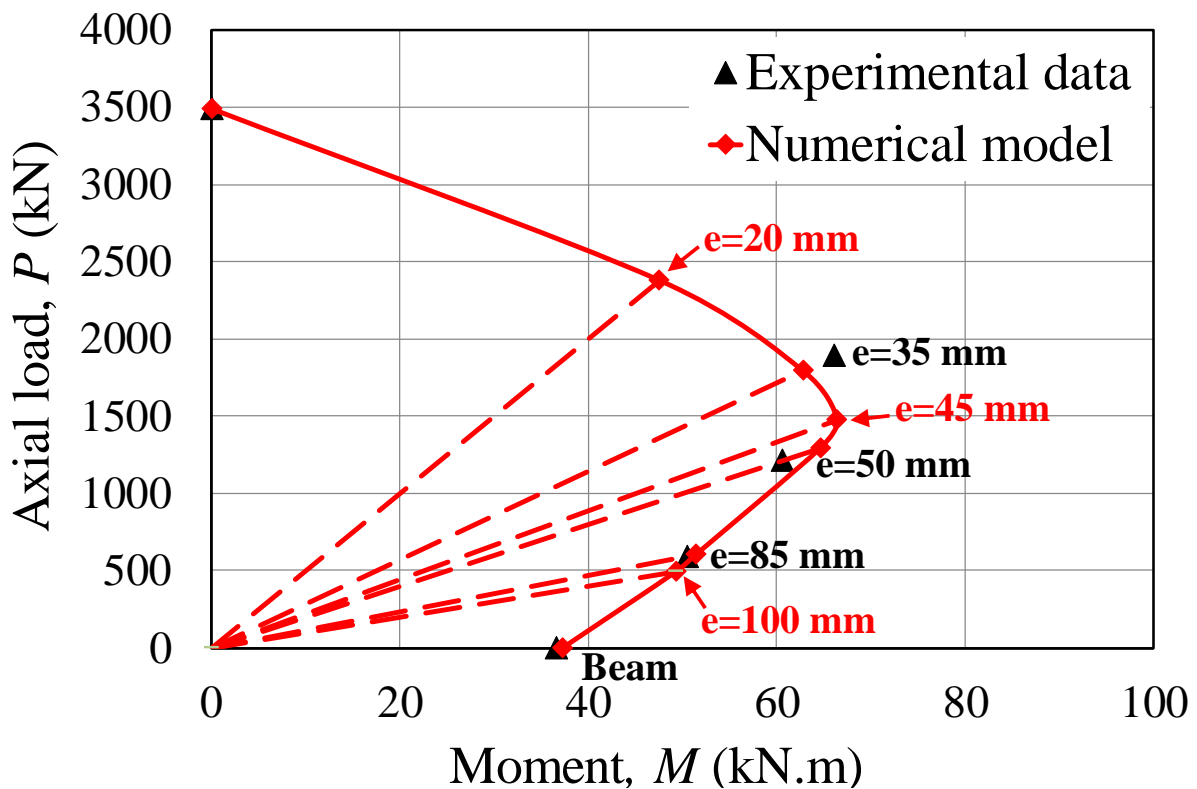
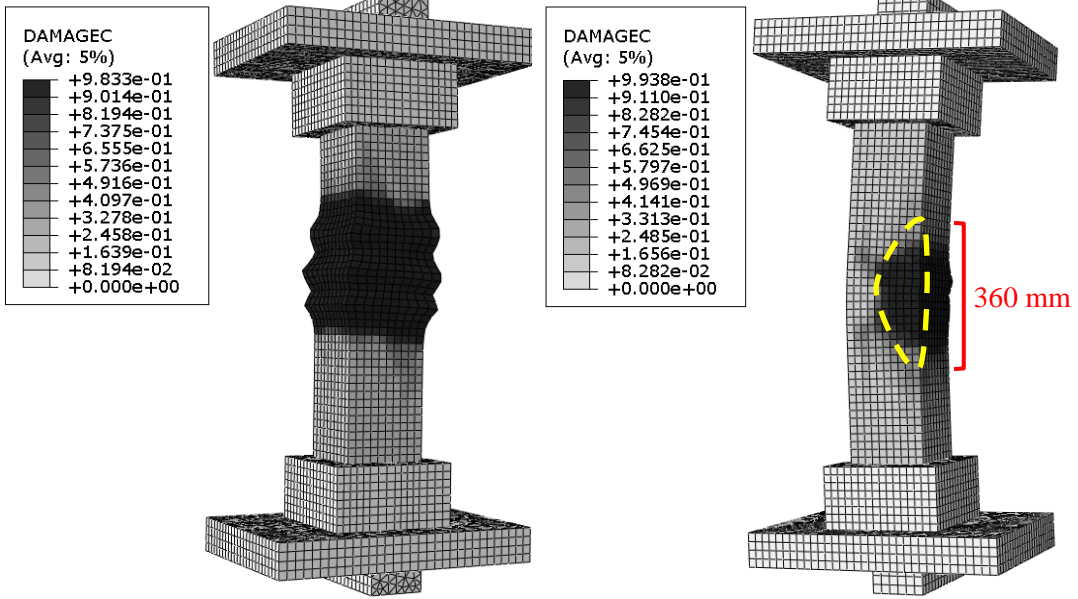


Figure 3-1-13. Load-Moment interaction diagram for UHPFRC short columns

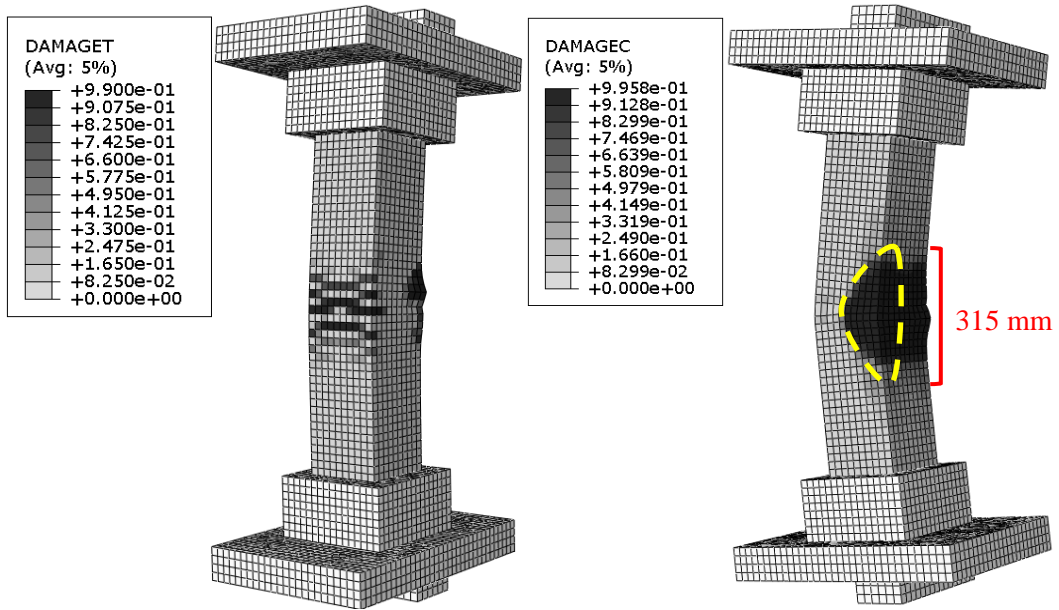
### 3.1.6. FAILURE MODES

The failure modes of all column specimens are presented in Fig. 3-1-14 (a)-(g). Having obtained the compressive damage parameters calculated by using Eqs. (11) and (12) and inputted to the CDP model, the compressive damage pattern for UHPFRC column under concentric load is determined by the FE model, as shown in Fig. 3-1-14 (a). A maximum compressive damage level of 98.33% has been observed in the middle region of the column, and this observation indicates that the UHPFRC column under concentric load failed predominated by the concrete spalling at the surface induced by the concrete softening of the UHPFRC. Similar failure patterns of UHPFRC columns subjected to concentric loads have been reported in the previous studies (Hosinie et al. 2015; Shin et al. 2017). With compressive and tensile damage parameters inputted in the FE models, compressive and tensile damage patterns for eccentrically loaded columns are exhibited in Fig. 3-1-14 (b)-(g). As shown in Fig. 3-1-14 (b), (d), and (f), significant concrete softening under compression were observed in the compressive damage patterns of eccentrically loaded columns with eccentricities of 35, 50, 85 mm. Additionally, comparisons of compressive damage patterns and maximum damage levels reveal that the compressive damage level decreased with an increase in loading eccentricity, for instance, the wedge length for columns ( $e=35, 50, 85$  mm) are approximately 360 mm, 315 mm, and 165 mm, respectively. Tensile damage patterns for eccentrically loaded columns are presented in Fig. 3-1-14 (c), (e), and (g), and small flexural tensile cracks can be observed in Fig. 3-1-14 (c) on the tensile face of the column which is loaded with an eccentricity of 35 mm. With increases in the eccentricity, more prominent tensile flexural cracks can be observed at the middle height of the columns with loading eccentricities of 50 and 85 mm. The above phenomenon suggests that the flexural failure governs the overall failure of UHPFRC short column over the compressive failure when the load eccentricity increases.



(a)

(b)



(c)

(d)

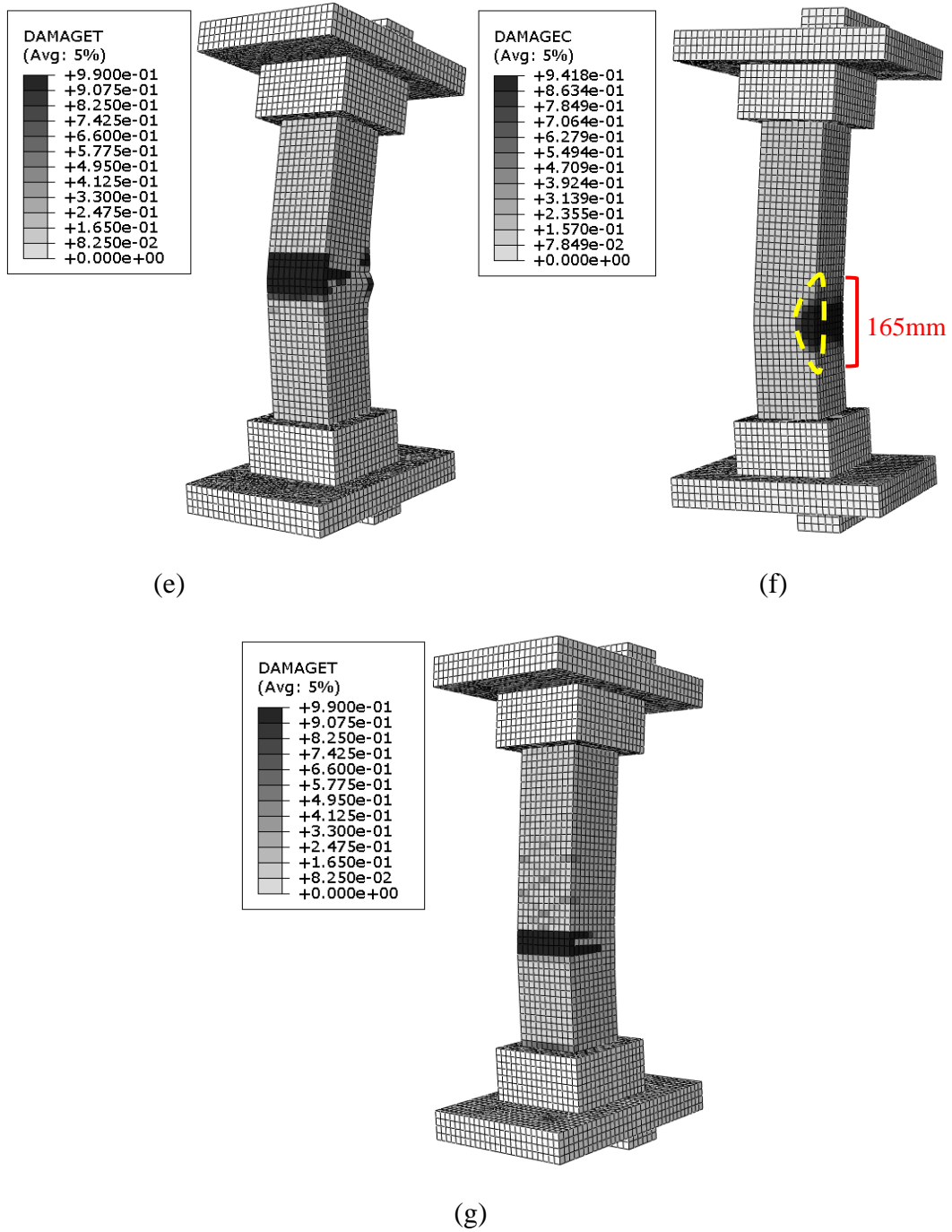


Figure 3-1-14. FEM simulation results of compressive and tensile damage pattern: (a) compressive damage pattern for ( $e=35$  mm); (b) compressive damage pattern for ( $e=35$  mm); (c) tensile damage pattern for ( $e=35$  mm); (d) compressive damage pattern for ( $e=50$  mm); (e) tensile damage pattern for ( $e=50$  mm) (f) compressive damage pattern for ( $e=85$  mm); (g) tensile damage pattern for ( $e=85$  mm)

### 3.1.7. CONCLUSIONS

In this study, a PI based numerical model as well as FE models were developed to simulate the behaviors of short UHPFRC columns subjected to concentric and eccentric loads, and a simply supported beam, and the following conclusions can be made:

- Both PI based and FEM models can be applied confidently to simulate  $P-\delta_{axial}$ , and  $P-\delta_{mid}$  relationships for both short UHPFRC columns and UHPFRC beams, respectively.
- To analyze the UHPFRC columns using these models, only the fundamental material properties of concrete and reinforcements are required to predict the  $P-\delta_{mid-height}$  relationships of eccentrically loaded columns without resorting to costly and time-consuming structural tests on UHPFRC columns.
- The proposed  $P-M$  interaction envelopes generated in this study accurately predict the behaviors of short column loaded with various eccentricities, and this highlights the reliability of the numerical models in simulating the behaviors of eccentrically loaded UHPFRC columns. Therefore, it can serve as the basis for further research and design of the UHPFRC columns.
- FE simulations successfully reproduced the damage patterns of UHPFRC members under different loading conditions. Comparisons of these simulated damage patterns indicate that the compressive damage level of short UHPFRC columns decreases with an increase in the eccentricity of the axial load.

### 3.1.8. LIST OF NOTATIONS

*The following symbols are used in this paper:*

$A_{bar}$  = area of one longitudinal reinforcement;

$A_c$  = area of the surrounding prism at the partial interaction (PI) region;

$B_1$  = bond force in the first element;

$B_2$  = bond force in the second element;

$b_1$  = empirical coefficient for bond slip relationship at the stage 2

$b_2$  = empirical coefficient for bond slip relationship at the stage 3

$b_3$  = empirical coefficient for bond slip relationship at the stage 4

$B_n$  = bond force in the  $n^{\text{th}}$  element;

$d_c$  = compressive damage parameter, defined in Eq.11

$d_t$  = tensile damage parameter, defined in Eq.12;

$d_{\Delta} / d_x$  = slip strain between the tensile reinforcement and surrounding concrete;

$(d_{\Delta} / d_x)_1$  = slip strain between the tensile reinforcement and surrounding concrete in the first element;

$(d_{\Delta} / d_x)_2$  = slip strain between the tensile reinforcement and surrounding concrete in the second element;

$(d_{\Delta} / d_x)_n$  = slip strain between the tensile reinforcement and surrounding concrete in the  $n^{\text{th}}$  element;

$E_0$  = the undamaged elastic modulus of concrete which is also the  $E_c$ ;

$E_c$  = young's modulus of UHPFRC;

$E_{ct}$  = elastic modulus of UHPFRC =  $E_c$ ;

$E_{fib}$  = young's modulus of steel fibre;

$E_h$  = modulus of steel hardening;

$E_{tl}$  = modulus of tensile hardening of UHPFRC;

$E_r$  = young's modulus of the steel reinforcement;

$f_c'$  = ultimate compressive strength of UHPFRC obtained from standard cylinder tests;

$f_{ct}$  = ultimate tensile strength of UHPFRC

$f_{tl}$  = maximum tensile stress of UHPFRC before tensile hardening;

$f_u$  = maximum strength of the steel reinforcement;

$f_y$  = yield stress of steel reinforcements;

$G$  = the flow potential;

$k_1$  = slope for bond slip relationship at the second stage;

$k_2$  = slope for bond slip relationship at the third stage;

$k_3$  = slope for bond slip relationship at the fourth stage;

$L_{def}$  = deformation length which is also a half of the crack spacing ( $S_{pr}$ );

$L_e$  = element length for each segment;

$L_{per}$  = contact perimeter of tensile reinforcement;

$L_w$  = width of compression wedge;

$P_c$  = force in surrounding concrete;

$P_{cc}$  = sectional compressive force from UHPFRC;

$P_{ct}$  = sectional tensile force from UHPFRC;

$P_{fib}$  = force owing to fibre bridging effect in UHPFRC after crack;

$P_{rb}$  = sectional force in reinforcements placed at the left;

$P_{rl}$  = lower boundary of initial guess for the force in tensile reinforcement;

$P_{rt}$  = sectional force in reinforcements placed at the right;

$P_{ru}$  = upper boundary of initial guess for the force in tensile reinforcement;

$P_{r\_max}$  = maximum force of the steel reinforcement;

$P_{r\_y}$  = tensile force of the steel reinforcement reaches yield stress;

$\bar{p}$  = the hydrostatic pressure based on effective stresses;

$\bar{q}$  = the effective von Mises equivalent stress;

$S_{pr}$  = crack spacing between primary cack and initial crack;

$W_{cr}/2$  = crack width at the initial crack;

$\alpha$  = a material dependent constant in Eq. (4);

$\alpha_1$  = constant coefficient of descending curve of concrete under tension;

$\alpha_2$  = empirical coefficient fitting the experimental result of bond test;

$\beta_1$  = constant coefficient of descending curve of concrete under tension;

$\beta_2$  = empirical coefficient fitting the experimental result of bond test;

$\gamma$  = a material dependent constant in Eq. (6);

$\Delta$  = relative slip between the tensile reinforcement and surrounding concrete;

$\Delta_1$  = relative slip between tensile reinforcement and surrounding concrete in the first element;

$\Delta_2$  = relative slip between tensile reinforcement and surrounding concrete in the second element;



$\Delta_n$  = relative slip between tensile reinforcement and surrounding concrete in the  $n^{\text{th}}$  element;

$\delta\Delta_1$  = differential slip between the tensile reinforcement and surrounding concrete in the first element;

$\delta\Delta_2$  = differential slip between the tensile reinforcement and surrounding concrete in the second element;

$\delta\Delta_n$  = differential slip between the tensile reinforcement and surrounding concrete in the  $n^{\text{th}}$  element;

$\varepsilon_{b1}$  = strain of the tensile reinforcement in the first element;

$\varepsilon_{b2}$  = strain of the tensile reinforcement in the second element;

$\varepsilon_{bn}$  = strain of the tensile reinforcement in the  $n^{\text{th}}$  element;

$\varepsilon_c$  = total compressive strain in concrete;

$\varepsilon_{\sigma_c}^{el}$  = elastic compressive strain corresponding to the yield stress of the concrete;

$\varepsilon_c^{in}$  = inelastic strain;

$\varepsilon_{c1}$  = strain of the concrete in the first element;

$\varepsilon_{c2}$  = strain of the concrete in the second element;

$\varepsilon_{cc}$  = the strain prior strain hardening;

$\varepsilon_{cn}$  = strain of the concrete in the  $n^{\text{th}}$  element;

$\varepsilon_{ct}$  = corresponding tensile strain of UHPFRC at the ultimate tensile strength;

$\varepsilon_{def}$  = strain in deformed region;

$\varepsilon_{mat}$  = material strain corresponding to the strain at the peak stress;

$\varepsilon_{pk}$  = strain corresponding to peak stress of UHPFRC;

$\varepsilon_{r1}$  = strain in reinforcements placed at the left;

$\varepsilon_{r2}$  = strain in reinforcements placed at the right;

$\varepsilon_{soft}$  = the strain corresponding to the peak stress;

$\varepsilon_t$  = total tensile strain in concrete;

$\varepsilon_t^{ck}$  = cracking strain;

$\varepsilon_t^{el}$  = elastic tensile strain corresponding to the yield stress of the concrete;

$\varepsilon_{test}$  = total strain based on standard cylinder test using a height of 200 mm cylinder;

$\varepsilon_y$  = yield strain of steel;

$\tilde{\varepsilon}^{pl}$  = equivalent plastic strain;

$\varepsilon_c^{pl}$  = plastic strains in compression;

$\varepsilon_t^{pl}$  = plastic strains in tension;

$\xi$  = a potential eccentricity parameter for describing the rate of the function approaches the asymptote;

$\sigma_{cc}$  = compressive stress in UHPFRC;

$\sigma_{ct}$  = tensile stress in UHPFRC;

$\sigma_{r1}$  = stress in reinforcements placed at the left;

$\sigma_{r2}$  = stress in reinforcements placed at the right;

$\sigma_{t0}$  = the uniaxial tensile stress;

$\bar{\sigma}_c(\varepsilon^{pl})$  = effective cohesive stresses under compressive corresponding to each equivalent plastic strain;

$\bar{\sigma}_t(\varepsilon^{pl})$  = effective cohesive stresses tensile compressive corresponding to each equivalent plastic strain;

$\hat{\sigma}_{\max}$  = the maximum principal effective stress;

$\tau_1$  = bond stress in the first element;

$\tau_2$  = bond stress in the second element;

$\tau_n$  = bond stress in the  $n^{\text{th}}$  element;

$\varphi$  = the dilation angle obtained from the measurement from the  $p$ - $q$  plane under high confining pressure;

### **3.1.9. ACKNOWLEDGEMENTS**

The authors would like to extend their sincere gratitude to Dr Phillip Visintin for his valuable advises on PI models used for this study. The authors would also like to extend their gratitude to Douglas. Fairweather, Jolly, Sedev, and Reid, who conducted the active confined cylinder and direct pullout tests presented in this paper.

### **3.1.10. REFERENCES**

Baby, F., Marchand, P. and Toutlemonde, F. (2014). “Shear behavior of ultrahigh performance fiber-reinforced concrete beams. I: experimental investigation.” *Journal of Structural Engineering*, 10.1061/(ASCE)ST.1943-541X. 07339445, 4013111.

Birtel, V. and Mark, P. (2006). "Parameterized finite element modelling of RC beam shear failure", *Abaqus user's Conf.* (2006) p95–p107.

Chen, Y., Visintin, P., Oehlers, D. J., and Alengaram, U. (2014). "Size-dependent stress-strain model for unconfined concrete." *Journal of Structural Engineering*. 140(4): 04013088.

Dagenais, M.A. and Massicotte, B. (2017). "Cyclic behavior of lap splices strengthened with ultrahigh performance fiber-reinforced concrete." *Journal of Structural Engineering*, 10.1061/(ASCE)ST.1943-541X.0001652, 143 (2), 4016163.

Hosinieh, M.M., Aoude, H., Cook, W.D. and Mitchell, D. (2015), "Behaviours of ultra-high performance fiber reinforced concrete columns under pure axial loading", *Engineering Structures*, 99, 388-401.

Lubliner, J., Oliver, J., Oller, S., & Onate, E. (1989). A plastic-damage model for concrete. *International Journal of solids and structures*, 25(3), 299-326.

Mahmud, G.H., Yang, Z. and Hassan, A.M.T., (2013), "Experimental and numerical studies of size effects of ultra high performance steel fibre reinforced concrete (UHPFRC) beams", *Construction and Building Materials*. 48, 1027–1034.

Mohamed Ali, M.S., Oehlers, D.J. and Griffith, M.C., (2008), "Simulation of Plastic Hinges in FRP-Plated RC Beams", *Journal of composites for construction*. 12(6), 617-625.

Razvi, S. and Saatcioglu, M., (1999), "Confinement model for high-strength concrete", *Journal of structural engineering*, 281-289.

Shin, H.O., Min, K.H. and Mitchell, D., (2017), "Confinement of ultra-high-performance fiber reinforced concrete columns", *Composite Structures*, 176, 124-142

Shin, H.O., Min, K.H. and Mitchell, D., (2018), "Uniaxial behavior of circular ultra-high-performance fiber-reinforced concrete columns confined by spiral reinforcement". *Construction and Building Materials*, 168, 379-393

Shukri, A.A., Visintin, P., Oehlers, D.J. and Jumaat, M.Z. (2016), “Mechanics model for simulating RC hinges under reversed cyclic loading”, *Materials*, 9, 305.

Singh, M. Mohamed Ali, M.S. and Sheikh, A.H., (2015), “Structural behaviour of ultra-high performance fibre reinforced concrete columns subjected to eccentric loading”, IABSE Conference – Structural Engineering: Providing Solutions to Global Challenges, Zürich, Switzerland: International Association for Bridge and Structural Engineering.

Singh, M., Mohamed Ali, M.S., Sheikh, A.H., Griffith, M.C. and Visintin, P. (2016), “Structural behaviour of ultra high performance fibre reinforced concrete beams with steel and polymer bar reinforcement”, Proc. of the 11th fib International PhD Symposium in Civil Engineering, Lausanne, Switzerland: CEB-Fib.

Singh, M., Sheikh, A.H., Mohamed Ali, M.S., Visintin, P. and Griffith, M.C. (2017), “Experimental and numerical study of the flexural behaviour of ultra-high performance reinforced concrete beams”, *Construction and Building Materials*, 138, 12-25.

Steven, G., and Empelmann, M. (2014). ”UHPFRC-columns with high-strength longitudinal reinforcement”, *Beton- und Stahlbetonbau*, 109, 344-354.

Sturm, A.B., Visintin, P., Oehlers, D.J. and Seracino, R., 2018. Time-Dependent Tension-Stiffening Mechanics of Fiber-Reinforced and Ultra-High-Performance Fiber-Reinforced Concrete. *Journal of Structural Engineering*, 144(8), p.04018122.

Visintin, P. and Oehlers, D.J. (2018), “Fundamental mechanics that govern the flexural behavior of reinforced concrete beams with fibre-reinforced concrete”, *Advances in Structural Engineering*, 21(7), 1088-1102.

Visintin, P. Oehlers, D.J. Haskett, M. and Wu, C. (2013), “Mechanics-Based Hinge Analysis for Reinforced Concrete Columns”, *Journal of Structural Engineering*, vol.139, 11, 1973-1980.

- Visintin, P., Sturm, A.B., Mohamed Ali, M.S. and Oehlers, D.J., (2018a). Blending macro-and micro-fibres to enhance the serviceability behaviour of UHPFRC. *Australian Journal of Civil Engineering*, pp.1-16.
- Visintin, P., Sturm, A. B., and Oehlers, D. J. (2018b). Long and short term serviceability behavior of reinforced concrete beams: Mechanics models for deflections and crack widths. *Structural Concrete*, 19(2), 489-507.
- Wille, K., EI-Tawil, S., Naaman, A.E. (2014), “Properties of strain hardening ultra-high performance fibre reinforced concrete (UHP-FRC) under direct tensile loading”, *Cement & Concrete Composite*, 48, 53-66.
- Xie, T., Mohamed Ali, M.S., Visintin, P., Oehlers, D.J. and Sheikh, A.H. (2018), “Partial Interaction Model of Flexural Behavior of PVA Fiber–Reinforced Concrete Beams with GFRP Bars”, *Journal of Composites for Construction*, 22(5)
- Yoo, D.Y. and Yoon., Y.S. (2016). “A review on structural behavior, design, and application of ultra-high-performance fiber-reinforced concrete”. *International Journal of Concrete Structures and Materials*, 10(2), 125-142.
- Yoo., D.Y. and Banthia., N. (2016).” Mechanical properties of ultra-high-performance fiber-reinforced concrete: A review”. *Cement and Concrete Composites*, 73, 267-280.
- Zhang,T., Visintin, P., Oehlers, D.J. and Griffith, M.C. (2014). “Presliding Shear Failure in Prestressed RC Beams. I: Partial-Interaction Mechanism”. *Journal of Structural Engineering*, 140(10).

**THIS PAGE HAS BEEN LEFT INTENTIONALLY BLANK**

## **3.2. Experimental and numerical investigation of the slenderness effects regarding ultrahigh performance fibre reinforced concrete column under concentric and eccentric loads**

### **3.2.1. INTRODUCTION**

Nowadays, with the highly intensified human civilizations and technology, more and more revolutionary landmark skyscrapers are being increasingly constructed. However, constructing these buildings by using a normal strength concrete associate with low strength and brittle nature raises concerns regarding durability and stability of the structures subjected to environmental and extreme loading scenarios such as seismic, impact or blast loads. For this purpose, ultra-high performance fibre reinforced concrete (UHPFRC) featured with exceptional compressive strength, ductile tensile behaviour, outstanding ductility and toughness was created along with the advancements in materials science to address the shortcomings of the normal strength concrete and hence to cater the demand of these high-rise buildings [1-4]. To date, the most recent research on UHPFRC mainly focus the shrinkage and optimization of the UHPFRC mixture [5-8], structural behaviours of UHPFRC flexural [9-17] and axial members [18-23], and blast resistance of UHPFRC structural members [24-27]. As demonstrated by these studies, using UHPFRC to manufacture structural members improves their flexural and shear capacities [9-15], energy absorption capacity [15-20], and impact resistance [24-27] compared to structural members manufactured with conventional concrete, and hence this reveals the enormous potential and importance of UHPFRC in the future applications.

To ensure a high robustness and durability of the high-rise structures, the exceptional compressive concrete strength and ductility of UHPFRC makes this material as a more



appropriate alternative of the conventional concrete for the column designs. To date, structural tests were conducted by Shin et al. [18, 19] and Hosinieh et al. [20] to investigate the structural response of UHPFRC short columns under concentric loads. It was found that the reductions in the spacing of transverse reinforcements lead to significant improvements in the squash load capacity, and a more ductile descending branch was observed in the load-axial displacement relationship compared to that of the reference specimens. With a given spacing of stirrup, additional cross-ties for the transverse reinforcements would enhance the total toughness of the short column, and no significant improvement in the squash load capacity can be observed. Furthermore, the structural responses of UHPFRC columns subjected to a combination of axial load and flexural bending were experimentally investigated by Steven and Empelmann [21] and Hung et al [22]. A further numerical study was then conducted by Fang et al. [28] to examine applications of a partial interaction model in simulating the structural response of the UHPFRC columns, and hence a load-moment interaction relationship was proposed to serve as a basis for developing design guidelines.

In order to achieve a high cost efficiency in the structural design without compromising its structural performance, using UHPFRC in the column design allows a reduced cross-section of the column and a high squash load capacity. However, with a given length of the column, reductions in the dimensions of the cross-section potentially increase the slenderness of the column, and this might lead to global buckling that compromise the robustness of the column. To date, it is recognized that there is a significant lack of investigation in structural response of slender UHPFRC columns conducted experimentally, and no numerical modelling was conducted to investigate their structural behaviour. Hence, in order to address this shortcoming, an experimental investigation regarding structural response of the slender UHPFRC columns under axial loads with a varying eccentricity was conducted by Douglas et al. [29]. A numerical

investigation was conducted based on the finite element analysis (FEA) technique in conjunction with a concrete damage plasticity (CDP) model for simulating the corresponding structural responses and damage patterns of all UHPFRC members. Subsequently, a parametric study was then conducted to investigate the effects of the slenderness ratio regarding to the load and moment capacities as well as the ductility indices of the column.

### 3.2.2. EXPERIMENTAL PROGRAM

#### 3.2.2.1. UHPFRC mixture and mixing process

Information of ingredients for manufacturing UHPFRC mixture and their corresponding ratios by weight are depicted in Table 3-2-1. Dry ingredients included sulphate resistant cement, silica fume (with an averaged particle size of 50 $\mu$ m), river washed sand (with an averaged particle size of 400  $\mu$ m) were mixed thoroughly in a pan mixer for 5 minutes, and both water and high range water reducer (HRWR) were subsequently added into the dry components for further mixing to obtain a good concrete flowability. Additional 2.25% by volume of Hooked-end steel fibres (with a diameter of 0.55 mm, a fibre length of 35 mm) having a tensile strength of 1345 MPa were added in to the available mixture to ensure a ductile tensile stress-strain response of UHPFRC, and the mixing process was continued for few minutes to evenly distribute the steel fibres in the mixture.

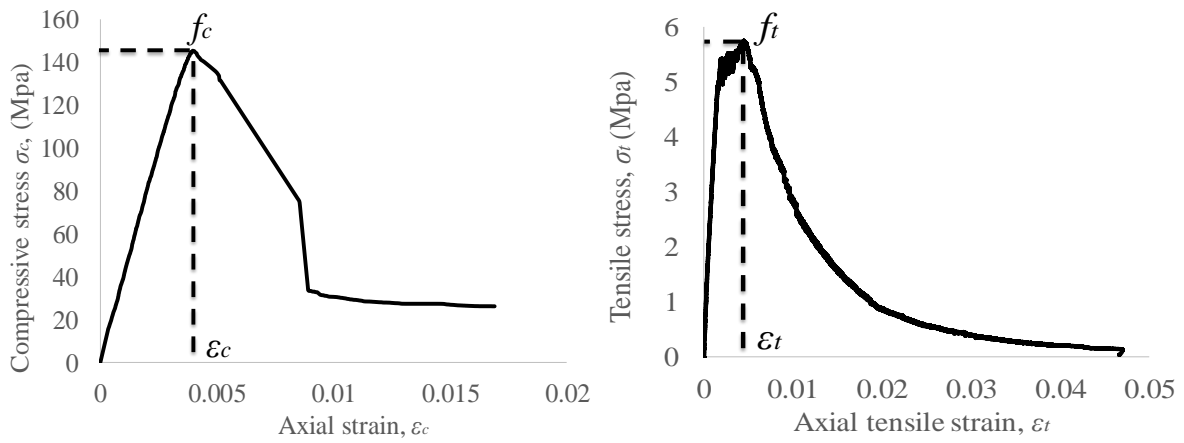
Table 3-2-1. Mixture proportion of UHPFRC

Sulphate resistant cement	Silica Fume	Clean washed sand	Water	High range water reducer (HRWR)	Steel fibre ( $V_f=2.25\%$ )
1	0.266	1	0.17	0.0565	0.175

### 3.2.2.2. Material tests for UHPFRC and steel reinforcements

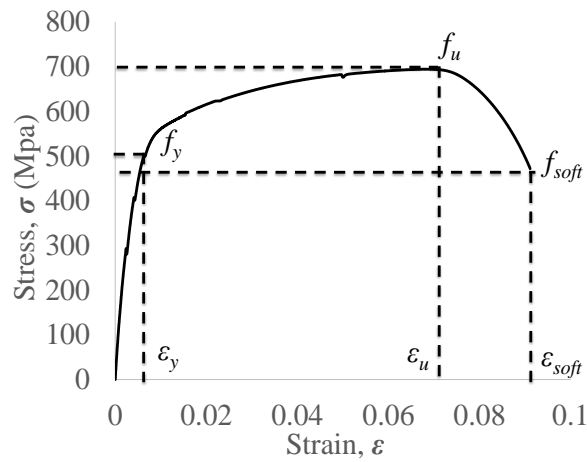
To obtain a full stress-strain response of UHPFRC under uniaxial compression, uniaxial compression tests were conducted on cylinders (a 100 mm in diameter and 200 mm in height), and the compression was acted on the cylinders with a constant rate of 0.05 mm/minutes. Moreover, to determine the responses of UHPFRC under direct tension, unnotched dog-bone specimens with a cross section of 120 mm×120 mm at the middle height were tested under tension with a constant loading rate of 0.05 mm/min. By performing these material tests, the young's modulus ( $E_c$ ), compressive strength ( $f_c$ ), and direct tensile strength ( $f_t$ ) have been determined as 145.4 MPa, 5.8 MPa, and 44 GPa, respectively, and the corresponding strains ( $\varepsilon_c$  and  $\varepsilon_t$ ) at the peak strengths are 3962 and 4477 micro strain. Corresponding stress-strain ( $\sigma_c - \varepsilon_c$ ,  $\sigma_t - \varepsilon_t$ ) responses of UHPFRC under compression and tension were generated, as demonstrated in Fig. 3-2-1 (a) and (b).

The stress-strain ( $\sigma$ - $\varepsilon$ ) response of steel reinforcements were generated experimentally by conducting direct tensile tests on the rebar with a diameter of 16 mm. As shown in the Fig. 3-2-1 (c), there are three stages of stress-strain ( $\sigma$ - $\varepsilon$ ) response: (1) elastic (with an elastic modulus  $E_s = 176$  GPa); (2) steel hardening; (3) steel softening, and the yield stress ( $\sigma_y$ ), the ultimate stress ( $\sigma_u$ ) and the softening stress ( $\sigma_{soft}$ ) in these stages were determined as 500 MPa, 694 MPa and 471 MPa, respectively with corresponding strain values ( $\varepsilon_y$ ,  $\varepsilon_u$  and  $\varepsilon_{soft}$ ) of 2840, 68054 and 91101 micro strain, respectively. Overall, these material properties were required as fundamental inputs to conduct the finite element (FE) analysis described later for simulating the structural responses of slender UHPFRC columns under axial loads and a UHPFRC beam under four point bending.



(a)

(b)



(c)

Figure 3-2-1. Material properties of: (a) compressive stress-strain response for unconfined UHPFRC; (b) tensile characterizations of UHPFRC; (c) steel reinforcement under direct tension

### 3.2.2.3. Structural member tests

It is to be stated that these tests described in this section were originally performed by Douglas et al. [29] and a detail summary is provided here to appreciate the simulation results from the FEA conducted by the author as a part of his PhD work.

### ***3.2.2.3.1. Specimen detail and designation***

Structural member tests, corresponding instrumentation and test setups are depicted schematically in Figs. 3-2-2 and 3-2-3. As presented in Fig. 3-2-2 (a), tested UHPFRC members are characterised with a square cross-section with both width and depth in 150 mm, and all UHPFRC members were reinforced with four longitudinal rebars with a diameter of 16 mm and transverse reinforcements (with dimensions of 110 mm × 110 mm) placed at a constant spacing of 85 mm. Designations of all UHPFRC members are detailed as follow: the letter “SL” indicates “Slender”, and following numbers denote the eccentricity of the axial load applied on the UHPFRC columns, while the designation “beam” was applied to denote the UHPFRC beam subjected to four-point bending. Taking the designation “SL-0” and “SL-50” as examples, “SL-0” indicates that the slender UHPFRC column was subjected to concentric load, and “SL-50” denotes that the slender UHPFRC column was axially loaded with an eccentricity of 50 mm.

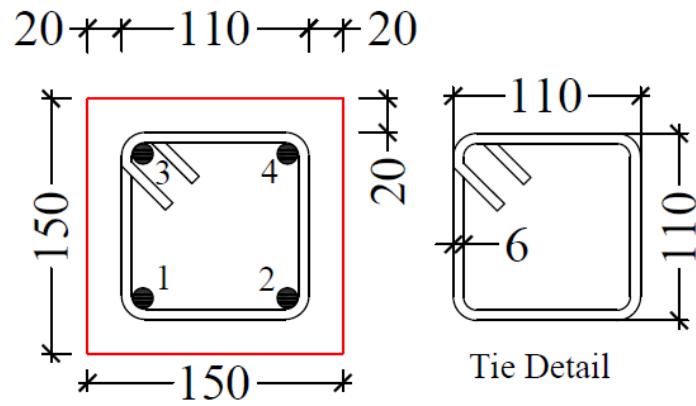
### ***3.2.2.3.2. Instrumentation and test setup***

Instrumentation and test setup are schematically detailed in Fig. 3-2-2 (b) - (e) and the corresponding photos of experimental program are also depicted in Fig. 3-2-3. Four slender UHPFRC columns with a total height of 1600 mm were tested in the universal testing machine (Amsler) under axial loading applied upward at eccentricities of 0, 35, 50, and 85 mm, as presented in Fig. 3-2-2 (b). Top and bottom ends of all slender UHPFRC columns were installed with two steel caps which was fabricated from steel rings and steel plates for providing appropriate eccentricities for the loads, and then the loading pivots were placed to the top and bottom surfaces of the steel plates for providing a pin to pin boundary condition, as presented in Fig. 3-2-2(b). For both the columns and the beam, initially, a load-controlled loading method

with a constant loading rate of 50 kN/minute was applied to load the column, and a displacement-controlled loading method with a rate of 0.15 mm/minute was then employed when the applied load reached to the maximum. To monitor the axial deformations of the slender UHPFRC columns during the tests, LVDTs 1-4 with a gauge length of 800 mm were placed vertically along the centreline of each column face, as detailed in the Figs. 3-2-2 (b) and 3-2-3 (a). Furthermore, the lateral deformations of the column at the middle height were measured by LVDTs 5-7 with a gauge length of 100 mm, and they were placed horizontally with a spacing of 300 mm and face to one of the concrete surfaces having compressive stress concentration, as illustrated in Figs. 3-2-2 (c) and 3-2-3 (b). To measure the localized strains at the middle height of the columns, four 30 mm strain gauges were placed vertically at middle-height of the column, and four 10 mm strain gauges were placed perpendicularly below the 30 mm strain gauges. Meanwhile, additional four strain gauges (with a gauge length of 10 mm) were attached to the surface of the steel reinforcements at the middle height region of the column to measure the localized strain of reinforcements, as presented in Fig. 3-2-2 (d).

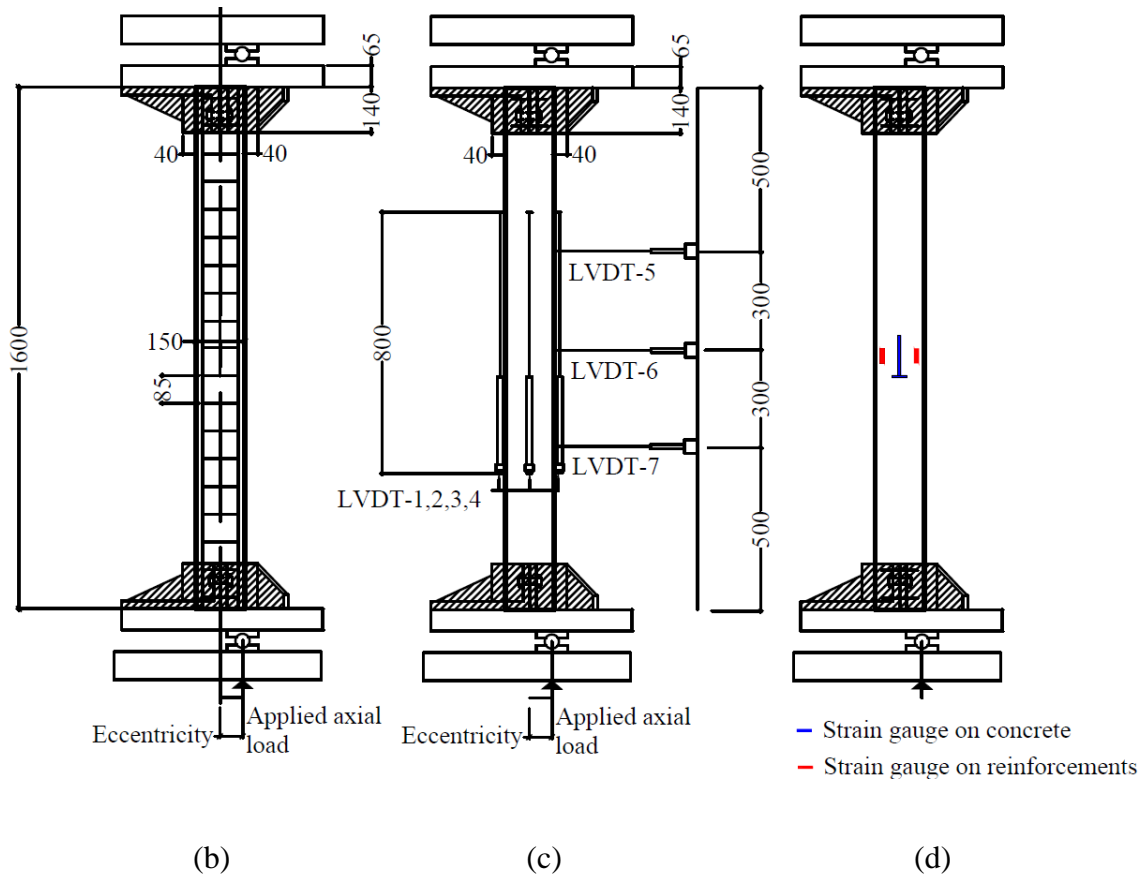
In addition to the column tests, a UHPFRC beam with a span of 2850 mm was tested under four-point bending using a 1000 kN capacity Avery machine, as shown in Figs. 3-2-2 (e) and 3-2-3 (c). To measure the displacement of the beam in the constant bending moment region, LVDTs# 1-3 with a gauge length of 200 mm were placed at the bottom of the beam with a spacing of 200 mm. The average mid-span displacement was determined through the measurements, and the corresponding applied load ( $P$ ) and flexural bending moment ( $M$ ) were determined through load cell readings. Furthermore, LVDTs# 4-7 with a gauge length of 500 mm were placed at two opposite sides longitudinally in order to measure the contractions at the top of the beam and elongation at the bottom of the beam, respectively, and hence to

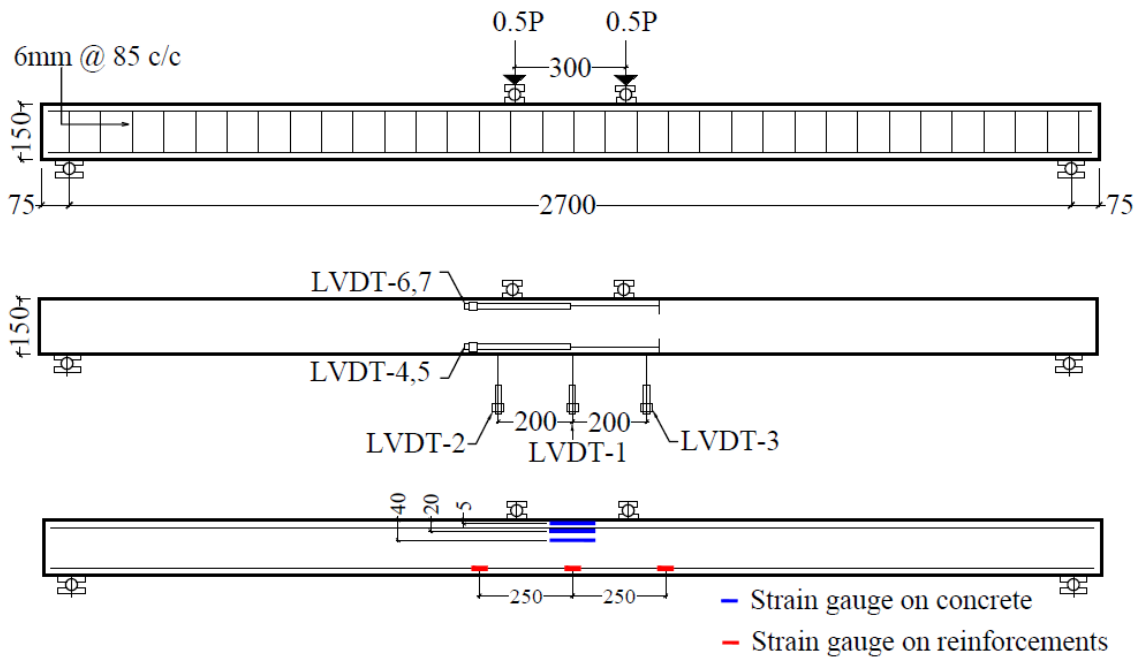
determine the rotations of the beam during the testing, as presented in Figs. 3-2-2 (e) and 3-2-3 (c).



Slender column-cross section  
 Bars-1,2,3,4 = 16 mm  
 Ties= 6mm diameter @ 85c/c throughout

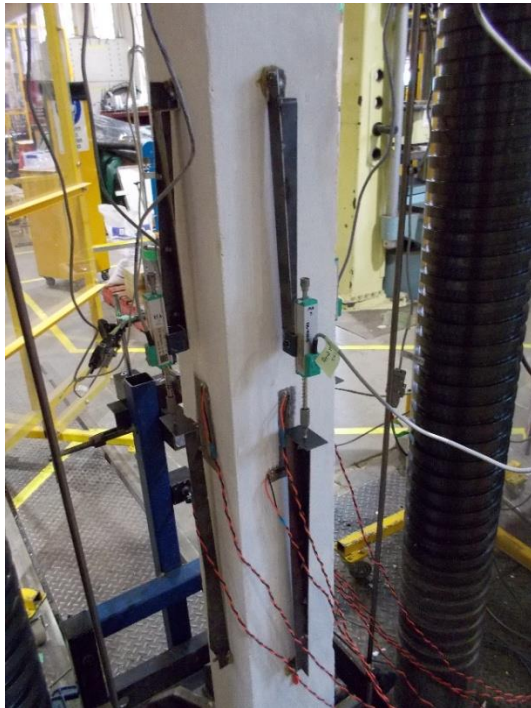
(a)





(e)

Figure 3-2-2. Test specimens' details and instrumentation set up: (a) cross-section of the beam and columns; (b) concentrically and eccentrically loaded columns; (c) four point-bending tests for the beam.

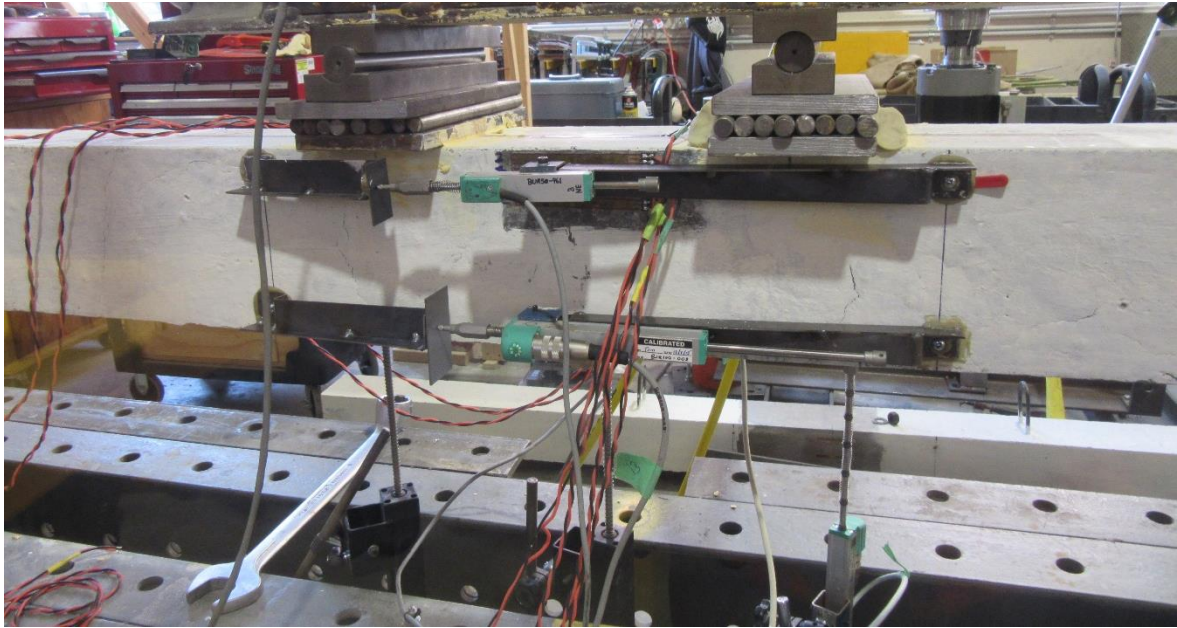


(a)



(b)





(c)

Figure 3-2-3. LVDT setup for UHPFRC members: (a) longitudinal LVDTs measuring axial deformations of slender columns; (b) horizontal LVDTs measuring lateral deformations of slender columns; (c) longitudinal and vertical LVDTs measuring rotations and vertical deformations of UHPFRC beam.

### 3.2.3. EXPERIMENTAL TEST RESULTS AND OBSERVATION

#### 3.2.3.1. Load-bearing, moment capacities, and ductility indices

In this study, the experimental results related to failure location, load bearing capacity ( $P_u$ ), moment capacity ( $M_u$ ), ductility indices ( $I_5$ ,  $I_{10}$ ) and residual strength factor ( $R_{5, 10}$ ), and axial and lateral deflections ( $\delta_{ap-exp}$ ,  $\delta_{lp-exp}$ , and  $\delta_{lu-exp}$ ) are reported in Table 3-2-2. The squash load capacity of slender UHPFRC column was determined as  $P_u = 3199.3$  kN when column SL-0 completely failed due to concrete softening. Comparisons in load bearing capacity ( $P_u$ ) of slender columns between columns SL-0 and SL-35 indicate that an increase in eccentricity of axial load from 0 mm to 35 mm results in a huge reduction (about 60% reduction) in  $P_u$ , and

further increases in the eccentricity (from 35 mm to 50 mm and from 50 mm to 85 mm) of the axial load lead to 26% and 47% decrease in  $P_u$ . Corresponding deflection values ( $\delta_{ap-exp}$  and  $\delta_{lp-exp}$ ) at the load bearing capacity ( $P_u$ ) are also indicated in Table 3-2-2, and it is worth noting that the magnitudes of the deflection increase with an increase in the eccentricity of the axial loading. Flexural moment capacities ( $M_u$ ) of the slender UHPFRC columns listed in Table 3-2-2 are calculated by considering the secondary moment effects induced by the lateral deflection at the peak load ( $\delta_{lp}$ ), and by comparing the values of the  $M_u$  in the table it can be found that the column SL-50 has the highest moment capacity ( $M_u = 64.1$  kN.m). Based on this, it is suggested that the balanced condition for the tested slender UHPFRC columns occurred when the eccentricity of the axial load was increased to 50 mm.

Table 3-2-2. Test results of all columns and beam

Specimen	Failure location (mm)	$P_{u-exp}$ (kN)	$\delta_{ap-exp}$ (mm)	$\delta_{lp-exp}$ (mm)	$\delta_{lu-exp}$ (mm)	$M_{u-exp}$ (kN.m)	$\epsilon_{conc}$ ( $\mu$ s)	$I_{5-exp}$	$I_{10-exp}$	$R_{5,10-exp}$
SL-0	+360 to +650	3199.3	2.6	0.6	29.8	1.8	3690	2.6	2.6	0.0
SL-35	0 to +160	1233.9	3.9	14.5	73.9	61.0	4130	5.0	7.1	41.7
SL-50	-70 to +75	910.2	5.2	20.5	74.1	64.1	4060	4.8	7.7	58.0
SL-85	+5 to +55	480.5	7.6	26.6	61.7	53.6	4040	5.0	7.9	59.2
SL-beam	-130 to +140	54.7	-	76.7	129.3	32.8	4010	-	-	-

\* “+” is above and “-” is below middle height of columns and middle span of the beam

Ductility indices ( $I_5$  and  $I_{10}$ ) are critical indicators to evaluate deformability, energy absorption capacity, and structural performance of the slender UHPFRC columns in design applications and residual strength factor ( $R_{5,10}$ ) was used as a further measurement for assessing the specimens reserve strength. Detailed definition and Fig. 3-2-4 can be obtained from Foster and Attard [30] as follows:

$$\xi = (\epsilon_{av} + \kappa e) \quad (1)$$

$$I_5 = \frac{\text{AreaOCD}}{\text{AreaOAB}} \quad (2)$$

$$I_{10} = \frac{\text{AreaOEF}}{\text{AreaOAB}} \quad (3)$$

$$R_{5,10} = 20(I_{10} - I_5) \quad (4)$$

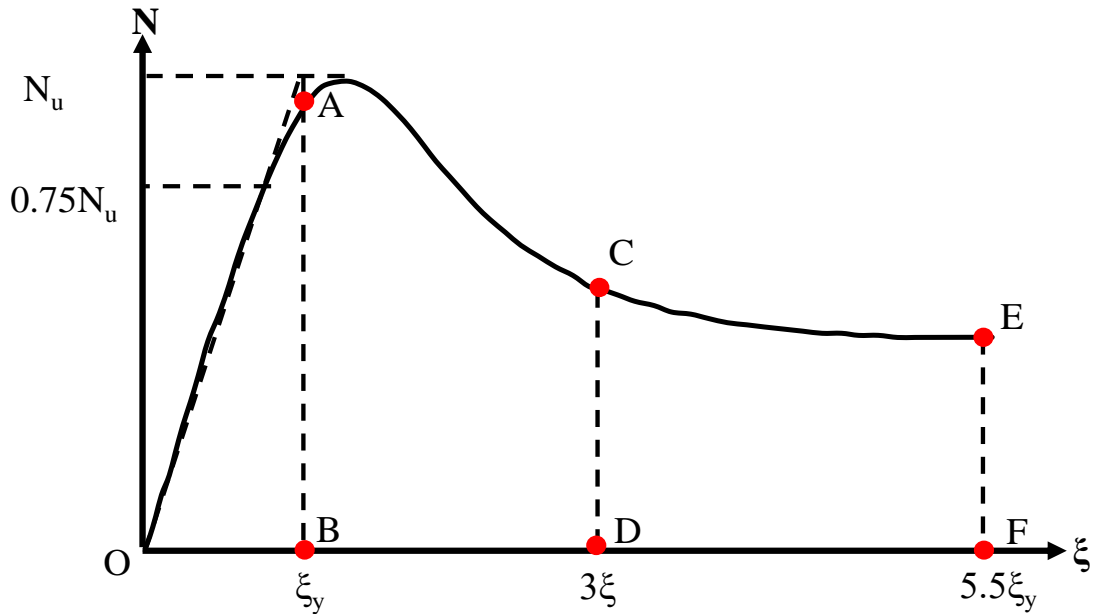


Figure 3-2-4. Energy Ductility in an eccentrically loaded column

A perfectly elastic-brittle material was attained when both  $I_5$  and  $I_{10} = 1$  and corresponding  $R_{5,10} = 0$ , and a perfectly elastic-plastic material was achieved when  $I_5 = 5$  and  $I_{10} = 10$  with the corresponding  $R_{5,10} = 100$  [30]. In practice, a range of 5 to 6.5 was recommended for the value of the ductility index ( $I_{10}$ ) through previous investigations to achieve a desirable robust behaviour of reinforced concrete columns, and a satisfactory  $I_{10} \geq 8$  was required to sustain a low to moderate seismic load [30]. Generally, as presented in Table 3-2-2, eccentrically loaded columns SL-35, SL-50 and SL-85 provide considerably high ductility index ( $I_{10} > 7$ ), and the values of  $I_{10}$  and  $R_{5,10}$  increase with an increase in eccentricity of axial loading, for instance, the  $I_{10}$  and  $R_{5,10}$  values of column ( $I_{10} = 7.9$ ,  $R_{5,10} = 59.2$ ) SL-85 are heights compared to companion specimens.

### 3.2.3.2. Load-axial strain and lateral deflection relationships

Load-axial compressive strain ( $P-\varepsilon$ ) and load-lateral deflection at the middle height ( $P-\delta_{lateral}$ ) relationships of all slender columns are presented in Figs. 3-2-5 and 3-2-6, respectively. Through observations from  $P-\varepsilon$  responses demonstrated that the sustained load  $P$  of concentrically loaded column experienced a huge drop when axial strain ( $\varepsilon$ ) reached 0.0039 with the corresponding residual load maintained at 600 kN, and then the curve terminated when axial strain reached a value of 0.005. It is worth noting that the slope of ascending branches of the curves decrease with an increase in the eccentricity of the loading, and it is also worth noting that the terminated axial strain of the columns increase with an increase in the eccentricity; for example, the terminated axial strain of columns SL-35, SL-50, and SL-85 are 0.0114, 0.0154, 0.0165, respectively.

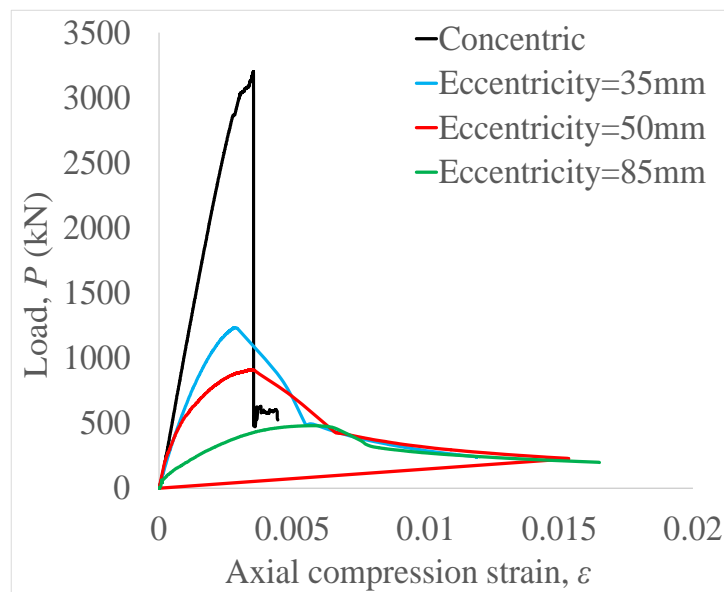


Figure 3-2-5. Load versus axial compression strain of slender columns

Comparisons regarding the lateral deflection – load responses at the middle height among all UHPFRC columns indicate that the column SL-0 has relatively lower lateral deflection at the peak axial load compared to that of other eccentrically loaded columns, which have a gradual increase in lateral deflection values with increasing axial loads. It is also worth noting that for

columns SL-35, SL-50 and SL-85, the axial loads start to gradually decrease when the lateral deflections of columns reached to 32 mm. Additionally, the load-middle span lateral deflection ( $P-\delta_{lateral}$ ) relationship of UHPFRC beam subjected to four-point bending is shown in Fig. 3-2-7 and a similar ascending trend as that of eccentrically load columns can be observed in Fig. 3-2-7 with a peak load of 54.7 kN and a corresponding deflection of 76.7 mm, and then the curve terminated with an applied load of 43.2 kN.

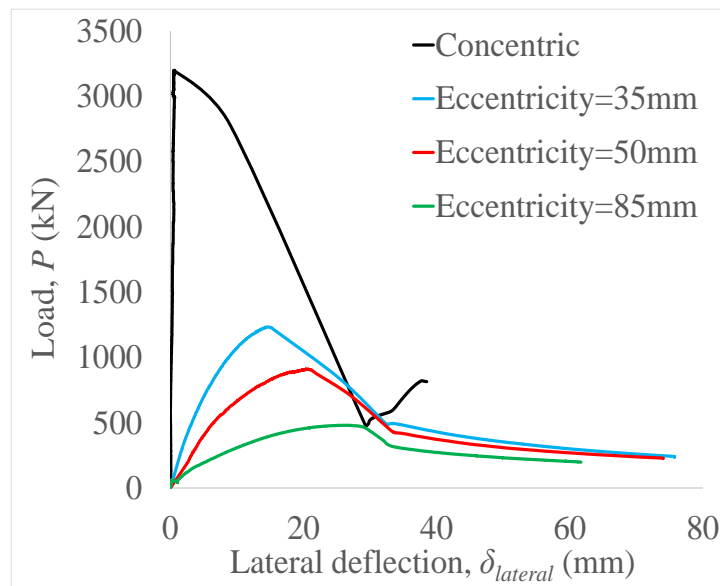


Figure 3-2-6. Load versus mid-height displacement of slender columns

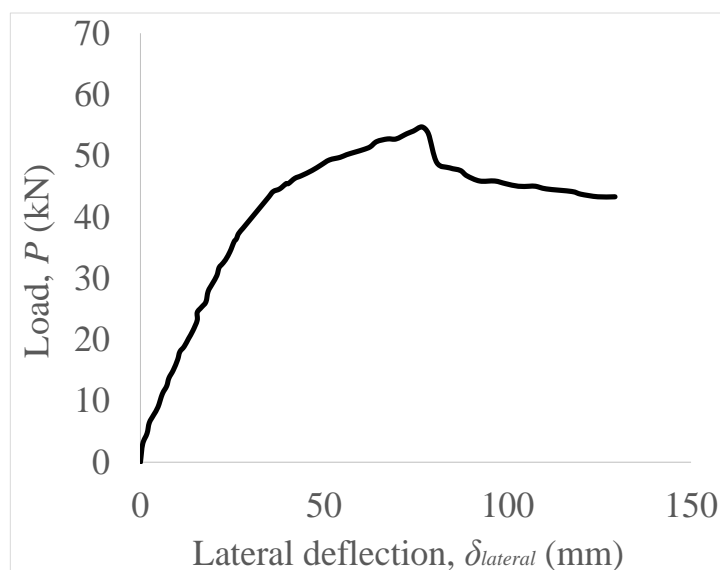


Figure 3-2-7. Load versus middle-span deflection of the beam

### 3.2.3.3. Failure location and damage pattern

Failure location of all UHPFRC members are reported in Table 3-2-2, and the corresponding failure modes are demonstrated clearly in Fig.3-2-8. As can be seen in both Table 3-2-2 and Fig. 3-2-8 (a), column SL-0 failed in an explosive manner with concrete spalling off a large area occurred from 360 mm above the middle height of the column up to 650 mm above the middle height. The corresponding compressive strain recorded by the 30 mm strain gauge placed at the middle height of the column is  $3690 \mu\text{s}$ , which is lower than the peak strain of  $3962 \mu\text{s}$  obtained from the standard cylinder compression tests presented in Fig. 3-2-1 (a). It is inferred that the strains at the top or bottom end of the column are normally larger than the strain measured at the middle height of the column, and this phenomenon is mainly attributed to the strain concentration induced by the high reaction forces at the ends of the column.

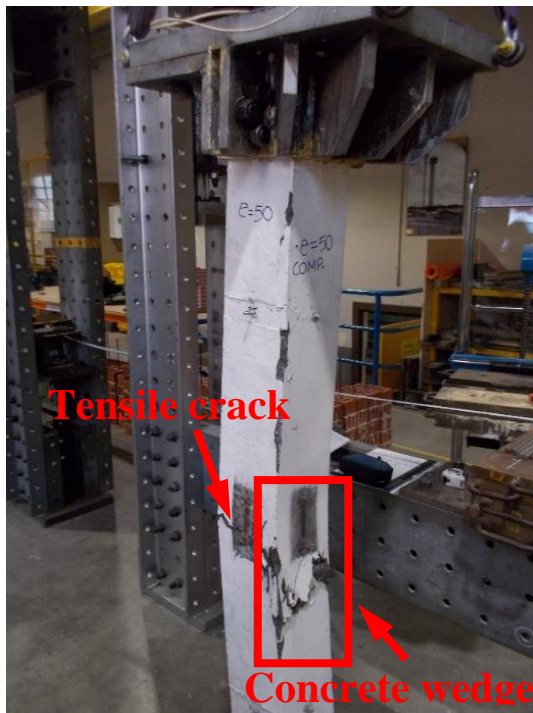
For slender UHPFRC columns subjected to eccentrically axial load (SL-35, SL-50, and SL-85), their failure locations were close to the middle height of the column and typical plastic hinges associate with concrete spalling and flexural tensile cracks formed at the middle height of the column, as illustrated in Fig. 3-2-8 (b)-(d). According to the measurement ( $\epsilon_{conc}$ ) from the strain gauges located at the middle height of all eccentrically loaded columns, it is suggested that the occurrence of concrete spalling is due to the concrete softening when the concrete strains ( $\epsilon_{conc}$ ) exceeded the compressive peak strain ( $\epsilon_c$ ). To note that, comparisons in concrete softening regions shown in Fig. 3-2-8 (b)-(d) indicate that the size of compression wedges reduced with an increase in the eccentricity of the loading, and also the column loaded with a large eccentricity tends to fail due to the flexural bending. For a simply supported UHPFRC beam under four-point bending, two tensile flexural cracks were observed at the bottom of the beam within the region between the constant moment region and accompanied by a slight concrete spalling occurred at the top of the beam, as shown in Fig. 3-2-8(e).



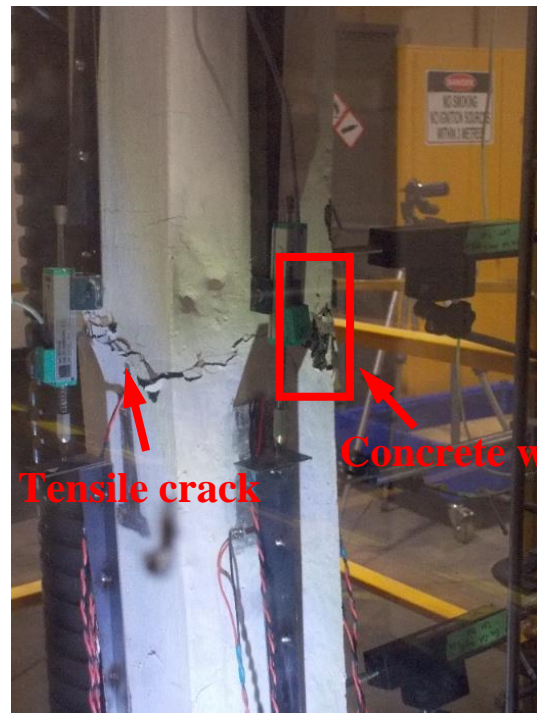
(a)



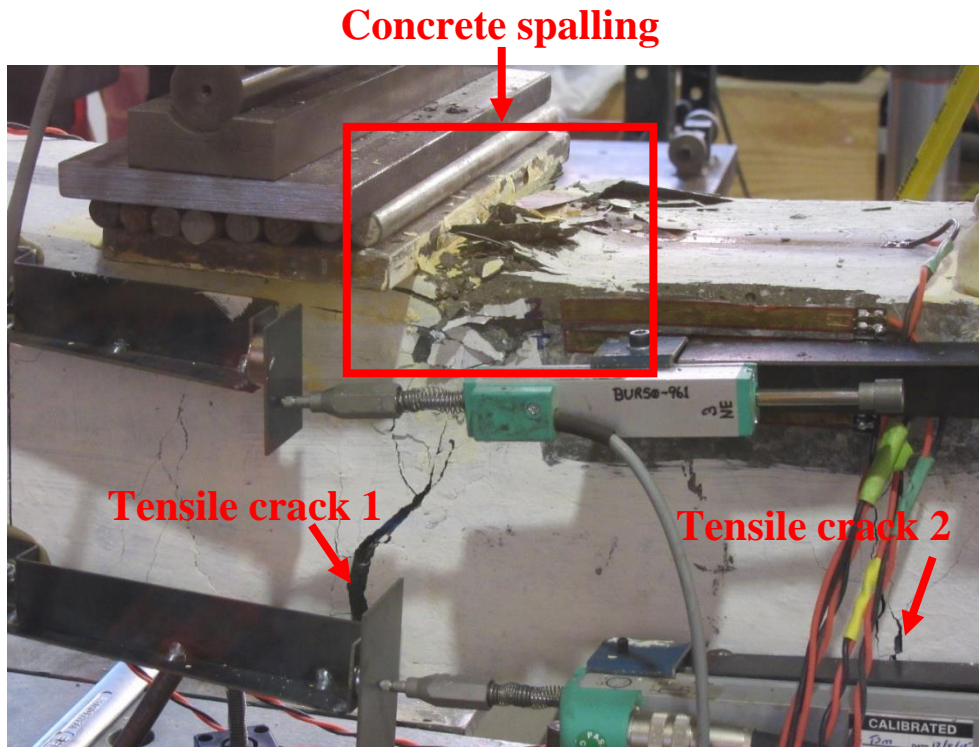
(b)



(c)



(d)



(e)

Figure 3-2-8. Failure modes of: (a) concentrically loaded column; (b) eccentrically loaded column ( $e=35$  mm); (c) eccentrically loaded column ( $e=50$  mm); (d) eccentrically loaded column ( $e=85$  mm); (e) beam under four point bending

### 3.2.4. NUMERICAL (FINITE ELEMENT) MODELLING

Compressive and tensile stress-strain ( $\sigma$ - $\epsilon$ ) responses of the unconfined UHPFRC were established in section 2.2, and these material properties are used to generate the compressive  $\sigma$ - $\epsilon$  responses of confined UHPFRC by adopting the Razvi and Saaticioglu's confinement model for high-strength concrete [31]. Hence, the stress-strain ( $\sigma$ - $\epsilon$ ) responses of both unconfined and confined UHPFRC are incorporated with the concrete damage plasticity (CDP) model along with the  $\sigma$ - $\epsilon$  response of steel reinforcements to simulate the structural behaviours of slender UHPFRC columns subjected to axial load with a varying eccentricity. Previous studies were conducted to simulate mechanical behaviour of UHPFRC members [28, 32, 33] and to investigate size effect of UHPFRC [34], and both these studies highlighted the applicability and accuracy for using the CDP model. For this purpose, FE numerical modelling



is undertaken in conjunction with the CDP model by using the commercial software package ABAQUS to simulate the load - lateral deflection at the middle height ( $P-\delta_{lateral}$ ) responses of slender UHPFRC under different loading conditions, and corresponding simulated results are also compared against experimental results. Subsequently, a parametric study was conducted based on the validated numerical model to further investigate the effects of the slenderness of the UHPFRC columns pertaining to their structural performances.

#### **3.2.4.1. FE modelling**

In terms of FE modelling, the concrete elements were modelled with 3D hexahedral solid elements with 8 nodes (C3D8R) featured in each element, and meanwhile, unconfined (a square hollow section) and confined UHPFRC (solid section) were created independently with the same modelling element but different geometries, as presented in Fig. 3-2-9 (a). To note that a tie constraint was characterised to achieve a perfect bonding for the interfaces between unconfined and confined UHPFRC in order to duplicate the tested specimens in reality. Furthermore, both transverse and longitudinal steel reinforcements were characterised as 3 dimensional truss element featured with 2 nodes (T3D2) as shown in Fig. 3-2-9 (b), and the reinforcements were then embedded in assembled geometry of unconfined and confined UHPFRC with a constraint of embedded region assigned to define the interactions between reinforcements and concrete.

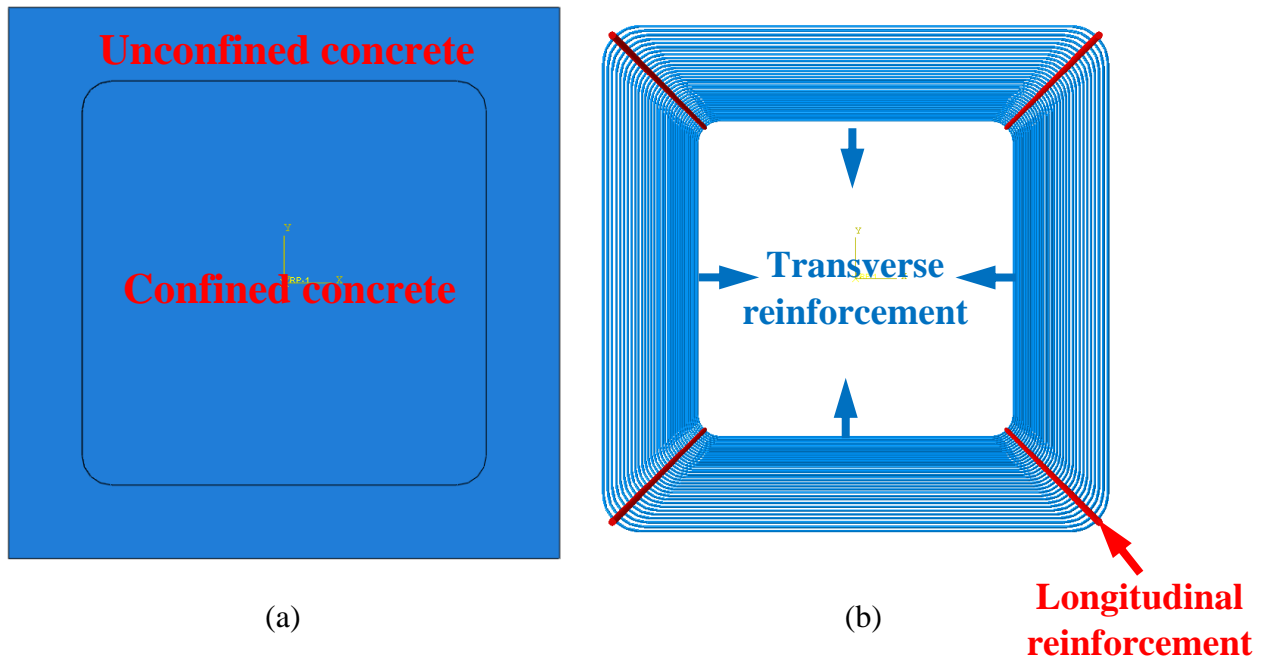


Figure 3-2-9. Finite element (FE) modelling of: (a) cross-section of UHPFRC slender columns: (b) longitudinal and transverse reinforcements

Figure 3-2-10 demonstrates the FE modelling of the initial experiment setup and subsequent testing process. As presented in Figs. 3-2-10 (a) and (b), to duplicate the experimental setup shown in Fig. 3-2-2 (b), a simplified steel cap composed by a square steel ring (length: 165 mm, thickness: 45 mm) and a flat steel plate (length: 500 mm, breadth: 350 mm, thickness: 65 mm) was modelled in ABAQUS with the same hexahedral solid elements (C3D8R) as used for modelling concrete element. Meanwhile, loading plates featured with a length of 250 mm, a width of 100 mm, and a thickness of 100 mm were placed on the both top and bottom steel caps with a tie constraint defined for the contact interfaces between flat plate and loading plate, as presented in Figs. 3-2-10 (a) and (b). A displacement load control was applied with the presence of the reference point (RP) located at the geometrical centre of the loading plate as shown in Fig. 3-2-10 (b), and a multiple points coupling constraint was defined between the reference point (RP) and the surface of the loading plate to conduct concentric or eccentric loads with a steady loading rate of 0.15 mm/min upwards in Z direction. A boundary condition

which fully restrains translation and only allow rotation in Y axis was assigned along the translational line of the top loading plate, and it was similarly adopted to the translational line of the lower loading plate except for the translation in the z direction to allow vertical movement.

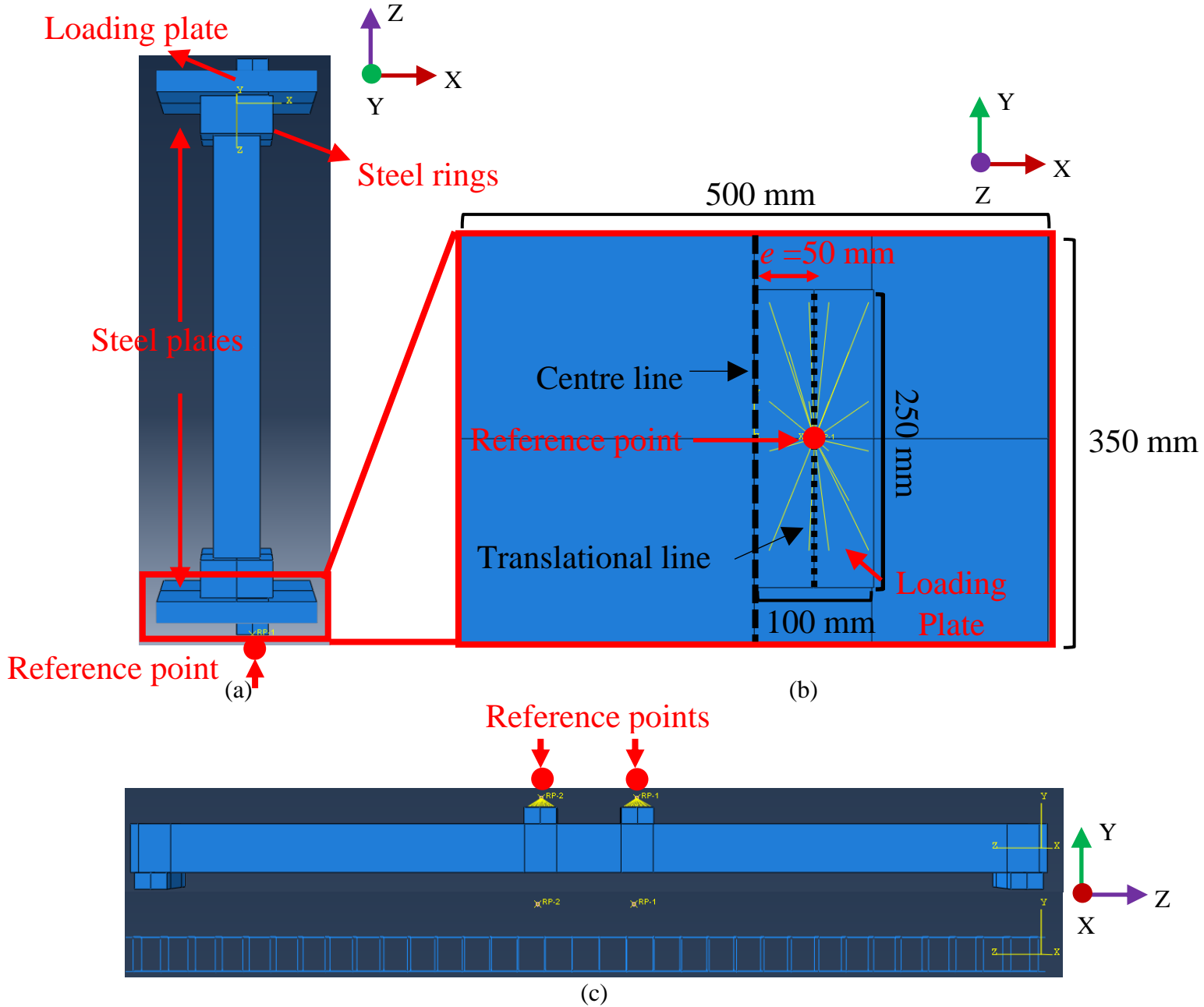


Figure 3-2-10. Finite element (FE) modelling for: (a)UHPFRC slender column and transverse steel arrangement; (b) Steel plate and loading plate; (c) four point bending test for UHPFRC beam.

Same loading configuration was applied on the two loading plates which have the same size of the loading plate used in the column setup for modelling of the UHPFRC beam subjected to four-point flexural bending, as shown in Fig. 3-2-10 (c), and the steady loading rate was assigned on the two reference points having an increasing displacement downward only in the Y direction. Furthermore, another two supporting plates with the same dimensions of the loading plates were placed underneath the UHPFRC beam, and only rotation in x-axis was allowed along the centre translational line of the bottom face of the plates. In ABAQUS, a surface-to-surface contact (standard) algorithm that include a hard contact related to normal displacement and sliding contact associated to the tangential displacements and characterised with a friction coefficient of 0.1 was adopted to all the contact interfaces between steel and concrete. To cooperate the modelling, an elasto-plastic material behaviour of steel was assigned to steel caps, loading plates, and supporting plates, whereas the stress-strain relationship of steel reinforcements was determined by the experimental results indicated in Fig. 3-2-2 (c). To appropriately perform an elastic-plastic material property of unconfined and confined UHPFRC, a concrete damage plasticity (CDP) model provided in ABAQUS was adopted in conjunction with given stress-strain relationships of UHPFRC presented in Fig. 3-2-2 (a)-(c) to perform the FE simulation of UHPFRC members.

#### **3.2.4.2. Theoretical background of CDP model**

Concrete damage plasticity (CDP) model is a plasticity-based continuum damage constitutive model that encompasses material elasticity, plasticity, and damage evolution, and it is adopted to represent the plastic behaviour of concrete material subjected to different loading protocols. Specifically, the elasticity of the material is represented by the elastic modulus ( $E_c$ ) and Poisson's ratio ( $\nu$ ) of the concrete, while the plasticity of concrete material is represented by the strain hardening and softening response of concrete in compression and strain softening

response of concrete in tension. A yield function ( $F$ ) developed by Lubliner [35] is adopted and incorporated with the plasticity of concrete material to using for determination of the material yielding. Furthermore, Drucker-Prager hyperbolic function is used to represent a plastic potential ( $G$ ) for determination of the plastic flow. Subsequently, these material characteristics are then incorporated with the yield function ( $F$ ) and plastic potential ( $G$ ) presented as follows:

$$F = \frac{1}{1-\alpha} \left( \bar{q} - 3\alpha\bar{p} + \beta(\tilde{\varepsilon}^{pl}) \left\langle \hat{\sigma}_{\max} \right\rangle - \gamma \left\langle -\hat{\sigma}_{\max} \right\rangle \right) - \bar{\sigma}_c(\tilde{\varepsilon}_c^{pl}) \leq 0 \quad (5)$$

$$G = \sqrt{(\xi\sigma_{t0} \tan \varphi)^2 + \bar{q}^2} - \bar{p} \tan \varphi \quad (6)$$

$$\alpha = \frac{\frac{\sigma_{bo}}{\sigma_{co}} - 1}{2 \times \frac{\sigma_{bo}}{\sigma_{co}} - 1}; \quad 0 \leq \alpha \leq 0.5 \quad (7)$$

$$\beta = \frac{\bar{\sigma}_c(\tilde{\varepsilon}_c^{pl})}{\bar{\sigma}_t(\tilde{\varepsilon}_t^{pl})} (1-\alpha) - (1+\alpha) \quad (8)$$

$$\gamma = \frac{3(1-k_c)}{2k_c - 1} \quad (9)$$

where  $\alpha$  and  $\gamma$  are constants for material,  $\bar{q}$  represents the Mises equivalent effective stress,  $\bar{p}$  represents the hydrostatic pressure stress.  $\bar{\sigma}_c(\tilde{\varepsilon}_c^{pl})$ ,  $\bar{\sigma}_t(\tilde{\varepsilon}_t^{pl})$  are functions of equivalent plastic strains  $\tilde{\varepsilon}_c^{pl}$  and  $\tilde{\varepsilon}_t^{pl}$ , and they represent effective compressive and tensile cohesion stresses, respectively;  $\beta$  is an expression of effective cohesion stresses ( $\bar{\sigma}_c, \bar{\sigma}_t$ ) and constant  $\alpha$ ;  $\hat{\sigma}_{\max}$  is the maximum principal effective stress;  $\xi$  referred to as the eccentricity (value is 0.1) which predominates the rate where the function approaches to the asymptote, and the curvature regarding to the flow potential increases with an increase in the value of  $\xi$ ;  $\sigma_{t0}$  is

the uniaxial tensile strength which obtained from the tensile stress-strain response of UHPFRC;

$\varphi$  is the dilation angle measured in the  $p$ - $q$  plane;  $\frac{\sigma_{bo}}{\sigma_{co}}$  stands for the ratio of the initial equibiaxial compressive yield stress to initial uniaxial compressive yield stress;  $k_c$  is the ratio of the second stress invariant on the tensile meridian to the second stress invariant on the compressive meridian at an initial yield condition with a domain  $0.5 < k_c < 1.0$ . In present study, the value of  $\frac{\sigma_{bo}}{\sigma_{co}}$  is taken as 1.05 for UHPFRC instead of 1.16 used for conventional concrete, as found from previous studies [28, 32 and 33]. The value of  $k_c$  is commonly set as 2/3 for concrete materials. By conducting from previous studies [28, 33], a value of the dilation angle  $\varphi$  for UHPFRC is determined as  $39^\circ$ , which is slightly higher than the value of  $30^\circ$  for conventional concrete due to an improved ductility of the material. Consequently, the envelope of the yield function was characterised with parameters defined as above.

Specified equivalent plastic strains  $\tilde{\varepsilon}^{pl}$ , which are  $\tilde{\varepsilon}_c^{pl}$  and  $\tilde{\varepsilon}_t^{pl}$ , were detailed in the following equations based on available elasto-plastic responses of concrete under uniaxial compression or direct tension to help the determination of aforementioned failure mechanism of yield function. To be more specific, by excluding the elastic strains ( $\varepsilon_{0c}^{el}$  and  $\varepsilon_{0t}^{el}$ ) from the total measurement of elasto-plastic responses of concrete ( $\varepsilon_c$  and  $\varepsilon_t$ ) obtained experimentally, compressive inelastic strain ( $\varepsilon_c^{in}$ ) and tensile cracking strain ( $\varepsilon_t^{ck}$ ) were subsequently obtained, as demonstrated from eq.10 - 13.

$$\varepsilon_c^{in} = \varepsilon_c - \varepsilon_{0c}^{el} = \varepsilon_c - \sigma_c / E_0 \quad (10)$$

$$\varepsilon_t^{ck} = \varepsilon_t - \varepsilon_{0t}^{el} = \varepsilon_t - \sigma_t / E_0 \quad (11)$$

$$\tilde{\varepsilon}_c^{pl} = \varepsilon_c^{in} - \frac{d_c}{(1-d_c)} \frac{\sigma_c}{E_0} \quad (12)$$

$$\tilde{\varepsilon}_t^{pl} = \varepsilon_t^{ck} - \frac{d_t}{(1-d_t)} \frac{\sigma_t}{E_0} \quad (13)$$

Furthermore, scalar (compressive and tensile) damage parameters ( $d_c, d_t$ ) are derived from available elasto-plastic responses of concrete obtained experimentally, and they are critical for the accurate prediction of load-displacement relationships and cracking patterns of RC column under concentric or eccentric loads.

$$d_c = 1 - \left[ \frac{\frac{\sigma_c}{E_0}}{0.2\varepsilon_c^{in} + \frac{\sigma_c}{E_0}} \right] \quad (14)$$

$$d_t = 1 - \frac{\sigma_t}{f_t} \quad (15)$$

### 3.2.5. COMPARISONS AND DISCUSSIONS

#### 3.2.5.1. Comparisons of experimental and simulated results

Comparisons of experimental and FEA simulated results for all UHPFRC members are given in Table 3-2-3, and the load-lateral deflection ( $P$ - $\delta_{lateral}$ ) relationships obtained experimentally and numerically are exhibited in Fig. 3-2-11. It can be seen that the failure locations of all UHPFRC members predicted by the FE model have a high correlation to the failure locations observed in the experimental program shown in Table 3-2-2; for specimens SL-0 and SL-beam, the failure locations were accurately predicted. Furthermore, the ratios between FE simulations to experimental results pertaining to  $P_u$ ,  $\delta_{lp}$ ,  $\delta_{lu}$ ,  $M_u$ ,  $I_5$ ,  $I_{10}$ , and  $R_{5,10}$  are also summarised in the Table 3-2-3. Based on the ratios reported in the Tables, it is worth noting that the mean of these

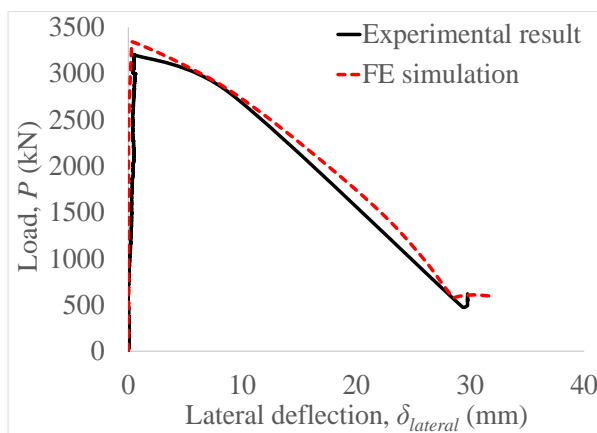
ratios ranges from 0.95 to 1.08 and the corresponding standard deviation found to be 0.02-0.16, and thereby this further highlight the high correlations between FE simulations and experimental results.

Table 3-2-3. Comparisons of experimental and FE simulation results for all UHPFRC members

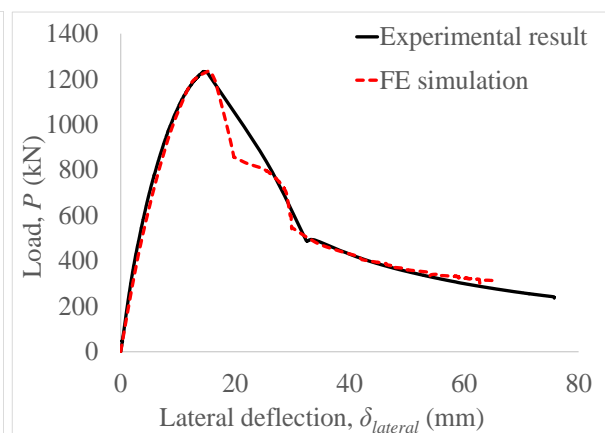
Specimen	Failure location (mm)	$\frac{P_{u-FEM}}{P_{u-exp}}$	$\frac{\delta_{lp-FEM}}{\delta_{lp-exp}}$	$\frac{\delta_{lu-FEM}}{\delta_{lu-exp}}$	$\frac{M_{u-FEM}}{M_{u-exp}}$	$\frac{I_{5-FEM}}{I_{5-exp}}$	$\frac{I_{10-FEM}}{I_{10-exp}}$	$\frac{R_{5,10-FEM}}{R_{5,10-exp}}$
SL-0	+350 to +660	1.04	0.67	1.06	0.78	1.02	1.02	-
SL-35	-100 to +100	1.00	1.06	0.88	1.02	0.98	1.02	1.12
SL-50	-80 to +80	0.99	1.01	0.98	1.00	1.01	1.08	1.19
SL-85	-40 to +40	1.04	0.98	0.98	1.04	0.99	0.97	0.92
SL-beam	-135 to +135	1.00	1.01	1.01	1.00	-	-	-
Mean		1.01	0.95	0.98	0.97	1.00	1.02	1.08
Standard deviation		0.02	0.16	0.07	0.11	0.02	0.05	0.14

\* “+” is above and “-” is below middle height of columns and middle span of the beam

Meanwhile, the load - lateral deflection ( $P - \delta_{lateral}$ ) relationships shown in Figs. 3-2-11 (a) to (e) further emphasize the high accuracy of FE simulations comparing to experimental results for both slender UHPFRC columns and the beam.



(a)



(b)



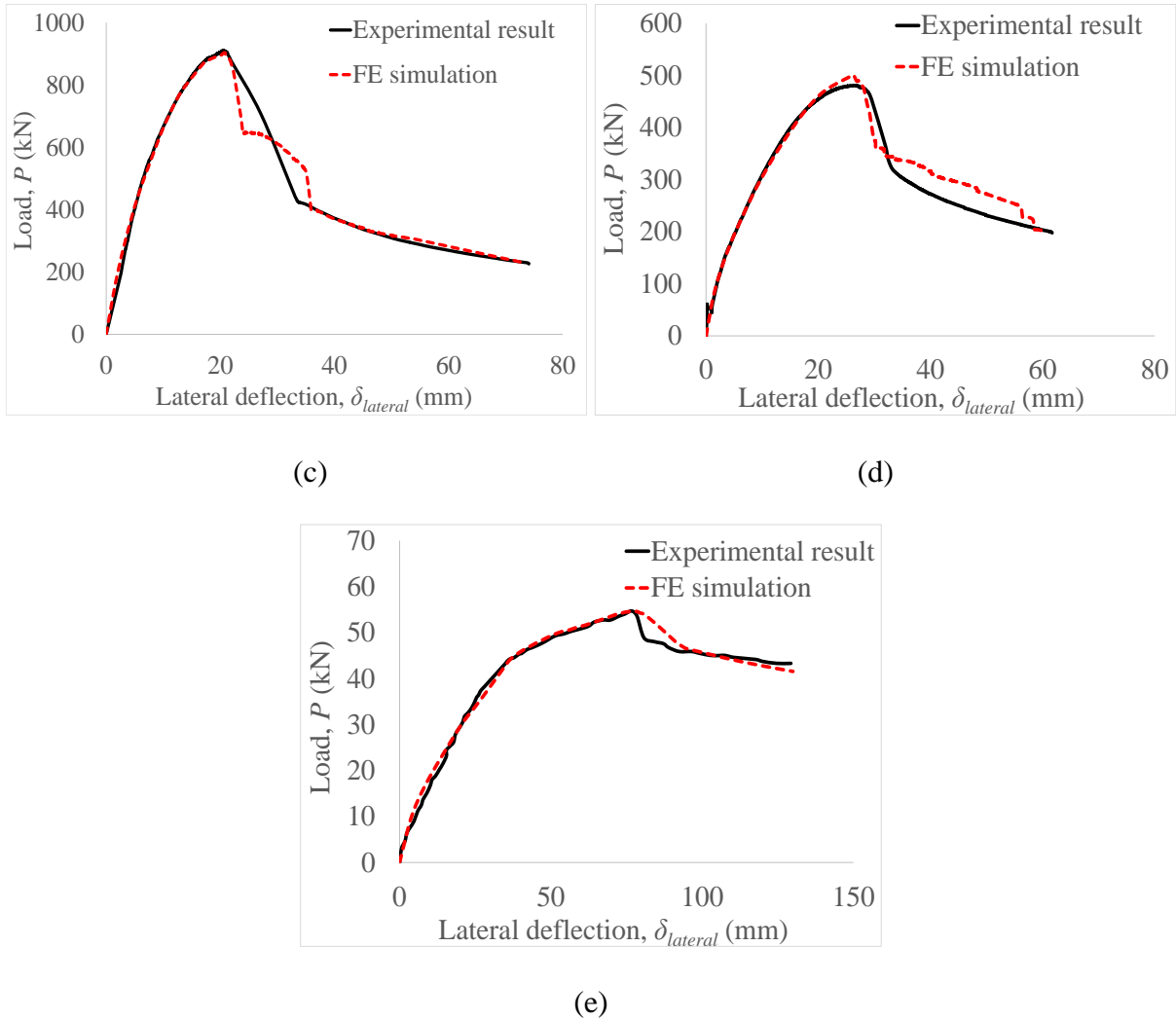
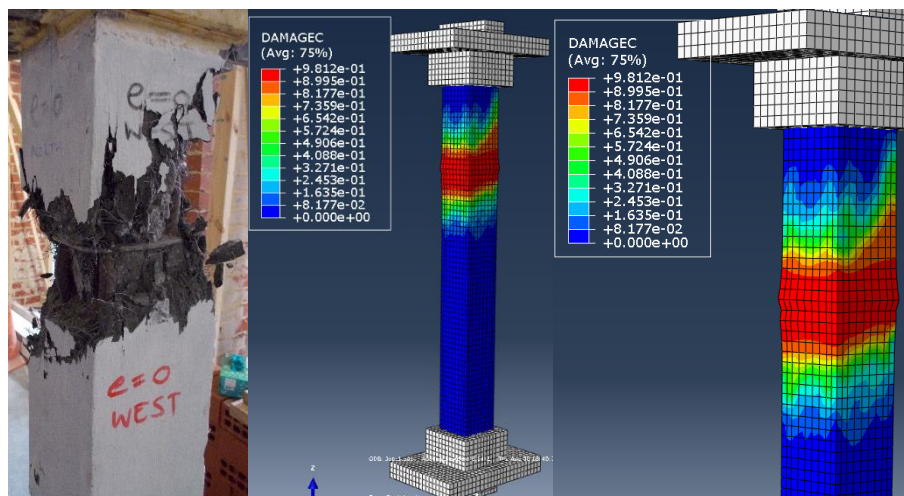


Figure 3-2-11. Comparisons among experimental results and FE simulation for UHPFRC columns loaded with different eccentricities: (a) concentrate; (b) eccentricity = 35 mm; (c) eccentricity = 50 mm; (d) eccentricity = 85 mm; (e) UHPFRC beam

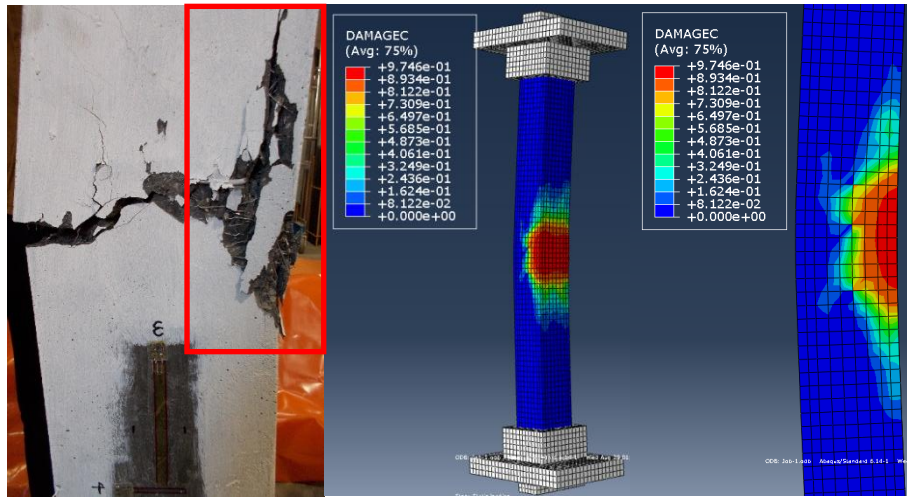
### 3.2.5.2. Comparisons of failure mode

With concrete damage parameters ( $d_c, d_t$ ) defined and input in the CDP model, FE models were able to reproduce the compressive and tensile damage patterns of UHPFRC members, and further comparisons between experimental observations and simulated damage patterns are shown in Fig. 3-2-12 and 3-2-13. As presented in Fig. 3-2-12 (a), the concrete spalling at the top region of the column observed from the experiment was appropriately reproduced by

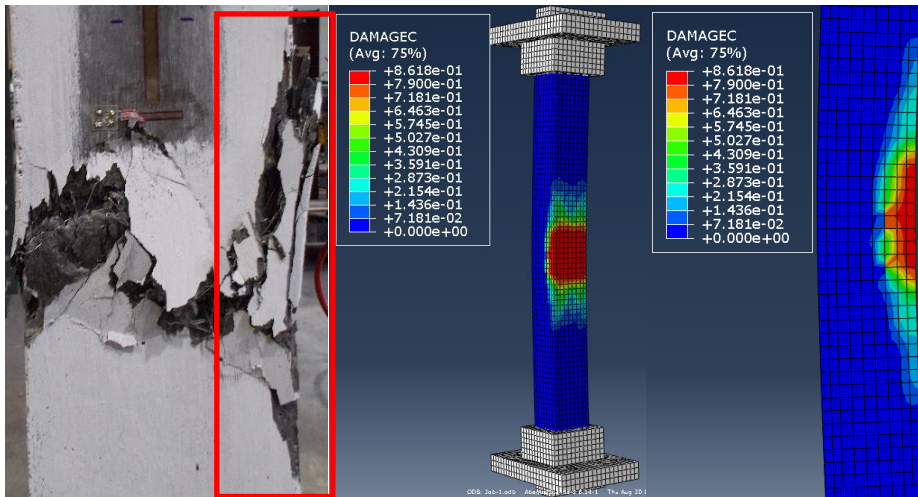
the damage pattern obtained from FE simulations, and more specifically, severe damaged regions with a maximum damage level of 98.1% highly match the concrete crushed regions observed from the tests. Compressive damage patterns for eccentrically loaded columns SL-35, SL-50, and SL-85 are demonstrated in Fig. 3-2-12 (b)-(d), where a wedge shape of region featured with a high damaged level is commonly observed from all compressive damage patterns. A typical compressive concrete wedge with a damage level of 97.5% shown in the simulated damage pattern of column SL-35 has a high agreement with the elevation view of the actual concrete crushed region presented in Fig. 3-2-12 (b), and similar patterns appear through the comparisons in Fig. 3-2-12 (c) and (d). It is also worth mentioning that the damage level of simulated damage pattern and its area of damage both reduced with an increase in the eccentricity of loading, and this finding can be further clarified by the observations and comparisons in actual crushed regions as illustrated in Fig. 3-2-12 (b)-(d). Furthermore, the high accuracy and reliability of the FE modelling also reflected in the simulation of the UHPFRC beam subjected to four-point flexural bending, for instance, a small region of concrete spalling located at the top of the beam and adjacent to the loading plate as observed in the experiment has been accurately simulated and presented in the compressive damage pattern shown in Fig. 3-2-12 (e).



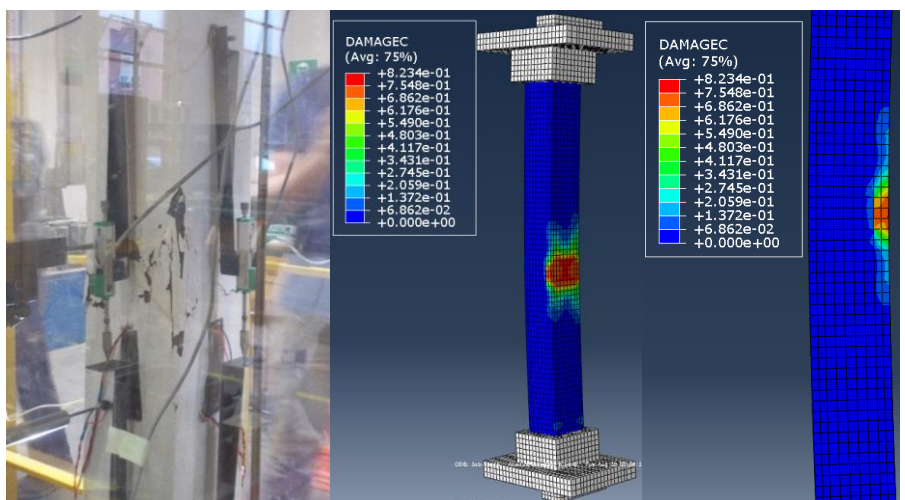
(a)



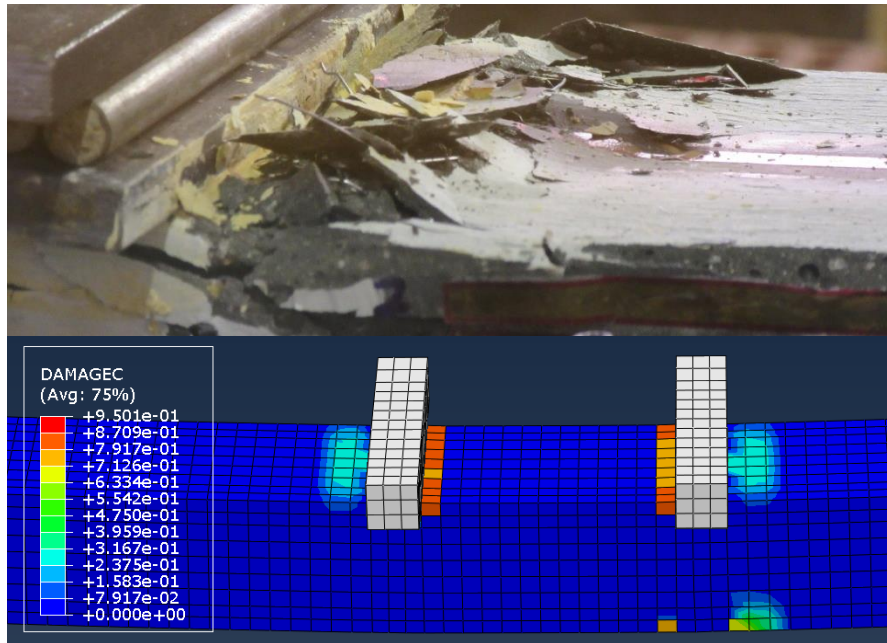
(b)



(c)



(d)

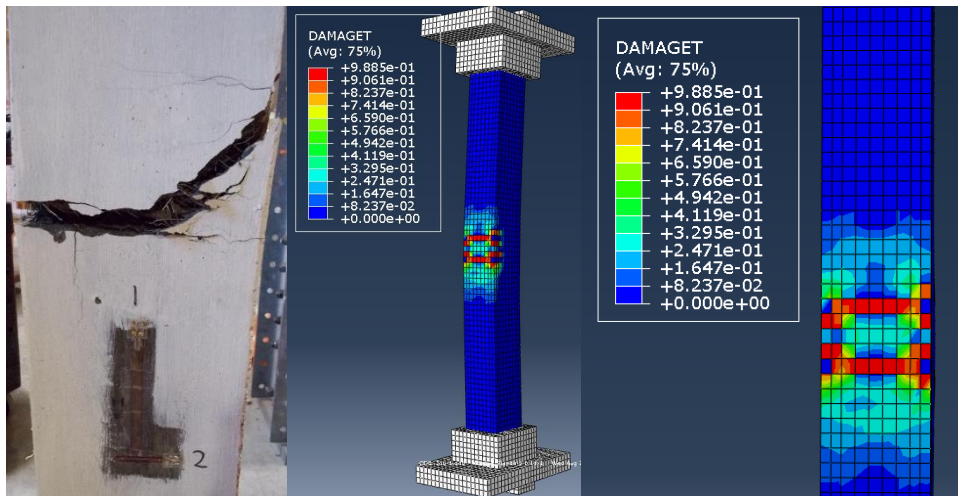


(e)

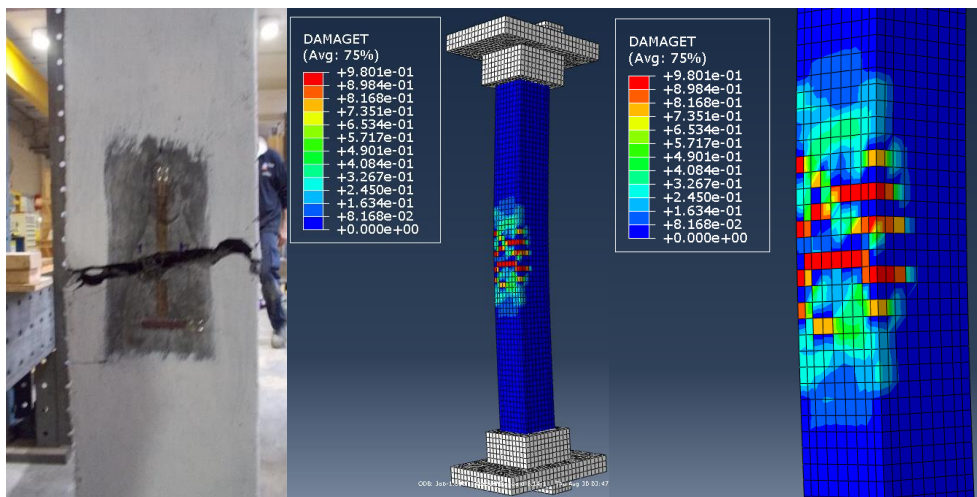
Figure 3-2-12. Comparisons between failure mode and compressive FE cracking pattern: (a) Concentrate column; (b) eccentricity = 35 mm; (c) eccentricity = 50 mm; (d) eccentricity = 85 mm; (e) beam

Similarly, an observation that a single flexural tensile crack occurred at the middle-height region is commonly observed in all eccentrically loaded UHPFRC columns, and hence been successfully captured by the FE model, as presented in Fig. 3-2-13 (a)-(c). In particular, for specimen SL-85, a severe major tensile crack occurred at the middle height of the column with few minor cracks distributed at the concrete surface, and this observation has been appropriately simulated by the FE model and the corresponding tensile cracking pattern is shown in Fig. 3-2-13 (c). Furthermore, two flexural tensile cracks initiated at the bottom of the UHPFRC beam propagated upwards and stopped just underneath the loading plates, which has been reproduced by the FE models and the corresponding tensile cracking pattern is shown in Fig. 3-2-13 (d). In conclusion, FE model exhibited a high accuracy in predicting both the

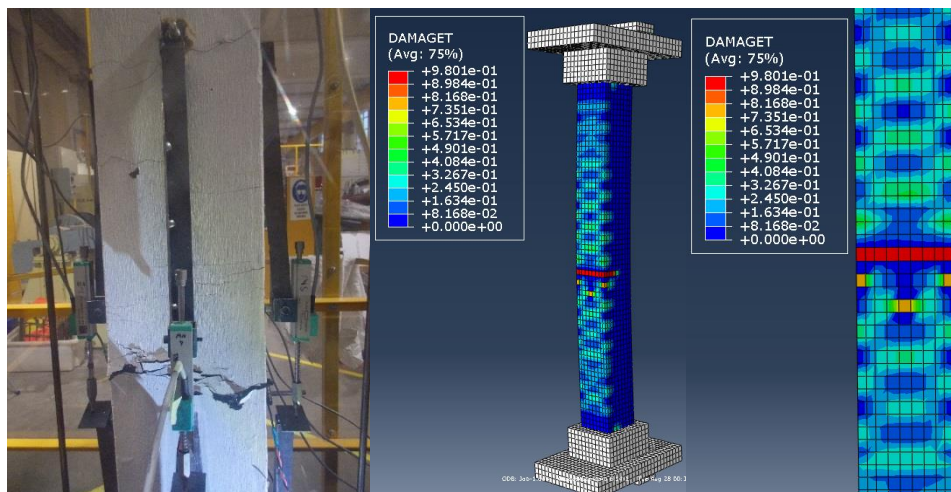
load-middle height deflection responses and the concrete damage (compressive and tensile) patterns, which further highlight the applicability and reliability of the developed FE models.



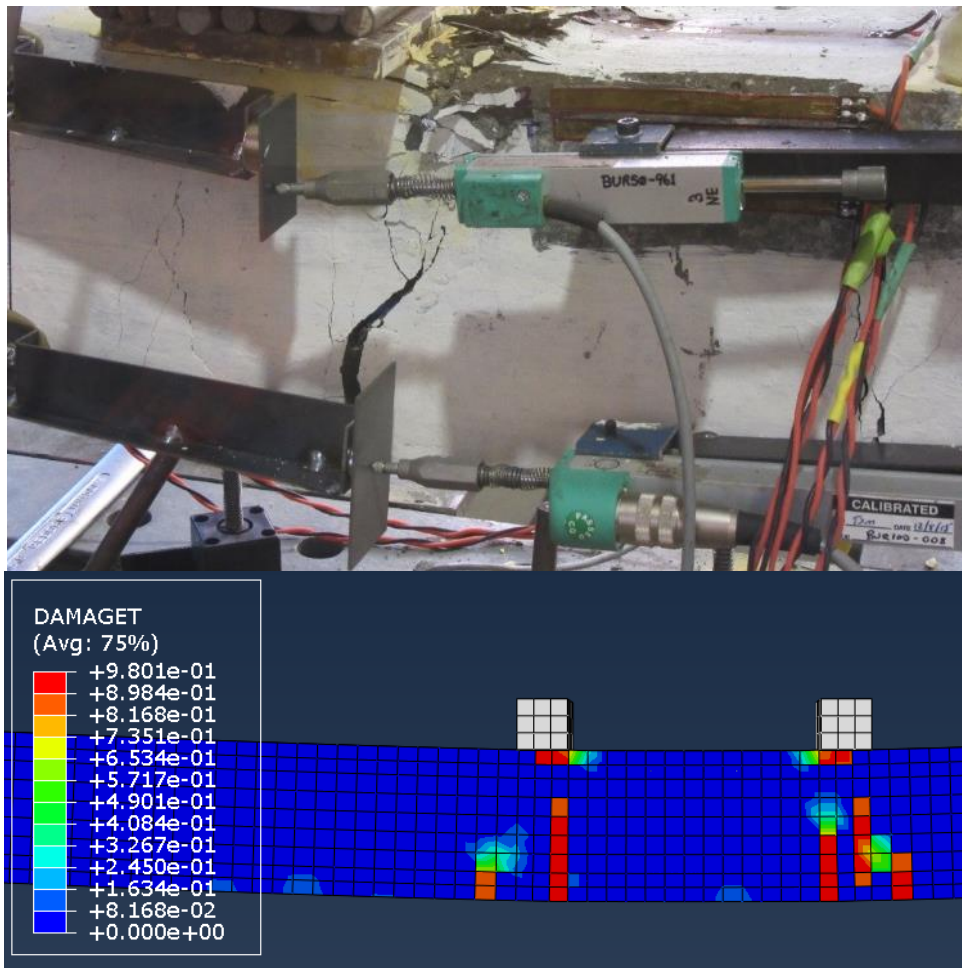
(a)



(b)



(c)



(d)

Figure 3-2-13. Comparisons between failure mode and FE tensile cracking pattern: (a) eccentricity = 35 mm; (b) eccentricity = 50 mm; (c) eccentricity = 85 mm; (d) UHPFRC beam;

### 3.2.5.3. Comparisons of load-moment interaction curves

By combining experimental results of slender UHPFRC columns subjected to eccentric loads (eccentricity from 0 mm to 85 mm) and the beam, a completed load-moment ( $P$ - $M$ ) interaction envelope was generated as shown in Fig. 3-2-14. Figure 3-2-14 also shows the load-moment ( $P$ - $M$ ) interaction envelope obtained from FE simulations and this shows a close agreement

with the test results. It is also worth mentioning that even the loading lines developed from the FE model closely match with the loading lines attained experimentally. For the slender UHPFRC column subjected to concentric load, FE model slightly overestimated (within 4.3%) the load-bearing capacity of the column and this may be due to the edge effects of randomly distributed fibre as well as the inhomogeneous nature of the concrete matrix in a full-scale structure that potentially compromised the compressive strength of the UHPFRC.

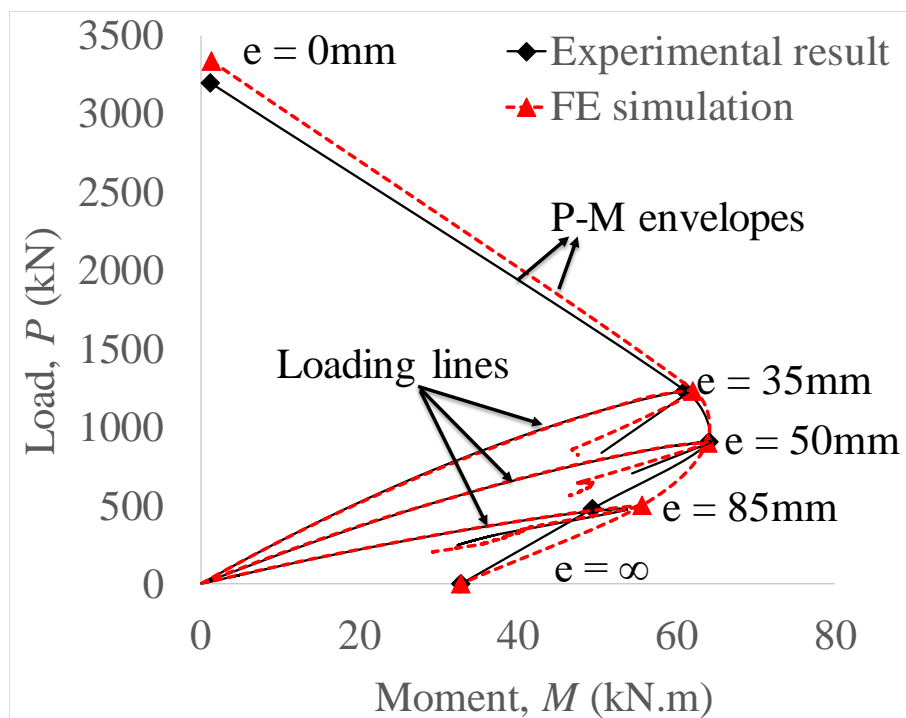


Figure 3-2-14. Load-Moment interaction diagram for UHPFRC slender columns

### 3.2.6. PARAMETRIC STUDY FOR SLENDERNESS EFFECT

An extended parametric study was conducted to investigate the effects of the slenderness of the slender UHPFRC columns. This study was conducted through FE modelling, showing a very good correlation as discussed in section 3.2.5. To conduct the parametric study, the UHPFRC columns with the same cross-section details and material properties of the tested specimens but the length of the columns were increased to study the influence of slenderness on the structural responses.

Specifically, additional four different lengths of UHPFRC columns were introduced in the extended parametric study including 2025 mm, 2450 mm, 2875 mm, and 3300 mm, and corresponding slenderness ratios ( $\lambda$ ) were calculated by complying with the AS 3600 with eq.16-17 defined below:

$$\lambda_n = \frac{kl_u}{r_g} \quad (16)$$

$$r_g = \sqrt{\frac{I}{A}} \quad (17)$$

where  $k$  represents an effective length factor which depends on the boundary and lateral bracing conditions of columns ( $k = 1$  defined for pin to pin condition);  $l_u$  stands for the length of column without supports; and  $r_g$  is defined as radius of gyration, which is also defined by the second moment inertia  $I$  and cross-section area  $A$  of the column. The initial slenderness ratio ( $\lambda$ ) for tested columns was 37, and then the values of slenderness ratio of columns investigated in the parametric study increased to 47, 57, 67, and 77, respectively.

Table 3-2-4. Effects of slenderness ratio ( $\lambda$ ) of the slender UHPFRC columns

Eccentricity	Slenderness ratio	0mm	35mm	50mm	85mm
$P_u$ (kN)	$\lambda=37$	3199.3	1233.9	910.2	480.5
	$\lambda=47$	3212.5	1033	753.4	421.6
	$\lambda=57$	3194.5	832.6	619.1	372.2
	$\lambda=67$	3137.8	662.2	509.7	323.5
	$\lambda=77$	1696.6	532.9	421.6	279.1
$\delta_{l-p}$ (mm)	$\lambda=37$	0.6	14.5	20.5	26.6
	$\lambda=47$	0.4	24.8	31.4	34.6
	$\lambda=57$	0.3	32.4	40.2	50.5
	$\lambda=67$	0.1	42.7	50.6	63.1
	$\lambda=77$	0.8	55.6	62.4	78.9
$M_u$ (kN.m)	$\lambda=37$	1.9	61	64.1	53.6
	$\lambda=47$	1.3	61.7	61.3	50.4
	$\lambda=57$	1.0	56.1	55.9	50.4
	$\lambda=67$	0.3	51.5	51.3	47.9
	$\lambda=77$	1.4	48.3	47.4	45.7
$I_{10}$	$\lambda=37$	2.6	7.1	7.7	7.9
	$\lambda=47$	2.5	6.7	7.6	7.1



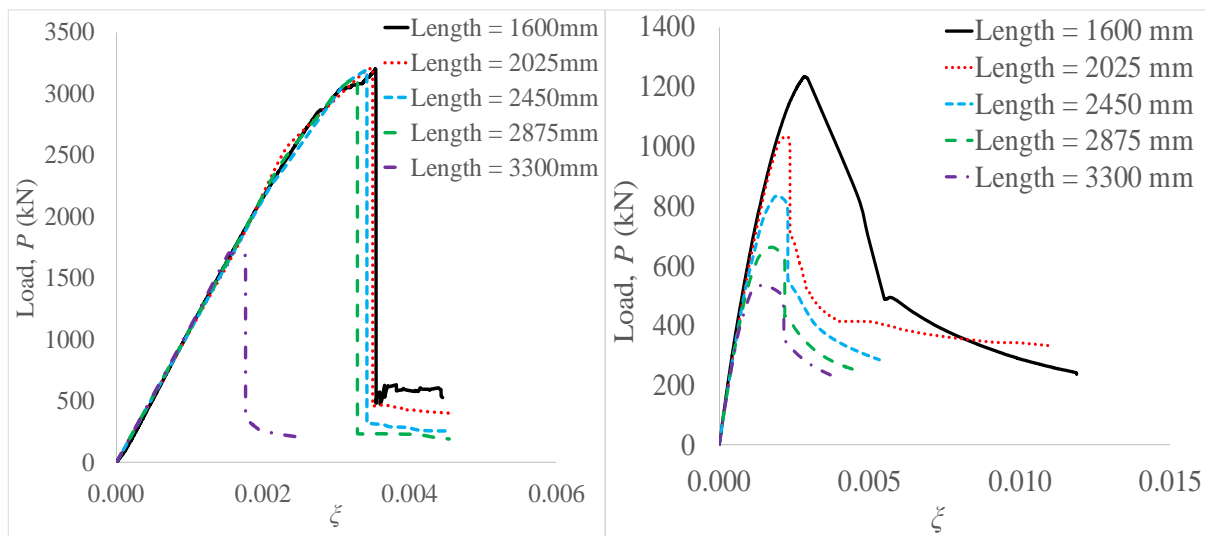
	$\lambda=57$	2.3	6.4	7.6	6.5
	$\lambda=67$	2.1	6.2	7.6	5.5
	$\lambda=77$	2.1	6.2	6.4	5.4
$R_{5,10}$	$\lambda=37$	0	41.7	58	59.2
	$\lambda=47$	0	47.8	60	41.3
	$\lambda=57$	0	33.8	56.4	32.4
	$\lambda=67$	0	18.3	49.8	9.4
	$\lambda=77$	0	10	21.2	0

Numerical results obtained from extended parametric studies are summarized in Table 3-2-4. Generally, comparisons in Table 3-2-4 indicate that the load bearing capacity ( $P_u$ ) decrease with an increase in slenderness ratio, and it is also worth mentioning that the  $P_u$  value of concentrically loaded column decrease significantly when the slenderness ratio ( $\lambda$ ) reached to 77 with a nearly 50% of reduction compared to concentrically loaded columns with a slenderness ratio of 67. Hence, it can be inferred that slenderness ratio ( $\lambda = 77$ ) is a threshold value for a slender UHPFRC column potentially causing global buckling when it is subjected to pure axial load, and the corresponding load bearing capacity is severely reduced. Moreover, comparisons regarding  $\delta_{l-p}$  in Table 3-2-4 show that the corresponding magnitudes increase with an increase in slenderness ratio for eccentrically loaded slender UHPFRC columns. In contrast, the magnitude of  $M_u$  decrease with an increase in slenderness ratio for eccentrically loaded columns, and the balanced condition for the slender UHPFRC column also influenced by the increase in slenderness ratio; for instance, the balance condition for  $\lambda = 37$  is 50 mm, when  $\lambda > 37$  the balanced condition changed to an eccentricity corresponding to 35 mm.

With the results reported in Table 3-2-4, it can be found that the magnitude of  $I_{10}$  gradually decrease with increases in the slenderness ratio, particularly, for eccentrically loaded column with an eccentricity of 85 mm; this is nearly 32% of decrease in the values of  $I_{10}$  due to the slenderness ratio increasing from 37 to 77. Note that, although the values of  $I_{10}$  decrease gradually with increases in slenderness ratio, the areas under the curves of  $P$ - $\xi$  relationships of

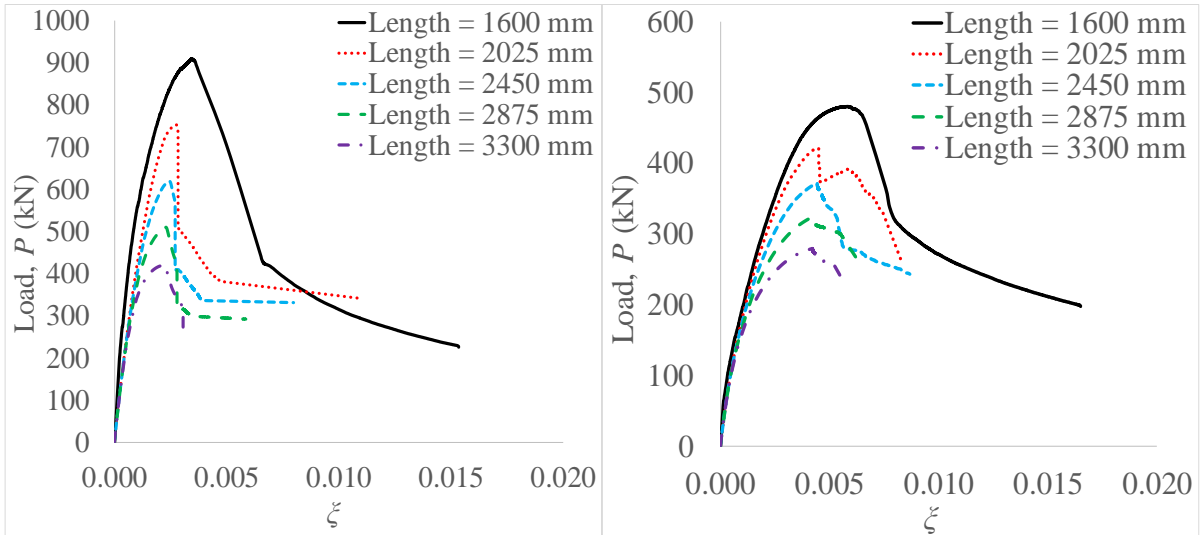
slender columns presented in Fig. 3-2-15 decrease significantly with increases in slenderness ratio, and the magnitudes of areas are strongly correlated to the values of  $R_{5,10}$  reported in the Table 3-2-4. Hence, it is inferred that an increase in slenderness ratio significantly affects the capability of the column to withstand the residual load.

Figures 3-2-16 (a) to (d) illustrate the  $-P-\delta_{lateral}$  relationships of slender columns with varying slenderness ratios subjected to axial loads with different eccentricities. It is worth noting that for eccentrically loaded columns presented in Fig. 3-2-16 (b) to (d), the slope of ascending branch of the curves decreases with an increase in slenderness ratio, and the following descending branch trends to behave like the response of the flexural members with a gradually decreasing load and a relatively large lateral displacement.



(a)

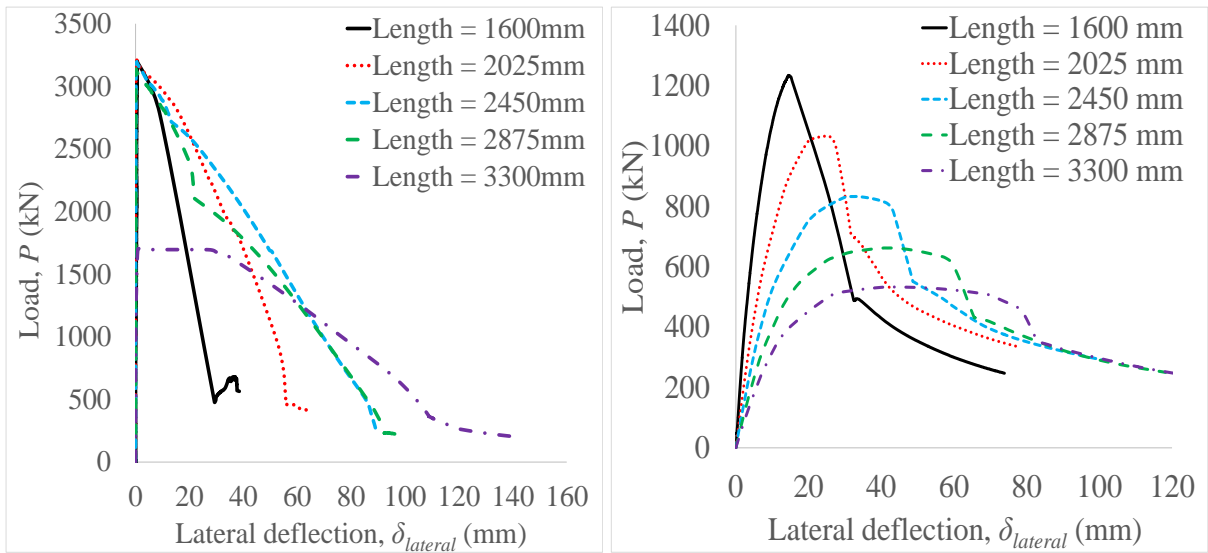
(b)



(c)

(d)

Figure 3-2-15.  $P$ - $\zeta$  relationships of slender columns subjected to axial loads with eccentricities: (a)  $e=0$  mm; (b)  $e=35$  mm; (c)  $e=50$  mm; (d)  $e=85$  mm



(a)

(b)

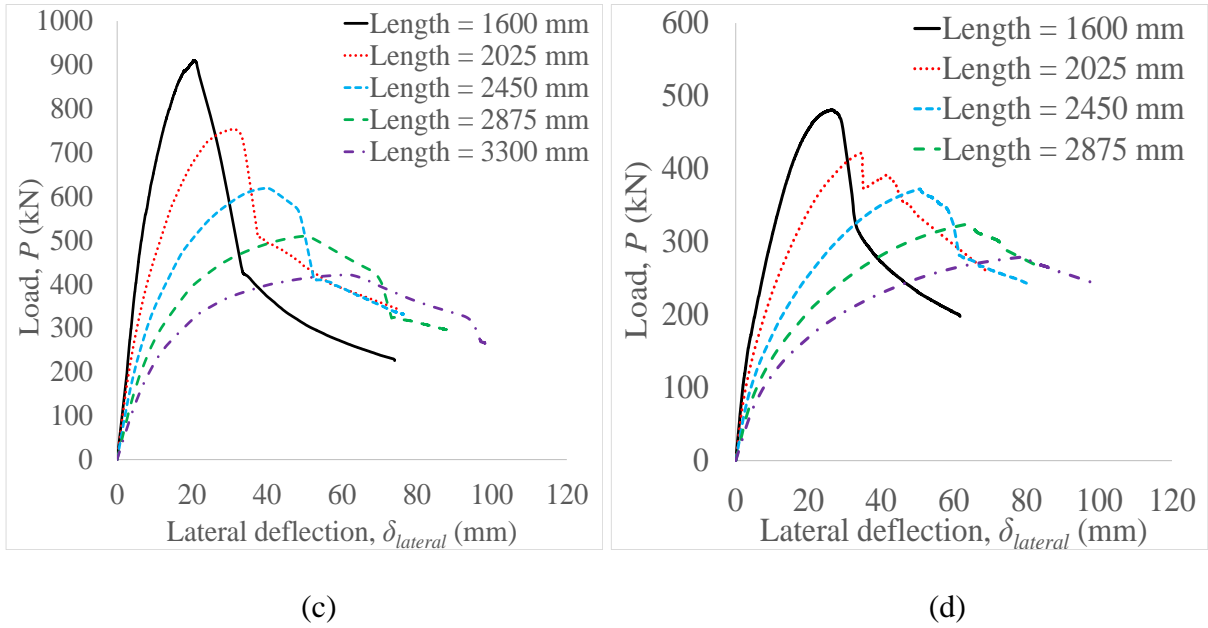


Figure 3-2-16.  $P$ - $\delta_{lateral}$  relationships of slender columns subjected to axial loads with eccentricities: (a)  $e=0$  mm; (b)  $e=35$  mm; (c)  $e=50$  mm; (d)  $e=85$  mm

Axial load-moment ( $P$ - $M$ ) interaction envelopes with various column slenderness ratios are illustrated in Fig. 3-2-17, and the comparisons between the envelopes indicate that increasing column slenderness results in reductions in both the values of eccentric axial loads and corresponding moments. Furthermore, when the slenderness ratio increases up to 77, it is suggested that the axial load is significantly reduced due to the column buckling in the compressive failure range before reaching to the balanced condition. Therefore, in order to maintain a good value for squash load ( $N_{uo}$ ) for the type of slender UHPFRC columns tested in this study, the upper value for slenderness ratio should be restricted to 67.

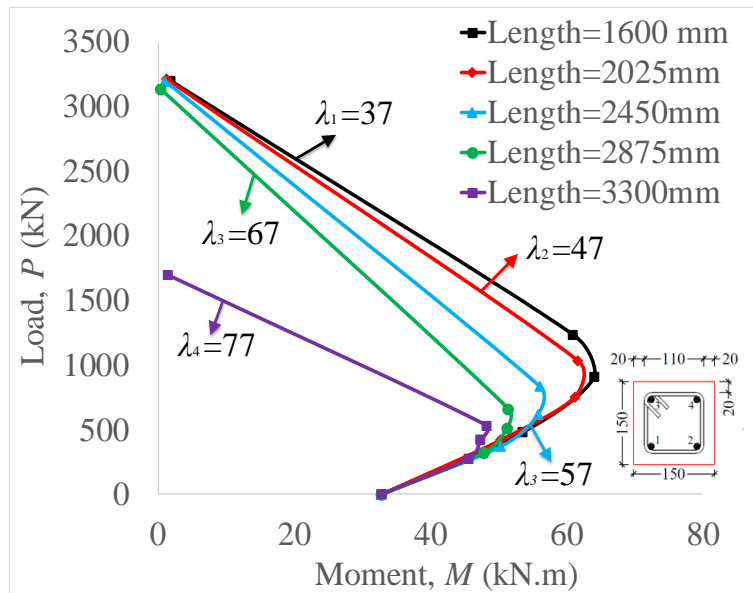


Figure 3-2-17. Load-Moment interaction diagram with different column slenderness ratios

### 3.2.7. CONCLUSION

In this study, the slender UHPFRC columns were analysed using FE model developed by incorporate a novel CDP model and the numerical results are then further extended to conduct a parametric study for investigating the influences of slenderness on the structural responses of the slender UHPFRC columns. The major conclusions from this study are:

- An increase in the eccentricity of the axial load from 0 mm to 35 mm results in a huge drop in the value of the load bearing capacity ( $P_u$ ), with increase with the corresponding values of ductility indices ( $I_5$ ,  $I_{10}$ ) and residual strength factor ( $R_5$ ,  $R_{10}$ ) which indicate an improve ductility.
- In order to conduct the analysis regarding the structural response of the slender UHPFRC columns and the UHPFRC beam, FE models accurately simulated the structural behaviours, damage patterns, and load-moment ( $P-M$ ) relationships with the established material properties of both UHPFRC and steel reinforcements.
- By conducting a parametric study with the developed FE models, the influences of slenderness ratio ( $\lambda$ ) in regards to the structural performance are investigated. It can be

inferred that the magnitudes of  $P_u$ ,  $M_u$ ,  $I_{10}$ , and  $R_{5,10}$  decrease with an increase in the values of  $\lambda$  ; particularly, the increases in the values of  $\lambda$  significantly reduce the residual strength and stability of the column.

- Based on the parametric study conducted numerically, it is worth mentioning that the slenderness ratio ( $\lambda = 77$ ) is a threshold value for the design application of a slender UHPFRC column as the high slenderness potentially causing global buckling when the column is subjected to pure axial load.
- Comparisons of load-moment ( $P$ - $M$ ) generated from the parametric study indicate that the areas under the envelope for the design purpose of the slender UHPFRC columns reduce significantly when the slenderness ratio reached to 77, and this can be inferred that the maximum value for slenderness ratio should be restricted to 67 for this type of UHPFRC columns tested at the University of Adelaide.

### **3.2.8. ACKNOWLEDGEMENTS**

The authors would like to extend their sincere gratitude to the undergraduate students Mr. B Douglas, Miss. A Fairweather, Mr. A Jolly, and Mr. C Reid, who conducted the experiments reported in this paper as a part of their bachelor thesis. The authors would also like to thank the project advisor Mr. Manpreet Singh and Lab Technician Mr. John Ayoub for their expertise in the laboratory and advice. Thanks are due to Dr. M Ridha, and Dr. MS Mohamed Ali for the usage of steel cap arrangement for the column tests.

### 3.2.9. REFERENCE

- [1] Yoo DY, Banthia N. Mechanical properties of ultra-high-performance fiber-reinforced concrete: A review. *Cement and Concrete Composites*. 2016 Oct 1;73:267-80.
- [2] Yoo DY, Yoon YS. A review on structural behavior, design, and application of ultra-high-performance fiber-reinforced concrete. *International Journal of Concrete Structures and Materials*. 2016 Jun 1;10(2):125-42.
- [3] Abrishambaf A, Pimentel M, Nunes S. A meso-mechanical model to simulate the tensile behaviour of ultra-high performance fibre-reinforced cementitious composites. *Composite Structures*. 2019 Aug 15;222:110911.
- [4] Yoo DY, Banthia N, Kang ST, Yoon YS. Effect of fiber orientation on the rate-dependent flexural behavior of ultra-high-performance fiber-reinforced concrete. *Composite Structures*. 2016 Dec 1;157:62-70.
- [5] Yoo DY, Kim S, Kim MJ. Comparative shrinkage behavior of ultra-high-performance fiber-reinforced concrete under ambient and heat curing conditions. *Construction and Building Materials*. 2018 Feb 20;162:406-19.
- [6] Sturm AB, Visintin P, Oehlers DJ, Seracino R. Time-dependent tension-stiffening mechanics of fiber-reinforced and ultra-high-performance fiber-reinforced concrete. *Journal of Structural Engineering*. 2018 Jun 13;144(8):04018122.
- [7] Visintin P, Sturm AB, Mohamed Ali MS, Oehlers DJ. Blending macro-and micro-fibres to enhance the serviceability behaviour of UHPFRC. *Australian Journal of Civil Engineering*. 2018 Jul 3;16(2):106-21.
- [8] Xie T, Fang C, Ali MM, Visintin P. Characterizations of autogenous and drying shrinkage of ultra-high performance concrete (UHPC): An experimental study. *Cement and Concrete Composites*. 2018 Aug 1;91:156-73.

- [9] Kodur V, Solhmirzaei R, Agrawal A, Aziz EM, Soroushian P. Analysis of flexural and shear resistance of ultra high performance fiber reinforced concrete beams without stirrups. *Engineering Structures*. 2018 Nov 1;174:873-84.
- [10] Baby F, Marchand P, Atrach M, Toutlemonde F. Analysis of flexure-shear behavior of UHPFRC beams based on stress field approach. *Engineering structures*. 2013 Nov 1;56:194-206.
- [11] Hung CC, Chueh CY. Cyclic behavior of UHPFRC flexural members reinforced with high-strength steel rebar. *Engineering Structures*. 2016 Sep 1;122:108-20.
- [12] Farzad M, Shafieifar M, Azizinamini A. Experimental and numerical study on an innovative sandwich system utilizing UPFRC in bridge applications. *Engineering Structures*. 2019 Feb 1;180:349-56.
- [13] Yoo DY, Banthia N, Yoon YS. Flexural behavior of ultra-high-performance fiber-reinforced concrete beams reinforced with GFRP and steel rebars. *Engineering Structures*. 2016 Mar 15;111:246-62.
- [14] Tanarlan HM. Flexural strengthening of RC beams with prefabricated ultra high performance fibre reinforced concrete laminates. *Engineering Structures*. 2017 Nov 15;151:337-48.
- [15] Naud N, Sorelli L, Salenikovich A, Cuerrier-Auclair S. Fostering GLULAM-UHPFRC composite structures for multi-storey buildings. *Engineering Structures*. 2019 Jun 1;188:406-17.
- [16] Xia J, Chan T, Mackie KR, Saleem MA, Mirmiran A. Sectional analysis for design of ultra-high performance fiber reinforced concrete beams with passive reinforcement. *Engineering Structures*. 2018 Apr 1;160:121-32.



- [17] Lampropoulos AP, Paschalis SA, Tsioulou OT, Dritsos SE. Strengthening of reinforced concrete beams using ultra high performance fibre reinforced concrete (UHPFRC). *Engineering Structures*. 2016 Jan 1;106:370-84.
- [18] Shin HO, Min KH, Mitchell D. Confinement of ultra-high-performance fiber reinforced concrete columns. *Composite Structures*. 2017 Sep 15;176:124-42.
- [19] Shin HO, Min KH, Mitchell D. Uniaxial behavior of circular ultra-high-performance fiber-reinforced concrete columns confined by spiral reinforcement. *Construction and Building Materials*. 2018 Apr 20;168:379-93.
- [20] Hosinieh MM, Aoude H, Cook WD, Mitchell D. Behavior of ultra-high performance fiber reinforced concrete columns under pure axial loading. *Engineering Structures*. 2015 Sep 15;99:388-401.
- [21] Steven G, Empelmann M. UHPFRC-columns with high-strength longitudinal reinforcement. *BETON-UND STAHLBETONBAU*. 2014 May 1;109(5):344-54.
- [22] Hung CC, Hu FY, Yen CH. Behavior of slender UHPC columns under eccentric loading. *Engineering Structures*. 2018 Nov 1;174:701-11.
- [23] Hung CC, Hu FY. Behavior of high-strength concrete slender columns strengthened with steel fibers under concentric axial loading. *Construction and Building Materials*. 2018 Jun 30;175:422-33.
- [24] Xu J, Wu C, Xiang H, Su Y, Li ZX, Fang Q, Hao H, Liu Z, Zhang Y, Li J. Behaviour of ultra high performance fibre reinforced concrete columns subjected to blast loading. *Engineering Structures*. 2016 Jul 1;118:97-107.
- [25] Fan W, Shen D, Yang T, Shao X. Experimental and numerical study on low-velocity lateral impact behaviors of RC, UHPFRC and UHPFRC-strengthened columns. *Engineering Structures*. 2019 Jul 15;191:509-25.

- [26] Fan W, Xu X, Zhang Z, Shao X. Performance and sensitivity analysis of UHPFRC-strengthened bridge columns subjected to vehicle collisions. *Engineering Structures*. 2018 Oct 15;173:251-68.
- [27] Astarlioglu S, Krauthammer T. Response of normal-strength and ultra-high-performance fiber-reinforced concrete columns to idealized blast loads. *Engineering structures*. 2014 Mar 1;61:1-2.
- [28] Fang C, Mohamed Ali MS, Sheikh AH, Singh M. Numerical and Finite-Element Analysis of Short Ultrahigh-Performance Fiber-Reinforced Concrete Columns. *Journal of Structural Engineering*. 2019 Aug 9;145(10):04019111.
- [29] Douglas B, Fairweather A, Jolly A, Reid C. Investigation into the behaviour of UHPFRC in slender columns. (2015). University of Adelaide. Adelaide. Australia.
- [30] Attard MM, Foster SJ. Ductility of high strength concrete columns. University of New South Wales; 1995.
- [31] Razvi S, Saatcioglu M. Confinement model for high-strength concrete. *Journal of Structural Engineering*. 1999 Mar;125(3):281-9.
- [32] Singh M, Sheikh AH, Ali MM, Visintin P, Griffith MC. Experimental and numerical study of the flexural behaviour of ultra-high performance fibre reinforced concrete beams. *Construction and Building Materials*. 2017 May 1;138:12-25.
- [33] Singh M, Sadakkathulla M, Sheikh AH, Griffith MC, Visintin P. Structural behaviour of ultra high performance fibre reinforced concrete beams with steel and polymer bar reinforcement. In: *Proceedings of The 11th fib International PhD Symposium in Civil Engineering*. 2016. pp.287-294
- [34] Mahmud GH, Yang Z, Hassan AM. Experimental and numerical studies of size effects of Ultra High Performance Steel Fibre Reinforced Concrete (UHPFRC) beams. *Construction and Building Materials*. 2013 Nov 1;48:1027-34.

- [35] Lubliner J, Oliver J, Oller S, Oñate E. A plastic-damage model for concrete. International Journal of solids and structures. 1989 Jan 1;25(3):299-326.

**THIS PAGE HAS BEEN LEFT INTENTIONALLY BLANK**

## **CHAPTER 4. Experimental and numerical investigations on concrete filled carbon FRP tube (CFRP-CFFT) columns manufactured with ultra-high-performance fibre reinforced concrete**

### **Introduction**

This chapter contains the paper entitled “Experimental and numerical investigations on concrete filled carbon FRP tube (CFRP-CFFT) columns manufactured with ultra-high-performance fibre reinforced concrete”. It presents both experimental and numerical investigations for studying the structural responses of concrete filled carbon FRP tube (CFRP-CFFT) UHPFRC columns subjected to concentric and eccentric axial loads. Subsequently, finite element (FE) analysis was also conducted to simulate the behaviours of these columns along with generating the corresponding damage patterns of UHPFRC filled CFRP tubes.

### **List of manuscripts**

Fang, C., M. S. Mohamed Ali, and A. H. Sheikh. 2019. “Experimental and numerical investigations on concrete filled carbon FRP tube (CFRP-CFFT) columns manufactured with ultra-high-performance fibre reinforced concrete.” Submitted on *composite Structures* (under review).

# Statement of Authorship

Title of Paper	Experimental and numerical investigations on concrete filled carbon FRP tube (CFRP-CFFT) columns manufactured with ultra-high-performance fibre reinforced concrete
Publication Status	<input type="checkbox"/> Published <input type="checkbox"/> Accepted for Publication <input checked="" type="checkbox"/> Submitted for Publication <input type="checkbox"/> Unpublished and Unsubmitted work written in manuscript style
Publication Details	Fang, C., Mohamed Ali, M. S., Sheikh, A. H. (2019). Experimental and numerical investigations on concrete filled carbon FRP tube (CFRP-CFFT) columns manufactured with ultra-high-performance fibre reinforced concrete. Submitted to Composite structures.

## Principal Author

Name of Principal Author (Candidate)	Chengfeng Fang		
Contribution to the Paper	Performed analysis on all specimens, interpreted data, wrote manuscript		
Overall percentage (%)	80%		
Certification:	This paper reports on original research I conducted during the period of my Higher Degree by Research candidature and is not subject to any obligations or contractual agreements with a third party that would constrain its inclusion in this thesis. I am the primary author of this paper.		
Signature		Date	23/09/2019

## Co-Author Contributions

By signing the Statement of Authorship, each author certifies that:

- i. the candidate's stated contribution to the publication is accurate (as detailed above);
- ii. permission is granted for the candidate to include the publication in the thesis; and
- iii. the sum of all co-author contributions is equal to 100% less the candidate's stated contribution.

Name of Co-Author	Mohamed Ali Mohamed Sadakkathulla		
Contribution to the Paper	Supervised development of experiment program, helped in data interpretation and manuscript evaluation		
Signature		Date	23/09/2019

Name of Co-Author	Associate Professor Abdul H. Sheikh		
Contribution to the Paper	Supervised development of finite element simulation, helped in data interpretation and manuscript evaluation		
Signature		Date	23/09/2019

**Experimental and numerical investigations on concrete filled carbon FRP tube (CFRP-CFFT) columns manufactured with ultra-high-performance fibre reinforced concrete**

Fang, C.<sup>1</sup>, Mohamed Ali, M.S.<sup>1</sup>, Sheikh, A.H.<sup>1</sup>

<sup>1</sup>School of Civil, Environmental and Mining Engineering, The University of Adelaide, SA  
5005, Australia

**ABSTRACT:**

This study aims to investigate the structural responses of five concrete filled carbon FRP tube (CFRP-CFFT) columns manufactured with ultra-high-performance fibre reinforced concrete (UHPFRC) under concentric or eccentric loading protocols with eccentricities ranging from 0.067D (depth) to 0.57D (depth). One CFRP-CFFT UHPFRC beam with the same cross-section configuration used for columns was subjected to four-point flexural bending. Furthermore, finite element (FE) analysis incorporating concrete damage plasticity (CDP) model was also conducted to simulate the behaviours of CFRP-CFFT UHPFRC members; the corresponding load-axial displacement and load-lateral deflection relationships were numerically generated to compare with the experimental results. FE simulations exhibit a high correlation compared to experimental results, which further highlights the applicability of FE modelling in predicting the structural response of the CFRP-CFFT UHPFRC members. A load-moment ( $P-M$ ) interaction envelope was generated from the FE modelling to facilitate the development of a design guideline of CFRP-CFFT UHPFRC columns subjected to axial load with a varying eccentricity.

**Keywords:** Concrete filled carbon FRP tube (CFRP-CFFT); Column; Concentric and eccentric loads; Finite-element analysis (FEA); Ultra-high performance fibre reinforced (UHPFRC)

## **4.1. INTRODUCTION**

High-performance based designs are increasingly being adopted to replace deteriorating infrastructures in order to cater for the increased urbanization and the limited availability of land in many cities. Limitations in mechanical strengths and material durability of conventional concrete limit its applications to fulfil requirements of the high-performance based design such as the needs for concrete with a high strength to weight ratio, higher seismic resistance, corrosion resistance from the chlorine penetration, and these shortcomings can be addressed with the development of Ultra-high performance fibre reinforced concrete (UHPFRC). With the rapid advancement in concrete material technology, UHPFRC, a specially formulated cement-based composite generally characterized with superior mechanical properties (with compressive strength greater than 150 MPa and ductile tensile strength characteristics), exceptional ductility, high durability and corrosion resistance and hence it possesses enormous potential in the high-performance based designs. Recent research on UHPFRC deals largely with the effects of fibre orientation on its tensile or flexural behaviour [1-5], applications of retrofitting reinforced concrete (RC) structural members [6-11], performance of UHPFRC member subjected to blasts or impact loads [12-16] and flexural behaviours of UHPFRC beams [6, 7, 8, 11,14]. These studies demonstrated that using UHPFRC with an optimal fibre content and type for constructing structural members would prevent concrete spalling and achieve significant enhancement in structural performances such as shear capacity [3, 5, 7-11], flexural moment capacity [6-9, 11, 12], and high impact resistance [12-16] compared to that of structures made with conventional concrete.

Due to its superior material characteristics, UHPFRC is also more suitable for designing heavily loaded columns of high-rise structures compared to conventional construction materials [17]. Recently, a number of studies were undertaken to explore the structural



behaviour of UHPFRC columns under axial loading conditions [17-23]. A life-cycle cost study regarding the application of UHPFRC columns in high-rise buildings was conducted by Empelmann et al. [17], and this involve comparing both energy demand and total costs among high strength concrete column, UHPFRC column, and composite column; this study showed that UHPFRC is highly economical for manufacturing axially loaded members. Additionally, an empirical model to predict the load bearing capacity for concentrically loaded UHPFRC column was proposed, and the model was further improved in a later study conducted by Steven and Empelmann [18]. Other research efforts have been focussed on exploring the axial loading behaviour on short UHPFRC columns by differing the transverse reinforcement pattern, stirrup spacing, and fibre volume fraction [19-21]. Examinations of structural performance for UHPFRC columns studied by Hosinieh et al. [19] indicated that reducing the spacing of transverse reinforcement led to significant enhancements in the peak strength, post-peak ductility, and toughness index of the UHPFRC columns, while increasing the confinement by changing the tie configuration only improved the total toughness index of the columns. Similar observations were also reported in the studies conducted by Shin et al. [20, 21], wherein the inclusion of steel fibres was found to be efficient in controlling the spalling of concrete cover and in improving the core concrete strength and post-peak ductility of UHPFRC columns with a high confinement.

Columns in practice normally subjected to combined axial compression and flexural bending moment at the same time. To study the structural behaviours of UHPFRC columns under both axial compression and flexural bending moment, Steven and Empelmann [18] conducted seven columns subjected to axial loads with an eccentricity ranged from 5 mm to 75 mm, and the corresponding load-moment interaction relationship and robustness index were investigated. Furthermore, Aarup et al. [22] experimentally studied the structural performances of 57 slender

UHPFRC columns under concentric or eccentric axial loads by varying a range of parameters (slenderness, shape, size, reinforcement, and fibre content). Additionally, they also derived formulas by suitably modifying classical methods for RC and they were able to predict the load bearing capacities for the columns under different loading protocols. Hung et al. [23] investigated the behaviour of slender UHPFRC columns under eccentric loading condition, and importantly, it has been found that the moment magnifier approach stipulated by ACI-318 (2014) yields reasonable predictions for the moment capacity of the tested slender UHPFRC columns.

Replacing normal strength concrete (NSC) by the UHPFRC in the construction of the high-performance based designs of columns allows a significant reduction in both dimensions of structural members, construction period, and life-cycle costs [24]. Nevertheless, concerns have been raised regarding the stability and robustness of the UHPFRC columns with the occurrence of early concrete spalling that potentially compromise the load bearing capacity and rigidity of these columns. Therefore, there is a need to address this challenge of using UHPFRC for building column with it externally confined by fibre reinforced polymer (FRP) which is well recognized with its superior strength that can be fabricated as concrete-filled FRP tubes (CFRP-CFFTs) to provide an easy solution for preventing early concrete spalling failure and subsequently to enhance the load bearing capacity and ductility of the columns [25]. However, it is recognized that there is a significant lack of investigation in structural response of CFRP-CFFTs UHPFRC columns conducted experimentally, and limited numerical modelling to predict their structural behaviour.

To fill this research gap, therefore, an experimental study was conducted in this research for exploring the structural performances of CFRP-CFFT UHPFRC columns under axial loads with differing the eccentricities of loading. Moreover, a CFRP-CFFT UHPFRC beam was also tested under four-point flexural bending to investigate its flexural bending capacity and hence to generate an axial load-moment ( $P$ - $M$ ) interaction relationship. In addition to these tests, a detailed of finite element (FE) analysis was carried out to develop a numerical modelling method in conjunction with concrete damage plasticity (CDP) model and Hashin's damage models for FRP provided by a commercially available FE software ABAQUS to reproduce the structural responses as well as concrete failure modes for all CFRP-CFFT UHPFRC members. Subsequently, the results obtained from the FE models are then compared and validated against the test results.

## **4.2. EXPERIMENTAL PROGRAM**

Experimental program was carried out in two phases; firstly, the tests to evaluate material properties and then the tests to evaluate structural behaviours of columns and the beam. Specifically, material tests were conducted to obtain stress-strain responses of unconfined UHPFRC under uniaxial compression or direct tension, and mechanical properties of the FRP fabric used for manufacturing the FRP tube and this was characterized by conducting direct tensile tests on FRP coupons. To obtain the stress-strain relationship of UHPFRC under lateral confinement pressure induced by the transverse reinforcements, a uniaxial compression test was conducted on UHPFRC cylinders subjected to uniform lateral confinement pressure. Hence, these obtained material properties were used as the fundamental inputs for the finite element (FE) analysis to simulate the behaviours of UHPFRC members. The major objectives for conducting structural member tests on UHPFRC members were to study the structural responses of CFRP-CFFT UHPFRC columns loaded either concentrically or eccentrically and

to generate a load-moment ( $P$ - $M$ ) interaction envelope for developing design guidelines for CFRP-CFFT UHPFRC columns.

#### 4.2.1. UHPFRC mixture and mixing procedure

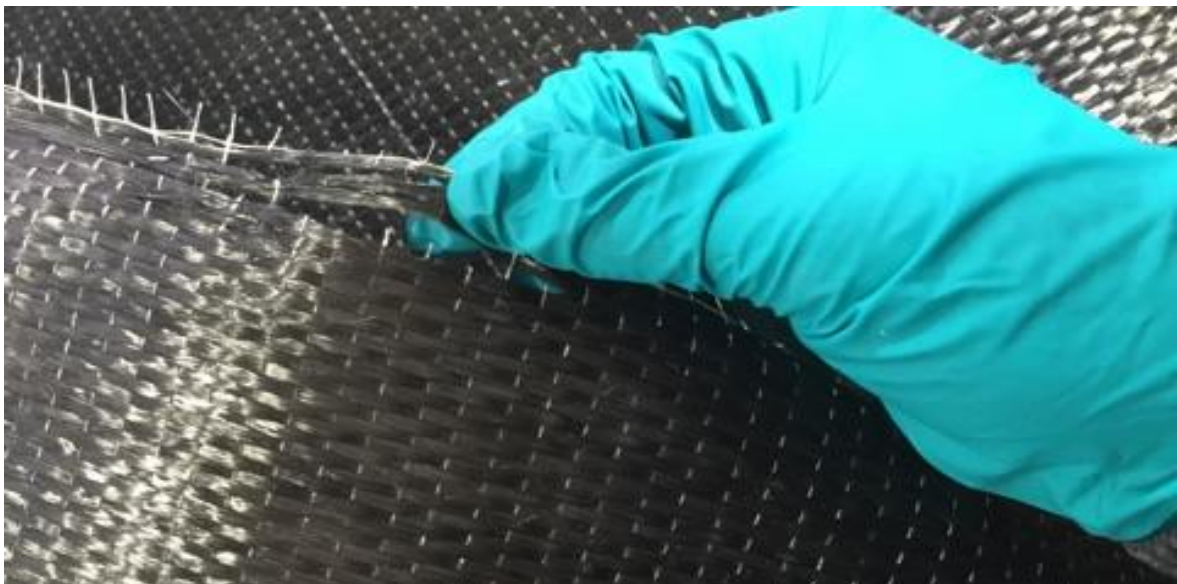
To manufacture UHPFRC, sulphate resistant cement (SRC) and silica fume (SF) were used as the binder and clean washed river sand was used as the only aggregate. The other ingredients used are water and high range water reducer (HRWR) admixture. The corresponding mix ratios by weight are sand: SRC: SF: water: HRWR = 1: 0.79: 0.21: 0.120: 0.061. As depicted in Fig. 4-1(a), a total volume of 1% steel fibre consisting of 75% of micro straight fibres and 25% of Hooked-end fibres with the weight proportions of 0.026 and 0.0776 were added to the mixture to attain a ductile tensile behaviour, and the corresponding material properties of both micro straight fibres and Hook-end fibres are presented in Table 4-1. Initially, all the dry ingredients were mixed thoroughly in a pan mixer for 5 minutes. After that, water and high range water reducer (HRWR) were added and the wet mixture was mixed further to achieve a good flowability and then steel fibres were added and the mixing was continued for a few more minutes to ensure a uniform distribution of the fibres.

Table 4-1. Steel fibre properties

Fibre type	Diameter, $d_f$ (mm)	Length, $L_f$ (mm)	Aspect ratio, $L_f/d_f$	Tensile strength, $f_{ft}$ (Mpa)	Young's modulus of steel fibres, $E_{ft}$ (Mpa)
Micro fibre: Straight	0.2	13	65	2850	210000
Hook end Dramix 3D-65/35 BG	0.55	35	65	1345	210000



(a)



(b)

Figure 4-1. Manufacture materials of CFRP-CFFT UHPFRC members: (a) micro steel fibre and macro steel fibre; (b) CFRP fabric

#### 4.2.2. FRP tubes fabrication

To fabricate the concrete-filled FRP tubes (CFRP-CFFTs) for CFRP-CFFT UHPFRC structural members, a high strength carbon fibre fabric featured with a predominantly unidirectional pattern as shown in Fig. 4-1 (b) was used. Although such a fabric has excellent

tensile strength along the fabric direction, it has negligible tensile resistance along the direction perpendicular to the fibre direction.

### **4.2.3. Material tests**

Specimen configuration and testing setup regarding material tests are detailed in Fig. 4-2, and the corresponding test results are shown in Fig. 4-3. The details are as follows:

#### ***4.2.3.1. Uniaxial compression and direct tensile tests on UHPFRC***

As stipulated by AS 1012 (2014), three cylinders with a 100 mm in diameter and 200 mm in height were casted and tested under uniaxial compression with a loading rate of 0.05 mm/minutes for determining of compressive stress-strain response. One 30 mm long strain gauge was vertically placed at the middle region of the cylinder to obtain the young's modulus ( $E_c$ ), peak strain ( $\epsilon_c$ ) of UHPFRC, and one 10 mm strain gauge was perpendicularly placed to the 30 mm strain gauge to measure the corresponding Poisson's ratio ( $\nu$ ) of UHPFRC. Two LVDTs were placed at corners of the Universal test machine (Seidner) to generate the complete compressive stress-strain ( $\sigma_c - \epsilon_c$ ) response, as shown in Fig. 4-2 (a). To determine the direct tensile behaviours of UHPFRC, an unnotched dog-bone specimen shown in Fig. 4-2 (b) with dimensions of 120 mm×120 mm at the middle height of the specimen were tested by applying the loading at the rate of 0.05 mm/min. One LVDTs with a gauge length of 300 mm was placed at the middle region of the dog-bone for determining the tensile stress-strain ( $\sigma_{ct} - \epsilon_{ct}$ ) response from elastic to post-cracking stage, and a typical tensile cracking failure was observed in the middle region of the dog-bone specimens, as shown in Fig. 4-2 (b). From these tests, the compressive strength ( $f_c'$ ), tensile strength ( $f_t$ ), and Young modulus ( $E_c$ ) of UHPFRC are estimated to be 145.2 MPa, 5.9 MPa, and 32.3 GPa, respectively, and the corresponding compressive and tensile strains ( $\epsilon_c$  and  $\epsilon_t$ ) at the peak strengths are 4847 and 939 micro strain,

respectively. Furthermore, the corresponding stress-strain ( $\sigma_c - \varepsilon_c$  and  $\sigma_{ct} - \varepsilon_{ct}$ ) responses of UHPFRC under compression and tension are illustrated in Fig. 4-3(a) and (b).

#### **4.2.3.2. Flat FRP coupon test**

In-plane tensile material properties of the carbon FRP (CFRP) tube was obtained by conducting tests on three flat CFRP coupons. By adhering to ASTM D3039/D3039M (2017) [26], each coupon was prepared and fabricated by three layers of CFRP sheets that was impregnated with the epoxy-based saturant. As shown in Fig. 4-2 (c), the CFRP coupons have dimensions of 300 mm in length, 15 mm in width, and an average thickness of 1.32 mm. These coupons were placed in stainless steel mould in longitudinal direction and cured for about 24 hours, and then two aluminium tabs with dimensions of 15 mm×80 mm was bonded to the FRP coupon at both ends. After an additional 7 days of curing at the ambient temperature, a strain gauge with a gauge length of 20 mm was placed at the middle region of the coupon for measuring the corresponding stress-strain relationship. In accordance with ASTM standard D3039/D3039M (2017), the fabricated CFRP coupons were tested under direct tension in the machine, as shown in Fig. 4-2 (c), and corresponding linear-elastic stress-strain ( $\sigma_{FRP,t} - \varepsilon_{FRP,t}$ ) response shown in Fig. 3 (c) was obtained to establish the ultimate tensile strength ( $f_{tu}$ ), ultimate tensile strain ( $\varepsilon_{tu}$ ), elastic modulus ( $E_f$ ), and hoop fibre rupture strain ( $\varepsilon_{hr}$ ), as listed in Table 4-2. Note that the tested ultimate tensile strength and strain were within the range of the manufacturer-supplied properties of the carbon fibres provided in the same table.

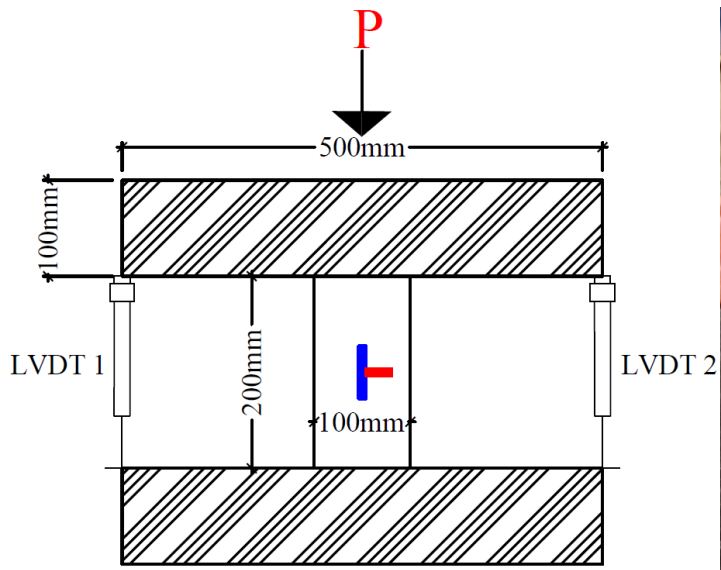
Table 4-2. Properties of carbon fibres used as FRP tube

Provided by manufacturer			Obtained from coupon tests			
Nominal fibre thickness, $t_{frp}$ (mm/ply)	Ultimate tensile strength, $f_{frp}$ (Mpa)	Elastic Modulus, $E_{frp}$ (Mpa)	Ultimate tensile strength, $f_{tu}$ (Mpa)	Ultimate tensile strain, $\epsilon_{tu}$ (%)	Elastic Modulus, $E_f$ (Mpa)	Hoop fibre rupture strain, $\epsilon_{hr}$ (%)
0.167	1720-3690	152000-580000	2142.08	1.01	211494.95	0.71

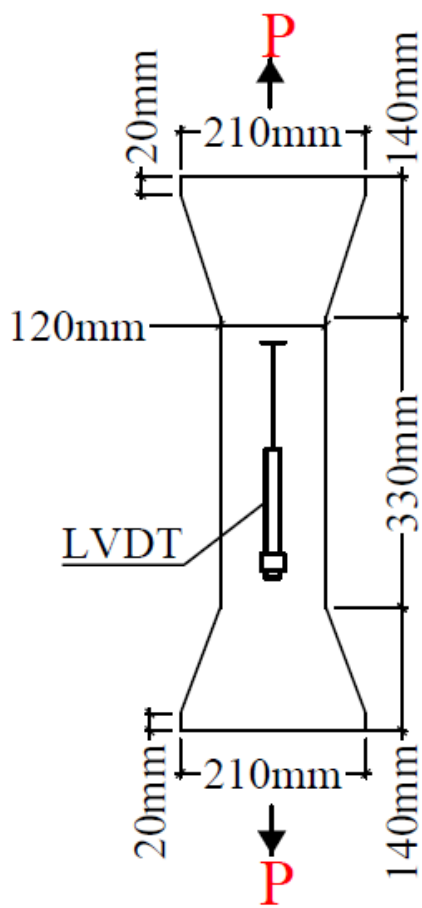
#### 4.2.3.3. Uniaxial compression tests on actively confined UHPFRC

In order to explore the compressive stress-strain ( $\sigma$ - $\epsilon$ ) response of UHPFRC with lateral confinement pressure induced by stirrups, three identical cylinders with a diameter of 63.5 mm and a height of 120 mm were placed in the Hoek cell and tested in the *Instron* machine complying with AS 2193 (2017), as presented in Fig. 4-2 (d). According to the confinement model for high strength concrete (HSC) proposed by Razvi and Saatcioglu [27], the lateral confinement stress ( $\sigma_2 = \sigma_3 = 5.80$  MPa) provided by transverse reinforcement was estimated as 5.80 MPa, and this uniformly distributed lateral pressure was applied through the hydraulic oil filled in the Hoek cell. Furthermore, the axial displacement ( $\delta_{axial}$ ) and load ( $P$ ) response of the confined cylinder was experimentally extracted from the tests, as presented in Fig. 4-3 (d), and the  $\delta_{axial} - P$  response was then used in the FE model to define the material property of core concrete inside the steel stirrups.

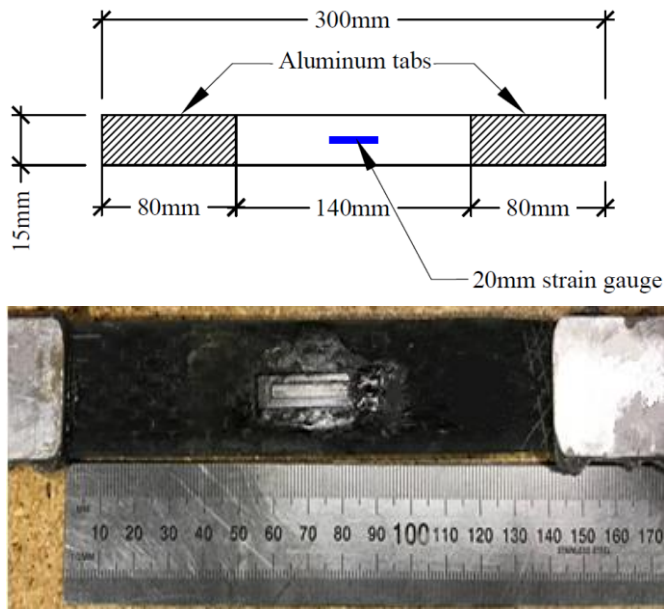




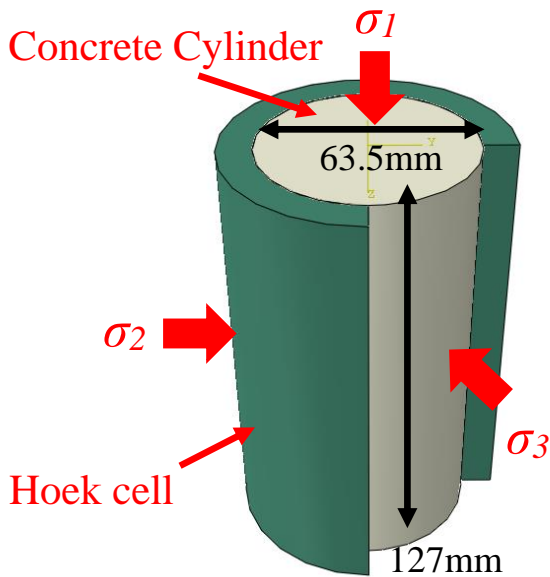
(a)



(b)



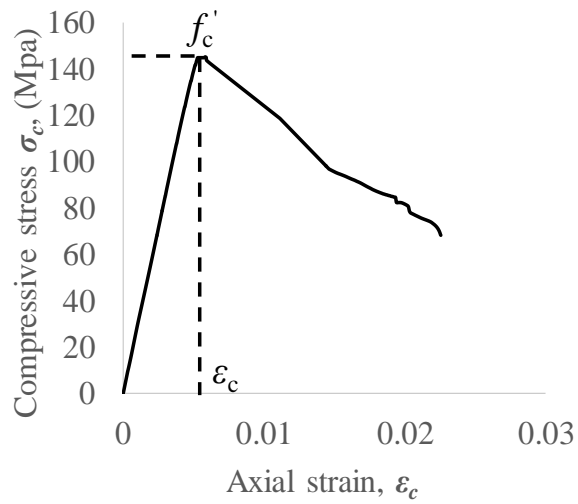
(c)



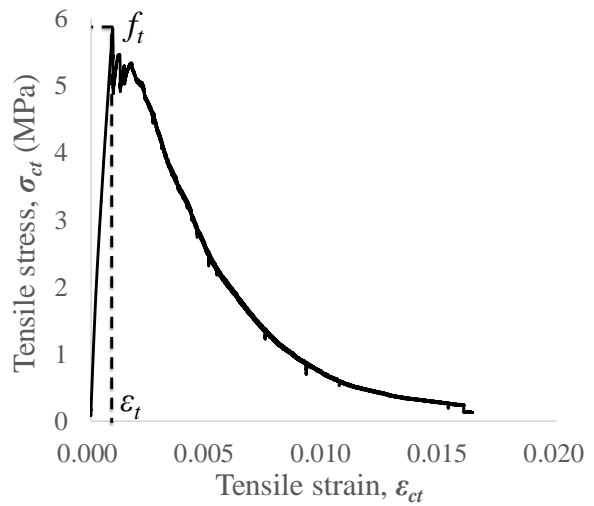
Hoek cell providing uniform lateral stress:  
 $\sigma_1 \gg \sigma_2, \sigma_2 = \sigma_3$

(d)

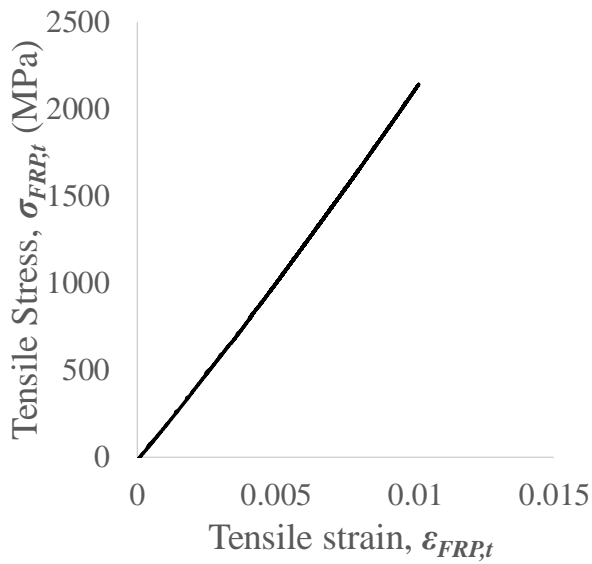
Figure 4-2. Material tests: (a) uniaxial cylinder compressive tests and compressive failure mode; (b) uniaxial tensile tests and cracking pattern under direct tension; (c) direct tensile tests for CFRP coupons; (d) uniaxial cylinder compressive tests on UHPFRC with active confinement provided by Hoek cell



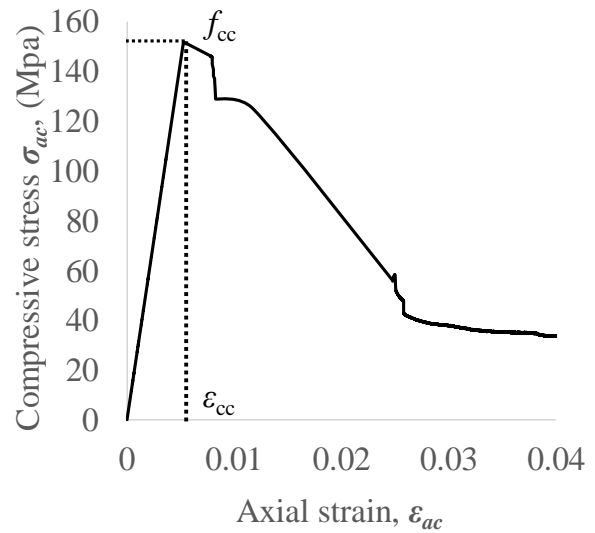
(a)



(b)



(c)



(d)

Figure 4-3. Material properties of: (a) compressive stress-strain response for unconfined UHPFRC; (b) tensile characterizations of UHPFRC; (c) tensile stress-strain ( $\sigma_{FRP,t} - \epsilon_{FRP,t}$ ) response for CFRP; (d) compressive stress ( $\sigma_{ac}$ ) - strain ( $\epsilon_{ac}$ ) responses active confined UHPFRC

#### 4.2.4. Structural member tests

##### 4.2.4.1. Specimen detail

All CFRP-CFFT UHPFRC members were constructed with the same batch of the UHPFRC mix to ensure the consistency of experiments, and an additional 1 % by volume of steel fibres were added to the concrete mix to comply with the stipulations of ASTM A820 (2016) [28]. Details of structural member tests in conjunction with the corresponding instrumentation and test setups are shown schematically in Figs. 4-4 and 4-5. All UHPFRC members were featured with a square cross-section with a dimension of 150 mm and corner radius of 20 mm, as exhibited in Fig. 4-4 (a). Furthermore, both the columns and the beam were reinforced by four longitudinal steel rebars with a diameter of 12 mm and 8 mm transverse reinforcements with a dimension of 110 mm, and transverse reinforcements were placed at a spacing of 85 mm with a clear cover of 20 mm, as shown in Fig. 4-4 (a). To manufacture the CFRP-CFFT tubes for UHPFRC members, a varied layering process was employed: 2 layers of longitudinal CFRP strips followed by 2 circumferential FRP layers on the top ( $90^\circ/90^\circ/0^\circ/0^\circ$ ), and overlap layers with a length of 142 mm were used at the two corners of the column to prevent debonding in the hoop direction, as presented in Fig. 4-4 (a). This FRP layering method proposed by Malik and Foster [29] aims to activate the internal longitudinal FRP fibre to sustain the tensile stress induced by the flexural bending, and hence to prevent the buckling of the column and to mitigate stress concentration of the circumferential CFRP layers. Specimen designations of the CFRP-CFFT UHPFRC members are detailed in Table 4-3: the first letter “C” denotes “Confined” and the second letter “C” stands for “Column”. The following numbers indicate the eccentricity of the axial load acting on the column, but a notation “beam” was used to describe the CFRP-CFFT UHPFRC beam under four-point bending. For example, “CC-35”

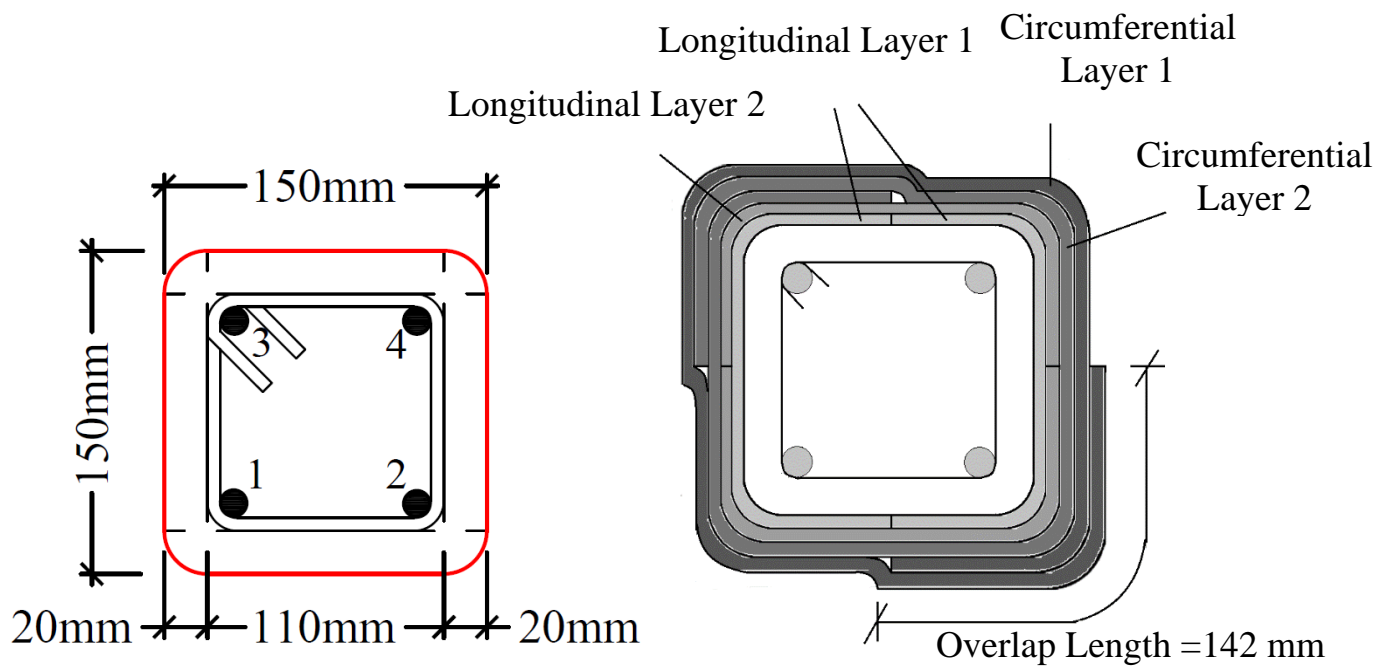
denotes that the confined CFRP-CFFT UHPFRC column was axially loaded with an eccentricity of 35 mm.

#### ***4.2.4.2. Instrumentation***

All five CFRP-CFFT UHPFRC columns with a total height of 1000 mm were tested in the Amsler machine under axial loading with varying eccentricities of 0, 10, 35, 50 and 85 mm, as demonstrated in Fig. 4-4 (b). To provide appropriate eccentricities for the applied axial loads, steel caps were used at the top and bottom of the CFRP-CFFT columns with loading pivots attached to the top and the bottom of the steel plate, respectively, as shown in Fig. 4-4 (b). To capture the lateral deformations of the columns at the eastern side of the column, LVDTs 1-3 with a gauge length of 100 mm were placed horizontally pointing to the compressive face of the column with a constant spacing of 200 mm (presented in Figs. 4-4 (c) and 4-5 (a)), and meanwhile, LVDT-4 was installed at the middle height of the column at the opposite side to measure corresponding lateral displacement (presented in Figs. 4-4 (c) and 4-5 (b)). Furthermore, the global axial displacements of the columns were measured by LVDTs 5 and 6 that were placed at the northern and southern sides of the columns, respectively, as depicted in Figs. 4-4 (c) and 4-5 (c). To monitor the strain variations of the external CFRP tube in both vertical and horizontal directions, three 30 mm strain gauges (SG1-3) and two 10 mm strain gauges (SG4-5) were placed on the CFRP, as illustrated in Figs. 4-4 (d) and 4-5 (d).

A CFRP-CFFT UHPFRC beam with a clear span of 1750 mm was also tested by subjecting it to four-point bending through a 1000 kN capacity Avery machine with two equal concentrated loads (spaced with 200 mm) applied on the top of the beam. To capture the vertical displacements at the middle span, LVDTs 1-3 with a gauge length of 200 mm were placed at

the bottom of the beam with a constant spacing of 200 mm, as shown in Figs. 4-4 (e) and 4-6. Moreover, five strain gauges (SG1-5) with a gauge length of 30 mm were placed horizontally across the depth of the beam and distributed with a spacing of 25 mm for measuring the strain profile of CFRP tube crossing the entire middle span. To capture the hoop strain of the beam, strain gauge 6 (SG6) with a gauge length of 10 mm was placed vertically and perpendicularly to the lateral centreline of the beam, as exhibited in Figs. 4-4 (e) and 4-6.

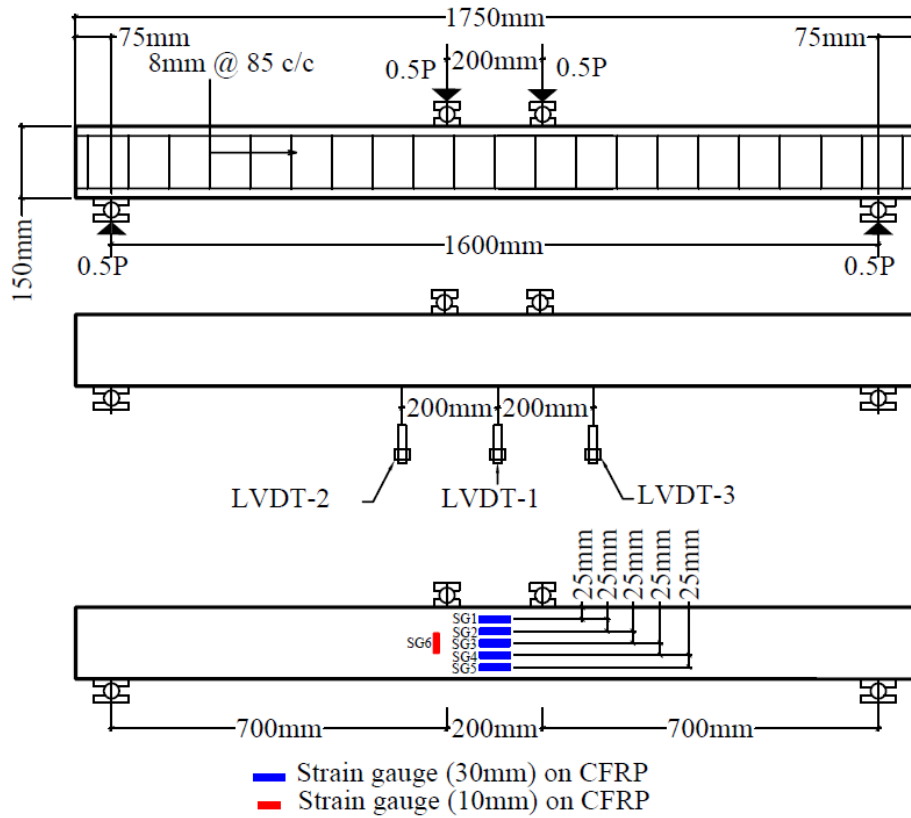
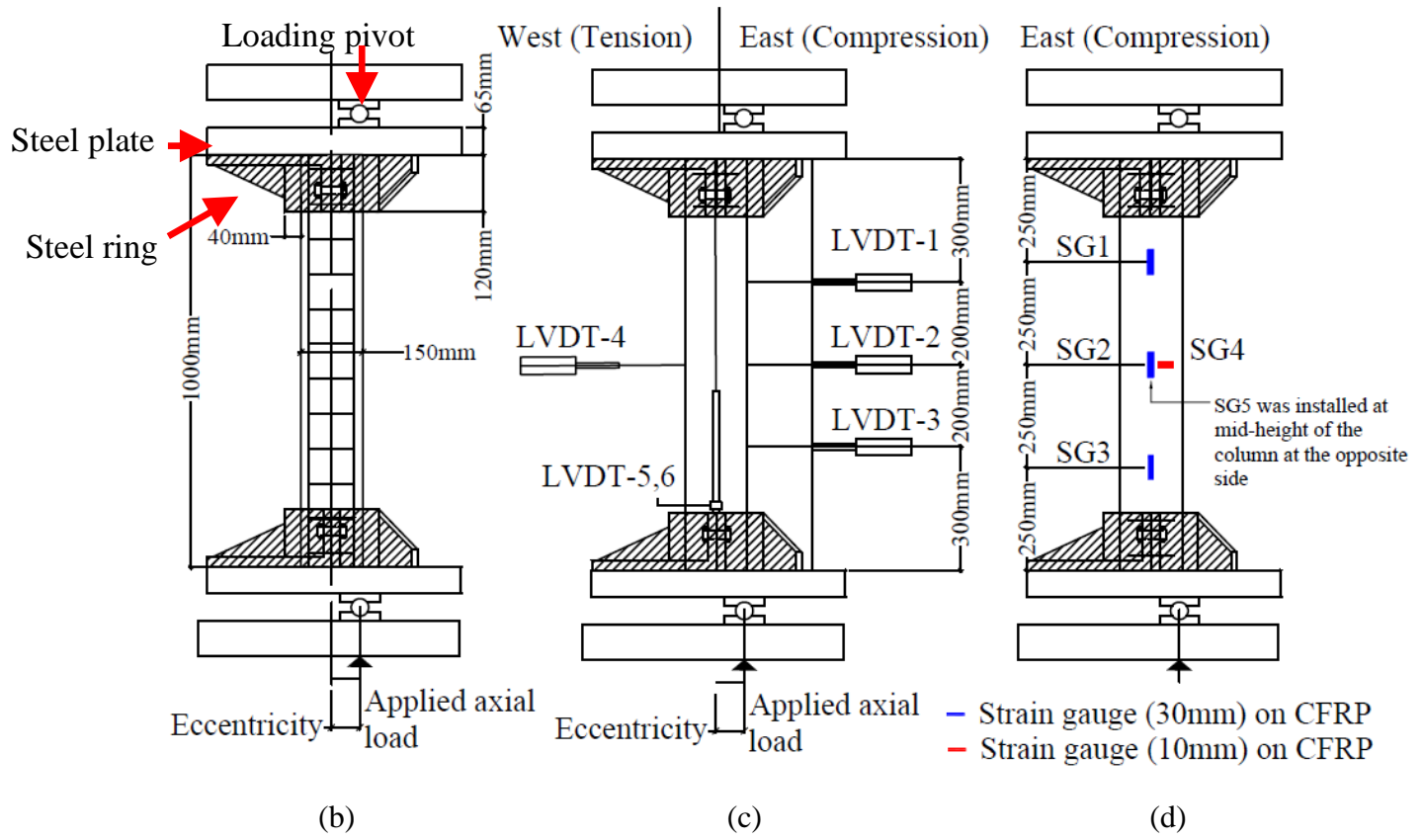


Steel reinforcement 1-4 diameter ( $\phi$ ) = 12 mm

Steel stirrups diameter ( $\phi$ ) = 8 mm at 85mm  
C/C throughout

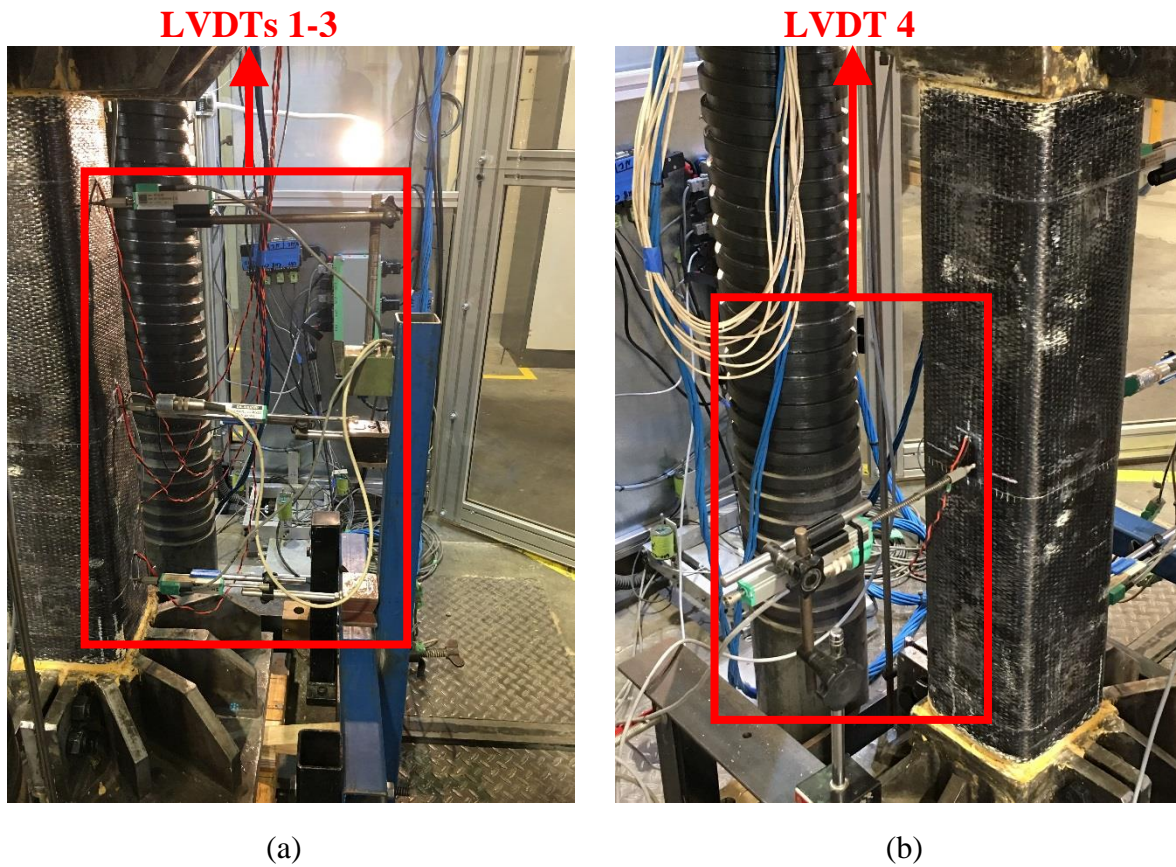
Corner Radius ( $R$ ) = 20 mm

(a)



(e)

Figure 4-4. Test specimens' details and instrumentation set up: (a) cross-section of the CFFTs-UHPFRC beam and columns and configuration of CFRP layers; (b) concentrically and eccentrically loaded CFFTs-UHPFRC columns; (c) Configuration of LVDTs 1-4; (d) experimental setup of strain gauges 1-5; (e) four point-bending tests for the CFFTs-UHPFRC beam.





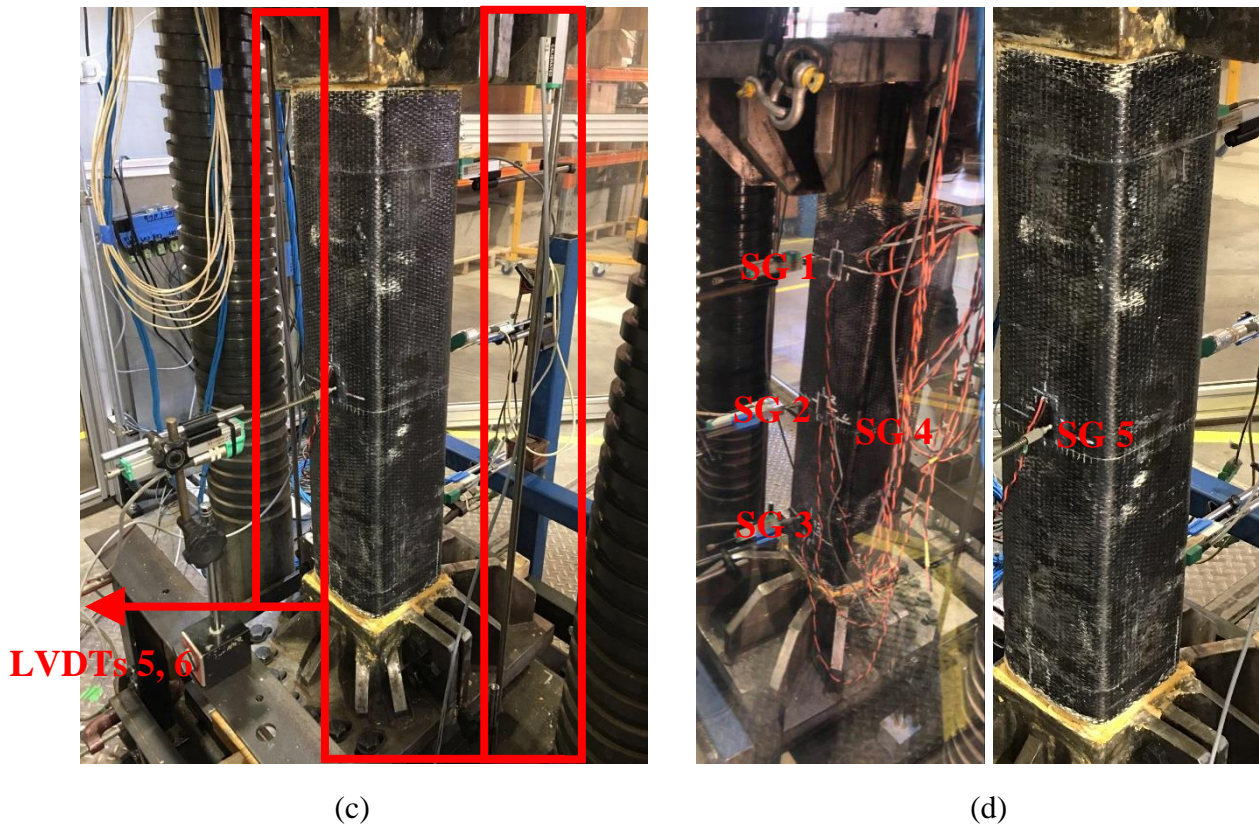


Figure 4-5. Structural test setup for CFFTs-UHPFRC columns: (a) LVDTs 1-3 measuring lateral deflection at compression face; (b) LVDTs 4 measuring lateral deflection of the middle height of the column at tension face; (c) LVDTs 5, 6 measuring global axial deformation of the column; (d) strain gauges (SG) 1-5 measuring the localized strain on CFRP

#### 4.2.4.3. Testing procedure

All CFRP-CFFT UHPFRC columns were tested by using Amsler testing machine having a maximum capacity of 5000 kN, and the columns were initially tested under a load-controlled protocol with a constant loading rate of 50 kN/minute until the applied axial load reached the maximum, and then a displacement controlled loading protocol with a steady rate of 0.15 mm/min was adopted to load the column. An Avery universal testing machine with a capacity of 1000 kN was used to test the CFRP-CFFT UHPFRC beam, and the load was acting through two loading pivots simultaneously, as shown in Figs. 4-4 (e) and 4-6. Similarly, the beam was

initially tested under a load-controlled protocol with a loading rate of 50 kN/minutes until the load reached the maximum, and the beam was then tested under a displacement-controlled protocol with a steady rate of 0.15 mm/min.

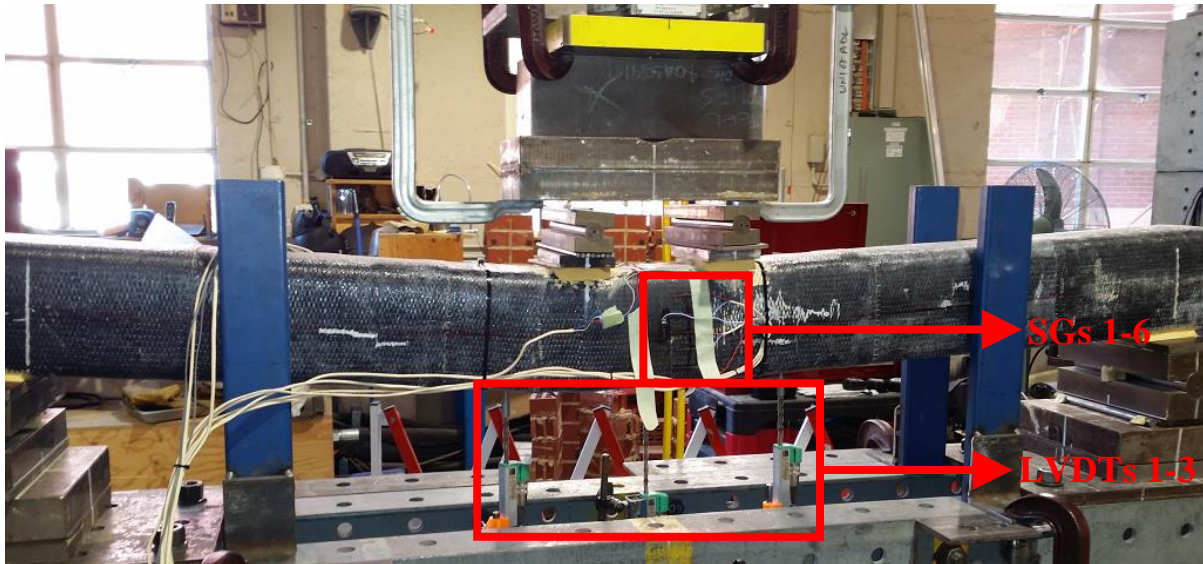


Figure 4-6. Structural test setup for CFFTs-UHPFRC beam

### 4.3. COLUMN TEST RESULTS AND OBSERVATIONS

#### 4.3.1. Load bearing and flexural moment capacities and corresponding deflections

Structural performance of CFRP-CFFT UHPFRC columns including the location of failure, strain of FRP, load bearing capacity ( $P_u$ ), moment capacity ( $M_u$ ), and corresponding deflections ( $\delta_{lateral-peak}$ ,  $\delta_{axial-peak}$ , and  $\delta_{axial-ult}$ ) are summarised in Table 4-3. Column CC-0 was used to determine the squash load capacity and it completely failed when the maximum axial load  $P_u = 3710.8$  kN. Through the comparisons between columns CC-0 and CC-10, it is worth highlighting that a slight increase in the loading eccentricity from 0 to 10 mm did not reduce drastically the load bearing capacity ( $P_u$ ), but the flexural moment capacity ( $M_u$ ) of the column increasing from 0kN.m to 38.49 kN.m further emphasize the high robustness and ductility of

the CFRP-CFFT UHPFRC columns eccentrically loaded with an eccentricity lower than 10 mm. With the eccentricity increased from 10 mm to 35 mm, more than 35% of reduction in  $P_u$  was observed from the comparisons between columns CC-10 and CC-35, and a further increase in the eccentricity of the load (from 35 mm to 50 mm) results in a 42% of decrease in the values of  $P_u$ . Hence, it can be inferred that for CFRP-CFFT UHPFRC columns subjected to eccentric loads, the load-bearing capacity for the columns is sensitive to a further increase in the eccentricity above 35 mm. Corresponding lateral deflections ( $\delta_{l-p}$ ) and axial deflections ( $\delta_{a-p}$ ) at the peak are listed in the Table 4-3 and the relationship between lateral ( $\delta_{lateral}$ ) or axial ( $\delta_{axial}$ ) deflections and applied load ( $P$ ). It is worth noting that the lateral deflection of column ( $\delta_{lateral-peak}$ ) at the peak increases with an increase in the eccentricity of axial loading. By comparing the magnitudes of the flexural bending moment capacities ( $M_u$ ) in Table 4-3, it can be found that the column CC-35 has the highest moment capacity ( $M_u = 96.78$  kN.m) among all tested CFFT-UHPFRC columns. Hence, it can be inferred that the balanced condition for the tested CFRP-CFFT UHPFRC columns occurred when the eccentricity of the axial load reached to 35 mm.

Table 4-3. Test results of all columns and beam

Specimen	Eccentricity $e$ (mm)	Failure location (mm)	$\epsilon_{FRP}$ ( $\mu$ s)	$P_{u-exp}$ (kN)	$\delta_{lp-exp}$ (mm)	$\delta_{ap-exp}$ (mm)	$\delta_{au-exp}$ (mm)	$M_{u-exp}$ (kN.m)
CC-0	0	+75 to +350	8770	3710.8	0.2	6.4	6.4	0
CC-10	10	+100 to +350	9514	3694.2	0.4	7.6	8.2	38.5
CC-35	35	+110 to +300	9933	2407.5	5.2	5.1	12.5	96.8
CC-50	50	-80 to +85	10133	1398.0	8.1	4.2	15.8	81.3
CC-85	85	-65 to +50	10174	774.2	13.5	6.1	11.3	76.3
CC-beam	-	-125 to +120	10068	101.7	21.0	-	-	35.6

\* “+” is above and “-” is below middle height of columns and middle span of the beam

### 4.3.2. Failure Mode and location

Typical failure modes of CFRP-CFFT UHPFRC members observed during the experiments are presented in Fig. 4-7. It was observed that columns CC-0 and CC-10 failed in an explosive manner associated with FRP fibre rupture at one corner of the column along with a minor concrete spalling and the crack propagated rapidly and vertically along the corner with cracking noises, as shown in Fig. 4-7 (a). Furthermore, the failure location of CC-0 ranged from 75 mm above the middle height of the column up to the location 350 mm above the middle height of the column, and a similar failure location was reported for column CC-10, as listed in Table 4-3. Compared to columns CC-0 and CC-10, a similar cracking pattern of carbon FRP tube was observed during the test of specimen CC-35, but the damages of the carbon FRP tube and formation of a plastic hinge which composited by a compression spalling and a flexural tensile crack were occurred slowly, and the corresponding failure location appeared from the location 110mm above the middle height of the column and extended to the place 300mm above the middle height of the column. For CFRP-CFFT UHPFRC columns loaded with eccentricities of 50 mm and 85 mm, a severe tensile crack appeared at the middle height of the column and the external bonded FRP tube was initially ruptured at the tensile face of the middle height of the column and the crack gradually opened and propagate fully ruptured in the circumferential direction until fully ruptured, as presented in Fig. 4-7 (b). In Table 4-3, the failure location of the column CC-50 ranges from 80 mm below the middle height of the column up to 85 mm above the middle height, and the failure location of the column CC-85 is slightly smaller than that of the column CC-50 (-65 mm to +50 mm). For the simply supported CFRP-CFFT UHPFRC beam under four-point bending, a flexural tensile crack appeared from the bottom of the beam and accompanied by a serve FRP rupture propagating from the bottom of the beam all the way up to the top of the beam, as illustrated in Fig. 4-7 (c).

FRP rupture and concrete spalling

FRP ruptured and a plastic hinge formed at the mid-height of the column



(a)



(b)



FRP ruptured and flexural cracks of concrete at the mid-span of the beam

(c)

Figure 4-7. Failure modes of: (a) CFFTs-UHPFRC columns ( $e=0$  mm, 10 mm, 35 mm); (b) CFFTs-UHPFRC columns ( $e=50$  mm, 85 mm); (c) CFFTs-UHPFRC beam

#### **4.4. FINITE-ELEMENT (FE) MODELLING**

Fundamental material properties of unconfined and confined UHPFRC, steel reinforcements, and CFRP under different stress states were determined using the recommended material tests (Section 2.3), which are utilised in the finite element (FE) modelling to simulate the behaviours of CFRP-CFFT UHPFRC beam and columns. Previous studies demonstrated encouraging features of finite element modelling in terms of its capabilities for accurately simulating UHPFRC members [30-32] to predict their corresponding structural behaviours. To simulate the damage and its evolution of CFRP, an elastic-brittle material with anisotropic behaviour, the inelastic material model based on Hashin's damage criteria has been employed in this study. The concrete damage plasticity (CDP) model has been used for the inelastic material behaviour of UHPFRC. For this purpose, the steel reinforcements have been modelled with elasto-plastic material model with hardening and softening behaviours as reported by Fang et al. [30]. In this study, FE modelling has been undertaken in conjunction with the above material models utilising a reliable FE code (ABAQUS) to simulate the responses of CFRP-CFFT UHPFRC members under different loading conditions. This is to extract the variations of axial load vs axial deflection ( $P-\delta_{axial}$ ), axial load vs lateral deflection at mid-height/span ( $P-\delta_{lateral}$ ), and failure mechanisms of FRP as well as UHPFRC.

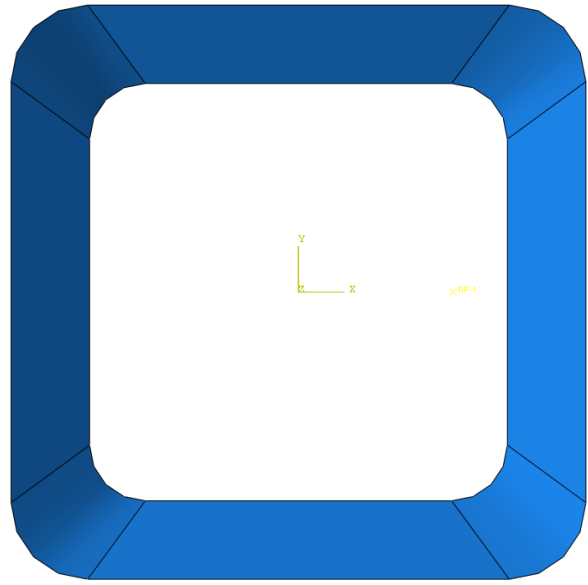
##### **4.4.1. FE modelling the CFRP-CFFT UHPFRC primary members**

The three-dimensional (3D) hexahedral solid elements with eight nodes (C3D8R) based on the reduced integration technique has been used to model the UHPFRC beams/columns where the portion outside the transverse reinforcements (stirrup) having a hollow cross-section and the central solid part have been created separately and they are combined together (using tie constrains between them) as shown in Fig. 4-8 (a). The intention of this is to assign material properties of unconfined UHPFRC to the outside region while assign those of actively confined

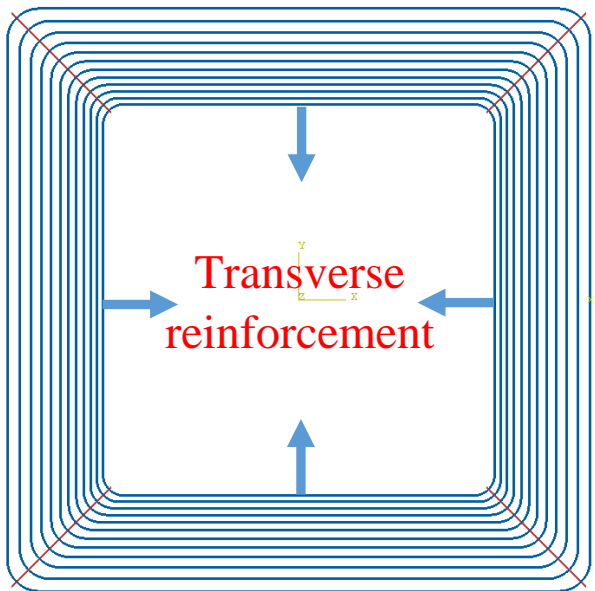
UHPFRC to the central part. The laminated composite shell element having quadrilateral curved shape with four corner nodes (S4R) has been used to model the CFRP tube as shown in Fig. 4-8(b) that has been externally bonded on the UHPFRC members using tie constraints (the concrete surface has been defined as a master surface and the inner surface of the FRP tube has been defined as a slave surface). In all cases, four layers of CFRP plies with a fibre orientation of  $90^0/90^0/0^0/0^0$  ( $90^0$  indicates fibre orientation along the member axis) have been used. Furthermore, both transverse (stirrup) and longitudinal steel reinforcements have been modelled with 3D truss elements having 2 end nodes (T3D2) as shown in Fig. 4-8 (c) and 4-8 (d). These truss elements have subsequently been embedded within the solid elements modelling UHPFRC where a perfect bonding between the reinforcements and the UHPFRC is established by the embedded feature. Hence, all essential elements have been assembled together to obtain the CFRP-CFFT UHPFRC members as exhibited in Fig. 4-8 (e).



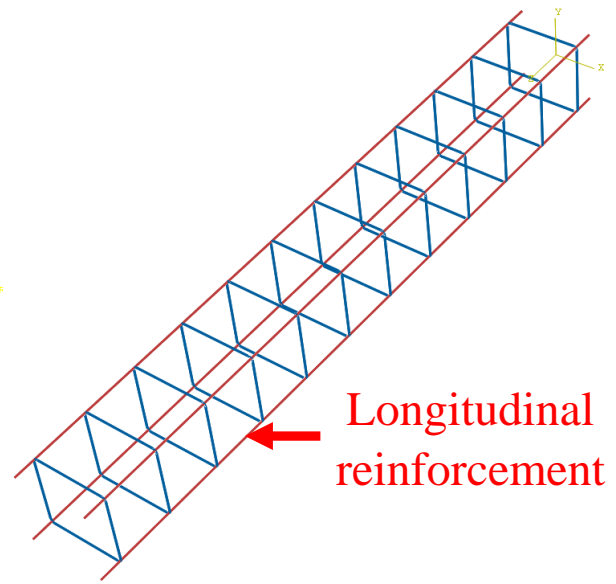
(a)



(b)

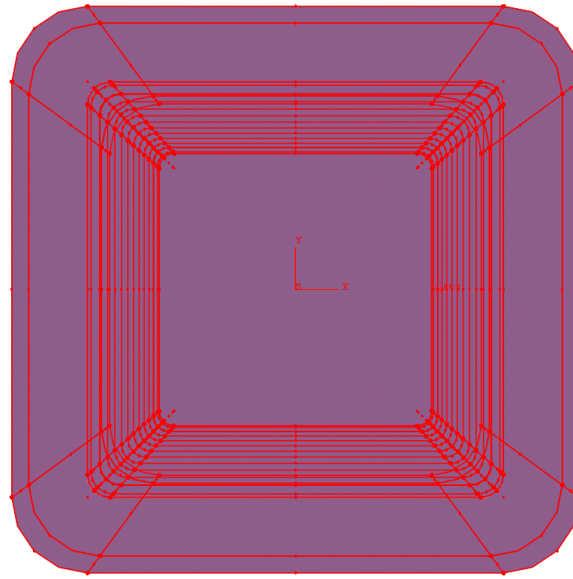


(c)



(d)





(e)

Figure 4-8. Finite element (FE) modelling of: (a) UHPFRC cross-section; (b) CFRP tube; (c) embedded transverse steel reinforcement; (d) embedded longitudinal steel reinforcement; (e) assembled cross-section of CFFTs-UHPFRC members

#### 4.4.2. Modelling of the CFRP-CFFT UHPFRC columns

Figure 4-9 shows the FE modelling of a column along with other components for its testing and some details of the loading process. The actual geometry of steel caps consisting of a square ring and a flat plate used in real experimental setup shown in Fig. 4-4 (b) is simplified slightly in the FE model (square ring: length/height = 120 mm, thickness = 45 mm; flat plate: length = 500 mm, breadth = 350 mm, thickness = 65 mm) as shown in Fig. 4-9(a). In addition, steel loading plates (length = 250 mm, width = 100 mm, and thickness = 50 mm) have been used at the end of two steel caps as shown in Fig. 4-9 (b) to apply the axial loads. The steel caps and loading plates have been modelled in ABAQUS using hexahedral solid elements (C3D8R) and elasto-plastic material model but the material behaved elastically in all cases. The standard surface-to-surface contact algorithm consisting of hard contact for the normal behaviour and penalty friction contact with coefficient of friction = 0.1 for the tangential behaviour has been

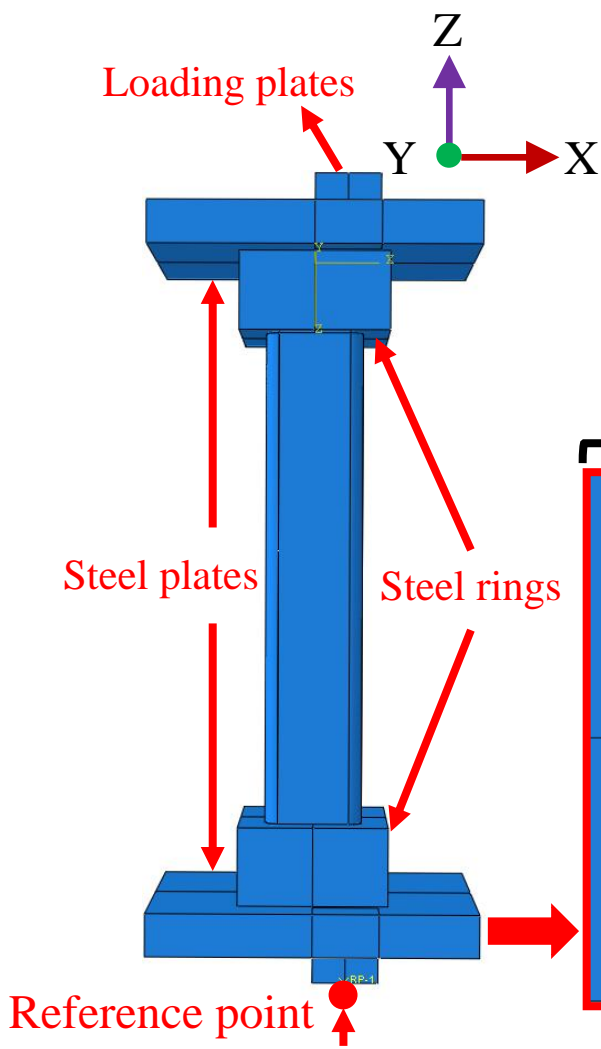
adopted to define the interaction between steel caps and column ends. Tie constrains have been used between steel caps and loading plates.

In order to simulate the post-peak response of these members successfully, the displacement control algorithm has been adopted to load/deform these members. For this purpose, a reference point (RP) located at the geometrical centre of the lower loading plate external surface but little bit away from that as shown in the Fig. 4-9 (b) has been created. A multipoint coupling constraint has been defined between the RP and the external surface of the loading plate to apply axial load with an eccentricity by steadily increasing the vertical displacement component of the RP (displacement components along X and Y axis at the translational line are restrained but rotations are free) at a constant rate of 0.15 mm/min vertically upwards. It is to be noted that the upper loading surface has been restrained at the translational line (all displacement components) along Y (Fig. 4-9 (b)) of its external surface. The loading plates at the two ends should be perfectly aligned to have same eccentricity at both ends. In order to get different values of eccentricity, the loading plates are shifting symmetrically but they were firmly connected with the steel caps using bolts in real case. Before analysing of CFRP-CFFT UHPFRC members with different eccentricities, a convergence study has been conducted to get an optimum mesh size, which indicated elements having 20 mm size are adequate for concrete, steel reinforcements, and steel caps while this is 10 mm for the CFRP tube. This has been adopted in the present study as shown in Fig. 4-9 (c).

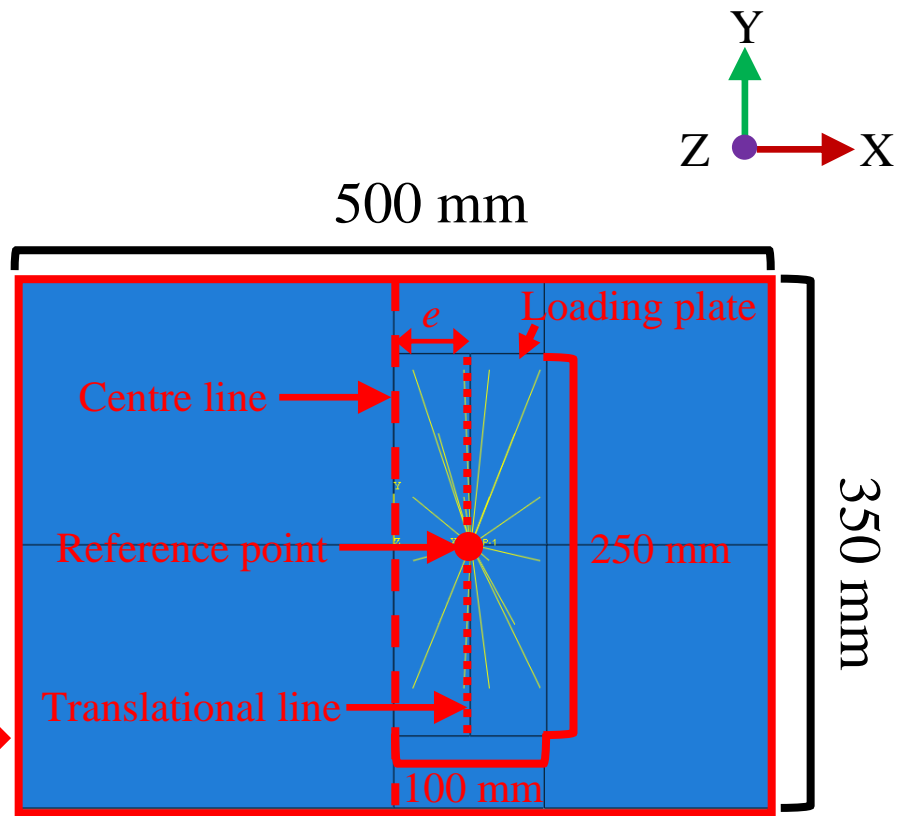
#### **4.4.3. Modelling of the CFRP-CFFT UHPFRC beam**

The FE modelling of the beam subjected to four-point flexural bending along with the details of loading configurations are illustrated in Fig. 4-9 (d). Two supporting plates placed underneath of the bottom surface of the beam have the same dimensions as the loading plate

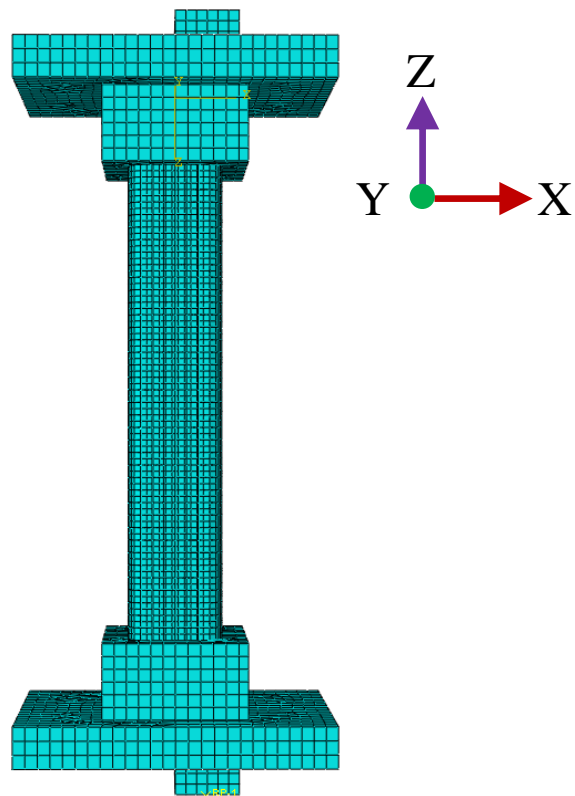
shown in Fig. 4-9 (b), in which the width of steel plates (100 mm) is aligned to the span of the beam. Two loading plates with a 50 mm in width, a 50 mm in depth, and a 250 mm in length were placed above the top surface of the beam, as presented in Fig. 4-9 (d). The same displacement control algorithm applied to the columns has been applied here to load the beam by creating a RP located at the middle span of the beam but slightly above the upper surface of the loading plates. A multipoint coupling constraint has been defined between the RP and the upper surface of the loading plate to apply flexural bending by steadily increasing the vertical displacement component of the RP (displacement in X and Z directions are fully restrained) at a constant rate of 0.15 mm/min vertically downwards. Furthermore, a boundary condition with all translational displacement restrained and free rotation about the X-axis was assigned to the transitional line of the lower face of the supporting plates. The same surface-to-surface contact (standard) interaction properties used in the modelling of the columns was also adopted to the contact interfaces between the supporting plates to the beam as well as the loading plates to the beam.



(a)



(b)



(c)

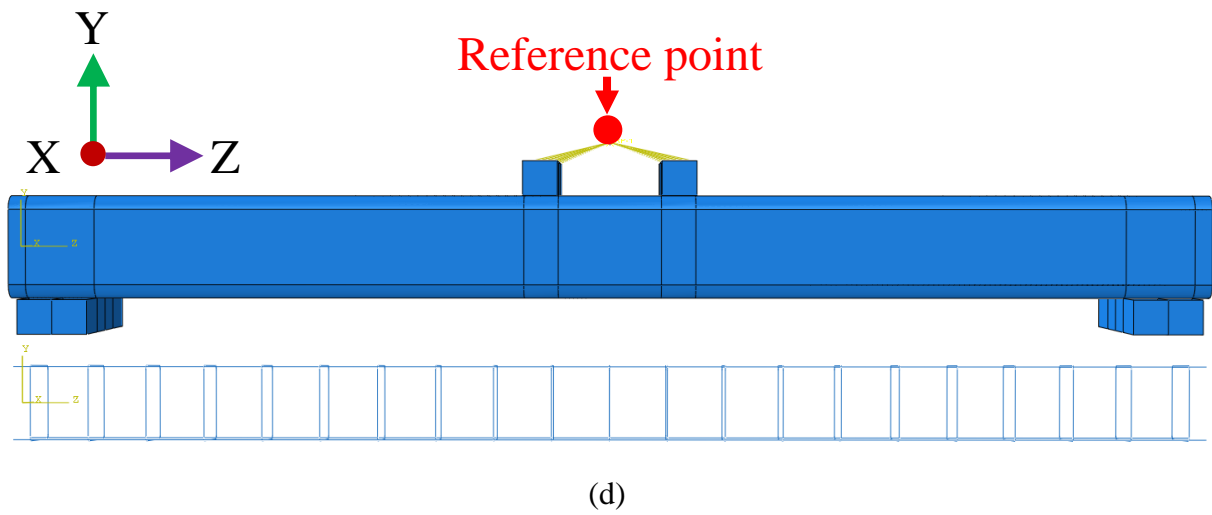


Figure 4-9. Finite element (FE) modelling of: (a) CFFTs-UHPFRC column; (b) configurations and dimensions of steel and loading plates; (c) meshed CFFTs-UHPFRC column; (d) CFFTs-UHPFRC beam and embedded steel reinforcements

#### 4.4.4. Concrete failure model

Concrete damage plasticity (CDP) model [33] is a plasticity-based continuum damage mechanisms model that couples the elasto-plastic response of concrete with its damage behaviour under multi-axial stress state to investigate the behaviour of concrete structures under various loading conditions. The elastic behaviour is simply represented by the undamaged elastic modulus of concrete ( $E_0$ ) and Poisson's ratio ( $\nu$ ) assuming concrete as an isotropic material. The plasticity of material is considered using the irrecoverable plastic deformation in the strain hardening and softening branches in compression while strain-softening branch in tension. A non-associated plasticity model is used where a yield function proposed by Lubliner [33] with some modifications by Lee and Fenves [34] is employed to check the material yielding and a plastic potential in the form of Drucker-Prager hyperbolic function incorporating dilation angle is used to determine the plastic flow. Scalar damage parameters (separate variables for tension and compression) are used for the degradation of material stiffness where the evolution of damage parameter is based on stress for tension and inelastic strain for compression. Specifically, the yield function ( $F$ ) and the plastic potential ( $G$ ) as stated above is taken in the following form.

$$F = \frac{1}{1-\alpha} \left( \bar{q} - 3\alpha\bar{p} + \beta(\tilde{\varepsilon}^{pl}) \langle \hat{\sigma}_{\max} \rangle - \gamma \langle -\hat{\sigma}_{\max} \rangle \right) - \bar{\sigma}_c(\tilde{\varepsilon}_c^{pl}) \leq 0 \quad (1)$$

$$G = \sqrt{(\xi\sigma_{t0} \tan \varphi)^2 + \bar{q}^2} - \bar{p} \tan \varphi \quad (2)$$

$$\alpha = \frac{\frac{\sigma_{bo}}{\sigma_{co}} - 1}{2 \times \frac{\sigma_{bo}}{\sigma_{co}} - 1}; \quad 0 \leq \alpha \leq 0.5 \quad (3)$$

$$\beta = \frac{\bar{\sigma}_c(\tilde{\varepsilon}_c^{pl})}{\bar{\sigma}_t(\tilde{\varepsilon}_t^{pl})} (1-\alpha) - (1+\alpha) \quad (4)$$

$$\gamma = \frac{3(1-k_c)}{2k_c - 1} \quad (5)$$

where  $\bar{q}$  is the von Mises/equivalent stress (based on effective stress as indicated by the bar above  $q$ ),  $\bar{p}$  is the hydrostatic pressure, and  $\hat{\sigma}_{\max}$  is the maximum principal stress. The other terms in above equations are:  $\bar{\sigma}_c(\tilde{\varepsilon}_c^{pl})$  and  $\bar{\sigma}_t(\tilde{\varepsilon}_t^{pl})$  are equivalent compressive and tensile stresses in terms of corresponding accumulated plastic strains  $\tilde{\varepsilon}_c^{pl}$  and  $\tilde{\varepsilon}_t^{pl}$  (these stresses are actually obtained from experimentally measured uniaxial stress-strain curves by substituting the accumulated plastic strains of a multi-axial stress state scenario as the uniaxial plastic strains);  $\xi$  is the eccentricity that defines the rate at which the curve approaches to the asymptote;  $\sigma_{t0}$  is the initial uniaxial tensile strength, obtained from the characterised tensile behaviours;  $\varphi$  is the dilation angle measured in the  $p$ - $q$  plane;  $\sigma_{bo}$  is the initial yield stress obtained from bi-axial compression test with equal stress in both directions; and  $\sigma_{co}$  is the initial yield stress obtained from uniaxial compression test; and  $k_c$  is the ratio of second stress invariant on the tensile and compressive meridians at an initial yield condition. The value of  $k_c$  varies from 0.5 to 1.0 and this is taken as 2/3 while the value of  $\xi$  is taken as 0.1 in this

study. The bi-axial stress ratio ( $\sigma_{bo}/\sigma_{co}$ ) is commonly taken as 1.16 for normal concrete but based on some previous studies [30-32], the value of this parameter is taken as 1.05 for UHPFRC in the present study. Similarly, based on the observations in some studies [30, 32], the value of dilation angle for UHPFRC is taken as  $39^0$  in this study while a commonly used value of this parameter is  $30^0$  for normal concrete.

Fig. 4-10 shows typical uniaxial stress-strain ( $\sigma$ - $\varepsilon$ ) curves of UHPFRC obtained from compression tests of UHPFRC cylinders and direct tensile tests of UHPFRC dog bone specimens. In the presence of damage, the strains ( $\varepsilon_c, \varepsilon_t$ ) are decomposed in terms of elastic strains ( $\varepsilon_{0c}^{el}, \varepsilon_{0t}^{el}$ ), inelastic (compression) or cracking (tension) strains ( $\varepsilon_c^{in}, \varepsilon_t^{ck}$ ), and plastic strains ( $\varepsilon_c^{pl} = \tilde{\varepsilon}_c^{pl}, \varepsilon_t^{pl} = \tilde{\varepsilon}_t^{pl}$ ) as follows.

$$\varepsilon_c^{in} = \varepsilon_c - \varepsilon_{0c}^{el} = \varepsilon_c - \sigma_c / E_0 \quad (6)$$

$$\varepsilon_t^{ck} = \varepsilon_t - \varepsilon_{0t}^{el} = \varepsilon_t - \sigma_t / E_0 \quad (7)$$

$$\tilde{\varepsilon}_c^{pl} = \varepsilon_c^{in} - \frac{d_c}{(1-d_c)} \frac{\sigma_c}{E_0} \quad (8)$$

$$\tilde{\varepsilon}_t^{pl} = \varepsilon_t^{ck} - \frac{d_t}{(1-d_t)} \frac{\sigma_t}{E_0} \quad (9)$$

Both damage parameters ( $d_c, d_t$ ) will have a value ranging from 0 to 1 to specify an undamaged and fully damaged scenarios, respectively. Our previous study [35] indicated that a good prediction of these damage parameters from the uniaxial stress-strain curves can be achieved with the following equations, which are also used in the present study.

$$d_c = 1 - \left[ \frac{\frac{\sigma_c}{E_0}}{0.2\varepsilon_c^{in} + \frac{\sigma_c}{E_0}} \right] \quad (10)$$

$$d_t = 1 - \frac{\sigma_t}{f_t} \quad (11)$$

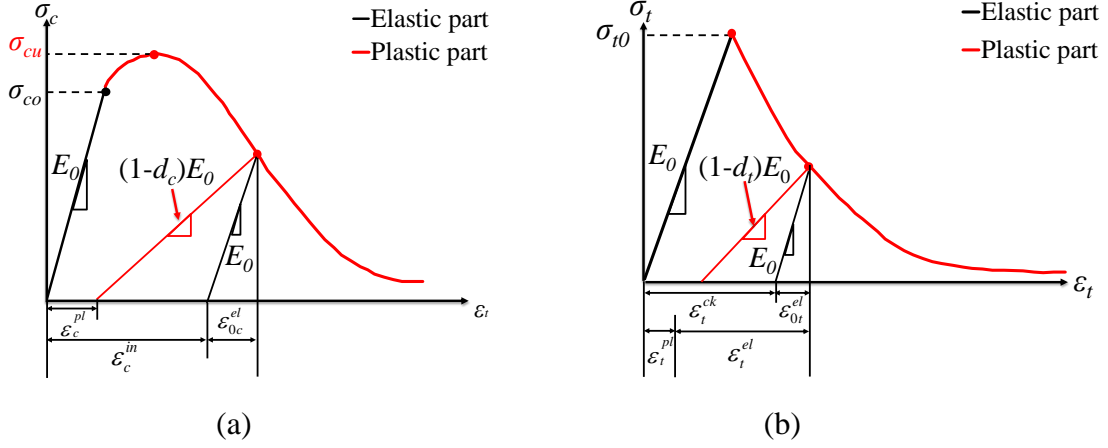


Figure 4-10. Concrete damage plasticity model: (a) compressive stress-strain; (b) tensile stress-strain

#### 4.4.5. FRP failure model

In the FE modelling of the structural members, the progressive failure analysis of fibre-reinforced composites used for CFRP tubes, the Hashin's failure criteria [36, 37] are used to indicate the initiation of damage. Specifically, this failure theory consists of four failure functions (initiation of damage), which are based on four independent failure modes namely, fibre failure in tension; fibre failure in compression; matrix failure in tension; matrix failure in compression.

$$F_f^t = \left(\frac{\bar{\sigma}_{11}}{X^T}\right)^2 + \alpha \left(\frac{\bar{\tau}_{12}}{S^L}\right)^2 - 1 \leq 0, \quad \bar{\sigma}_{11} \geq 0 \quad (12)$$

$$F_f^c = \left(\frac{\bar{\sigma}_{11}}{X^C}\right)^2 - 1 \leq 0, \quad \bar{\sigma}_{11} \leq 0 \quad (13)$$

$$F_m^t = \left(\frac{\bar{\sigma}_{22}}{Y^T}\right)^2 + \left(\frac{\bar{\tau}_{12}}{S^L}\right)^2 - 1 \leq 0, \quad \bar{\sigma}_{22} \geq 0 \quad (14)$$



$$F_m^c = \left(\frac{\bar{\sigma}_{22}}{2S^L}\right)^2 + \left[\left(\frac{Y^c}{2S^T}\right)^2 - 1\right] \frac{\bar{\sigma}_{22}}{Y^c} + \left(\frac{\bar{\tau}_{12}}{S^L}\right)^2 - 1 \leq 0, \bar{\sigma}_{22} \leq 0 \quad (15)$$

where  $\bar{\sigma}_{11}$ ,  $\bar{\sigma}_{22}$ ,  $\bar{\tau}_{12}$  are effective stresses components;  $X^T$ ,  $X^C$  are longitudinal (along fibre direction) tensile and compressive strengths;  $Y^T$ ,  $Y^C$  are transverse (perpendicular to fibre direction) tensile and compressive strengths; and  $S^L$ ,  $S^T$  are longitudinal and transverse shear strengths. These the strength parameters used in this study are provided in Table 4-4. The parameter  $\alpha$  used in Eq. (12) is to include the effect of shear stress on fibre failure initiation in tension. The value of the parameter is taken as 1.0 in the present study as used by Hashin [36].

Table 4-4. Summary of mechanical properties for FRP-Composites

Elastic						Hashin's Damage Model					
Elastic modulus (Gpa)		Poisson's ratio	Shear modulus (Gpa)			Longitudinal Tensile Strength, $X^T$ (MPa)	Longitudinal Compressive Strength, $X^C$ (Mpa)	Transverse Tensile Strength, $Y^T$ (Mpa)	Transverse Compressive Strength, $Y^c$ (Mpa)	Longitudinal Shear Strength, $S_{12}$ (Mpa)	Transverse Shear Strength, $S_{13}$ (Mpa)
$E_1$	$E_2$	$\nu_{12}$	$G_{12}$	$G_{13}$	$G_{23}$						
211.49	7.93	0.35	5.3	5.3	4	2142.08	1414	37	169	134	120

The four damage variables corresponding to the four above mentioned failure modes are replaced in terms of three damage parameters (fibre damage, matrix damage and shear damage) by the composite failure model and it helps to express the effective stress tensor  $\bar{\sigma}$  in terms of true stress  $\sigma$  using the damage operator M consisting of the three resulting damage parameters as follows.

$$\bar{\sigma} = M\sigma \quad (16)$$

$$M = \begin{bmatrix} \frac{1}{(1-d_f)} & 0 & 0 \\ 0 & \frac{1}{(1-d_m)} & 0 \\ 0 & 0 & \frac{1}{(1-d_s)} \end{bmatrix} \quad (17)$$

$$d_f = \begin{cases} d_f^t & (\text{if } \bar{\sigma}_{11} \geq 0) \\ d_f^c & (\text{if } \bar{\sigma}_{11} < 0) \end{cases} \quad (18)$$

$$d_m = \begin{cases} d_m^t & (\text{if } \bar{\sigma}_{22} \geq 0) \\ d_m^c & (\text{if } \bar{\sigma}_{22} < 0) \end{cases} \quad (19)$$

$$d_s = 1 - (1-d_f^t)(1-d_f^c)(1-d_m^t)(1-d_m^c) \quad (20)$$

where  $d_f$ ,  $d_m$ , and  $d_s$  are damage parameters, internal variables, corresponding to fibre, matrix, and shear failure modes, respectively, and  $d_f^t$ ,  $d_f^c$ ,  $d_m^t$ , and  $d_m^c$  are the damage parameters corresponding to the four independent failure modes, respectively.

With these damage parameters, the constitutive equation of fibre reinforced composite materials after damage initiation can be expressed as follows.

$$\sigma = C_d \varepsilon \quad (21)$$

$$C_d = \frac{1}{D} \begin{bmatrix} (1-d_f)E_1 & (1-d_f)(1-d_m)v_{21}E_2 & 0 \\ (1-d_f)(1-d_m)v_{12}E_2 & (1-d_m)E_2 & 0 \\ 0 & 0 & (1-d_s)GD \end{bmatrix} \quad (22)$$

$$D = 1 - (1 - d_f)(1 - d_m)v_{12}v_{21} \quad (23)$$

where  $C_d$  is the damaged elasticity/stiffness matrix;  $\varepsilon$  the strain vector;  $E_1$  is the elastic modulus in the fibre direction,  $E_2$  is the elastic modulus in the transverse direction;  $G$  is the shear modulus;  $v_{12}$  and  $v_{21}$  are Poisson's ratios. All these material properties of CFRP are also included in Table 4-4. It is worth mentioning that the values of  $E_1, v_{12}$  and  $X^T$  are obtained from the coupon tests undertaken in the present study while the other properties are determined from the study conducted by Hoang [38].

The modelling of material response after damage initiation is based on stress-displacement relationship utilising fracture energy ( $G^c$ ) in order avoid mesh sensitivity in the analysis. A bi-linear stress-displacement relationship (elastic with linear softening model) along with the evolution of damage parameter as shown in Fig. 4-11 is used that is applicable for the four failure modes as mentioned earlier. The displacement at the final failure when the damage parameter will be 1.0 (Fig. 4-11) can be determined from the fracture energy ( $\delta_{eq}^f = 2G^c / \sigma_{eq}^0$ ) where  $\sigma_{eq}^0$  is the strength of the specific failure mode. During the analysis, the strains produced at an integration point within a load step are used to express equivalent displacement  $\delta_{eq}$  at that point, which is used to determine the damage parameter from Fig. 4-11 as follows.

$$d = \frac{\delta_{eq}^f (\delta_{eq} - \delta_{eq}^0)}{\delta_{eq} (\delta_{eq}^f - \delta_{eq}^0)} \quad (\delta_{eq}^0 \leq \delta_{eq} \leq \delta_{eq}^f) \quad (24)$$

where  $\delta_{eq}^0$  is the equivalent displacement when the damage will initiate (Eq. (12)-(15)). The equivalent displacement  $\delta_{eq}$  for the four failure modes are estimated as follows.

$$\text{Fibre in tension: } \delta_{eq} = L^c \sqrt{\langle \varepsilon_{11} \rangle^2 + \alpha \varepsilon_{12}^2} \quad (25)$$

$$\text{Fibre in compression: } \delta_{eq} = L^c \langle -\varepsilon_{11} \rangle \quad (26)$$

$$\text{Matrix in tension: } \delta_{eq} = L^c \sqrt{\langle \varepsilon_{22} \rangle^2 + \varepsilon_{12}^2} \quad (27)$$

$$\text{Matrix in compression: } \delta_{eq} = L^c \sqrt{\langle -\varepsilon_{22} \rangle^2 + \varepsilon_{12}^2} \quad (28)$$

Where  $L^c$  is the characteristic length that is dependent on the size and type of the element.

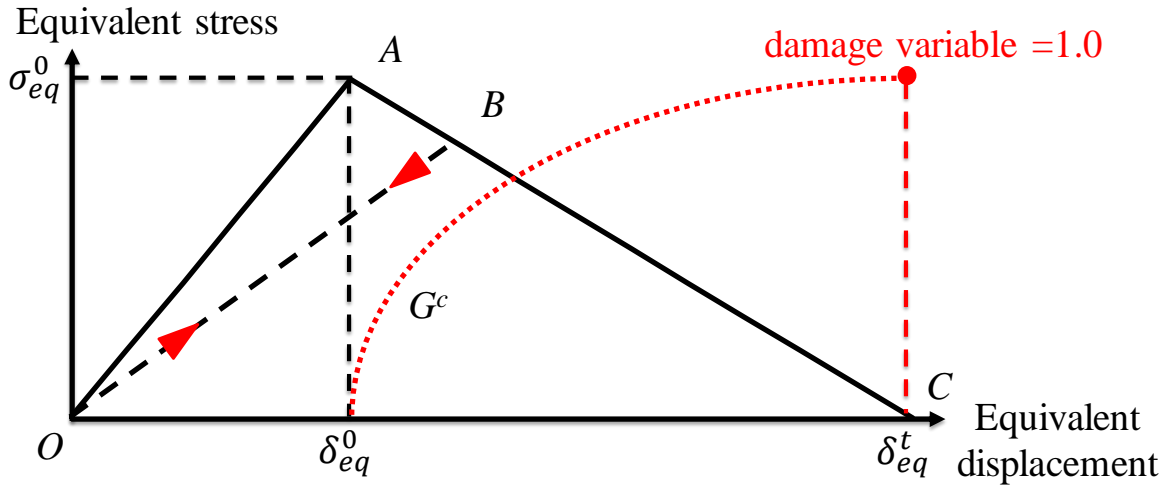


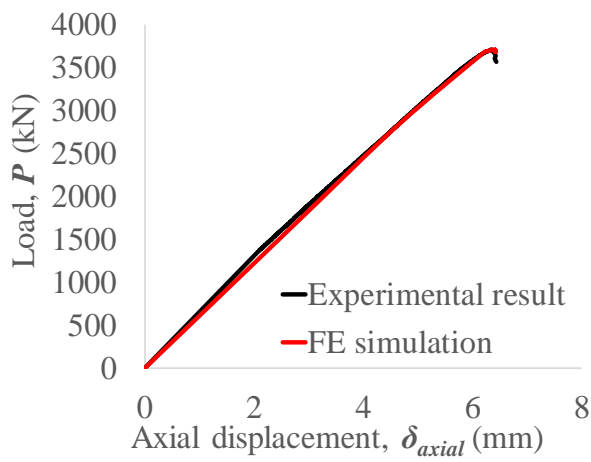
Figure 4-11. Equivalent stress-equivalent displacement response and linear damage evolution

## 4.5. VALIDATIONS OF FE MODEL

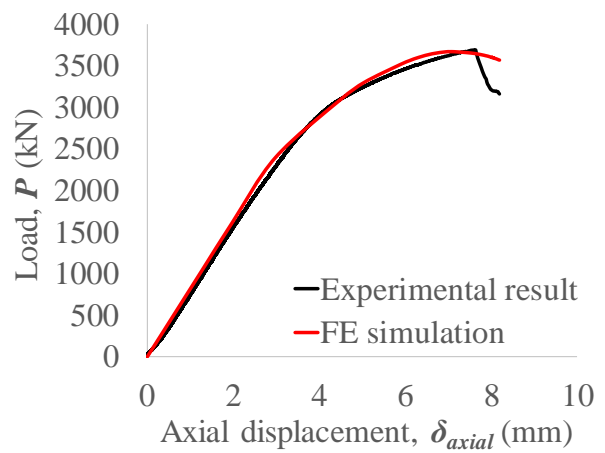
### 4.5.1. Comparisons of experimental and simulated results

The load-axial displacement ( $P$ -  $\delta_{axial}$ ) and load - middle height/span lateral displacement ( $P$ -  $\delta_{lateral}$ ) relationships that were obtained experimentally and numerically are illustrated in Figs. 4-12 and 4-13, respectively, and these figures indicate generally a high agreement between FE simulation and test results. This can also be specifically corroborated by the comparisons between results obtained from FE simulations and the corresponding test results that the ratios between FE simulation to test results for  $P_u$ ,  $\delta_{lp}$ ,  $\delta_{ap}$ , and  $M_u$  are found to be 0.99 to 1.06 with a standard deviation (SD) ranges from 0.006-0.055; hence this indicates a very strong correlation between FE simulation and test results. It can be seen that the failure locations of

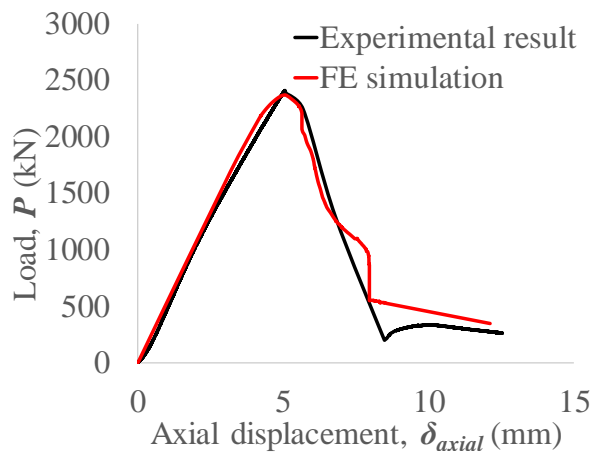
CFRP-CFFT UHPFRC members predicted by the FE model closely agrees with the corresponding failure locations obtained in the tests (Refer to Tables 4-3 and 4-5).



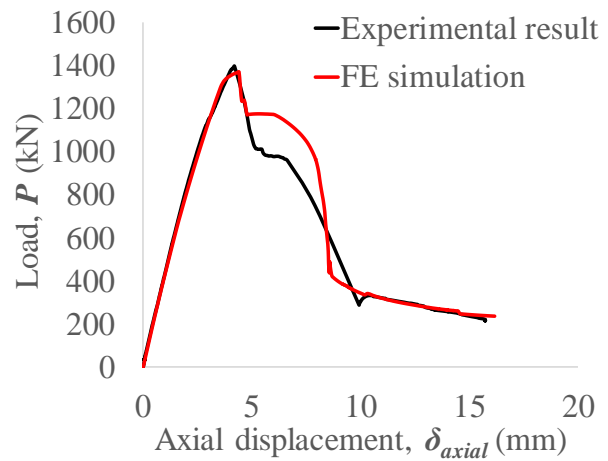
(a)



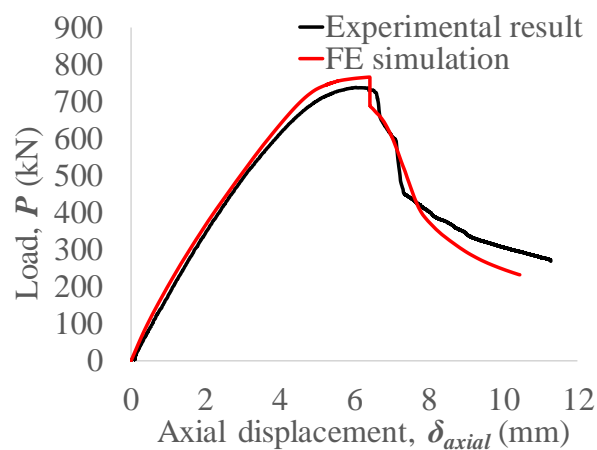
(b)



(c)



(d)



(e)

Figure 4-12. Load ( $P$ ) and axial displacement ( $\delta_{axial}$ ) relationships obtained from experiments results and FE simulations for CFFTs-UHPFRC columns loaded with different eccentricities: (a) concentrate; (b) eccentricity = 10 mm; (c) eccentricity = 35 mm; (d) eccentricity = 50 mm; (e) eccentricity = 85 mm

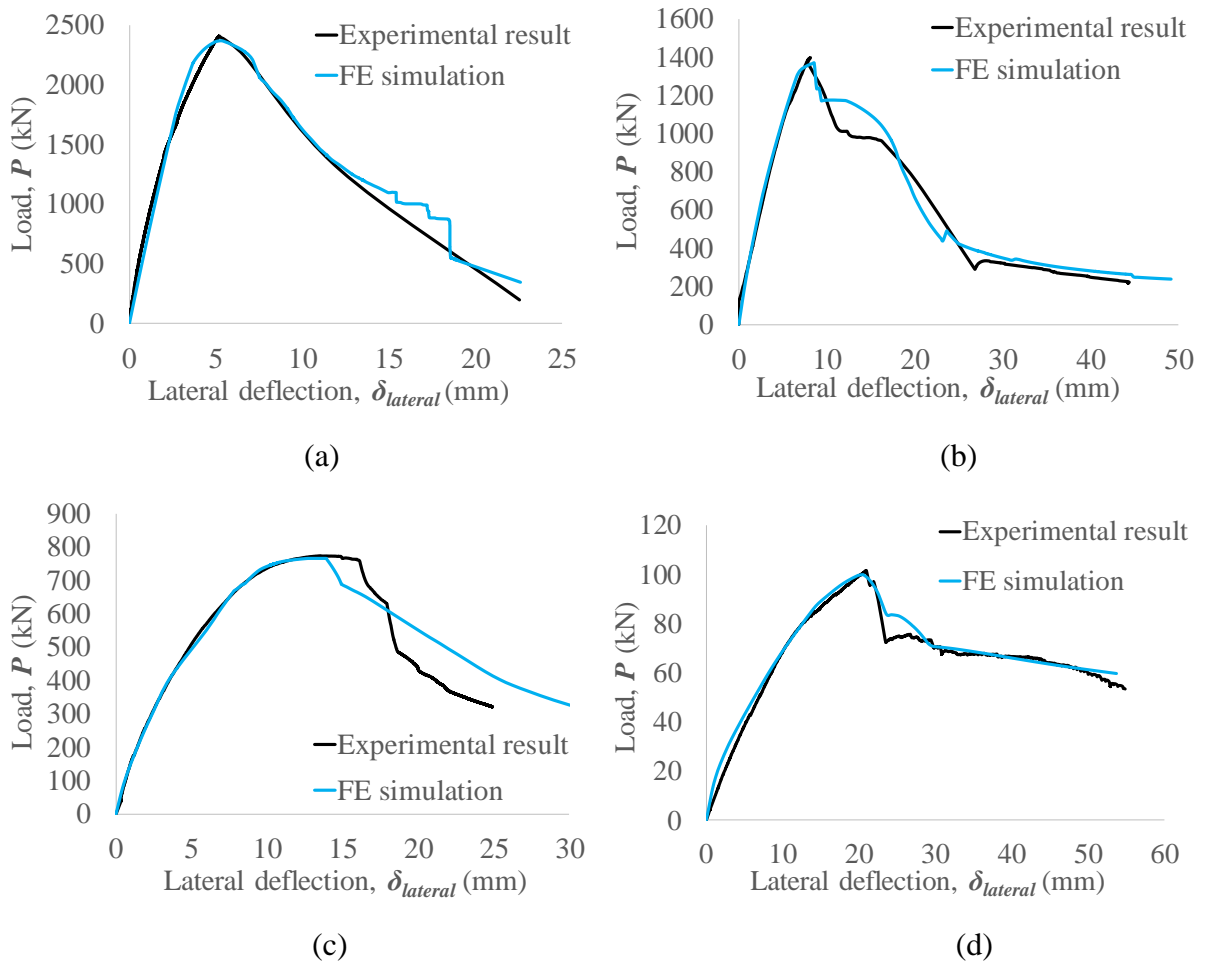


Figure 4-13. Load ( $P$ ) and lateral deflection at mid-height/span ( $\delta_{lateral}$ ) relationships obtained from experiments results and FE simulations for CFFTs-UHPFRC members loaded with different eccentricities: (a) eccentricity = 35 mm; (b) eccentricity = 50 mm; (c) eccentricity = 85 mm; (d) beam

Table 4-5. Comparisons of experimental and FE simulation results for all CFTT-UHPFRC members

Specimen	Failure location (mm)	$P_{u-FEM} / P_{u-exp}$	$\delta_{lp-FEM} / \delta_{lp-exp}$	$\delta_{ap-FEM} / \delta_{ap-exp}$	$M_{u-FEM} / M_{u-exp}$
CC-0	+75 to +350	1.00	1.00	1.01	1.00
CC-10	+100 to +340	0.99	0.93	0.92	0.99
CC-35	+180 to +360	0.98	1.04	1.01	0.99
CC-50	-70 to +70	0.98	1.05	1.05	0.99
CC-85	-55 to +50	0.99	1.03	1.06	0.99
CC-beam	-120 to +120	0.98	0.98	-	0.98
Mean		0.99	1.01	1.01	0.99
Standard deviation		0.008	0.045	0.055	0.006

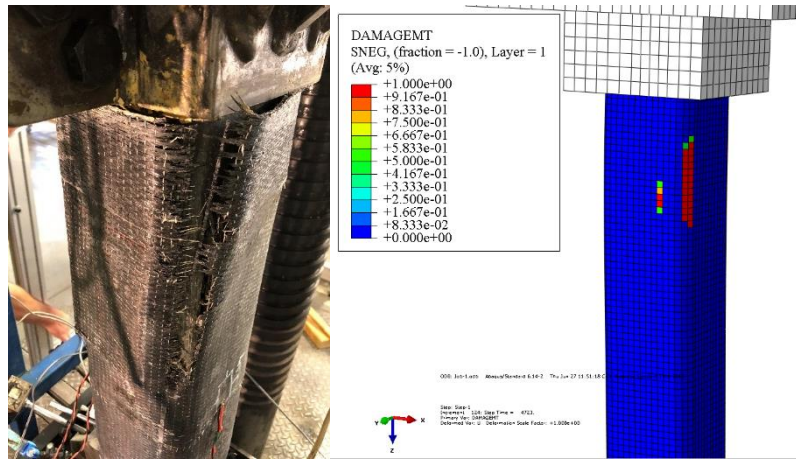
\* “+” is above and “-“is below middle height of columns and middle span of the beam

#### 4.5.2. Comparisons of damage pattern regarding CFRP tube

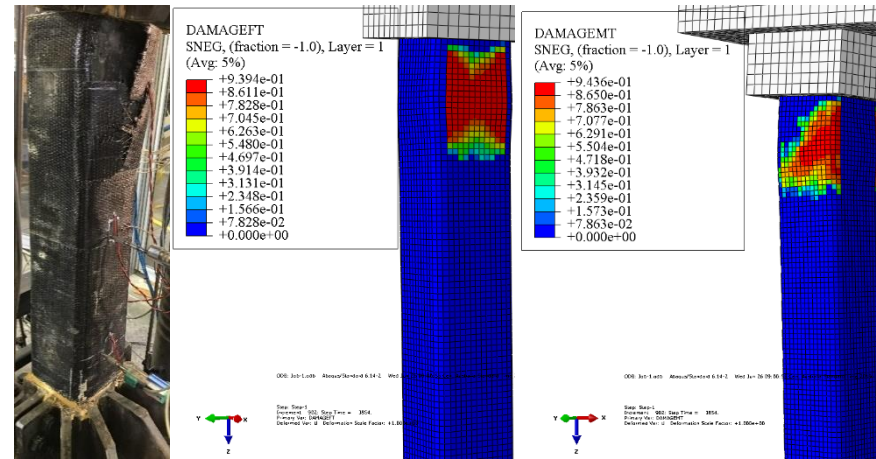
In this study, the rupture failure of CFRP tube mainly contributed to the tension, and the corresponding damage patterns of CFRP are represented by the damage parameters of  $d_f^t$ ,  $d_m^t$  (Refer to Eq.(18)-(19)). Furthermore, the information of these two damage parameters are also provided by ABAQUS with the contours of DAMAGEFT - fibre tensile damage; DAMAGEMT - matrix tensile damage, as presented in Fig. 4-14 to represent the damage patterns of the CFRP tubes. Comparisons between the experimental observation and FE simulated damage indicate that a qualitative agreement between the experimental and FE simulated damage patterns can be seen. Note that the damages in DAMAGEFT and DAMAGEMT are identical for column CC-10. The damage pattern DAMAGEMT shown in Fig. 4-14 (a) successfully simulated the rupture of CFRP in vertical direction as observed in the tests. It is also worth highlighting that the both fibre and matrix damage patterns at the plastic hinge areas of column CC-50 and the beam were accurately simulated and exhibited in Fig. 4-14 (c) and (d), for instance, the fibre damage (DAMAGEFT) initiated from the corner of the column CC-50 at inner 2 longitudinal layers of CFRP and propagated circumferentially across the middle height of the column, and the matrix damage (DAMAGEMT) of outer 2



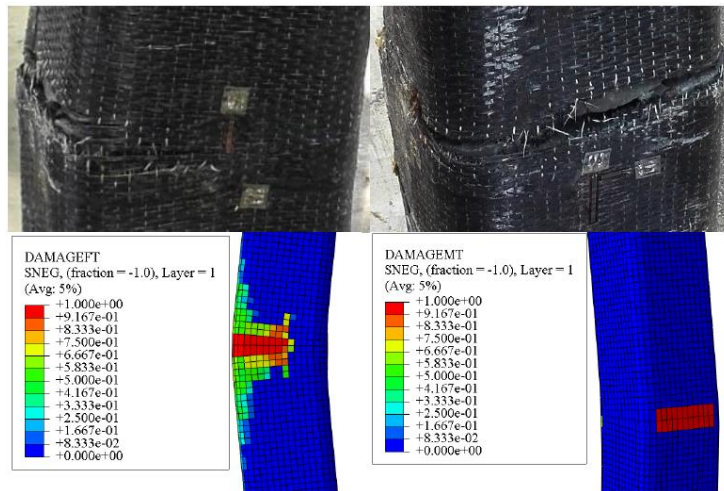
circumferential layers of CFRP occurred subsequently due to the opening of the tensile flexural cracking.



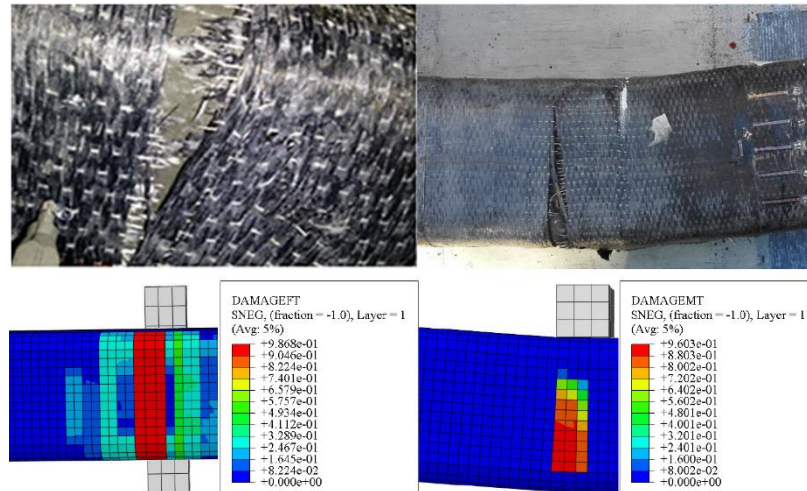
(a)



(b)



(c)

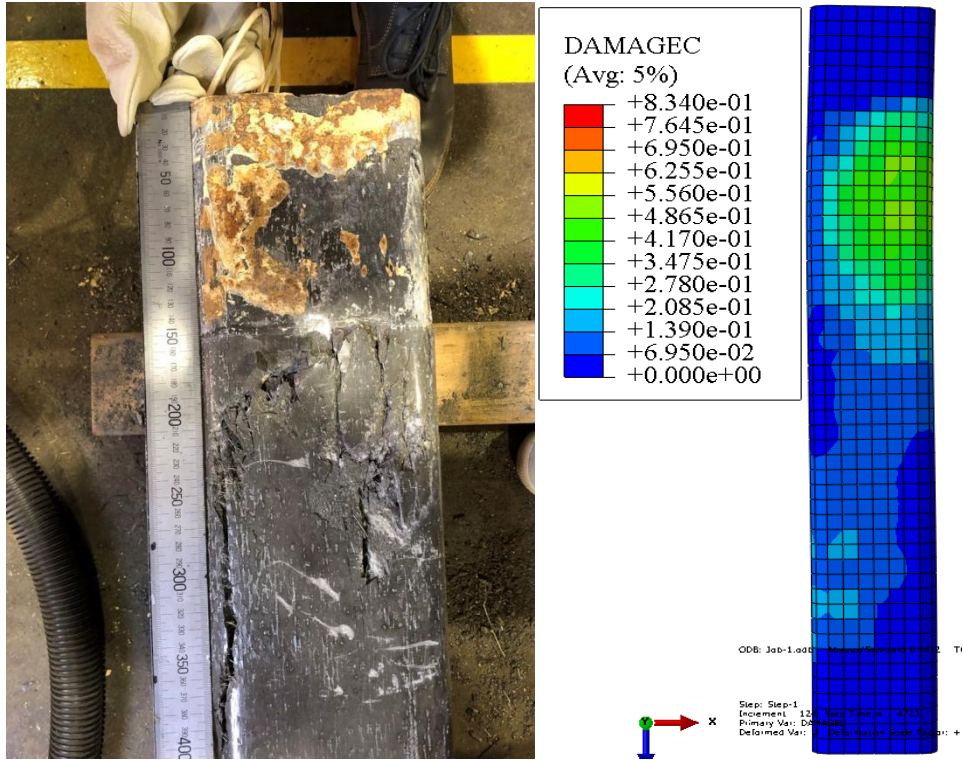


(d)

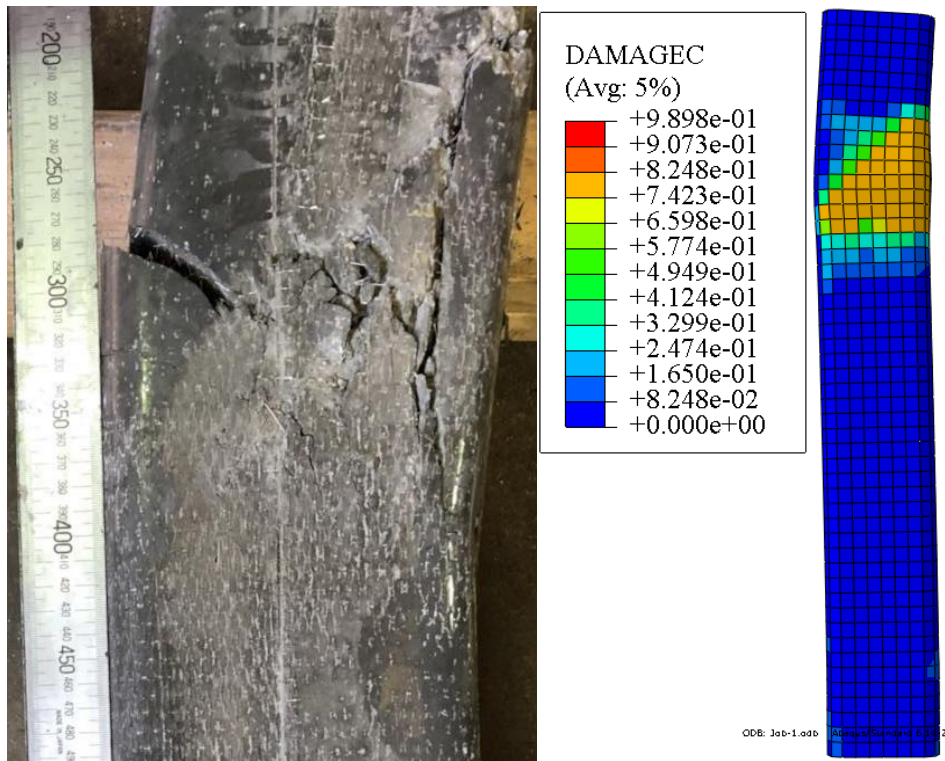
Figure 4-14. Comparisons between localized failure pattern and FE simulated damage patterns (DAMAGEFT and DAMAGEMT) of CFRP tube: (a) eccentricity = 10 mm; (b) eccentricity = 35 mm; (c) eccentricity = 50 mm; (d) beam

### 4.5.3. Comparisons of failure mode regarding UHPFRC

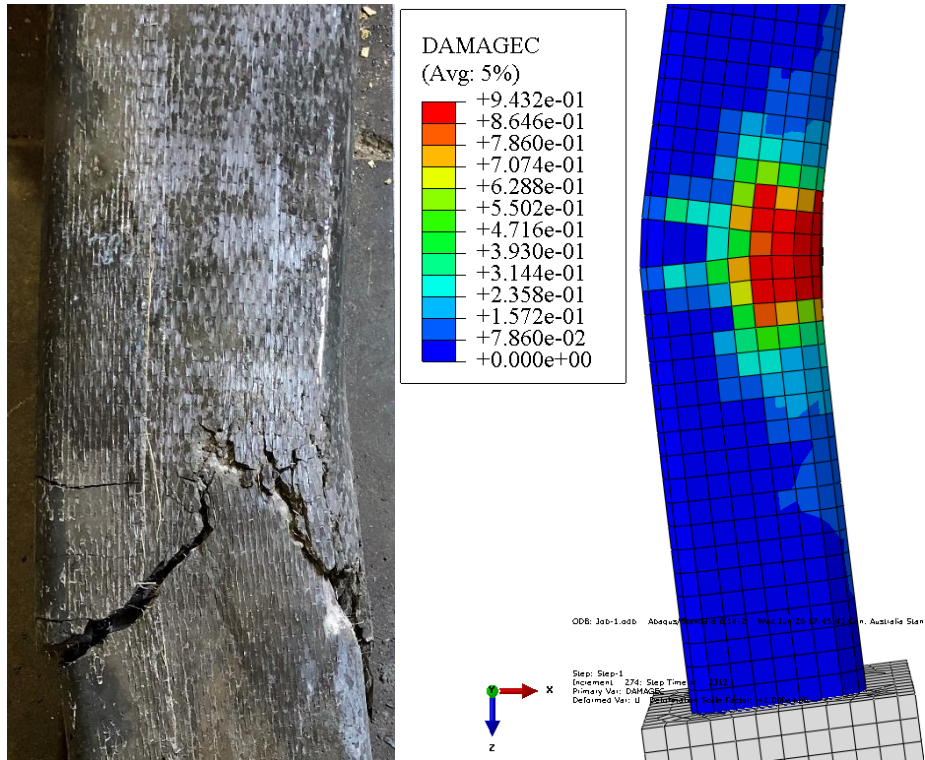
The concrete damage parameters were defined using values of  $d_c$  and  $d_t$  (refer to Eq. 9 and 10), and these were input into the CDP model. FE model exhibited a high accuracy in predicting both the load-middle height deflection responses and the concrete damage (compressive and tensile) patterns as shown in Figs.4-15 and 4-16, which further highlight the applicability and reliability of the developed FE models. For example, compressive damage patterns for eccentrically loaded columns CC-35 and CC-50 are demonstrated in Fig. 4-15 (b)-(c), where a wedge shape of region featured with a high damage level is clearly observed from all compressive damage patterns. A typical compressive concrete wedge with a damage level of 82.5% shown in the simulated damage pattern of column CC-35 and this agrees well with the actual concrete crushed region shown in Fig. 4-15 (b). Similar observations appear through the comparisons in Fig. 4-16 (c) with a damage level of 94.3%. For CFRP-CFFT UHPFRC columns loaded with an eccentricity of 35 mm, a single flexural tensile crack occurred close to the location of top steel cap has been successfully simulated by the FE model as presented in Fig. 4-16 (a) with a severe damage level of 98%. Furthermore, for both columns CC-50 and CC-85, a severe major tensile crack occurred at the middle height of the column, and this observation has been appropriately simulated by the FE model and the corresponding tensile cracking pattern is shown in Fig.4-16 (b).



(a)

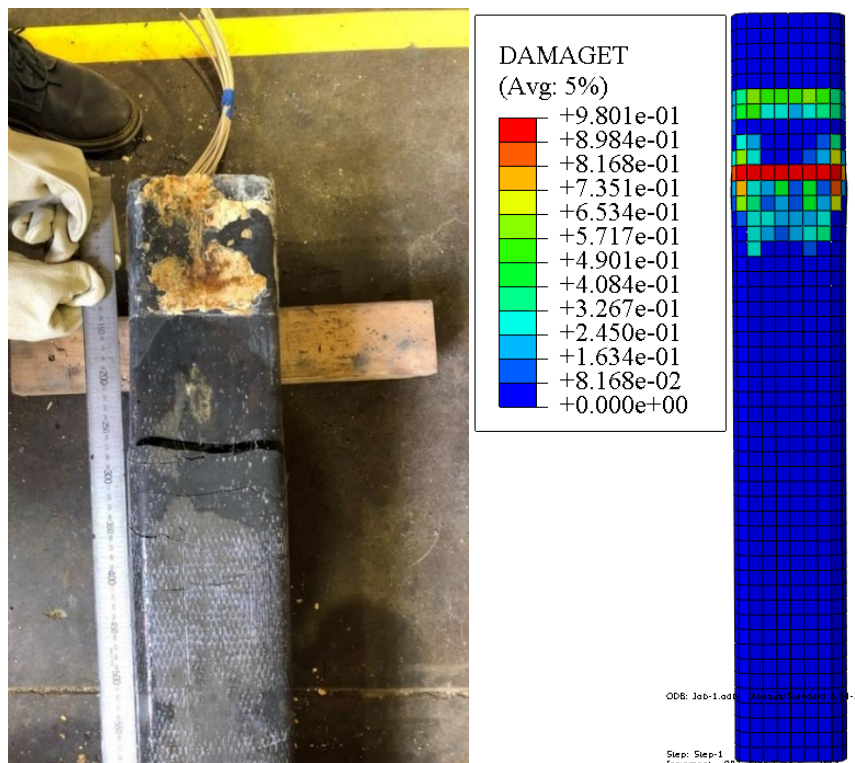


(b)

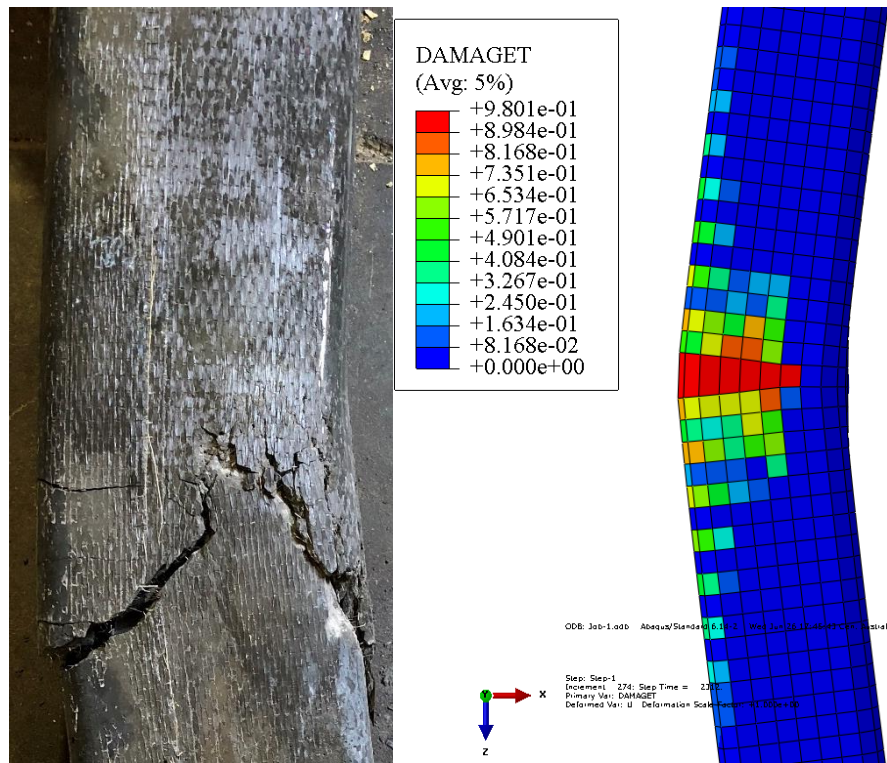


(c)

Figure 4-15. Comparisons between failure modes and compressive FE damage patterns: (a) eccentricity = 10 mm; (b) eccentricity = 35 mm; (c) eccentricity = 50 mm



(a)



(b)

Figure 4-16. Comparisons between failure modes and tensile FE damage patterns: (a) eccentricity = 35 mm; (b) eccentricity = 50 mm

#### 4.5.4. Comparisons of load-moment interaction curves

By combining the results obtained from the FE simulation for CFRP-CFFT UHPFRC columns loaded with eccentricities from 0 to 85 mm and the CFTT-UHPFRC beam subjected to four point bending, a complete load-moment ( $P$ - $M$ ) interaction envelope was generated in conjunction with the experimental results, as indicated in Fig. 4-17. The load-moment ( $P$ - $M$ ) interaction curve generated by FE simulation agrees very well with the corresponding curve obtained experimentally. Note that the ratios of  $P_{u-FEM} / P_{u-exp}$  and  $M_{u-FEM} / M_{u-exp}$  is almost equal to 1 with very low standard deviations (SD) of 0.008 and 0.006, respectively.

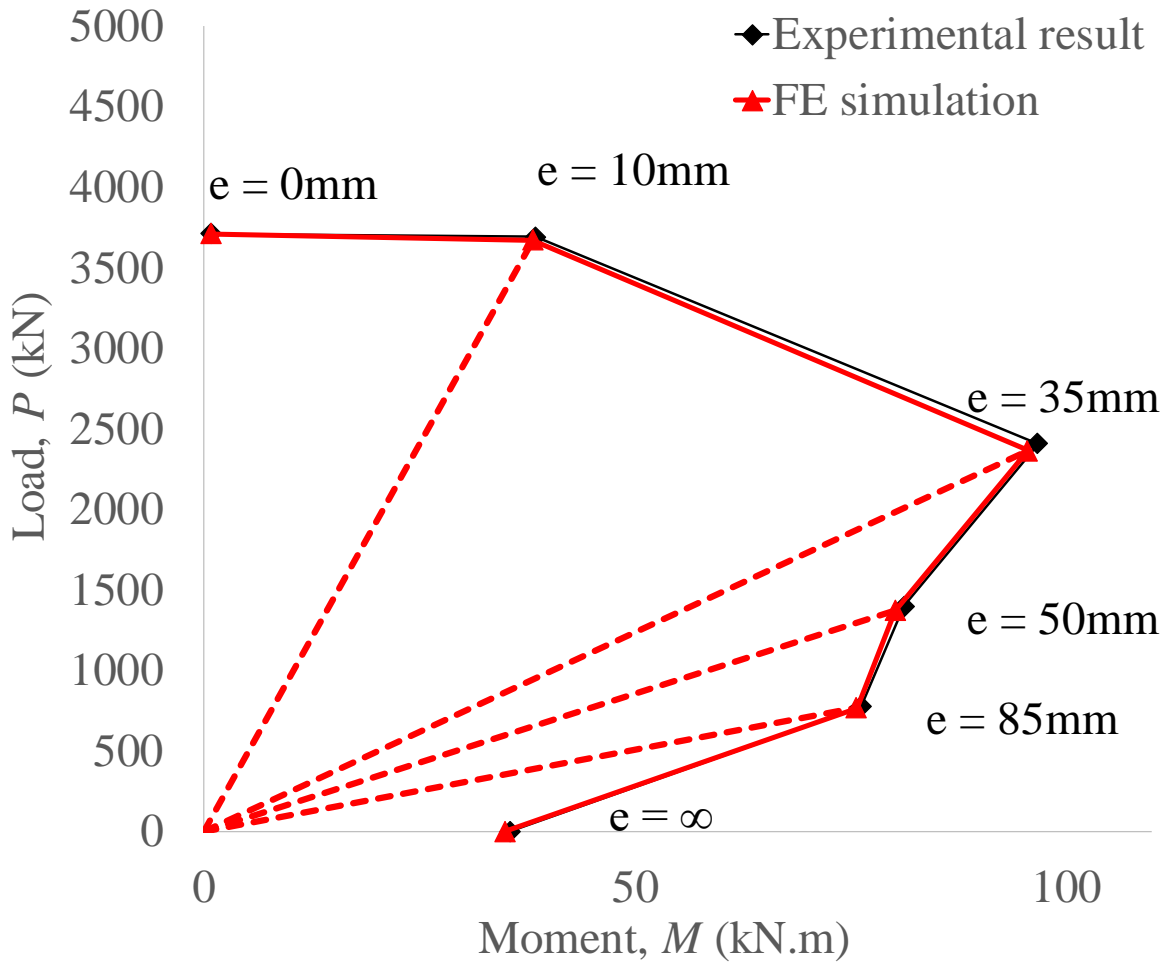


Figure 4-17. Load-Moment interaction diagram for CFRP-CFFT UHPFRC columns

#### 4.6. CONCLUSIONS

This paper presents the results of an experimental and numerical study aimed to investigate the structural mechanism of five CFRP-CFFT UHPFRC columns subjected to concentric and eccentric axial loads together with a simply supported CFRP-CFFT UHPFRC beam subjected to four-point bending. Based on the discussions and results presented in this study, the following major conclusions can be drawn:

- A slight increase in eccentricity of loading from 0 mm to 10 mm only leads to a minor reduction in the magnitude of the  $P_u$  but induces a considerable enhancement in the values of  $M_u$ , and a further increase in the eccentricity of loading above 35 mm would significantly affect both magnitudes of  $P_u$  and  $M_u$ .

- Based on comparisons in load-moment ( $P_u - M_u$ ) interaction relationship in present study, it is suggested that the balanced failure of the CFRP-CFFT UHPFRC columns commences when the eccentricity of loading is increased to 35 mm.
- To analyse the structural performance of the CFRP-CFFT UHPFRC members, FE models were successfully developed using only the fundamental material properties of the constituents of the beam and the columns and these models exhibit a good correlation with test results.
- Developed FE models were able to simulate accurately the structural response ( $P - \delta_{axial}$  and  $P - \delta_{lateral}$ ) of the tested CFRP-CFFT UHPFRC columns and the beam in this study, and the corresponding damage patterns of CFRP tubes and concrete were also successfully simulated. It is worth noting that the proposed load-moment ( $P-M$ ) interaction envelope has a high correlation with the corresponding curve obtained experimentally, and it forms a foundation for the future design of the CFRP-CFFT UHPFRC columns.

#### **4.7. ACKNOWLEDGMENTS**

Sincere thanks are due to the undergraduate students Mr. M Liu, Mr. K Ariyawansa, Mr. H Wu, Miss. M Tang and master students Mr. X Cui, and Mr. Z Wang who assisted the experiments reported in this paper as a part of their bachelor and master thesis. Thanks are due to Dr. M Ridha, Dr. MS Mohamed Ali and Mr. J Ayoub for the usage of steel cap arrangement for the column tests.



#### 4.8. REFERENCES

- [1] Kang ST, Lee Y, Park YD, Kim JK. Tensile fracture properties of an Ultra High Performance Fiber Reinforced Concrete (UHPFRC) with steel fiber. *Composite Structures*. 2010 Jan 1;92(1):61-71.
- [2] Yoo DY, Banthia N, Kang ST, Yoon YS. Effect of fiber orientation on the rate-dependent flexural behavior of ultra-high-performance fiber-reinforced concrete. *Composite Structures*. 2016 Dec 1;157:62-70.
- [3] Cao YY, Yu QL. Effect of inclination angle on hooked end steel fiber pullout behavior in ultra-high performance concrete. *Composite Structures*. 2018 Oct 1;201:151-60.
- [4] Abrishambaf A, Pimentel M, Nunes S. A meso-mechanical model to simulate the tensile behaviour of ultra-high performance fibre-reinforced cementitious composites. *Composite Structures*. 2019 Aug 15;222:110911.
- [5] Zhou B, Uchida Y. Influence of flowability, casting time and formwork geometry on fiber orientation and mechanical properties of UHPFRC. *Cement and Concrete Research*. 2017 May 1;95:164-77.
- [6] Safdar M, Matsumoto T, Kakuma K. Flexural behavior of reinforced concrete beams repaired with ultra-high performance fiber reinforced concrete (UHPFRC). *Composite structures*. 2016 Dec 1;157:448-60.
- [7] Tanarslan HM. Flexural strengthening of RC beams with prefabricated ultra high performance fibre reinforced concrete laminates. *Engineering Structures*. 2017 Nov 15;151:337-48.
- [8] Nguyen H, Mutsuyoshi H, Zatar W. Hybrid FRP-UHPFRC composite girders: Part 1– Experimental and numerical approach. *Composite Structures*. 2015 Jul 1;125:631-52.

- [9] Shams A, Stark A, Hoogen F, Hegger J, Schneider H. Innovative sandwich structures made of high performance concrete and foamed polyurethane. *Composite Structures*. 2015 Mar 1;121:271-9.
- [10] Nguyen H, Mutsuyoshi H, Zatar W. Push-out tests for shear connections between UHPFRC slabs and FRP girder. *Composite Structures*. 2014 Dec 1;118:528-47.
- [11] Khan MI, Al-Osta MA, Ahmad S, Rahman MK. Seismic behavior of beam-column joints strengthened with ultra-high performance fiber reinforced concrete. *Composite Structures*. 2018 Sep 15;200:103-19.
- [12] Guo W, Fan W, Shao X, Shen D, Chen B. Constitutive model of ultra-high-performance fiber-reinforced concrete for low-velocity impact simulations. *Composite Structures*. 2018 Feb 1;185:307-26.
- [13] Xu J, Wu C, Xiang H, Su Y, Li ZX, Fang Q, Hao H, Liu Z, Zhang Y, Li J. Behaviour of ultra high performance fibre reinforced concrete columns subjected to blast loading. *Engineering Structures*. 2016 Jul 1;118:97-107.
- [14] Yoo DY, Banthia N, Kim SW, Yoon YS. Response of ultra-high-performance fiber-reinforced concrete beams with continuous steel reinforcement subjected to low-velocity impact loading. *Composite Structures*. 2015 Aug 1;126:233-45.
- [15] Li PP, Yu QL. Responses and post-impact properties of ultra-high performance fibre reinforced concrete under pendulum impact. *Composite Structures*. 2019 Jan 15;208:806-15.
- [16] Hassan AM, Mahmud GH, Jones SW, Whitford C. A new test method for investigating punching shear strength in Ultra High Performance Fibre Reinforced Concrete (UHPFRC) slabs. *Composite Structures*. 2015 Nov 1;131:832-41.
- [17] Empelmann M, Teutsch M, Steven G. Expanding the application range of RC-columns by the use of UHPC. *Tailor Made Concrete Structures*. 2008: 461-468.

- [18] Steven G, Empelmann M. UHPFRC-columns with high-strength longitudinal reinforcement. *BETON-UND STAHLBETONBAU*. 2014 May 1;109(5):344-54.
- [19] Hosinieh MM, Aoude H, Cook WD, Mitchell D. Behavior of ultra-high performance fiber reinforced concrete columns under pure axial loading. *Engineering Structures*. 2015 Sep 15;99:388-401.
- [20] Shin HO, Min KH, Mitchell D. Confinement of ultra-high-performance fiber reinforced concrete columns. *Composite Structures*. 2017 Sep 15;176:124-42.
- [21] Shin HO, Min KH, Mitchell D. Uniaxial behavior of circular ultra-high-performance fiber-reinforced concrete columns confined by spiral reinforcement. *Construction and Building Materials*. 2018 Apr 20;168:379-93.
- [22] Aarup B, Jensen LR, ApS HC, Ellegaard P. Slender CRC columns. *Nordic Concr Res*. 2005;34:80-97.
- [23] Hung CC, Hu FY, Yen CH. Behavior of slender UHPC columns under eccentric loading. *Engineering Structures*. 2018 Nov 1;174:701-11.
- [24] Yoo DY, Yoon YS. A review on structural behavior, design, and application of ultra-high-performance fiber-reinforced concrete. *International Journal of Concrete Structures and Materials*. 2016 Jun 1;10(2):125-42.
- [25] Zohrevand P, Mirmiran A. Cyclic behavior of hybrid columns made of ultra high performance concrete and fiber reinforced polymers. *Journal of Composites for Construction*. 2011 Jun 15;16(1):91-9.
- [26] ASTM D3039/D3039M. Standard Test Method for Tensile Properties of Polymer Matrix Composite Materials. ASTM International; 2017
- [27] Razvi S, Saatcioglu M. Confinement model for high-strength concrete. *Journal of Structural Engineering*. 1999 Mar;125(3):281-9.

- [28] ASTM A820. Standard Specification for Steel Fibers for Fiber-Reinforced Concrete. ASTM International; 2016
- [29] Malik AR, Foster SJ. Carbon Fiber-Reinforced Polymer Confined Reactive Powder Concrete Columns--Experimental Investigation. *ACI Structural Journal*. 2010 May 1;107(3).
- [30] Fang C, Mohamed Ali MS, Sheikh AH, Singh M. Numerical and Finite-Element Analysis of Short Ultrahigh-Performance Fiber-Reinforced Concrete Columns. *Journal of Structural Engineering*. 2019 Aug 9;145(10):04019111.
- [31] Singh M, Sheikh AH, Ali MM, Visintin P, Griffith MC. Experimental and numerical study of the flexural behaviour of ultra-high performance fibre reinforced concrete beams. *Construction and Building Materials*. 2017 May 1;138:12-25.
- [32] Singh M, Sadakkathulla M, Sheikh AH, Griffith MC, Visintin P. Structural behaviour of ultra high performance fibre reinforced concrete beams with steel and polymer bar reinforcement. In: *Proceedings of The 11th fib International PhD Symposium in Civil Engineering*. 2016. pp.287-294
- [33] Lubliner J, Oliver J, Oller S, Oñate E. A plastic-damage model for concrete. *International Journal of solids and structures*. 1989 Jan 1;25(3):299-326.
- [34] Lee, J., and G. L. Fenves, Plastic-Damage Model for Cyclic Loading of Concrete Structures, *Journal of Engineering Mechanics*, 1998, vol. 124, no.8, pp. 892–900.
- [35] Birtel V, Mark P. Parameterised finite element modelling of RC beam shear failure. In *ABAQUS users' conference 2006* May (pp. 95-108).
- [36] Hashin Z, Rotem A. A fatigue failure criterion for fiber reinforced materials. *Journal of composite materials*. 1973 Oct;7(4):448-64.
- [37] Hashin Z. Failure criteria for unidirectional fiber composites. *Journal of applied mechanics*. 1980 Jun 1;47(2):329-34.

[38] Hoang H, Toan V. Simplified design of a commercial aircraft wing made of carbon fiber. universidad carlos iii de madrid, Spain, 2015

**THIS PAGE HAS BEEN LEFT INTENTIONALLY BLANK**

## **CHAPTER 5. Conclusions and Future Work**

### **5.1. INTRODUCTION**

The detailed scientific findings from this body of thesis work and suggestions for promoting future investigations are summarised in this chapter. In this thesis work, the research primarily focused on issues pertaining to UHPC and UHPFRC from the level of material characteristics and then extended to the level of structural responses and the details are as follows:

- (1) The first major area of research was to study the relevant critical factors that dominate both the dry and autogenous shrinkage characteristics of the UHPC and hence to propose effective techniques to reduce the shrinkage strain and the corresponding impacts. Subsequently, characteristic tests were conducted to address the major underlying mechanisms corresponding to the experimental observations.
- (2) The second major area of research was to investigate the effects of the different characteristics of fibre such as fibre volume fraction, the fibre aspect ratio, and the type of steel fibre on the total and autogenous shrinkage mechanisms.
- (3) The third major area of research was to develop structural mechanics based analytical procedures to accurately simulate the structural responses of short UHPFRC columns subjected to either concentric or eccentric axial loads. Additionally, finite element (FE) analysis was also conducted to simulate both the structural responses and corresponding damage patterns of the short columns.
- (4) The fourth major research area was to investigate the structural behaviour of slender UHPFRC columns by conducting a series of structural testing on slender UHPFRC columns subjected to either concentric or eccentric axial loads. Subsequently, FE analysis was conducted to simulate both the structural responses and corresponding damage patterns; the FE modelling was also extended to conduct a parametric study for investigating the

influences of slenderness ratio in regards to the corresponding structural responses such as the load bearing capacity, moment capacity, ductility index, and residual strength factor.

(5) Lastly, detailed investigations were performed to experimentally study the structural performances of CFRP-CFFT UHPFRC columns loaded concentrically and eccentrically. Furthermore, FE analysis was conducted in conjunction with the concrete damage plasticity (CDP) model for concrete and Hashin's damage model for CFRP to simulate the structural responses and corresponding damage patterns for both UHPFRC and CFRP tubes.

## **5.2. INVESTIGATIONS IN SHRINKAGE CHARACTERISTICS OF UHPC**

In this investigation, total shrinkage and autogenous shrinkage strains were measured and compared. The main parameters investigated in this study are the binder to sand ratio ranged from 0.8 to 1.266, volume content of shrinkage reducing agent (SRA), and percentage of crushed ice dosages substituting the normal tap water. The major conclusions from this study are as follows:

- Autogenous shrinkage of the UHPC decreases with an increase in the binder to sand ratio due to the restraint effects of remaining unreacted binders in UHPC which reduced the autogenous shrinkage strain values.
- An increase in the binder to sand ratio in the UHPC mix leads to a decrease in the porosity of the concrete. For UHPC prepared using a lower binder to sand ratio, the abundance of crystalline ettringite and C-H in the pores and cracks in the concrete minimized the drying shrinkage of the concrete.
- A binder to sand ratio of 1 is the optimal ratio for UHPC to achieve the minimum autogenous and dry shrinkage strains without a reduction in the compressive strength.



- Additional dosage of SRA is effective in reducing the autogenous shrinkages (up to 55% at 90 days with 3% of SRA dosage), but the corresponding compressive strength also reduced with an increase in the dosage of the SRA.
- The replacement of half of the normal mixing water by crushed ice in a UHPC mix can reduce the autogenous shrinkage values of the UHPC up to 22% and has nearly no effect on the drying shrinkage properties of the UHPCs. This technique is cost-effective and easier to apply in any cast in-situ or pre-casting constructions.

### **5.3. INVESTIGATIONS OF THE EFFECTS OF STEEL FIBRES ON THE SHRINKAGE OF UHPFRC**

Having established an optimal UHPC mixture with a binder to sand ratio of 1, additional steel fibres with dosages from 1.5% to 2.5% were added to the mixture to investigate their influences associated with the corresponding shrinkage strains. Effects of fibre aspect ratios of 45, 65, and 80, and the fibre types (hooked end fibre and straight fibre) were experimentally studied. Direct pull-out tests were also conducted on specimens in which steel fibres were embedded in the UHPC, and the corresponding results were interpreted to explain the underlying mechanism governing the magnitudes of both autogenous and drying shrinkages. The following major conclusions can be drawn based on the test results on the shrinkage properties of the UHPFRCs:

- Incorporation of discrete steel fibres into a UHPC matrix can significantly reduce the total- and autogenous- shrinkage due to the restraint effects induced by the bond stress between the fibres and matrix. The evaluations of measurements also revealed that an increase in fibre volume fraction or fibre aspect ratio results in significant reduction of both total and autogenous shrinkage magnitudes.

- It was found that adding steel fibres with hooked ends into the UHPC matrix is more efficient than adding the straight micro-fibres into the UHPC matrix for the purpose of reducing the total and autogenous shrinkage values.
- In reducing the shrinkage strains, the aspect ratio of the fibre is not as influential as the volume fraction and the shape of fibre on the long-term shrinkage properties of the UHPFRCs.

#### **5.4. NUMERICAL AND FE MODELLING OF SHORT UHPFRC COLUMNS**

In this study, a numerical model was developed based on the moment-rotation ( $M/\theta$ ) approach incorporating the partial-interaction (PI) mechanism using concrete and reinforcement material properties in these model successfully simulated the structural responses such as load-axial deflection ( $P-\delta_{axial}$ ) or load-middle height deflection ( $P-\delta_{mid}$ ) relationships of the short UHPFRC columns when they are either subjected to concentric or eccentric loads, and the following conclusions can be made:

- With the fundamental material properties of concrete and steel reinforcements obtained the  $P-\delta_{mid}$  relationships of eccentrically loaded columns without resorting to costly and time-consuming structural tests on UHPFRC columns.
- The proposed axial load-moment ( $P-M$ ) interaction envelopes generated in this study accurately predict the behaviors of short column loaded with various eccentricities, and this highlights the reliability of the numerical models in simulating the behaviors of eccentrically loaded UHPFRC columns. Therefore, it can serve as the basis for further research and design of the UHPFRC columns.
- FE simulations successfully reproduced the damage patterns of UHPFRC members under different loading conditions. Comparisons of these simulated damage patterns indicate that

the compressive damage level of short UHPFRC columns decreases with an increase in the eccentricity of the axial load.

## **5.5. EXPERIMENTAL AND NUMERICAL INVESTIGATIONS SLENDER UHPFRC COLUMNS AND THE CORRESPONDING EFFECTS OF SLENDERNESS**

In this study, the slender UHPFRC columns were analysed using FE model developed by incorporate a novel CDP model and the numerical results are then further extended to conduct a parametric study for investigating the influences of slenderness on the structural responses of the slender UHPFRC columns. The major conclusions from this study are:

- An increase in the eccentricity of the axial load from 0 mm to 35 mm results in a huge drop in the value of the load bearing capacity ( $P_u$ ), with increase with the corresponding values of ductility indices ( $I_5$ ,  $I_{10}$ ) and residual strength factor ( $R_{5, 10}$ ) which indicate an improve ductility.
- In order to conduct the analysis regarding the structural response of the slender UHPFRC columns and the UHPFRC beam, FE models accurately simulated the structural behaviours, damage patterns, and load-moment ( $P-M$ ) relationships with the established material properties of both UHPFRC and steel reinforcements.
- By conducting a parametric study with the developed FE models, the influences of slenderness ratio ( $\lambda$ ) in regards to the structural performance were investigated. It can be inferred that the magnitudes of  $P_u$ ,  $M_u$ ,  $I_{10}$ , and  $R_{5,10}$  decrease with an increase in the values of  $\lambda$ ; particularly, the increases in the values of  $\lambda$  significantly reduce the residual strength and stability of the column.
- From the simulated results, it can be inferred that the magnitudes of load bearing capacity, moment capacity, ductility index and residual strength ratio decrease with an increase in

the values of slenderness ratio, and a threshold value of the slenderness ratio was found to be to prevent the occurrences of the global buckling in UHPFRC slender columns.

## **5.6. EXPERIMENTAL AND NUMERICAL INVESTIGATIONS ON CFRP-CFFT UHPFRC COLUMNS**

In this study, the both experimental and numerical investigation were carried out to understand the structural mechanism of five CFRP-CFFT UHPFRC columns subjected to concentric and eccentric axial loads together with a simply supported CFRP-CFFT UHPFRC beam subjected to four-point bending. Based on the discussions and results presented in this study, the following major conclusions can be drawn:

- A slight increase in eccentricity of loading from 0 mm to 10 mm only leads to a minor reduction in the magnitude of the  $P_u$  but induces a considerable enhancement in the values of  $M_u$ , and a further increase in the eccentricity of loading above 35 mm would significantly affect both magnitudes of  $P_u$  and  $M_u$ .
- Based on comparisons in load-moment ( $P_u - M_u$ ) interaction relationship, it was suggested that the balanced failure of the CFRP-CFFT UHPFRC columns commences when the eccentricity of loading is increased to 35 mm.
- To analyse the structural performance of the CFRP-CFFT UHPFRC members, FE models were successfully developed using only the fundamental material properties of the constituents of the beam and the columns and these models exhibited a good correlation with test results.

## **5.7. SCOPE FOR FUTURE WORK**

Having both the shrinkage characteristics in the material of UHPC and structural responses of UHPFRC axial members investigated further extensions of the investigation on UHPC and UHPFRC should be undertaken:

1. To fully understand the material properties of UHPC or UHPFRC in a time dependent behaviour, influences of both compressive and tensile creep can be investigated.
2. It is also worth developing a numerical model for quantifying the influences of the compressive and tensile creep with regards to the corresponding compressive and tensile strength based on a well-organised database.
3. Having proposed numerical models that successfully simulated the structural response of short UHPFRC columns, it can be further extended to simulate the structural behaviours of slender columns.
4. It is worth to extend both experimental and numerical investigations on UHPFRC columns which were subjected to lateral cyclic loads, as limited studies are available on the seismic response of UHPFRC columns and the design codes require enrich databases for their recommendations.
5. Beam-column joint assembly play a crucial role both during the design and construction stages of a high-rise building. They are considered to be critical regions with complex stress states and hence the concrete material properties plays a key role in maintaining the stability of the structure. Considerable high strength and exceptional ductility of UHPFRC make it an attractive option for replacing normal concrete to resist cyclic and seismic loads and this area needs further research.

## **5.8. SUMMARY**

The major contribution of this thesis is towards the investigations of the shrinkage characteristics and associated factors that affect the magnitudes of both drying and autogenous shrinkage strains. This facilitates the optimization of the UHPC and UHPFRC recipes and hence to widen the application of UHPC in the modern constructions. Moreover, the development of the analytical approaches and FE modelling contribute towards developing guidelines for the design of UHPFRC columns.

## **APPENDIX I. Published paper**

**Copy of Paper 1: Characterizations of Autogenous and drying shrinkage of ultra-high performance concrete (UHPC): An experimental study (As published).**

**Copy of paper 3: Numerical and Finite-Element Analysis of Short Ultrahigh-Performance Fiber-Reinforced Concrete Columns (As published).**



## Characterizations of autogenous and drying shrinkage of ultra-high performance concrete (UHPC): An experimental study

T. Xie, C. Fang, M.S. Mohamad Ali, P. Visintin\*

School of Civil, Environmental and Mining Engineering, The University of Adelaide, South Australia 5005, Australia



### ARTICLE INFO

#### Keywords:

Ultra-high performance concrete (UHPC)  
Autogenous shrinkage  
Free total shrinkage  
Compressive strength  
Microstructure  
Hydration

### ABSTRACT

Due to the high content of binder and low water to cement ratio, ultra-high performance concrete (UHPC), exhibits higher levels of autogenous shrinkage compared to ordinary concrete. This shrinkage has been shown to lead to a reduction in strength over time as a result of the formation of thermal and shrinkage cracks. Aiming to mitigate the negative impacts associated with shrinkage, the efficacy of three different techniques to reduce the impact of shrinkage are investigated, namely: reducing the binder content; incorporating high levels of shrinkage reducing admixture; and using crushed ice to partially replace mixing water. The effects of these techniques are experimentally investigated and the underlying mechanisms of the actions are characterized. It is found that autogenous shrinkage predominates the overall shrinkage of UHPC and that the three techniques can effectively reduce shrinkage without significantly compromising its mechanical strength. The results also suggest, that from the perspective of reducing shrinkage: the optimal binder-to-sand ratio is in the range of 1–1.1; the optimal dosage rate of shrinkage reducing admixture is 1%; and replacing of mixing water by crushed ice up to 50% by weight has also induced a significant reduction in shrinkage.

### 1. Introduction

Ultra-high performance concrete (UHPC) is characterized by very high compressive strength and superior durability [1–5]. These characteristics are typically achieved using mix designs with high quantities of binder (cement and silica fume) and low water to cement ratios (in the order of 0.2 or less). As a result, partially hydrated binder is often present within the mortar resulting in an increase in autogenous shrinkage [6,7] up to an order of magnitude greater than that of conventional concrete [8–13]. Hence total shrinkage strains in UHPC (including both the autogenous- and drying-shrinkage) are expected to be higher than conventional concrete. This is significant as high early age shrinkage strains may result in early age cracking [4,9,14–16]; and if containing fibers, a reduction in strength over time due to the restraint provided by fibers [9,11,17,18].

The importance of quantifying shrinkage strains has led to a number of recent studies aimed at understanding the underlying mechanisms governing autogenous shrinkage of UHPC and its impact on performance. For example, experimental programs conducted by Yoo et al. [15,19,20] and Şahmaran et al. [16,21,22] systematically examined the effects of mixing proportion, curing condition, geometry and specimen restraint on autogenous shrinkage of UHPC specimens. Research has also identified several means for reducing both the magnitude of

shrinkage strains, as well as the time over which they develop. For example, Rößler et al. [23] have shown that by curing at a temperature of 20 °C, a reduction of 85% in autogenous shrinkage strains is possible compared to those obtained under at 90 °C heat curing. Alternatively [24,25] have shown that it is possible to reduce drying shrinkage via the inclusion of moisture retaining superabsorbent polymers into the mix. These release water over time, replacing that lost due to hydration and drying, resulting in a reduction of shrinkage strains of up to 75%. The effects of shrinkage reducing admixtures on the autogenous shrinkage of UHPC have been investigated by Refs. [11,26,27].

In this paper a standard UHPC mix which has been widely investigated at both the material [14,28,29] and member levels [1,30,31] is taken as a baseline, and simple means for improving its dimensional stability is investigated. Approaches considered in this study include:

- The use of iced water in the mix design to lower concrete temperature and hence reduce the potential for autogenous shrinkage and temperature induced deformations [32].
- Varying mix design proportions to identify the beneficial restraining influence of (fine) aggregate, and the presence of unhydrated binders that may act as a filler providing additional dimensional stability.
- Varying mix design proportions to identify the reduction in

\* Corresponding author.

E-mail address: [phillip.visintin@adelaide.edu.au](mailto:phillip.visintin@adelaide.edu.au) (P. Visintin).

<https://doi.org/10.1016/j.cemconcomp.2018.05.009>

Received 9 February 2018; Received in revised form 23 April 2018; Accepted 8 May 2018

Available online 26 May 2018

0958-9465/ © 2018 Elsevier Ltd. All rights reserved.



**Table 1**  
Mix proportion of the UHPCs.

Mix	Cement (wr)	Silica fume (wr)	Sand (wr)	water (wr)	Crushed ice (wr)	SRA <sup>1</sup> (wr)	SP <sup>2</sup> (wr)	w/b	b/s	Paste weight fraction	Mixing water weight fraction
U-0.8	0.632	0.168	1.000	0.104			0.024	0.152	0.800	0.480	0.063
U-0.9	0.711	0.189	1.000	0.117			0.027	0.152	0.900	0.509	0.067
U-1.0/SRA-0/ Ice-0	0.790	0.210	1.000	0.130			0.030	0.152	1.000	0.535	0.070
U-1.1	0.869	0.231	1.000	0.143			0.033	0.152	1.100	0.559	0.073
U-1.266	1.000	0.266	1.000	0.165			0.038	0.152	1.266	0.593	0.078
SRA-1	0.790	0.210	1.000	0.129		0.008	0.030	0.152	1.000	0.535	0.070
SRA-2	0.790	0.210	1.000	0.127		0.016	0.030	0.152	1.000	0.535	0.070
SRA-3	0.790	0.210	1.000	0.126		0.024	0.030	0.152	1.000	0.535	0.070
Ice-25/75	0.790	0.210	1.000	0.098	0.033		0.030	0.152	1.000	0.535	0.070
Ice-50/50	0.790	0.210	1.000	0.065	0.065		0.030	0.152	1.000	0.535	0.070

<sup>1</sup>. Containing 20% water.  
<sup>2</sup>. Containing 70% water.

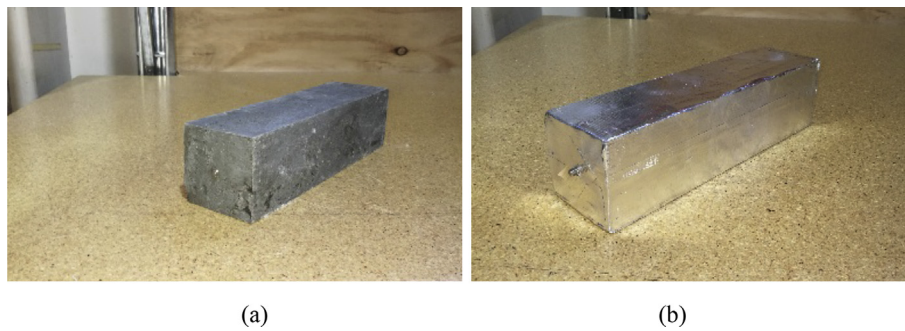


Fig. 1. Shrinkage test specimens: a) sealed prism for autogenous shrinkage measurement; b) unsealed prism for free total shrinkage measurements.

**Table 2**  
Influence of binder-to-sand ratio on rheological properties of fresh UHPCs.

Specimen	b/s ratio	Slump (mm)	Flow table (mm)	J-ring (mm)
U-0.8	0.8	165	375	412
U-0.9	0.9	240	440	451
U-1.0	1	235	425	443
U-1.1	1.1	250	430	455
U-1.266	1.266	250	470	506

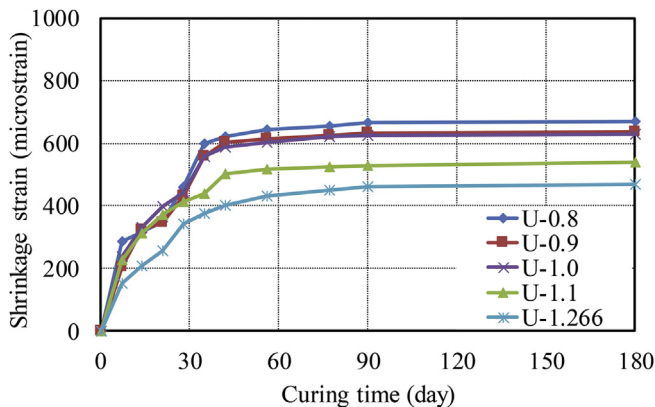


Fig. 2. Effect of binder-to-sand ratio on autogenous shrinkage.

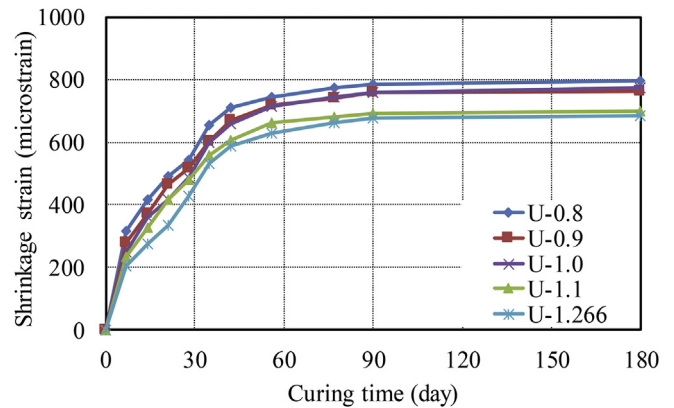


Fig. 3. Effect of binder-to-sand ratio on free total shrinkage.

characterization tests are conducted to determine the relative effectiveness of each approach, as well as the underlying mechanism of action. It is envisaged that this work will assist in allowing concrete technologists to decide on the most appropriate means for achieving the desired reduction in shrinkage.

In the remainder of the paper the characteristics and constituents of the UHPC materials investigated are first described. This is followed by a description of the experimental method and tests conducted; finally, the change in autogenous and drying shrinkage achieved by each approach is presented as well as a discussion of the mechanism of action.

## 2. Experimental program

### 2.1. Ingredients used for UHPC mix

Two types of cementitious binder were used, namely sulphate resisting cement and silica fume. The sulphate resisting cement, which

autogenous shrinkage due to a reduction in cementitious binder content.

- The use of high dosages of conventional shrinkage reducing admixtures to physically reduce shrinkage by reducing the surface tension in the concrete pore water.

For each approach investigated a range of material and

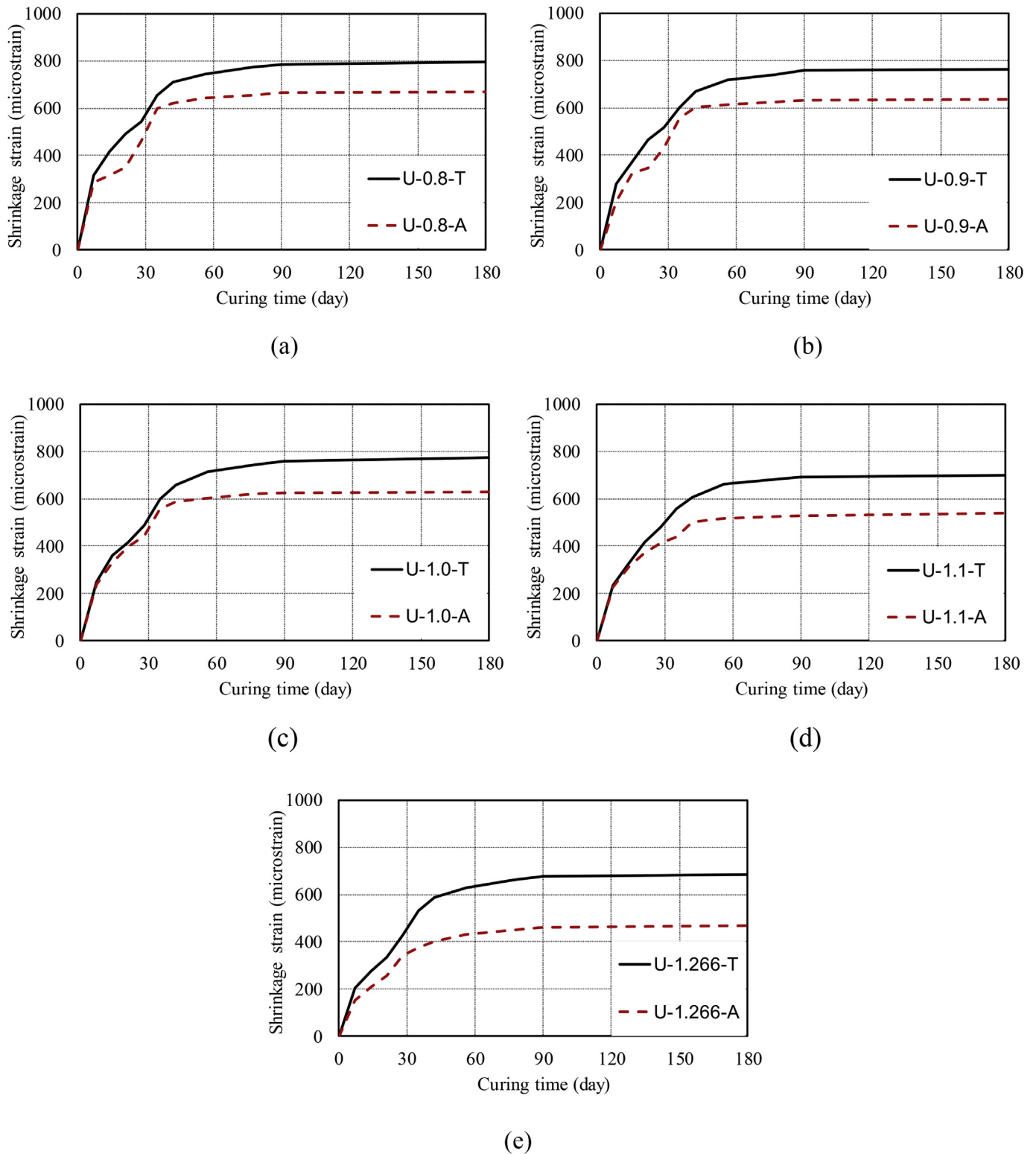


Fig. 4. Effect of binder-to-sand ratio on free drying component: a) U-0.8; b) U-0.9; c) U-1.0; d) U-1.1; (e) U-1.266.

contains 3–8% gypsum by weight, has a 28-day compressive strength of 60 MPa and a 28-day mortar shrinkage strain of 650 (microstrain) as determined through the tests performed as per AS 2350. 11 [33] and AS 2350. 13 [34], respectively. The undensified silica has a bulk density of 635 kg/m<sup>3</sup> and has a silicon dioxide (SiO<sub>2</sub>) content over 89.6%. A natural washed river sand with a maximum nominal grain size of 0.4 mm was used as the fine aggregate for all UHPC mixes. A third

generation high range water reducer with an added retarder was added to each UHPC during the mixing. For the purpose of further minimizing shrinkage, a shrinkage reducing admixture (SRA), which meets and exceeds all requirements of Australian Standard 1478.1–2000 [35] as special purpose admixture type (SN), was added to the UHPC mix with different dosages. As an alternative to the use of an SRA, aiming to prevent the generation of a large amount of heat and therefore

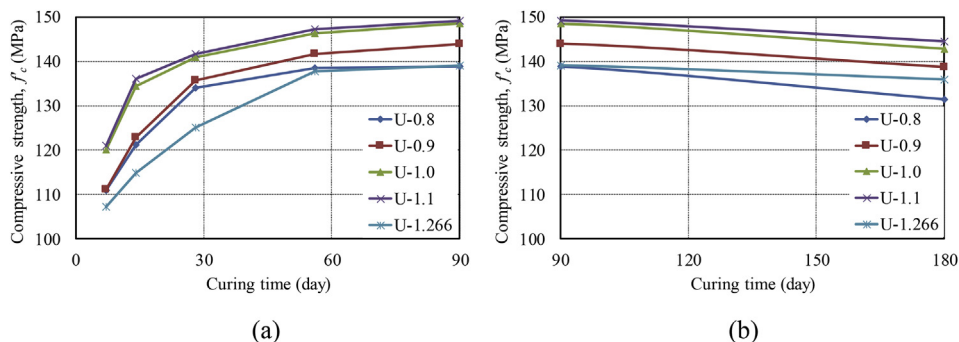


Fig. 5. Effect of binder-to-sand ratio on compressive strength: (a) curing time from 0 to 90 day; (b) curing time from 90 to 180 day.

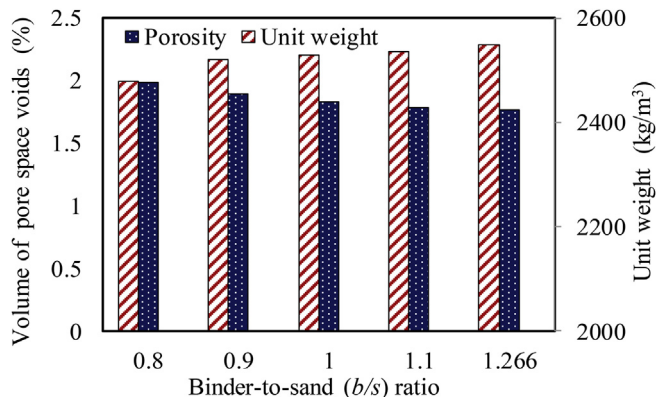


Fig. 6. Effects of binder-to-sand ratio on unit weight and porosity of hardened UHPCs.

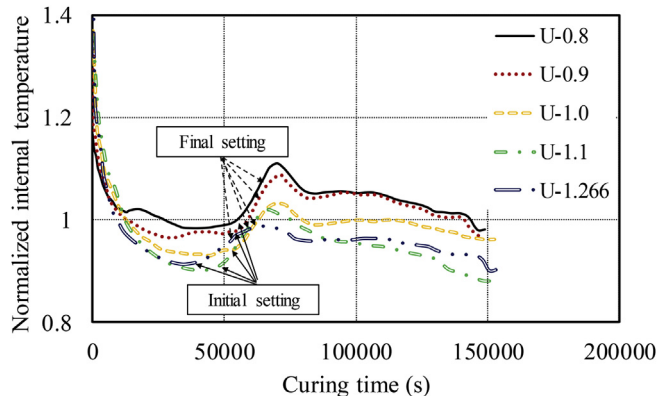


Fig. 7. Effect of binder-to-sand ratio on variations of the internal temperature with curing time.

thermally and chemically induced plastic shrinkage cracks, the use of crushed ice to partially replace mixing water is also examined.

A total of ten batches of UHPC mortar were manufactured. The first five batches of UHPCs designated as U- series were prepared using the same water-to-binder ( $w/b$ ) ratio but with different binder-to-sand ( $b/s$ ) ratios. A UHPC mix with a  $b/s$  ratio of 1.266 and  $w/b$  ratio of 0.152, which was identified as optimal using the same raw materials in the previous study [14], was used as the reference mix design. Note that the water content from the chemical admixtures (i.e. 20% in SRA and 70% in SP) has been included in the calculation of the water-to-binder ratio for each mix. In the first stage of testing, the compressive strengths and total shrinkage strains of five batches of UHPC with varying  $b/s$  ratio were measured. The mix with the overall best performance was then taken for the second stage of testing. This stage included: the addition of SRA to three mixes in dosages of SRA-to-cement weight ratio of 1, 2

or 3% (designated as SRA series) or the addition of crushed ice (designated as Ice series) was incorporated into the remaining two UHPC mixes as a partial replacement of water by a weight ratio of 25 or 50%. The proportions of all mixes are given in Table 1. For manufacturing UHPCs, all the dry materials, including sand and binders were initially mixed in an 80 L capacity rotating pan mixer with fixed blades for approximately 5 min. Following the dry mixing, water, crushed ice, superplasticizer and SRA, were subsequently added to the mixer and the mixing was continued until the concrete started to flow.

### 2.2. Test concepts and methods

To assess the effectiveness of each approach in reducing shrinkage, standard shrinkage tests were performed according to Australian Standard 2350.13 [34] over a period of 180 days when subjected to constant environmental conditions (25 °C and humidity < 50%).

To monitor the total shrinkage properties of UHPCs, square prism specimens which were 75 mm wide, and 285 mm long (shown in Fig. 1 (a)) were regularly monitored to measure the change in length. To provide an indication of the drying shrinkage relative to the total observed shrinkage, autogenous shrinkage was determined from the length change of the prisms in Fig. 1(b) which were carefully sealed with water-proof aluminum tape to prevent the moisture loss to the environment.

It is known that the evolution of autogenous shrinkage of cementitious composite is strongly related to the time when the paste develops a ‘stable’ solid skeleton to transfer tensile stress, which is defined as ‘time-zero’ for autogenous shrinkage measurement. In the present study, the final setting time obtained from calorimetry curve was adopted as the ‘time-zero’ where autogenous shrinkage initiated in according to ASTM C1698-09 [36] and the studies reported previously [37,38].

To further characterize the materials tested, and in order to identify the mechanisms controlling the change in shrinkage, a series of further material and characterization tests were undertaken as follows:

#### 2.2.1. Compressive strength

The compressive strengths ( $f_c$ ) of the UHPCs at different concrete ages were obtained through axial compression tests, performed on cylinders (100 mm diameter × 200 mm height) in accordance with Australian Standard [39].

#### 2.2.2. Flowability and passing ability

The rheological properties of each mix was assessed through a slump flow test performed in accordance with ASTM standard C143/C143M [40] and a flow-table test according to ASTM C1621 [41] including the use of a J-ring to assess passing ability around reinforcement.

#### 2.2.3. Exothermic reaction at early curing ages

Heat generated as a result of the exothermic reaction associated

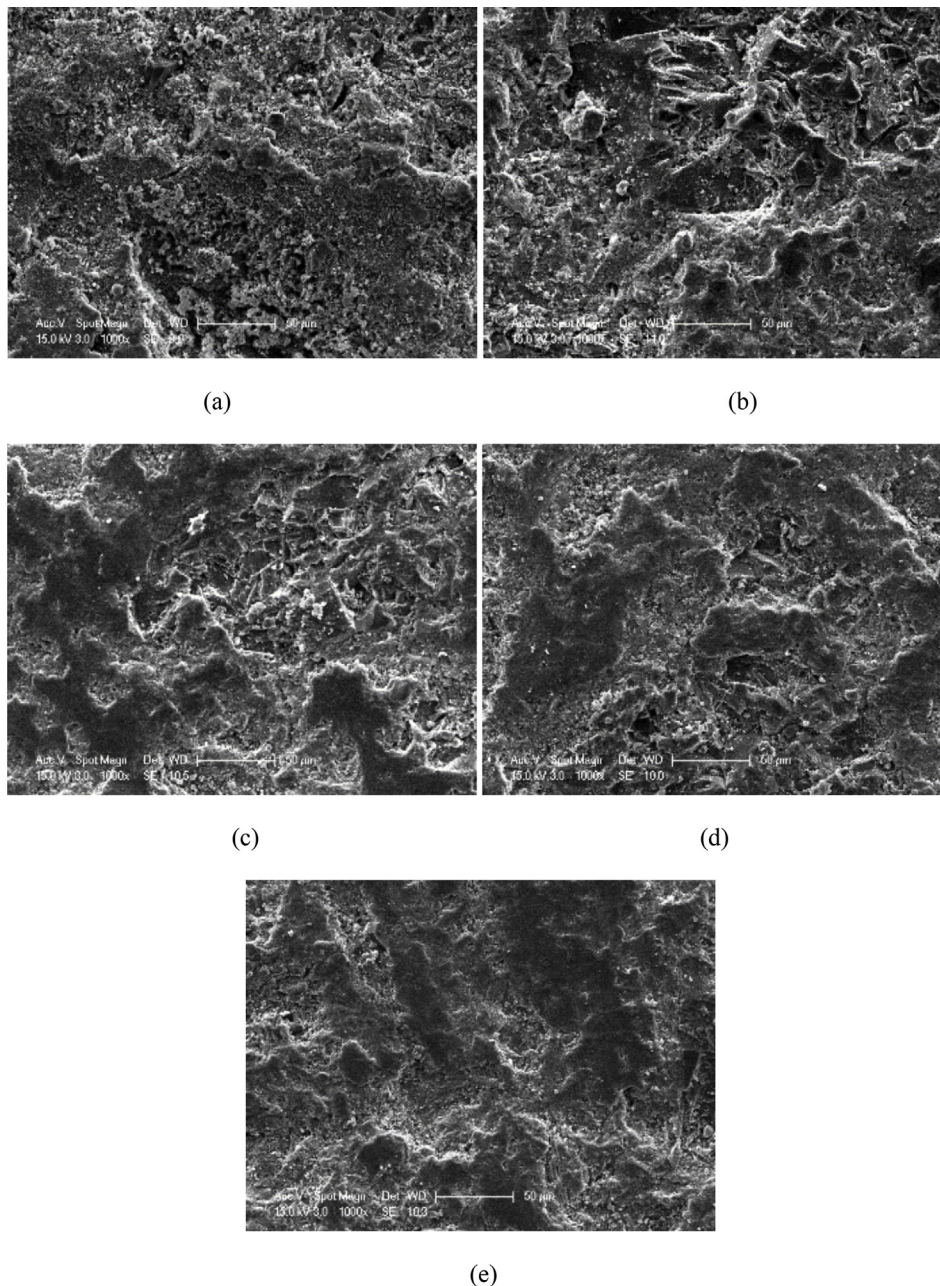


Fig. 8. SEM images of the fracture surface of the UHPCs (1000 $\times$  magnification): a) U-0.8; b) U-0.9; c) U-1.0; d) U-1.1; e) U-1.266.

with cement hydration accelerates the autogenous shrinkage of the concrete [42,43] and may result in the formation of micro-cracks [44–46]. To examine the exothermic reaction of the UHPCs, a thermal sensor was embedded at the center of a 100 mm cubic specimen. The ambient room temperature and internal concrete temperature was also continuously recorded monitored for a period of three days, after which no significant change in temperature occurred.

#### 2.2.4. Unit weight and porosity

The unit weight of the hardened UHPCs was obtained by weighing concrete cylinders (100 mm diameter  $\times$  200 mm height) 90 days after casting, such that the hydration reaction can be considered to be complete. The porosity of each series of the UHPC was quantified by measuring the volume of pore space voids in disc specimens of 150 mm diameter and 50 mm thickness through tests performed in accordance with ASTM C642-13 [47] using a hot water bath. Measurements of porosity were taken because porosity of concrete is an essential

indicator associated with not only the mechanical strength but also the durability characteristics of the concrete.

#### 2.2.5. Scanning electron microscopy (SEM) analysis and energy-dispersive X-ray spectroscopy (EDS)

Scanning electron microscopy (SEM) characterization was performed to evaluate the microstructure of the UHPC matrix and hence assist in identifying the: unreacted binder component, homogeneity of the matrix, and pores and cracks seen in the microstructure of the matrix. Energy-dispersive X-ray spectroscopy (EDS) analysis was also conducted to identify any change in the hydration products resulting from the shrinkage reduction methods applied.

#### 2.2.6. Thermal gravity (TG) analysis

Thermal gravity (TG) analysis was undertaken to estimate the degree of hydration of the UHPC 90-days after casting. The analysis was undertaken to assess both the non-evaporable water content and the

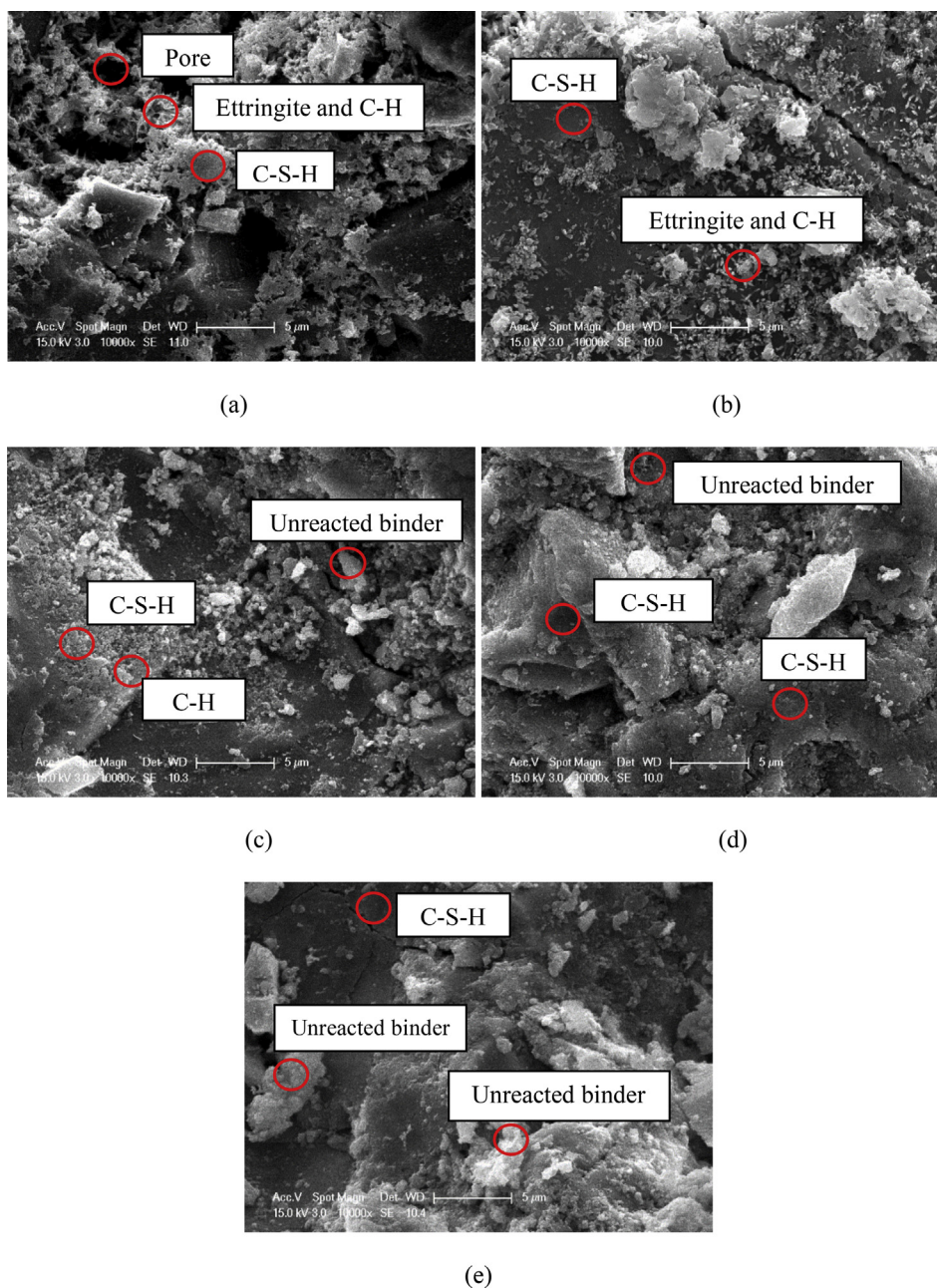


Fig. 9. SEM images of the fracture surface of the UHPCs (10000 $\times$  magnification): a) U-0.8; b) U-0.9; c) U-1.0; d) U-1.1; e) U-1.266.

calcium hydroxide ( $\text{Ca}(\text{OH})_2$ ) content. These approaches have been commonly applied cementitious mortar, for example see Refs. [48–50].

TG analysis was conducted using METTLER TOLEDO TGA testing machine, for each mix a sample weighing 2.5 kg was oven-dried at 105 °C for 24 h to remove the evaporable water, and the sample was then pulverized to a size of < 45  $\mu\text{m}$ . About 20  $\mu\text{g}$  of this sample was placed in a ceramic crucible and heated in the furnace from ambient temperature to 900 °C in a nitrogen atmosphere at a rate of 10 °C/min to determine the weight loss of matrix due to decomposition of the hydration products.

**2.2.6.1. Non-evaporable water content.** The amount of hydration products and the degree of hydration ( $D_h$ ) of UHPC is obtained by determining the non-evaporable water content ( $W_{ne}$ ) using loss-on-ignition (LOI) method. Cementitious paste is commonly used for this test as the non-evaporable water content is present due to the reactive cementitious binders only, and the degree of hydration is strongly

correlated with the  $w/b$  ratio of the cementitious paste [51–53]. The effects of coarse and fine aggregates on hydration are usually ignored due to their inertness. It is worth noting that in this study cement mortar was used instead of cement paste as the: pore diameter, paste-to aggregate interfacial transition zone (ITZ), distribution of aggregate and the mixing efficiency are all affected by the aggregate content, and hence their effects on hydration cannot be neglected. The LOIs of the UHPC mortar were estimated using the LOIs of cementitious powder without moisture damage and considering the LOIs of the sand [48–50].

Previous studies by Lam et al. and Wong et al. [53,54] have shown that absolute hydration of 1 g anhydrous cement can produce approximately 0.23g of non-evaporable water and this non-evaporable water content-to-cement ratio ( $W_{neo}/C_0$ ) of 0.23g/g was applied as the reference value to determine the degree of hydration of the UHPCs in the following calculations for  $D_h$ .

To calculate  $D_h$ , the  $LOI_{raw}$  of the raw cementitious powder, silica fume and sand are firstly calculated using:

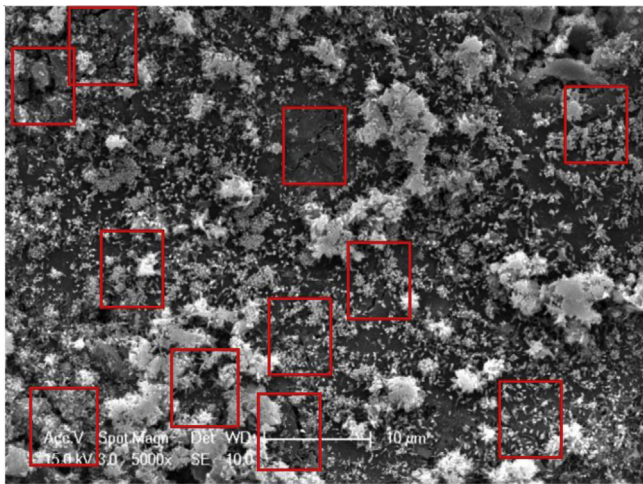


Fig. 10. Observed shrinkage induced micro-cracks in the micro-structure of the UHPC.

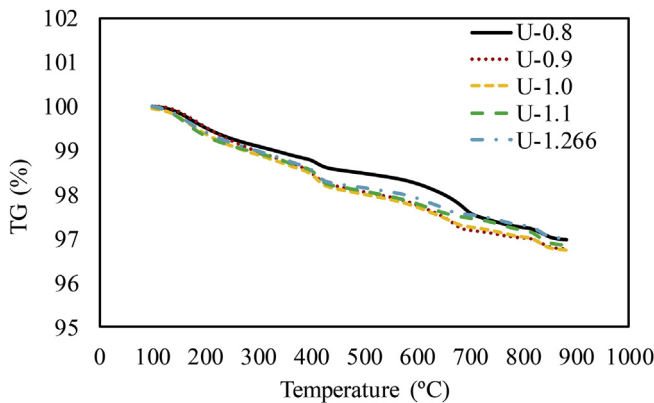


Fig. 11. TG analysis for U-0.8, -0.9, -1.0, -1.1, and -1.266 UHPC series.

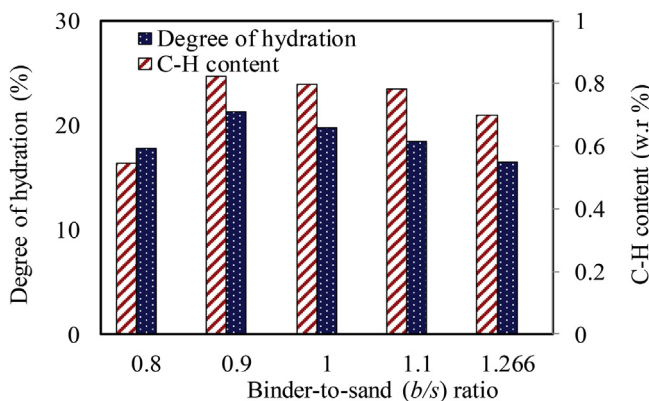


Fig. 12. Effect of binder-to-sand ratio on degree of hydration and C-H content.

Table 3  
Effect of SRA content on rheological properties of fresh UHPCs.

Specimen	b/s ratio	SRA content (%)	Slump (mm)	Flow table (mm)	J-ring (mm)
SRA-0	1	0	235	425	443
SRA-1	1	1	280	512	529
SRA-2	1	2	Full	579	568
SRA-3	1	3	Full	560	585

$$LOI_{raw} = \frac{W_{d-raw} - W_{i-raw}}{W_{i-raw}} \tag{1}$$

where  $W_{d-raw}$  is the dry weight of the as-received raw material, and  $W_{i-raw}$  is the ignited weight of the as-received raw material after TG test. These  $LOI_{raw}$  values are required to correct the calculations of non-evaporable water content ( $W_{ne}$ ) as follows:

$$W_{ne} = [W_{d-U} - W_{i-U} * (1 + \sum LOI_{raw})] \tag{2}$$

where  $W_{d-u}$  is the dry weight of the UHPC mortar sample,  $W_{i-u}$  is the ignited weight of the UHPC mortar sample after TG test and  $\sum LOI_{raw}$  is the total ignited weight of the as-received raw materials, including sand cement and silica fume. The effective residual cementitious binder content ( $C_{eff}$ ) is calculated by

$$C_{eff} = \left[ W_{i-U} * \left( 1 - \frac{\sum LOI_{raw}}{W_{ne0}/C_0} \right) \right] \tag{3}$$

Finally, the degree of hydration of UHPC ( $D_h$ ) is defined as the function of  $W_{ne}$ , effective residual cementitious binder content ( $C_{eff}$ ) and the reference value of the non-evaporable water content-to-cement ratio ( $W_{ne0}/C_0$ ), as given in Eq. (4):

$$D_h(\%) = \frac{W_{ne}/C_{eff}}{W_{ne0}/C_0} \times 100 \tag{4}$$

The loss of the non-evaporable water that is chemically bonded in hydration products can be determined by calculating the difference in weights between at 100 °C and 700 °C from TG. This temperature interval is selected to avoid the interference due to the water evaporation at 100 °C and de-carbonation of calcium carbonate ( $CaCO_3$ ) of the composite when the temperature overs 700 °C [55].

**2.2.6.2. Calcium hydroxide ( $Ca(OH)_2$ ) content.** A fully hydrated cementitious-silica fume material usually consists of dicalcium silicate ( $C_2S$ ) and tricalcium silicates ( $C_3S$ ) [56–58]. The formations of these calcium silicates ( $C_nS$ ) consume around 20–25% by weight of the water in the mix and produce 20–25% by weight of the calcium hydroxide ( $Ca(OH)_2$ ). Therefore, the degree of hydration of the UHPC can also be assessed by the  $Ca(OH)_2$  content in the concrete. The amount of  $Ca(OH)_2$  products can be determined by calculating the drop in weight of the sample within 400–450 °C during TG tests [55,59], which indicates the decomposition of  $Ca(OH)_2$  in the hydration products.

In the remainder of the paper the effectiveness of each shrinkage reduction approach including 1) reducing binder usage; 2) using SRA; 3) partially reducing mixing water with crushed ice will be presented and the mechanism of their action explored using the characterization tests above.

### 3. Effect of binder-to-sand ratio on the properties of the UHPCS

#### 3.1. Flowability of concrete

Table 2 presents the results of slump flow and flow-table tests of the UHPC specimens, from which it can be inferred that the flow- and passing ability of the UHPC generally increased with an increase in the b/s ratio. This can be attributed to the fact that the increased b/s ratio in the UHPC mix resulted in an increased volume of paste that covered the surface of the fine aggregates leading to the reduction in friction between the sand particles in the fresh UHPC [60].

#### 3.2. Autogenous shrinkage

The autogenous shrinkage strains ( $\epsilon_a$ ) plotted in Fig. 2 for each mix with a different b/s ratio, were measured using the sealed prisms shown in Fig. 1(b). These values can be seen to decrease with an increase in b/s ratio. Further it is also observed that for all mixes, regardless of the

**Table 4**  
Effect of crushed ice dosage on rheological properties of fresh UHPCs.

Specimen	<i>b/s</i> ratio	Crushed ice dosage (%)	Slump (mm)	flow table (mm)	J-ring (mm)
Ice-0	1	0	235	425	443
Ice-25/75	1	25	240	418	456
Ice-50/50	1	50	235	431	462

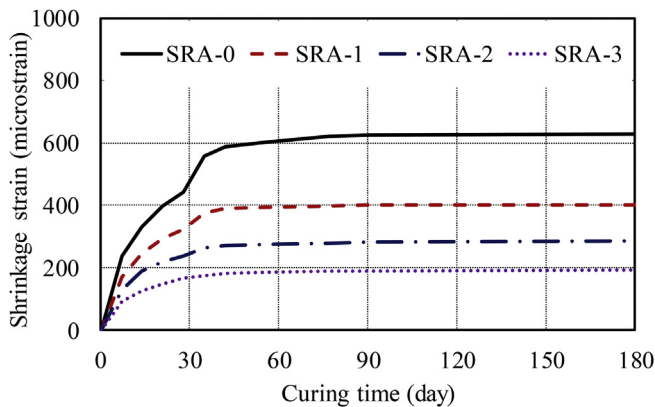


Fig. 13. Effect of SRA content on autogenous shrinkage properties.

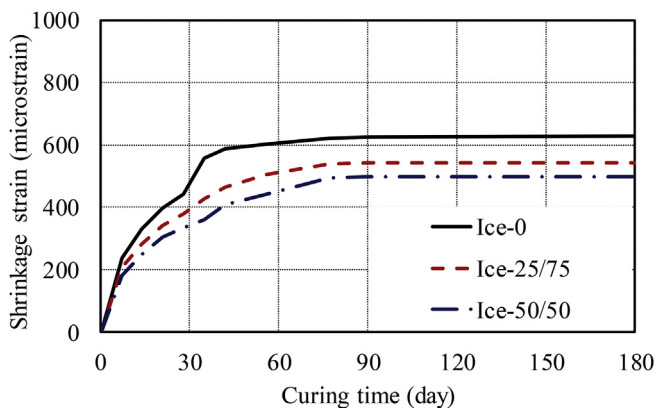


Fig. 14. Effect of crushed ice dosage on autogenous shrinkage properties.

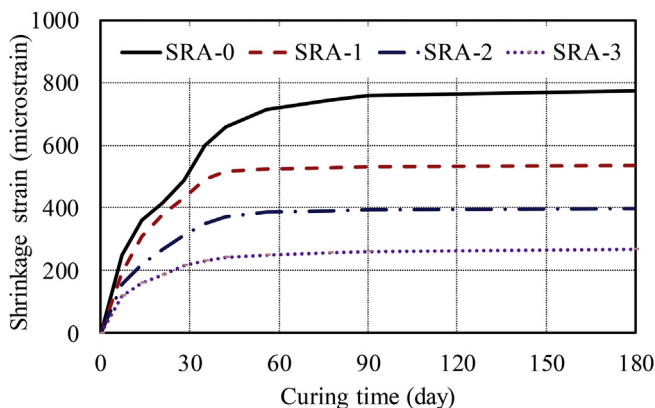


Fig. 15. Effect of SRA content on total shrinkage.

variation in *b/s*, the autogenous shrinkage began to plateau 42 days after casting, indicating the completion of hydration. At the concrete age of 42 days, the  $\epsilon_a$  of U-1.266 was up to 35% lower than those of the companion specimens. Furthermore, the UHPC prepared using a higher *b/s* ratio (i.e. U-1.1 and -1.266 series) exhibited a lower rate of

autogenous shrinkage gain which can be inferred by the reduced slope of the curves.

Moreover, when comparing the autogenous shrinkage strains in Fig. 2 with those expected from conventional concrete (e.g. Refs. [61,62]) for a given age (i.e. concrete age of 28 days), the autogenous shrinkage of UHPCs (> 400 macrostrain) are significantly higher than those of the conventional normal- and high-strength concrete (< 150 macrostrain). This difference is because the increased binder and reduced mixing water in UHPC means it tends to undergo a more rapid self-desiccation than conventional concrete and potentially to form more micro-cracks as further shown and discussed in section 3.8.

### 3.3. Free total shrinkage

Fig. 3 illustrates the effect of *b/s* ratio on free total shrinkage measured using the unsealed prisms shown in Fig. 2(a). Similar to the results of the autogenous shrinkage tests, the free total shrinkage strains ( $\epsilon_t$ ) of the UHPC specimens generally decreased with an increase in *b/s* ratio for a given concrete age. Unlike the autogenous shrinkage tests, where the shrinkage deformations stabilized at 42 days, it is observed that the free total shrinkage increased in all five mixes continued up to the concrete age of 90 days. This is due to the continuous drying of the UHPCs, which is associated with loss of moisture from the concrete to the environment and is in contrast to the significant slowing of autogenous shrinkage after 42 days as a result of the decreased rate of hydration.

### 3.4. Assessment of free drying component

The free drying shrinkage component of the UHPCs can be estimated and assessed by the difference between the free total (solid line) and autogenous (dashed line) shrinkage properties shown in Fig. 4 (a) to (e). It is evident from the Fig. 4 that at the early curing ages (i.e. before the concrete age of 7 days), the difference between the free total and autogenous shrinkage of each UHPC series was negligible. The difference between the  $\epsilon_a$  and  $\epsilon_t$  of each series increased up to 110% with an increase in the *b/s* ratio from 0.8 to 1.266 at the concrete age of 180 days. Note that although the *w/b* ratio for a UHPC mix is low, with adequate mixing energy the moisture (including water and superplasticizer) can be evenly distributed to form a high paste volume [63,64]. This suggests that more moisture was able to diffuse from the UHPC for mixes with a higher paste volume owing to the higher *b/s* ratio, as reported in Table 1, and the observation is in consistent with previous research [65–67]. In addition, as illustrated in Fig. 4 (a) and (b), the drying shrinkage component of each specimen was significantly lower than the corresponding autogenous shrinkage at each given concrete age, indicating that the autogenous shrinkage predominates the overall free total shrinkage of UHPCs.

### 3.5. Compressive strength

The effect of *b/s* ratio on  $f_c$  is shown in Fig. 5. It is observed that the U-1.266 series developed a lower compressive strength than the other four companion mixes for a given age. The reduction in strength associated with the reduction in fine aggregate could be a result of the mechanism of stress transfer within the concrete as per the well-known theory for conventional mortars [68]. That is the transfer of normal force in a mortar is largely due to the interaction of sand to sand interfaces. For the UHPC with a lower *w/b* ratio, its compressive strength is not predominated by failures of cementitious paste but by adhesive failures between aggregates and cementitious materials [69,70]. The presence of excessive unhydrated cementitious materials in the UHPC series with higher binder content weakened the interfacial transition zones (ITZs) between the fine aggregate and binder, which led to the observed reduction in compressive strength. It is also worth noting in Fig. 5 that, all these five UHPC series experienced reduction (up to

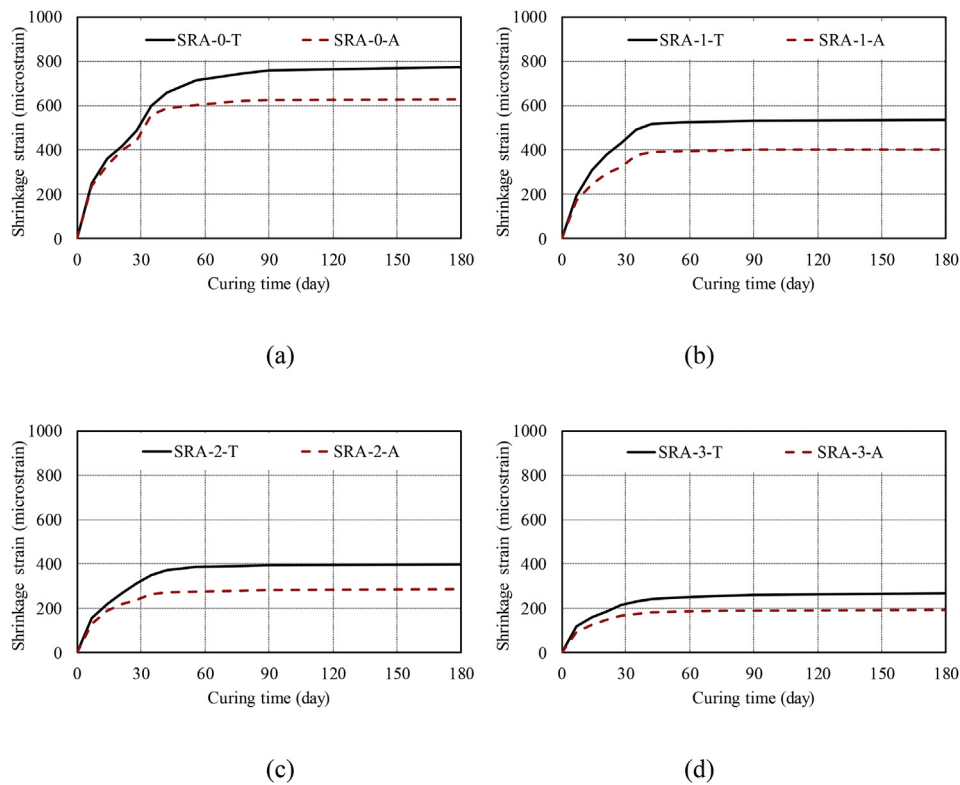


Fig. 16. Effect of SRA content on free drying component: (a) SRA = 0%; (b) SRA = 1%; (c) SRA = 2%; (d) SRA = 3%.

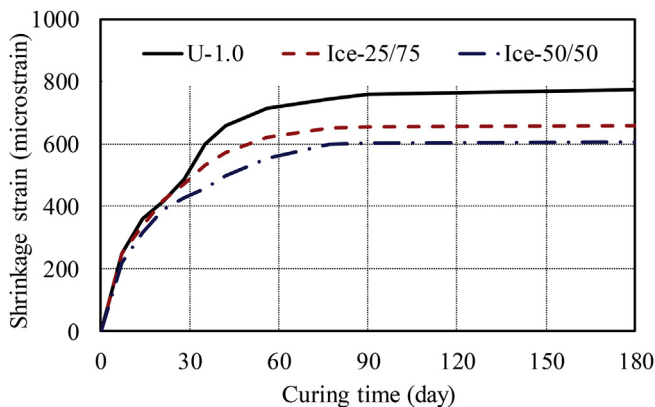


Fig. 17. Effect of crushed ice dosage on total shrinkage.

5.3%) in their compressive strengths within the curing age from 90 to 180 days, as shown in Fig. 5. This reduction in the  $f_c$  was caused by the formation of internal micro cracks (discussed further in section 3.8) as a consequence of the increased shrinkage of the concrete [14]. The above observations indicate that the most appropriate  $b/s$  ratio for UHPC should be within 1–1.1 to achieve adequate aggregate interaction without compromising the  $f_c$ .

### 3.6. Unit weight and porosity of the UHPCs

Fig. 6 shows the effect of  $b/s$  ratio on the unit weight and porosity of the hardened UHPCs measured at the concrete age of 28 days. It is observed that the unit weight of the UHPC increased with an increase in  $b/s$  ratio due to the higher unit weight of the cementitious materials (approximate  $3500 \text{ kg/m}^3$ ) compared to that of the sand (approximate  $2000 \text{ kg/m}^3$ ). The porosity of the UHPC also decreased approximately 10% with an increase in  $b/s$  ratio from 0.8 to 1.266. This reduction in porosity may be attributed to the increased amount of residual

unhydrated binder which fills the pore spaces. The reduction in binder also reduces the total amount of porous ITZs around the sand particles [71,72].

### 3.7. Exothermic reaction at early curing period

Fig. 7 illustrates the variations of internal temperature of the five different specimens with the curing time. It is worth noting that the temperature measured at the center of each UHPC series was normalized by the corresponding ambient temperature in order to remove its influence. From the calorimetry curves in Fig. 7, it can be observed that a decrease in  $b/s$  ratio led to an increase in the magnitude of the peak temperature measured at the center of the sample, with the maximum magnitude of change being approximately 10%. The increase in temperature with a reduction in  $b/s$  indicates that the UHPC with a lower  $b/s$  ratio had a higher degree of exothermic reaction and generated more heat as the consequence of a higher degree of reaction. This is due to the residual unhydrated binders in the UHPC with a higher  $b/s$  which act to fill the pores and voids and absorbed water to their surface, which hindered the level and rate of hydration in the concrete [73]. These facts can be further verified using the TG analysis and SEM characterizations presented in the following sections. The above observation indicates that the UHPC prepared using a lower  $b/s$  ratio underwent a more significant chemical reaction process, which consumed more raw materials and achieved a higher degree of hydration. Therefore, UHPC prepared using a lower  $b/s$  ratio tended to have a more significant autogenous shrinkage at the early curing stage, which can be inferred from the curves in Fig. 2.

The initial and final setting times of each mix can be identified as the first trough and the end point of the linear ascending branch on the calorimetry curves in Fig. 7. These points were also affected by the  $b/s$  ratio, in which the initial and final setting time of the UHPC were delayed by approximately 4 h when the highest quantity of aggregate was considered. This could be explained by the fact that the increased amount of aggregates hindered the contact between water and binder



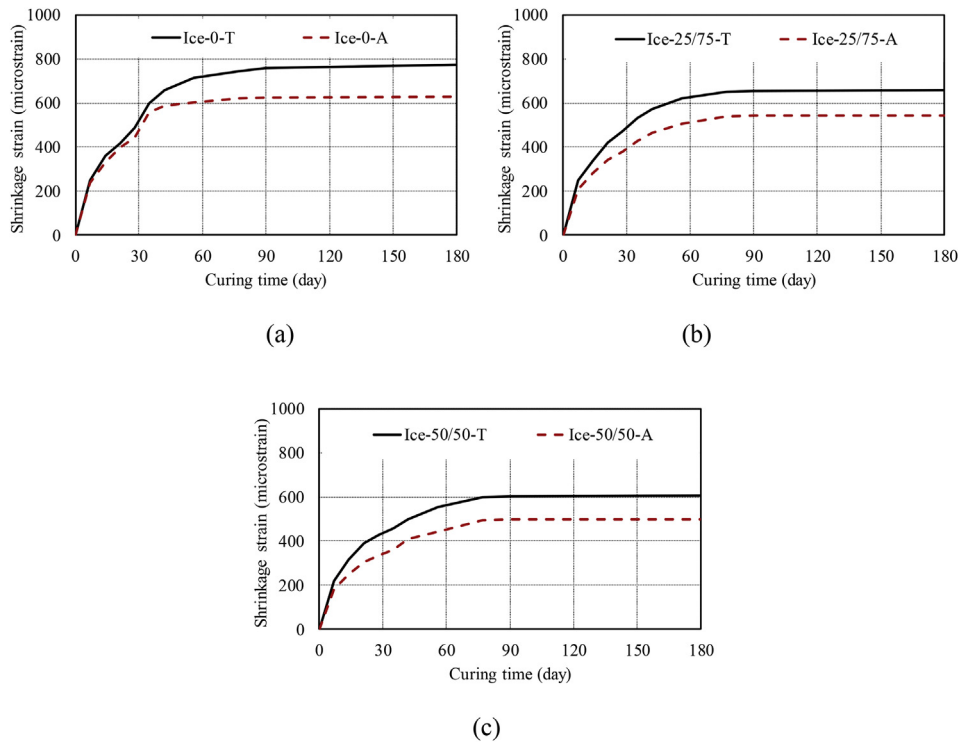


Fig. 18. Effect of ice replaced water ratio on free drying shrinkage: (a) Ice = 0%; (b) Ice = 25%; (c) Ice = 50%.

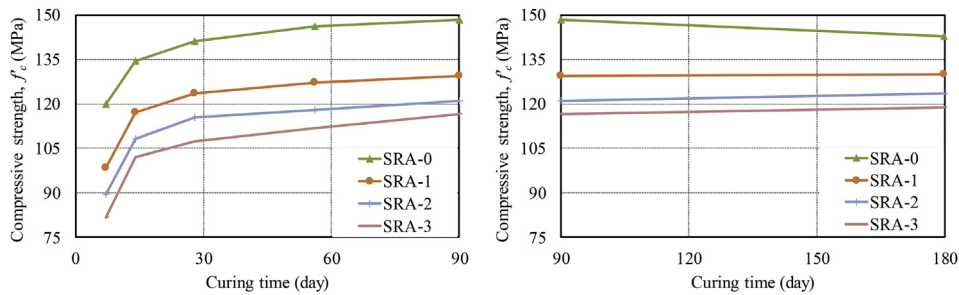


Fig. 19. Effect of SRA content on compressive strength: (a) curing time from 0 to 90 day; (b) curing time from 90 to 180 day.

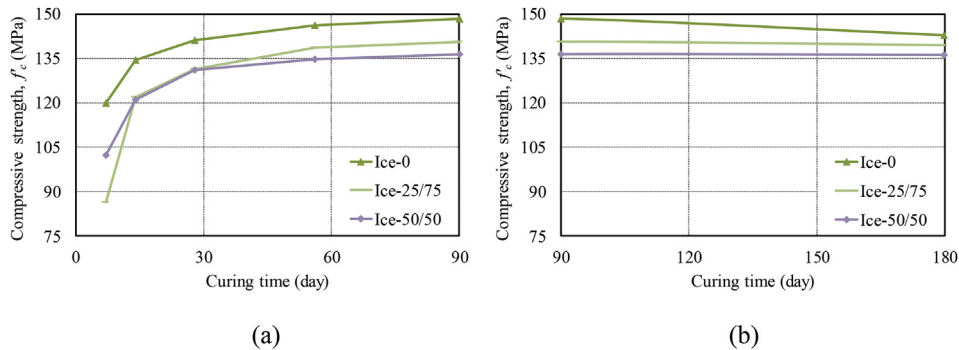


Fig. 20. Effect of ice replaced water ratio on compressive strength: (a) curing time from 0 to 90 day; (b) curing time from 90 to 180 day.

which led to a longer induction period (referred to the initial gentle trough stage) and resulted in this later setting of the concrete [74,75].

### 3.8. Morphological characterization by scanning electron microscopy (SEM) and energy-dispersive X-ray spectroscopy (EDX)

The scanning electron microscopy (SEM) micrographs were evaluated to investigate the effect of *b/s* ratio on the microstructure of the

UHPCs, as depicted in Figs. 8 and 9 at different magnifications. It is evident from the SEM micrographs at 1000× magnification that the increased volume of cementitious paste (at higher *b/s* ratio) led to a much denser microstructure as a result of the reduction in volume fraction of the porous aggregate-paste ITZs. This fact also caused by the micro-filler effect offered by unreacted cementitious binders. Moreover, as shown on the SEM micrographs at 10000× magnification, a large amount of ettringite ( $3CaO \cdot Al_2O_3 \cdot 3CaSO_4 \cdot 32H_2O$ ) and calcium

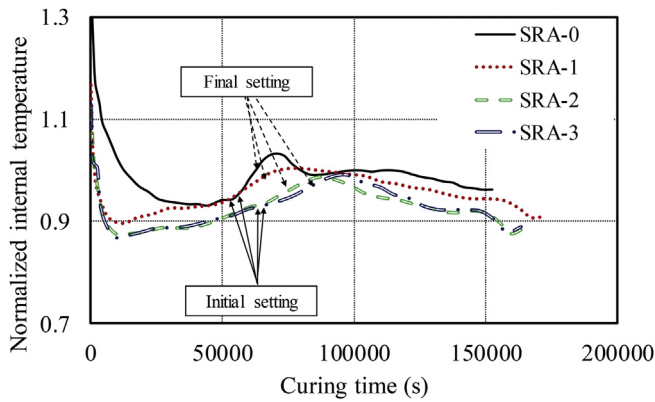


Fig. 21. Effect of SRA content on variations of the internal temperature with curing time.

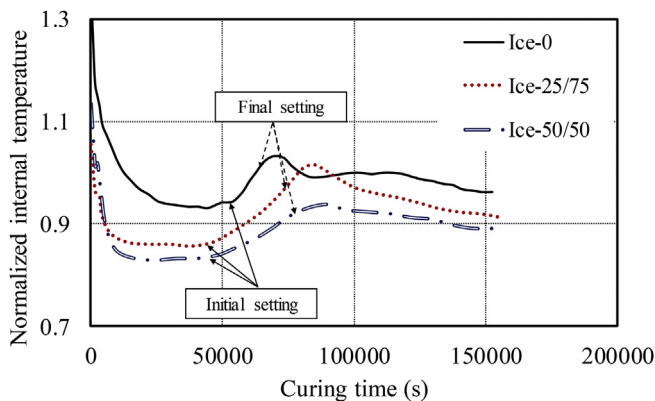


Fig. 22. Effect of ice replaced mixing water ratio on variations of the internal temperature with curing time.

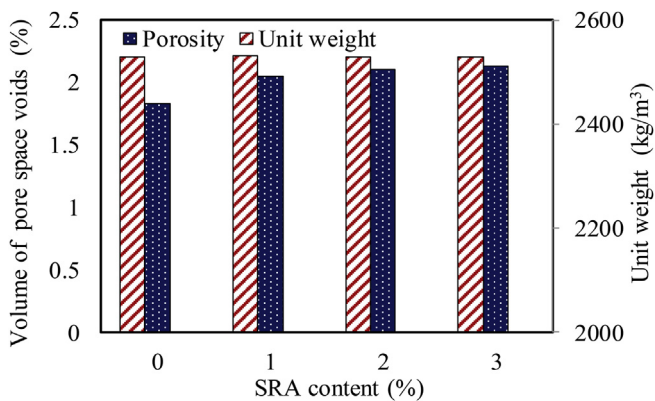


Fig. 23. Effects of ice replaced water ratio on unit weight and porosity of hardened UHPCs.

hydroxide (C-H) were observed and characterized using EDX spectroscopy in the microstructure of the UHPC prepared using the lower *b/s* ratio (i.e. U-0.8, and -0.9). This is because the increased porosity in the concrete provided the space for the growth of ettringite and C-H crystals owing to their expansive nature [76]. For the UHPC prepared using a relatively higher *b/s* ratio (i.e. U-1.0, -1.1 and -1.266), a larger amount of unreacted cementitious materials were detected, as indicated in Fig. 9. Ettringite and C-H crystals were rarely observed in the matrix of U-1.0, -1.1 and -1.266 series owing to the increased denseness and reduced pore space in their matrix shown in Fig. 8. The presence of these unreacted binders may restrain the shrinkage of the matrix contributing to the reduction in autogenous- and drying-shrinkage shown

in Figs. 2 and 3. The presence of the unreacted binder is also a clear indication of the decreased degree of hydration in the UHPC prepared using a higher *b/s* ratio. It is worth mentioning that the observed increased pore space in UHPC adversely affected the drying shrinkage of the concrete, which seemingly contradicts to the observations reported in the literature [77]. The possible explanation is that the expansion resulting from the abundance of crystalline ettringite and C-H in the pores and cracks was more significant than the drying shrinkage of the concrete [76,78]. To verify the deduction on the decrease in mechanical strength of UHPC after a long-term curing, Fig. 10 illustrates a representative SEM micrograph of U-1.1 series with the indications of the micro-cracks that were induced by thermal and autogenous shrinkage.

### 3.9. Results of thermal gravity (TG) analysis

The TGA curves of the comparing UHPCs are shown in Fig. 11 and the effect of binder to sand ratio on the degree of hydration and C-H content are shown in Fig. 12. It should be noted that the paste weight fraction factor for each specimen series, as given in Table 1, was considered in the calculations of the chemically bonded water and C-H content of the paste that is the actual materials for hydration. In general, except for U-0.8 series, the calculated degree of hydration and the C-H content decreased with an increase in the *b/s* ratio (i.e. up to approximately 18% lower). While the *w/b* ratio remained the same for the mixes being compared, the UHPC prepared using a higher *b/s* underwent a lower degree of hydration and hence contained less hydration products. This further confirmed the previously observed less significant autogenous shrinkage for the UHPC prepared using a lower *b/s* ratio.

#### 3.9.1. Selection of the mix for further investigations to migrate autogenous shrinkage

A comprehensive study of the experimental results of among U-0.8, -0.9, -1.0 -1.1 and -1.266 UHPC series led to the selection of the mix design of U-1.0 as the mix for further investigation. These investigations include: the incorporation of shrinkage reducing admixture (SRA) and the used crushed ice to partially replace mixing water. Mix designs for the second stage of this work are shown in Table 3.

## 4. Effects of applied techniques on the properties of the UHPCS

### 4.1. Flowability

#### 4.1.1. Effect of shrinkage reducing admixture (SRA) content

For the flow test results reported in Table 3, it can be seen that the UHPC series prepared with a higher SRA content exhibited better flowability and passing ability. This is due to the higher liquid content (i.e. 80% of the organic liquid component in SRA) in the UHPC mix with a higher SRA content that provides better lubrication, resulting in a better rheology of the UHPC.

#### 4.1.2. Effect of crushed ice dosage

The flow test results presented in Table 4 indicate that the replacement of water with crushed ice had negligible impact on the flowability and passing ability of the UHPC as the added crush ice completely melted after sufficient mixing. The temperature of the mixing water was recorded immediately prior to adding to the mixer. For mixes without using crushed ice the water temperature was found to be the same as the ambient temperature (i.e. 25 °C) while for water with crushed ice the temperature was found to be 2.6 °C and 1.2 °C at 25% and 50% replacement ratio (by weight) respectively. The incorporations of crushed ice in a UHPC mix are expected to reduce the internal temperature of the specimens and hence lessen the potential formations of thermal cracks.

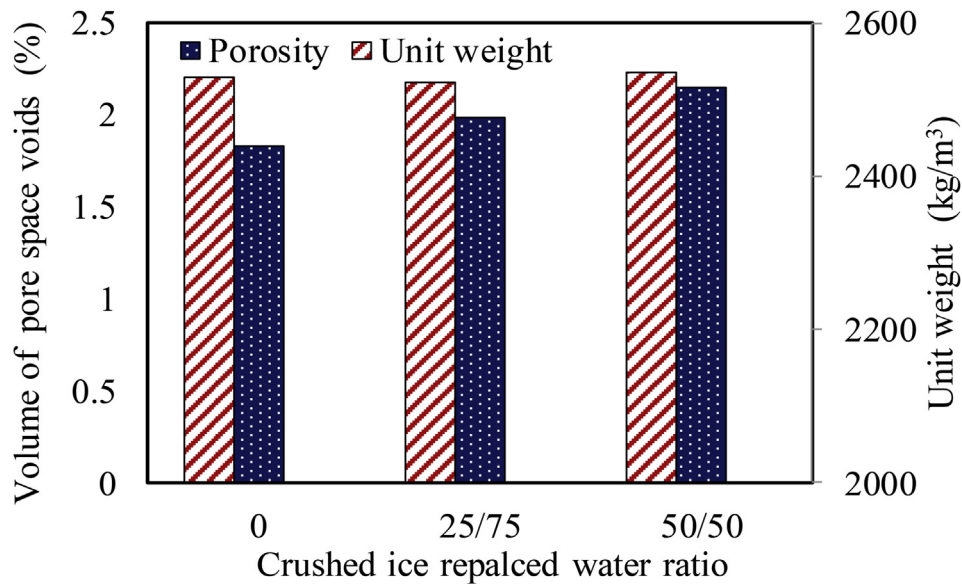


Fig. 24. Effects of SRA content on unit weight and porosity of hardened UHPCs.

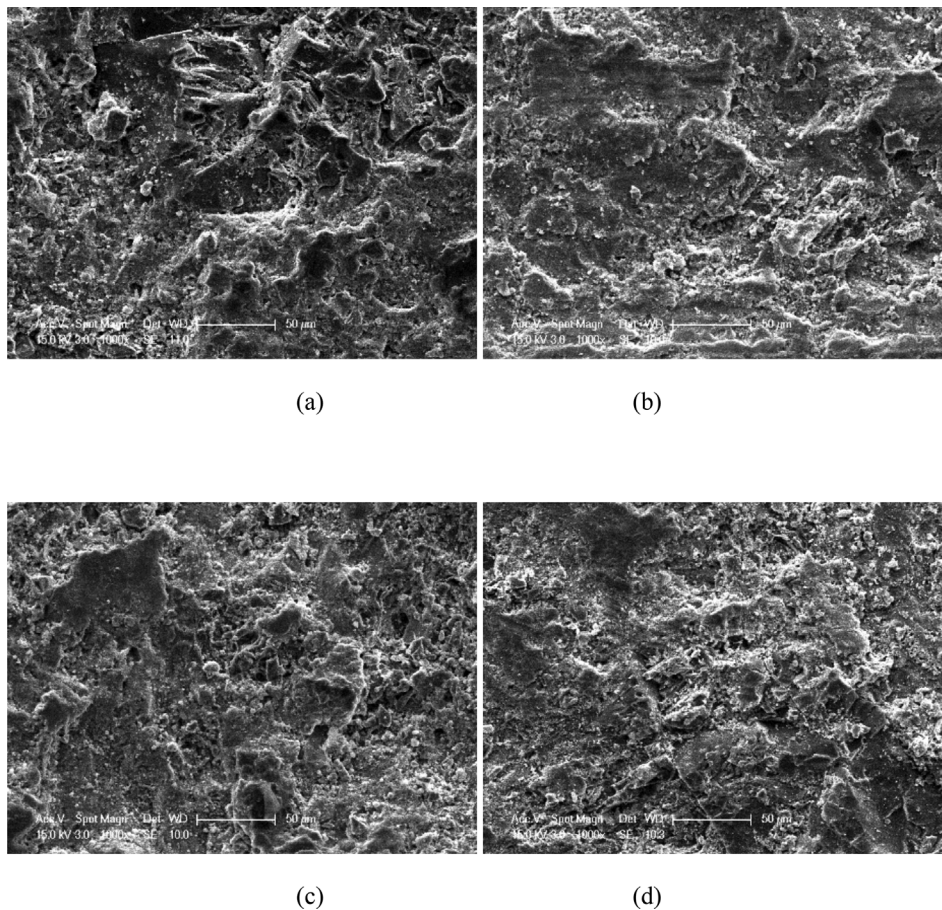


Fig. 25. SEM images of the fracture surface of the UHPCs (1000 × magnification): a) SRA-0; b) SRA-1; c) SRA-2; d) SRA-3.

## 4.2. Autogenous shrinkage

### 4.2.1. Effect of shrinkage reducing admixture (SRA) content

Fig. 13 shows the effects of SRA contents on the autogenous shrinkage of the UHPC. It can be seen that the  $\epsilon_a$  of the UHPC decreased significantly with an increasing SRA content (up to approximately 69% for UHPC at age of 90 days). It is also observed that the SRA started

reducing the autogenous shrinkage right after the initial casting of the UHPC. As stated by Collepardi et al., Folliard et al. [79,80] and Lura et al. [44], SRA incorporation eases the surface tension in the capillary pores of the concrete and subsequently reduces the drying- and autogenous-shrinkage of the concrete. The reduction in autogenous shrinkage with incorporation of SRA seen in the present study is also in reasonable agreement with those reported by studies on UHPC mortar.

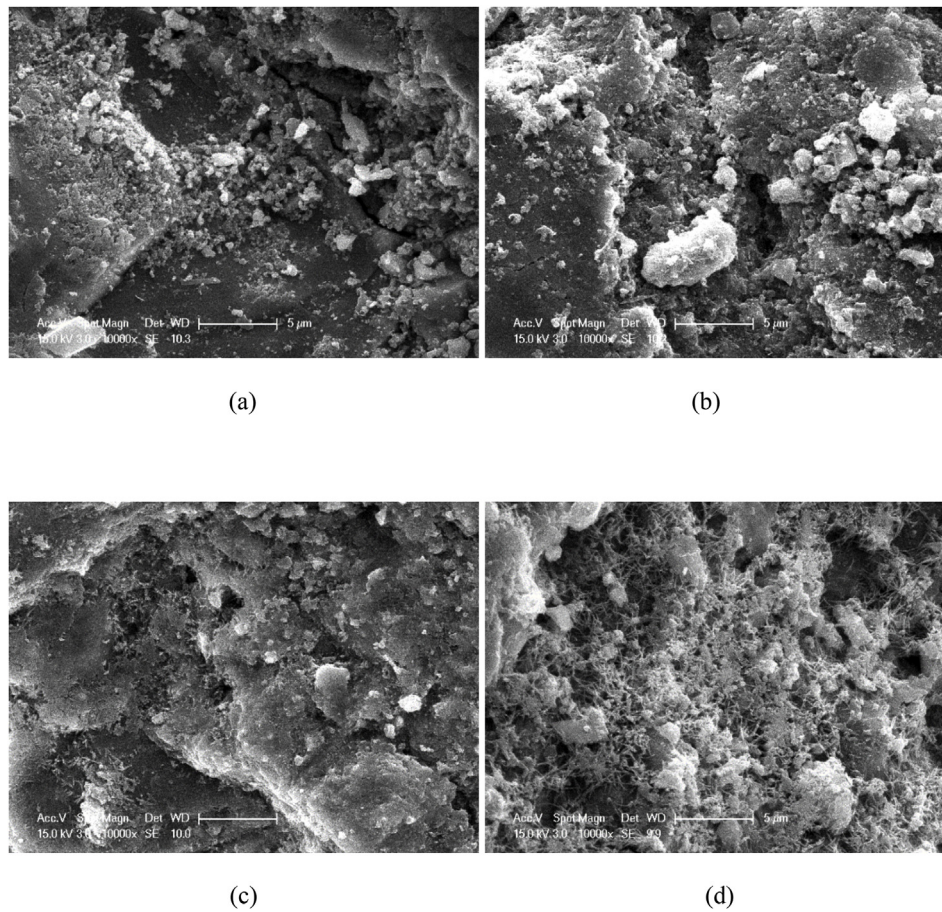


Fig. 26. SEM images of the fracture surface of the UHPCs (10000 × magnification): a) SRA-0; b) SRA-1; c) SRA-2; d) SRA-3.

For example, Su et al. [81] reported an up to 95% reduction in autogenous shrinkage with 2% SRA dosage at 7 days (compared to 65.6% as reported in the present study) and an approximated 61% reduction in autogenous shrinkage with 2% SRA dosage at 160 days was observed by Soliman and Nehdi [11] (compared to 57.8% as reported in the present study). In addition, the comparison of the efficacy of using SRA on autogenous shrinkage between UHPC and conventional cementitious mortar (i.e. as reported in Ref. [82]) suggests the nearly the same performance of SRA to reduce autogenous shrinkage at a given dosage of SRA.

#### 4.2.2. Effect of crushed ice dosage

The effect of crushed ice on the autogenous shrinkage of the UHPCs is depicted in Fig. 14. At each given curing age, the UHPC manufactured using a higher crushed ice exhibited a lower  $\epsilon_a$  (up to approximately 19% at concrete age of 180 days). This observation is expected as the internal temperature of UHPC decreased with the incorporation of crushed ice, which led to the deceleration of the rate of hydration of the concrete and hence reduced autogenous shrinkage.

### 4.3. Free total shrinkage and assessment of free drying component

#### 4.3.1. Effect of shrinkage reducing admixture (SRA) content

The effect of SRA content on the free total shrinkage of the UHPC is illustrated in Fig. 15, where it can be seen that the UHPC prepared using a higher content of SRA exhibited a lower  $\epsilon_t$ . Fig. 16 (a) to (c) illustrate the comparisons between the free total shrinkage and the autogenous shrinkage at all curing ages of each of the four comparing UHPC series, in which the difference between the free total shrinkage and the autogenous shrinkage of each UHPC series yields

approximately the free drying shrinkage component of the concrete. It is observed that the UHPC prepared using a higher SRA content developed a lower drying shrinkage than their counterparts with lower SRA contents. This observation is consistent with the findings of previous studies by Yoo et al. [9,12] and suggests that the SRA is particularly effective to mitigate the free drying shrinkage of the UHPC through reducing the surface tension in the capillary pores of the concrete during the drying process.

#### 4.3.2. Effect of crushed ice

The  $\epsilon_t$  of the UHPC series with different crushed ice dosages were also periodically measured up to the concrete age of 180 days and illustrated in Fig. 17 as the corresponding values of the  $\epsilon_r$  and  $\epsilon_a$  are also shown in Fig. 18. It is observed that the  $\epsilon_t$  of the UHPC decreased with an increase in crushed ice dosage whereas the replacement of mixing water with crushed ice led to no impact on the free drying shrinkage property of the concrete. This is observed because the drying shrinkage only depends on the moisture movement out of the concrete.

### 4.4. Compressive strength

#### 4.4.1. Effect of shrinkage reducing admixture (SRA) content

The effect of SRA content on  $f'_c$  at all curing time are illustrated in Fig. 19. For each given concrete age,  $f'_c$  decreased significantly with an increase in the SRA dosage (up to 21.5% decrease in  $f'_c$  at 90 days with SRA content of 3%), which is in agreement with those reported in the previous studies on UHPCs [12,13]. It is also worth noting that the mixes incorporating SRA exhibited no compressive strength losses ( $\Delta f'_c$ ) for the concrete age ranging between 90 and 180 days. This finding further validates the hypothesis of Sobuz et al. [14] that the reduction

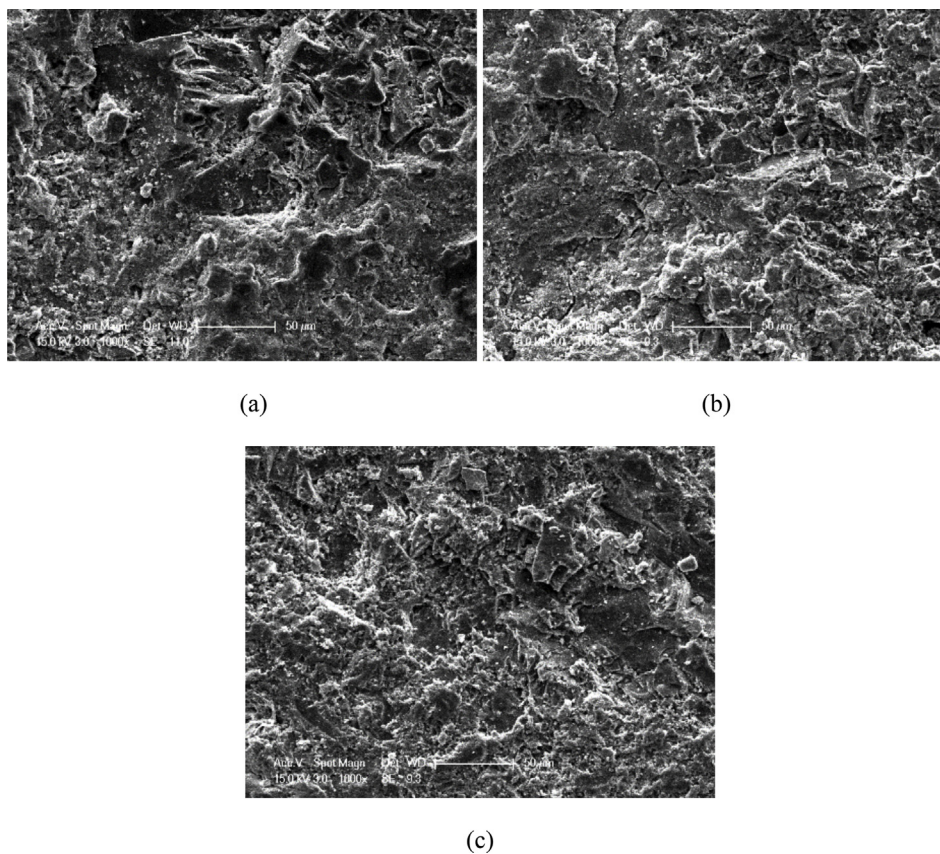


Fig. 27. SEM images of the fracture surface of the UHPCs (1000 × magnification): (a) Ice = 0%; (b) Ice = 25%; (c) Ice = 50%.

in strength of UHPC over time is due to the formation of micro-shrinkage cracks.

#### 4.4.2. Effect of crushed ice dosage

Fig. 20 illustrates the variations of  $f_c$  with curing time of the UHPCs manufactured using different crushed ice replacement ratios. For a given concrete age, the U-25/75 and -50/50 series, which were prepared with crushed ice, developed a lower  $f_c$  than the corresponding UHPC without crushed ice (up to 8% reduction when replacing 50% of water by crushed ice), whereas there was only a slight difference in  $f_c$  between U-25/75 and -50/50 series. This is likely due to the small difference in temperature between mix U-25/75 and -50/50 compared to the control without ice. Moreover, as shown in Fig. 20, U-25/75 and -50/50 UHPC series all exhibited insignificant strength losses (< 1%) between concrete age between 90 and 180 days compared to that seen in U-1.0. This can be explained by the fact that less thermal and plastic shrinkage cracks formed during the exothermic reaction stage, due to the reduction in the heat generation by the incorporation of crushed ice at the early curing stage (i.e. within 72 h after casting). This will be shown in the calorimetry curves of these UHPC series are presented and their effects are discussed in the following sections. This finding indicates that the simple replacement of a proportion of the mixing water with ice may be all that is required to mitigate the excessive shrinkage strains which causes a reduction in strength of UHPC over time.

#### 4.5. Exothermic reaction at early curing ages: effects of SRA and crushed ice dosage

The effects of SRA content and crushed ice dosage on the internal temperature of the UHPC are depicted in Figs. 21 and 22, respectively. As can be seen from both figures, the incorporation of SRA or replaced mixing water by crushed ice in the UHPC mix can significantly delay

the initial and final setting time and reduce the magnitude of peak temperature, which indicates a lower degree of hydration. It is also observed that the strength development period (referred to the width of the hump of the temperature history curve) was increased by using SRA or replacing mixing water with crushed ice. This indicates that the UHPC mixed with SRA or crushed ice could experience a slightly slower strength gain within the very early age (i.e. 72 h) due to the decelerated reaction rate.

#### 4.6. Unit weight and porosity of the hardened UHPCs

As illustrated in Fig. 23, it is observed that the SRA content has marginal effect on the unit weight of the hardened UHPC, however it did lead to an increase in the volume of pore space. This was as expected as SRA, which is a type of organic substance (mainly chemically stable ethanol derivatives) [83], is inert to during hydration and thus causes formation of additional pores in the UHPCs.

The test results of the unit weight and porosity of the hardened UHPCs shown in Fig. 24 suggest that partially replacing the mixing water by crushed ice resulted had no significant effect on the unit weight of the concrete. However, a slight increase in the porosity of the UHPC with an increase in the crushed ice dosage was observed due to the decreased reaction rate. This is because the lower temperature caused amount of unreacted raw materials (i.e. water and binder) to remain in the structure of the matrix. The gradual evaporation of the residual water subsequently led to the increased porosity of the concrete.

#### 4.7. Morphological characterization of the UHPCs

##### 4.7.1. Effect of SRA content

Figs. 25 and 26 illustrated the SEM micrographs of the fracture

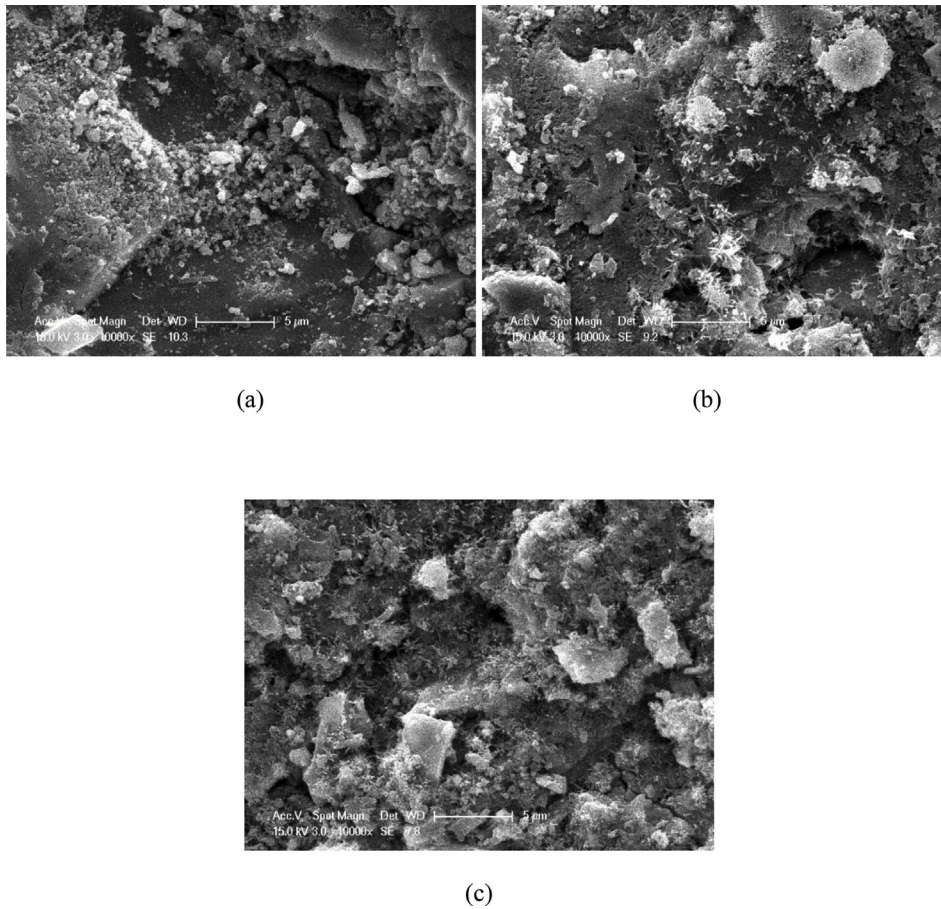


Fig. 28. SEM images of the fracture surface of the UHPCs (10000× magnification): (a) Ice = 0%; (b) Ice = 25%; (c) Ice = 50%.

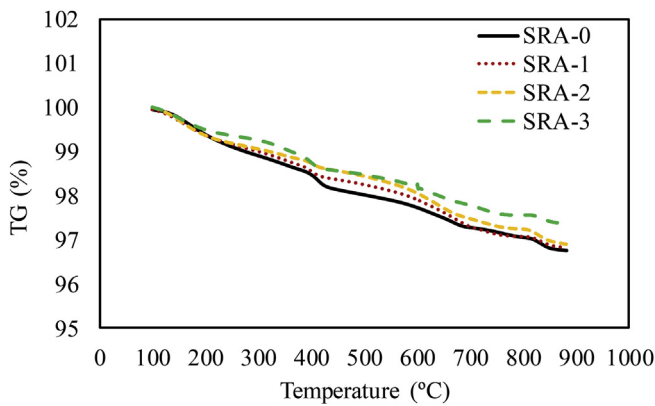


Fig. 29. TG analysis for SRA -0,-1, -2 and -3 UHPC series.

surface of SRA -0, -1, -2 and -3 UHPCs with different magnifications. The comparisons among these micrographs at the lower magnification (i.e. 1000×) suggest that the increased SRA content in the UHPC mix led to increased porosity of the concrete, which is in agreement with the findings from the porosity test mentioned earlier. For the SEM micrographs at the higher magnification (i.e. 10000×), an increased amount of unhydrated binder and ettringite were observed, which indicated lower degree of hydration and increased pore space in the concrete. As discussed previously, this arises because the SRA does not participate in the hydration process but rather acts to slow the hydration process by reducing the contact between the water and binder. In addition, based on the porosity tests results and SEM micrograph, the increased porosity of the UHPC with SRA incorporation might be another potential

explanation for the reduction in the autogenous shrinkage of the concrete, where the presence of pores limited the space for the autogenous shrinkage of the matrix for a given content of aggregate in the mix.

#### 4.7.2. Effect of crushed ice dosage

Figs. 27 and 28 show SEM micrographs of the fracture surface of Ice -0, -25/75, and -50/50 UHPCs at the different magnifications. From SEM micrographs of these UHPC series at the lower magnification (i.e. 1000×), the denseness of the UHPC is observed to decrease with an increase in the crushed ice dosage, indicating an increase in porosity. The comparisons of the SEM micrographs at the higher magnification (i.e. 10000×) show the increased amount of unhydrated binder and ettringite, which suggest the lower degree of hydration and increased pore space for the UHPC prepared using a higher crushed ice replaced water ratio. The increased porosity, formation of ettringite in the concrete and the reduced heat of hydration together explain the mechanism by which the replacement of mixing water with crushed ice reduces self-desiccation.

#### 4.8. Thermal gravity (TG) analysis

The TGA curves of SRA -0,-1, -2 and -3 UHPC series and Ice -0, -25/75, and -50/50 UHPC series are shown in Figs. 29 and 30 respectively and the degree of hydration of these UHPCs at their hardened stage are shown in Figs. 31 and 32 in conjunction with the calculated C-H contents. It is evident from Fig. 31 that the increased SRA content generally lowered the degree of hydration of the UHPCs (i.e. up to around 20%). An even more pronounced reduction in the degree of hydration (i.e. up to approximately 95%) was observed for the UHPC using a higher crushed ice replaced dosage. These characterizations further confirm

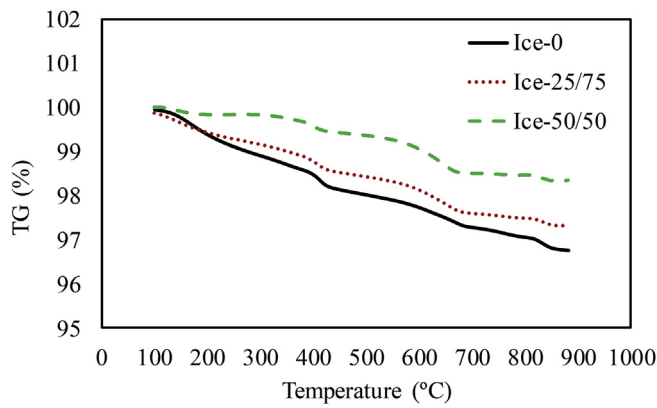


Fig. 30. TG analysis Ice = 0%, Ice = 25% and Ice = 50% UHPC series.

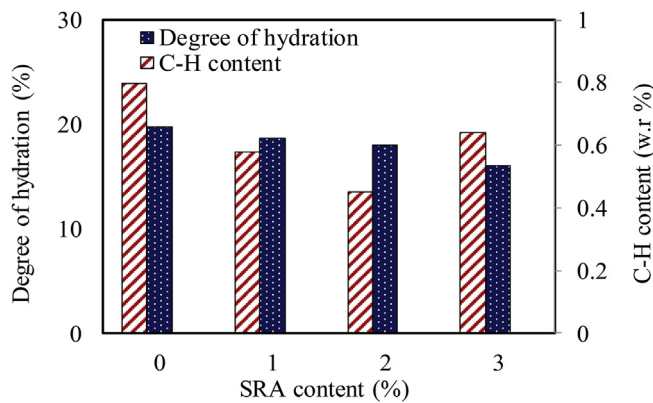


Fig. 31. Effect of SRA content on degree of hydration and C-H content.

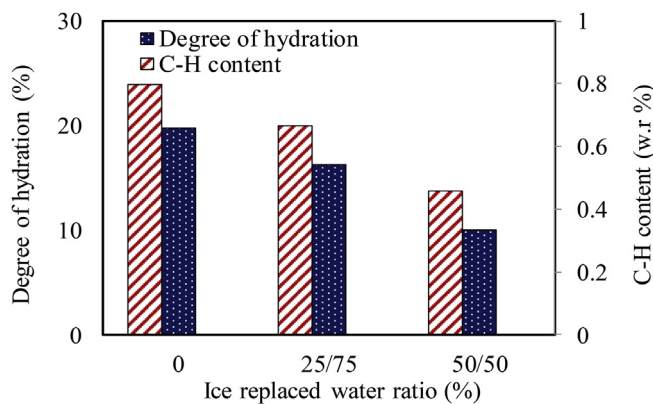


Fig. 32. Effect of ice replaced water ratio on degree of hydration and C-H content.

that using SRA or replacing mixing water by crushed ice can efficiently reduce the shrinkage of UHPC due to chemical reaction.

**5. Comparisons among the three techniques and further suggestions for UHPC mix**

To compare the effectiveness of the three techniques used in the present study to mitigate shrinkage of the UHPCs, the key findings of each test are summarized in Table 5. To make a valid comparison, the test results of each UHPC series are compared with the reference mix, U-1.0 series. It can be seen from Table 5 that compared to U-1 series, both U-1.1 and 1.266 had significantly lower 90-day autogenous- and total-shrinkage strains and a marked Δf<sub>c</sub> at 90 days. All five U-series of UHPCs experienced strength drop after 90 days. Incorporation of SRA

**Table 5**  
Effects of nominated techniques on shrinkage and other properties of the UHPCs.

Specimen	Change in autogenous shrinkage strain at 90 days	Change in total shrinkage strain at 90 days	Change in f <sub>c</sub> at 90 days	Δf <sub>c</sub> between 90 and 180 days
U-0.8	6.4%	3.3%	-6.5%	-5.3%
U-0.9	0.8%	-0.2%	-3.0%	-3.6%
U-1.0/SRA-0/Ice-0	0.0%	0.0%	0.0%	-3.8%
U-1.1	-15.7%	-8.6%	0.5%	-3.9%
U-1.266	-26.3%	-10.9%	-6.3%	-2.3%
SRA-1	-36.1%	-30.0%	-12.9%	0.6%
SRA-2	-69.6%	-47.9%	-18.5%	2.0%
SRA-3	-55.0%	-65.7%	-21.5%	1.8%
Ice-25/75	-13.5%	-13.7%	-5.3%	-0.8%
Ice-50/50	-20.7%	-20.4%	-8.1%	-0.2%

and partially replaced of mixing water in UHPC mix by crushed ice can both led to the reduction in autogenous- and total-shrinkage of the concrete, hence minimizing the compressive strength loss (Δf<sub>c</sub>) after long term. While the use of SRA is more efficient in reducing shrinkage and the associated reduction in strength over time than replaced mixing water by ice, the low cost and simplicity of using ice has significant benefits. However, it is also noted that the application of either of the technique causes a reduction the maximum compressive strength achieved. Therefore, from this study, it can be concluded that the best mix for reducing the impact of shrinkage without significant Δf<sub>c</sub> in the long-term will be 1) SRA-1 using 1% SRA dosage and 2) Ice-50/50 prepared using crushed ice dosage of 50%.

**6. Conclusions**

The following major inferences can be made from the results of the present study to investigate the effects of b/s ratio, SRA content and crushed ice dosage on the shrinkage properties of the UHPC:

1. Autogenous shrinkage of the UHPC decreases with an increase in the b/s ratio due to the more significant shrinkage restraint provided by the residual binders in the UHPC prepared with a higher b/s ratio.
2. An increase in the b/s ratio in the UHPC mix leads to a decrease in the porosity of the concrete. For UHPC prepared using a lower b/s ratio, the abundance of crystalline ettringite and C-H seen in the pores and cracks in the concrete minimized the drying shrinkage of the concrete
3. An optimal b/s ratio will be 1–1.1 for a typical UHPC mix to minimize the shrinkage effect without significantly comprising f<sub>c</sub>.
4. The autogenous shrinkage has more significant effect than the drying shrinkage on total shrinkage of the UHPCs.
5. The porosity and the amount of unreacted binder, which are related to the degree of hydration of the concrete, are the two influential factors on the shrinkage properties of UHPCs.
6. SRA is not only able to reduce the drying shrinkage but also the autogenous shrinkage (i.e. up to 55% at 90 days with 3% of SRA dosage) of UHPCs
7. The replacement of half of the mixing water by crushed ice in a UHPC mix can reduce the autogenous shrinkage of the UHPC up to 22% and has nearly no effect on the drying shrinkage properties of the UHPCs. This technique is cost-effective and relatively practical to apply in any cast in-situ or pre-casting scenarios.

**Acknowledgments**

The first author would like to thank Australian Research Training Program (RTP) for financial support.

## References

- [1] M. Singh, A. Sheikh, M.M. Ali, P. Visintin, M. Griffith, Experimental and numerical study of the flexural behaviour of ultra-high performance fibre reinforced concrete beams, *Construct. Build. Mater.* 138 (2017) 12–25.
- [2] M.A. Mosaberpanah, O. Eren, Relationship between 28-days compressive strength and compression toughness factor of ultra high performance concrete using design of experiments, *Procedia Eng.* 145 (2016) 1565–1571.
- [3] D.-Y. Yoo, N. Banthia, Mechanical properties of ultra-high-performance fiber-reinforced concrete: a review, *Cement Concr. Compos.* 73 (2016) 267–280.
- [4] D. Wang, C. Shi, Z. Wu, J. Xiao, Z. Huang, Z. Fang, A review on ultra high performance concrete: Part II. Hydration, microstructure and properties, *Construct. Build. Mater.* 96 (2015) 368–377.
- [5] C. Shi, Z. Wu, J. Xiao, D. Wang, Z. Huang, Z. Fang, A review on ultra high performance concrete: Part I. Raw materials and mixture design, *Construct. Build. Mater.* 101 (2015) 741–751.
- [6] D. Youssef, The Use of Lightweight Sand for Internal Curing and its Effect on Performance of HPC Used for Concrete Infrastructures, Université de Sherbrooke, 2013.
- [7] L. Wu, N. Farzadnia, C. Shi, Z. Zhang, H. Wang, Autogenous shrinkage of high performance concrete: a review, *Construct. Build. Mater.* 149 (2017) 62–75.
- [8] Ç. Yalçınkaya, H. Yazıcı, Effects of ambient temperature and relative humidity on early-age shrinkage of UHPC with high-volume mineral admixtures, *Construct. Build. Mater.* 144 (2017) 252–259.
- [9] D.-Y. Yoo, K.-H. Min, J.-H. Lee, Y.-S. Yoon, Shrinkage and cracking of restrained ultra-high-performance fiber-reinforced concrete slabs at early age, *Construct. Build. Mater.* 73 (2014) 357–365.
- [10] J.-J. Park, D.-Y. Yoo, S.-W. Kim, Y.-S. Yoon, Benefits of using expansive and shrinkage-reducing agents in UHPC for volume stability, *Mag. Concr. Res.* 66 (14) (2014) 745–750.
- [11] A. Soliman, M. Nehdi, Effects of shrinkage reducing admixture and wollastonite microfiber on early-age behavior of ultra-high performance concrete, *Cement Concr. Compos.* 46 (2014) 81–89.
- [12] D.-Y. Yoo, S.-T. Kang, J.-H. Lee, Y.-S. Yoon, Effect of shrinkage reducing admixture on tensile and flexural behaviors of UHPFRC considering fiber distribution characteristics, *Cement Concr. Res.* 54 (2013) 180–190.
- [13] A. Soliman, M. Nehdi, Effect of drying conditions on autogenous shrinkage in ultra-high performance concrete at early-age, *Mater. Struct.* 44 (5) (2011) 879–899.
- [14] H. Sobuz, P. Visintin, M.M. Ali, M. Singh, M. Griffith, A. Sheikh, Manufacturing ultra-high performance concrete utilising conventional materials and production methods, *Construct. Build. Mater.* 111 (2016) 251–261.
- [15] D.-Y. Yoo, J.-J. Park, S.-W. Kim, Y.-S. Yoon, Influence of ring size on the restrained shrinkage behavior of ultra high performance fiber reinforced concrete, *Mater. Struct.* 47 (7) (2014) 1161–1174.
- [16] M. Şahmaran, M. Lachemi, K.M. Hossain, V.C. Li, Internal curing of engineered cementitious composites for prevention of early age autogenous shrinkage cracking, *Cement Concr. Res.* 39 (10) (2009) 893–901.
- [17] D.-Y. Yoo, N. Banthia, Y.-S. Yoon, Ultra-high-performance fiber-reinforced concrete: shrinkage strain development at early ages and potential for cracking, *J. Test. Eval.* 45 (6) (2017) 2061–2070.
- [18] D.-Y. Yoo, J.-J. Park, S.-W. Kim, Y.-S. Yoon, Influence of reinforcing bar type on autogenous shrinkage stress and bond behavior of ultra high performance fiber reinforced concrete, *Cement Concr. Compos.* 48 (2014) 150–161.
- [19] D.-Y. Yoo, M.-J. Kim, S. Kim, G.-S. Ryu, K.-T. Koh, Effects of mix proportion and curing condition on shrinkage behavior of HPPFRCs with silica fume and blast furnace slag, *Construct. Build. Mater.* 166 (1) (2018) 241–256.
- [20] D.-Y. Yoo, N. Banthia, Y.-S. Yoon, Geometrical and boundary condition effects on restrained shrinkage behavior of UHPFRC slabs, *KSCE J. Civil Eng.* 22 (1) (2018) 185–195.
- [21] M. Şahmaran, M. Lachemi, K.M. Hossain, R. Ranade, V.C. Li, Influence of aggregate type and size on ductility and mechanical properties of engineered cementitious composites, *Mater. J.* 106 (3) (2009) 308–316.
- [22] M. Şahmaran, M. Al-Emam, G. Yıldırım, Y.E. Şimşek, T.K. Erdem, M. Lachemi, High-early-strength ductile cementitious composites with characteristics of low early-age shrinkage for repair of infrastructures, *Mater. Struct.* 48 (5) (2015) 1389–1403.
- [23] C. Röbler, D.-D. Bui, H.-M. Ludwig, Rice husk ash as both pozzolanic admixture and internal curing agent in ultra-high performance concrete, *Cement Concr. Compos.* 53 (2014) 270–278.
- [24] O.M. Jensen, Use of superabsorbent polymers in concrete, *Concr. Int.* 35 (1) (2013) 48–52.
- [25] L. Dudziak, V. Mechtcherine, Mitigation of volume changes of ultra-high performance concrete (UHPC) by using super absorbent polymers, *Proceedings of the 2nd International Symposium on Ultra High Performance Concrete*, Kassel University Press, Kassel, 2008, pp. 425–432.
- [26] D.-Y. Yoo, N. Banthia, Y.-S. Yoon, Effectiveness of shrinkage-reducing admixture in reducing autogenous shrinkage stress of ultra-high-performance fiber-reinforced concrete, *Cement Concr. Compos.* 64 (2015) 27–36.
- [27] K. Koh, G. Ryu, S. Kang, J. Park, S. Kim, Shrinkage properties of ultra-high performance concrete (UHPC), *Adv. Sci. Lett.* 4 (3) (2011) 948–952.
- [28] H.R. Sobuz, D.J. Oehlers, P. Visintin, N.M.S. Hasan, M.I. Hoque, A.S.M. Akid, Flow and strength characteristics of ultra-high performance fiber reinforced concrete: influence of fiber type and volume-fraction, *J. Civil Eng. Construct.* 6 (1) (2017) 15.
- [29] P. Visintin, A.B. Sturm, M.M. Ali, D.J. Oehlers, Blending macro and micro fibres to enhance the serviceability behaviour of UHPFRC, *Aust. J. Civ. Eng.* (2018), <http://dx.doi.org/10.1080/14488353.2018.1463608>.
- [30] P. Visintin, M.M. Ali, T. Xie, A.B. Sturm, Experimental investigation of moment redistribution in ultra-high performance fibre reinforced concrete beams, *Construct. Build. Mater.* 166 (2018) 433–444.
- [31] A.B. Sturm, P. Visintin, K. Ferris, D.J. Oehlers, A new testing approach for extracting the shear friction material properties of ultra-high performance fibre reinforced concrete, *ASCE J. Mater. Civil Eng.* (2018).
- [32] B.G. Smith, Durability of silica fume concrete exposed to chloride in hot climates, *J. Mater. Civ. Eng.* 13 (1) (2001) 41–48.
- [33] Australian Standard, AS/NZS 2350.11. Methods for Testing Portland, Blended and Masonry Cements, Standards Australia, Sydney, 2006.
- [34] Australian Standard, AS/NZS 2350.13. Methods for Testing Portland, Blended and Masonry Cements – Determination of Drying Shrinkage of Cement Mortars, Standards Australia, Sydney, 2006.
- [35] Australian Standard, AS 1478.1–2000. Chemical Admixtures for Concrete, Mortar and Grout Admixtures for Concrete, Standards Australia, Sydney, 2000.
- [36] ASTM A, C1698–09 Standard Test Method for Autogenous Strain of Cement Paste and Mortar, ASTM International, West Conshohocken, PA, 2009.
- [37] A. Darquennes, S. Staquet, B. Espion, Determination of time-zero and its effect on autogenous deformation evolution, *Eur. J. Environ. Civil Eng.* 15 (7) (2011) 1017–1029.
- [38] V. Mechtcherine, M. Gorges, C. Schroefl, A. Assmann, W. Brameshuber, AnB. Ribeiro, et al., Effect of internal curing by using superabsorbent polymers (SAP) on autogenous shrinkage and other properties of a high-performance fine-grained concrete: results of a RILEM round-robin test, *Mater. Struct.* 47 (3) (2014) 541–562.
- [39] Standard Australia, AS 1012.9:2014. Methods of Testing Concrete Compressive Strength Tests - Concrete, Mortar and Grout Specimens, Standards Australia, Sydney, 2014.
- [40] ASTM International, ASTM C143/C143M - 00, Standard Test Method for Slump of Hydraulic Cement Concrete, ASTM International, West Conshohocken, 2000.
- [41] ASTM International, ASTM C1621/C1621M–09 Standard Test Method for Passing Ability of Self-consolidating Concrete by J-ring, ASTM International, West Conshohocken, 2009.
- [42] B. Langan, K. Weng, M. Ward, Effect of silica fume and fly ash on heat of hydration of Portland cement, *Cement Concr. Res.* 32 (7) (2002) 1045–1051.
- [43] E.-H. Kadri, R. Duval, Hydration heat kinetics of concrete with silica fume, *Construct. Build. Mater.* 23 (11) (2009) 3388–3392.
- [44] P. Lura, O.M. Jensen, K. van Breugel, Autogenous shrinkage in high-performance cement paste: an evaluation of basic mechanisms, *Cement Concr. Res.* 33 (2) (2003) 223–232.
- [45] P. Aitcin, 17 autogenous shrinkage measurement, *Autogenous Shrinkage of Concrete: Proceedings of the International Workshop*, Organised by JCI (Japan Concrete Institute), vol. 1999, Taylor & Francis, Hiroshima, June 13–14, 1998, p. 257.
- [46] G.-Y. Kim, E.-B. Lee, J.-S. Nam, K.-M. Koo, Analysis of hydration heat and autogenous shrinkage of high-strength mass concrete, *Mag. Concr. Res.* 63 (5) (2011) 377–389.
- [47] ASTM International, ASTM C642–13. Standard Test Method for Density, Absorption, and Voids in Hardened Concrete, ASTM International, West Conshohocken, 2013.
- [48] Y. Maltais, J. Marchand, Influence of curing temperature on cement hydration and mechanical strength development of fly ash mortars, *Cement Concr. Res.* 27 (7) (1997) 1009–1020.
- [49] X. Chen, S. Wu, Influence of water-to-cement ratio and curing period on pore structure of cement mortar, *Construct. Build. Mater.* 38 (2013) 804–812.
- [50] D.P. Bentz, Capitalizing on Self-desiccation for Autogenous Distribution of Chemical Admixtures, Lund University, Citeseer, 2005.
- [51] M. Yio, J. Phelan, H. Wong, N. Buenfeld, Determining the slag fraction, water/binder ratio and degree of hydration in hardened cement pastes, *Cement Concr. Res.* 56 (2014) 171–181.
- [52] W. Huang, H. Kazemi-Kamyab, W. Sun, K. Scrivener, Effect of cement substitution by limestone on the hydration and microstructural development of ultra-high performance concrete (UHPC), *Cement Concr. Compos.* 77 (2017) 86–101.
- [53] L. Lam, Y. Wong, C. Poon, Degree of hydration and gel/space ratio of high-volume fly ash/cement systems, *Cement Concr. Res.* 30 (5) (2000) 747–756.
- [54] H. Wong, N. Buenfeld, Determining the water–cement ratio, cement content, water content and degree of hydration of hardened cement paste: method development and validation on paste samples, *Cement Concr. Res.* 39 (10) (2009) 957–965.
- [55] R. Vedalakshmi, A.S. Raj, S. Srinivasan, K.G. Babu, Quantification of hydrated cement products of blended cements in low and medium strength concrete using TG and DTA technique, *Thermochim. Acta* 407 (1) (2003) 49–60.
- [56] S. Brunauer, D. Kantror, The hydration of tricalcium silicate and  $\beta$  dicalcium silicate from 5 C to 50 C, *Chem. Cement* 1 (1964) 287.
- [57] S.P. Newman, S.J. Clifford, P.V. Coveney, V. Gupta, J.D. Blanchard, F. Serafin, et al., Anomalous fluorescence in near-infrared Raman spectroscopy of cementitious materials, *Cement Concr. Res.* 35 (8) (2005) 1620–1628.
- [58] B. Hasanzadeh, F. Liu, Z. Sun, Monitoring hydration of UHPC and conventional paste by quantitative analysis on Raman patterns, *Construct. Build. Mater.* 114 (2016) 208–214.
- [59] J. Dweck, P.M. Buchler, A.C.V. Coelho, F.K. Cartledge, Hydration of a Portland cement blended with calcium carbonate, *Thermochim. Acta* 346 (1) (2000) 105–113.
- [60] G. Hermida, M. Moranville, R. Flatt, The role of paste volume on performance of concrete, *Spec. Publ.* 261 (2009) 201–214.
- [61] A. Bentur, Kovler K. Igarashi S-I, Prevention of autogenous shrinkage in high-



- strength concrete by internal curing using wet lightweight aggregates, *Cement Concr. Res.* 31 (11) (2001) 1587–1591.
- [62] M. Zhang, C. Tam, M. Leow, Effect of water-to-cementitious materials ratio and silica fume on the autogenous shrinkage of concrete, *Cement Concr. Res.* 33 (10) (2003) 1687–1694.
- [63] H.G. Russell, B.A. Graybeal, Ultra-high Performance Concrete: a State-of-the-art Report for the Bridge Community, (2013).
- [64] P. Schießl, O. Mazanec, D. Lowke, SCC and UHPC—effect of Mixing Technology on Fresh Concrete Properties. *Advances in Construction Materials 2007*, Springer, 2007, pp. 513–522.
- [65] J. Ma, M. Orgass, F. Dehn, D. Schmidt, N. Tue, Comparative investigations on ultra-high performance concrete with and without coarse aggregates, *Proceedings of International Symposium on Ultra High Performance Concrete, Germany, 2004*, pp. 205–212.
- [66] A. Soliman, M. Nehdi, Effect of partially hydrated cementitious materials and superabsorbent polymer on early-age shrinkage of UHPC, *Construct. Build. Mater.* 41 (2013) 270–275.
- [67] W. Shen, X. Li, G. Gan, L. Cao, C. Li, J. Bai, Experimental investigation on shrinkage and water desorption of the paste in high performance concrete, *Construct. Build. Mater.* 114 (2016) 618–624.
- [68] B.V. Reddy, A. Gupta, Influence of sand grading on the characteristics of mortars and soil–cement block masonry, *Construct. Build. Mater.* 22 (8) (2008) 1614–1623.
- [69] P.J. Jun, K.S. Tae, R.G. Sung, K.S. Wook, L.J. Hwa, The effect of material factors on the compressive strength of ultra-high strength Steel Fiber Reinforced Cementitious Composites, *Proceedings of the Korea Concrete Institute Conference, Korea Concrete Institute, 2004*.
- [70] J.J. Park, S.T. Kang, K.T. Koh, S.W. Kim, Influence of the ingredients on the compressive strength of UHPC as a fundamental study to optimize the mixing proportion, *Proceedings of the International Symposium on Ultra-high Performance Concrete, Structural Materials and Engineering Series, 2008*, pp. 105–112.
- [71] K.L. Scrivener, A.K. Crumbie, P. Laugesen, The interfacial transition zone (ITZ) between cement paste and aggregate in concrete, *Interface Sci.* 12 (4) (2004) 411–421.
- [72] A. Brough, A. Atkinson, Automated identification of the aggregate–paste interfacial transition zone in mortars of silica sand with Portland or alkali-activated slag cement paste, *Cement Concr. Res.* 30 (6) (2000) 849–854.
- [73] R. Yu, P. Spiesz, H. Brouwers, Effect of nano-silica on the hydration and micro-structure development of Ultra-High Performance Concrete (UHPC) with a low binder amount, *Construct. Build. Mater.* 65 (2014) 140–150.
- [74] I. Odler, Hydration, setting and hardening of Portland cement, *Lea's Chemistry of Cement and Concrete 4* (1998) 241–297.
- [75] H. Jennings, P. Pratt, An experimental argument for the existence of a protective membrane surrounding Portland cement during the induction period, *Cement Concr. Res.* 9 (4) (1979) 501–506.
- [76] P.K. Mehta, Mechanism of expansion associated with ettringite formation, *Cement Concr. Res.* 3 (1) (1973) 1–6.
- [77] M.Y. Han, R.L. Lytton, Theoretical prediction of drying shrinkage of concrete, *J. Mater. Civ. Eng.* 7 (4) (1995) 204–207.
- [78] P. Yan, F. Zheng, J. Peng, X. Qin, Relationship between delayed ettringite formation and delayed expansion in massive shrinkage-compensating concrete, *Cement Concr. Compos.* 26 (6) (2004) 687–693.
- [79] M. Collepardi, A. Borsoi, S. Collepardi, J.J.O. Olagot, R. Troli, Effects of shrinkage reducing admixture in shrinkage compensating concrete under non-wet curing conditions, *Cement Concr. Compos.* 27 (6) (2005) 704–708.
- [80] K.J. Folliard, N.S. Berke, Properties of high-performance concrete containing shrinkage-reducing admixture, *Cement Concr. Res.* 27 (9) (1997) 1357–1364.
- [81] S. Anshuang, Q. Ling, Z. Shoujie, Z. Jiayang, L. Zhaoyu, Effects of shrinkage reducing agent and expansive admixture on the volume deformation of ultrahigh performance concrete, *Adv. Mater. Sci. Eng.* 2017 (2017).
- [82] D. Bentz, M.R. Geiker, K.K. Hansen, Shrinkage-reducing admixtures and early-age desiccation in cement pastes and mortars, *Cement Concr. Res.* 31 (7) (2001) 1075–1085.
- [83] N. Shlonimskaya, J.J. Biernacki, H.M. Kayello, D.P. Visco, An application of computer-aided molecular design (CAMD) using the signature molecular Descriptor—Part 2. Evaluating Newly identified surface tension-reducing substances for potential use as shrinkage-reducing admixtures, *J. Am. Ceram. Soc.* 97 (2) (2014) 378–385.

# Numerical and Finite-Element Analysis of Short Ultrahigh-Performance Fiber-Reinforced Concrete Columns

C. Fang<sup>1</sup>; M. S. Mohamed Ali<sup>2</sup>; A. H. Sheikh<sup>3</sup>; and M. Singh<sup>4</sup>

**Abstract:** This paper describes the development of numerical and finite-element (FE) models for investigating the behaviors of short ultrahigh-performance fiber-reinforced concrete (UHPFRC) columns under concentric or eccentric loading conditions. A generic mechanic-based partial-interaction (PI) approach that is applicable to both flexural and axial members manufactured by conventional fiber-reinforced concrete has been suitably modified to analyze the structural response of the short UHPFRC columns. Moreover, FE modeling was also conducted to study the behaviors of UHPFRC members subjected to different loading conditions. Both models aim to generate load-axial deflection ( $P-\delta_{axial}$ ) or load-midheight deflection ( $P-\delta_{mid}$ ) relationships for concentrically or eccentrically loaded columns, as well as a load-midspan deflection ( $P-\delta_{mid}$ ) relationship for a beam subjected to three-point bending. Simulated results display an excellent agreement with test results, and the model can accurately predict the structural response of the UHPFRC columns. To aid in the development of a design guideline for the short UHPFRC columns, a load-moment ( $P-M$ ) interaction envelope generated by the numerical model is proposed, and it shows a good correlation to the experimental results. DOI: 10.1061/(ASCE)ST.1943-541X.0002389. © 2019 American Society of Civil Engineers.

**Author keywords:** Ultrahigh-performance fiber-reinforced concrete (UHPFRC); Short column; Partial-interaction analysis (PI); Finite-element analysis (FEA).

## Introduction

Ultrahigh-performance fiber-reinforced concrete (UHPFRC) is a novel construction material produced using a fine granular mixture, and it exhibits enhanced mechanical strength, durability, and ductile tensile behaviors, as well as high damage resistance, due to of the confining effect offered by the inner steel fibers in the homogeneous cementitious-based matrix (Hosinieh et al. 2015; Yoo and Banthia 2016; Yoo and Yoon 2016; Visintin et al. 2018b). Because of UHPFRC's superior material characteristics, its use can significantly reduce structural member size, shorten the construction period, and lower their life cycle costs (Yoo and Yoon 2016). Recent research on UHPFRC mostly focused on investigating the behaviors of structural members manufactured using UHPFRC, such as beams (Baby et al. 2014; Singh et al. 2017; Dagenais and Massicotte 2017; Sturm et al. 2018) and columns (Steven and Empelmann 2014; Hosinieh et al. 2015; Singh et al. 2015; Shin et al. 2017, 2018), and these studies indicated that using UHPFRC as construction material can significantly enhance the shear, axial-load-carrying, and flexural moment capacities of the structures.

To date, a number of studies have been carried out to investigate the structural performance of UHPFRC structural members, for instance columns under the uniaxial compression protocol (Steven and Empelmann 2014; Hosinieh et al. 2015; Shin et al. 2017; Shin et al. 2018), and the experimental results showed that structures produced using UHPFRC exhibited higher load-carrying capacity and improved ductility, in which no catastrophic collapses of the entire structure were observed. Pure axial loading tests on short UHPFRC columns with square cross sections were conducted by Hosinieh et al. (2015) and Shin et al. (2017), and their test results indicated that increasing the volumetric ratio or reducing the spacing of the transverse reinforcement for a given configuration results in pronounced increases in the axial-load-carrying capacities and ductility index of the UHPFRC short columns. They also observed that for a given value of transverse reinforcement spacing, the configuration of reinforcement affected both postpeak strength decay and toughness of the short UHPFRC columns, where the column with a high steel reinforcement ratio withstood a larger axial load at the postpeak stage compared with that of the column with a low steel reinforcement ratio, which allows high energy absorption and robustness.

A series of uniaxial compression tests on UHPFRC columns with circular cross sections and reinforced by spiral reinforcements were conducted by Shin et al. (2018), and experimental results demonstrated that over 80% of axial load capacity was maintained with the presence of the transverse reinforcements (e.g., 3%–5.1%) until the axial strain reached 0.02. Steven and Empelmann (2014) conducted experimental investigations to study the behavior of rectangular UHPFRC columns subjected to concentric or eccentric loads with eccentricities ranging from 5 to 75 mm and hence derived an empirical expression to predict the load-carrying capacity of UHPFRC columns.

Based on the preceding literature review, it recognized that most existing studies have investigated the behavior of concentrically loaded UHPFRC columns experimentally, with few reported

<sup>1</sup>Ph.D. Candidate, School of Civil, Environmental and Mining Engineering, Univ. of Adelaide, Adelaide, SA 5005, Australia (corresponding author). ORCID: <https://orcid.org/0000-0003-3599-8109>. Email: [chengfeng.fang@adelaide.edu.au](mailto:chengfeng.fang@adelaide.edu.au)

<sup>2</sup>Senior Lecturer, School of Civil, Environmental and Mining Engineering, Univ. of Adelaide, Adelaide, SA 5005, Australia.

<sup>3</sup>Associate Professor, School of Civil, Environmental and Mining Engineering, Univ. of Adelaide, Adelaide, SA 5005, Australia.

<sup>4</sup>Ph.D. Candidate, School of Civil, Environmental and Mining Engineering, Univ. of Adelaide, Adelaide, SA 5005, Australia.

Note. This manuscript was submitted on July 10, 2018; approved on February 22, 2019; published online on August 9, 2019. Discussion period open until January 9, 2020; separate discussions must be submitted for individual papers. This paper is part of the *Journal of Structural Engineering*, © ASCE, ISSN 0733-9445.

analytical procedures with strong physical senses to fully describe the underlying mechanism. To fill this research gap, this study primarily aims to develop a rational procedure to analyze short UHPFRC columns to generate individual load-displacement relationships and the load-moment interaction envelope, and hence to initiate the design guidelines of the UHPFRC columns; this will further promote the utilization of UHPFRC for construction.

To achieve this objective, first, a step-by-step procedure is developed by suitably modifying the classical structural mechanical-based model, namely, the moment-rotation ( $M/\theta$ ) approach, that has been successfully applied to simulate the axial behavior of conventional reinforced concrete columns (Visintin et al. 2013) and flexural behaviors of FRP-plate reinforced beams (Mohamed Ali et al. 2008) and fiber-reinforced concrete beams (Visintin and Oehlers 2018; Visintin et al. 2018a). In this study, this generic approach is further extended to simulate UHPFRC short columns by incorporating the effects of steel fibers in the UHPFRC (i.e., tensile strain hardening).

Furthermore, to more accurately predict the performance of eccentrically loaded short UHPFRC columns, the active-confinement effects induced by the transverse reinforcements cannot be neglected and need to be properly considered in the analytical approaches. Existing confinement models (Razvi and Saatcioglu 1999) pertaining to high-strength concrete (HSC) with steel stirrups were verified based on the specific actively confined test results of UHPFRC and were hence adopted in the proposed numerical model to simulate the stress-strain relationship of UHPFRC confined by stirrups. In addition to the mechanics-based model, a detailed finite-element (FE) analysis is also undertaken to incorporate a purposely developed concrete-damage plasticity (CDP) model into commercially available FE software ABAQUS version 6.14 to simulate the behaviors observed experimentally in UHPFRC column tests. Both models are then compared and validated against experimental results published in previous studies (Steven and Empelmann 2014; Singh et al. 2015), wherein these columns were subjected to concentric or eccentric loads.

## Developing Numerical Models Using Partial-Interaction Analysis

The structural response of a short UHPFRC column under an eccentric loading condition can be considered to contain the following stages:

- Stage 1: precracking stage. A conventional sectional analysis that assumes a full-interaction between reinforcements and adjacent UHPFRC was adopted to generate the  $M-\theta$  relationship of the section.
- Stage 2: postcracking stage. An increase in flexural bending ( $M$ ) initiates and gradually enlarges tensile cracks at the surface of the columns. Here full interaction-based analysis is not able to capture this localized behavior, whereas a partial-interaction (PI) analysis considering the tension-stiffening mechanism well accommodates the relationships between slips ( $\Delta$ ) and forces ( $P_{rb}$ ) in tensile reinforcement in the displacement-based moment rotation ( $M/\theta$ ) approach to obtain the  $M-\theta$  relationship of the column section at the postcracking stage.
- Stage 3: formation of plastic hinge. The postcracking stage is then followed by the formation of a plastic hinge with the occurrence of concrete softening (i.e., due to the concrete crushing under compression). The development of compression wedge also occurs with gradual yielding of tensile reinforcements. To obtain the  $M-\theta$  relationship of the columns in this phase, a size-dependent approach was adopted to quantify the

concrete-to-concrete sliding mechanism that occurred at the sliding interfaces.

Details of the formation of plastic hinge, segmental approach, and PI mechanisms, including tension stiffening and concrete softening, are described in the following sections.

### Fundamental Mechanism of the Column Plastic Hinge

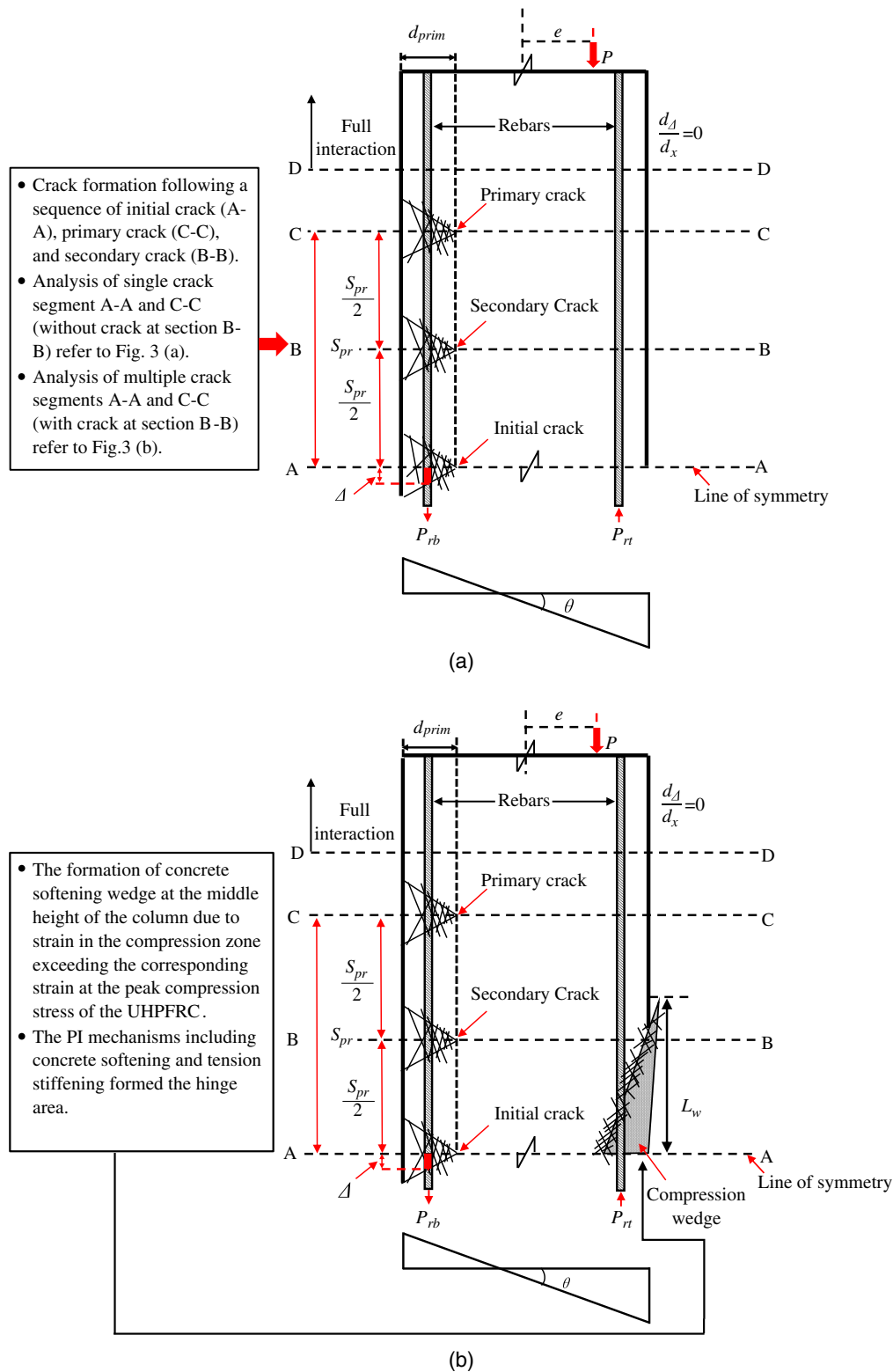
A displacement-based partial-interaction moment-rotation ( $M/\theta$ ) approach for simulating the structural behaviors of the eccentrically loaded UHPFRC short column after the precracking stage is illustrated in Fig. 1. This technique successfully reproduced the load-lateral deflection ( $P-\delta_{mid}$ ) relationships of conventional RC columns subjected to eccentric load (Visintin et al. 2013) from serviceability to structural failure, and it has been further extended to fiber-reinforced concrete (FRC) flexural members with consideration of crack-bridging effects (Visintin and Oehlers 2018; Sturm et al. 2018; Xie et al. 2018).

Fig. 1(a) depicts the conceptual model of the PI tension-stiffening mechanism on the short UHPFRC column in the postcracking stage. Initially, an increase in flexural bending moment ( $M$ ) induced by eccentric axial load ( $P$ ) resulted in the formation of the initial crack in Section AA located at the midheight of the column. Right after the concrete tensile cracking, slip ( $\Delta$ ) between tensile rebar and surrounding concrete prism with a width of  $d_{prism}$  also affected the force in tensile rebar ( $P_{rb}$ ) at the initial crack section (Section AA). Specifically, to model the tension-stiffening mechanism and hence accommodate its effect on the  $M-\theta$  relationship of the section, a shooting method is applied whose details are described in a subsequent section.

Furthermore, widening of tensile cracks with increasing moment leads to a subsequent increase in the discrete rotation ( $\theta$ ) of the short column and consequently affects the moment-rotation ( $M-\theta$ ) relationships of the UHPFRC columns after the precracking stage. With increasing in bending moment ( $M$ ) along the short column, a primary crack (at Section CC in Fig. 1) occurred adjacent to the initial crack, where the distance between the primary crack and initial crack is defined as a crack spacing ( $S_{pr}$ ), also shown in Fig. 1(a). A secondary crack (Section BB in Fig. 1), which is ideally located at the middle between initial and primary cracks, is subsequently formed with further increasing applied load. Hence, in the analysis provided in the remainder of the paper, column Region AA-DD is identified as a partial-interaction zone and the region above Section DD is defined as the full interaction (FI) zone.

With a large discrete rotation ( $\theta$ ) attained, concrete softening initiates at the compressive region of the section because the strain in the compression zone exceeds the corresponding strain at the peak compression stress of the UHPFRC, in which this softening region can be idealized as the compressive wedge ( $L_w$ ) as presented in Fig. 1(b). A mechanics-based hinge analysis (Visintin et al. 2013), including PI tension-stiffening mechanism and PI concrete softening mechanism, accurately quantified the discrete rotation of the column at the plastic hinge stage and hence obtained the load-lateral deflection relationship at the plastic hinge region of the columns. To simulate the behavior of an eccentrically loaded short column using the mechanics-based hinge analysis, the following assumptions were made:

- The Euler-Bernoulli principle of plane sections remaining plane was applied for the sectional analysis in all loading stages the columns (Visintin et al. 2013).
- A constant moment (i.e.,  $M = P \times e$ ) acting along the column was assumed.
- Premature buckling caused by the secondary moment effect was neglected.



**Fig. 1.** Schematic diagram of UHPFRC short column under an eccentric load: (a) postcracking stage; and (b) plastic hinge formation.

### Cross-Sectional Analysis at Partial-Interaction Region

The displacement-based moment rotation ( $M/\theta$ ) approach is a direct application of Euler-Bernoulli theorem of plane section accommodating with the stress-strain relationships for both UHPFRC and reinforcements to determine the internal moment within the cross section of the column. Generally, the failure of an eccentrically

loaded column can be categorized into two modes depending on the magnitude of the eccentricity: (1) failed by concrete compressive softening when the column loaded at zero or a small eccentricity, and (2) failed by flexural bending when the column loaded at a large eccentricity. Figs. 2(a and b) graphically shows the mechanisms governing the two failure modes of eccentrically loaded UHPFRC short columns, respectively.

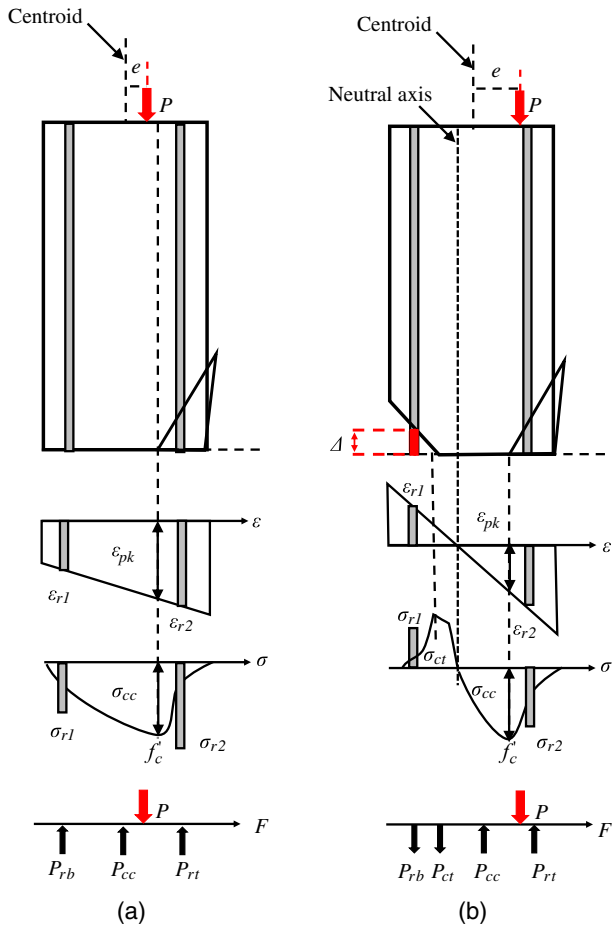


**Fig. 2.** Cross-section profiles for (a) column loaded at a small eccentricity; and (b) column loaded at a large eccentricity.

For the short column loaded at a small eccentricity shown in Fig. 2(a), the strain profile indicates that the neutral axis of column is located outside of the column cross section and the entire cross section is fully under compression. For this case, softening of the UHPFRC causes relative slippage along the concrete-to-concrete interface and determines the friction force of UHPFRC. The total rotation ( $\theta$ ) of the column is affected by the concrete softening after the formation of the compression wedge. The shear friction mechanism is size-dependent and can be accurately modeled using the size-dependent approach developed by Chen et al. (2014).

The second strain profile of column hinge in Fig. 2(b) presents the mechanisms governing the failure of UHPFRC columns loaded with a relatively large eccentricity ( $e$ ), and the performance of the column is predominated by the flexural bending moment ( $M$ ) induced by the eccentric loads rather than the applied load ( $P$ ). By inputting the material properties into the PI-based sectional analysis, the location of the neutral axis can easily be found, and hence, the  $M$ - $\theta$  relationship of the section be obtained at all loading stages. In the PI-based analysis, the effect of the tension-stiffening mechanism should be considered, and this can be simply achieved by using the force ( $P_{rb}$ ) based on the relative slip ( $\Delta$ ) between reinforcement and adjacent concrete.

### PI Tension-Stiffening Mechanism

The tension-stiffening mechanism presented in Fig. 3 is an essential component for quantifying the actual performance of an eccentrically loaded columns at the plastic hinge region. A shooting method for tension-stiffening numerical analysis to attain a force-slip ( $P_{rb}$ - $\Delta$ ) relationship and the detailed modeling procedure are schematically shown in Figs. 4 and 5, respectively. As presented in Fig. 3(a), the area of a tensile reinforcement is  $A_{bar}$ , and the cross section of the surrounding concrete is idealized as a square prism with cross-sectional area of  $A_c$ . With the formation of the initial

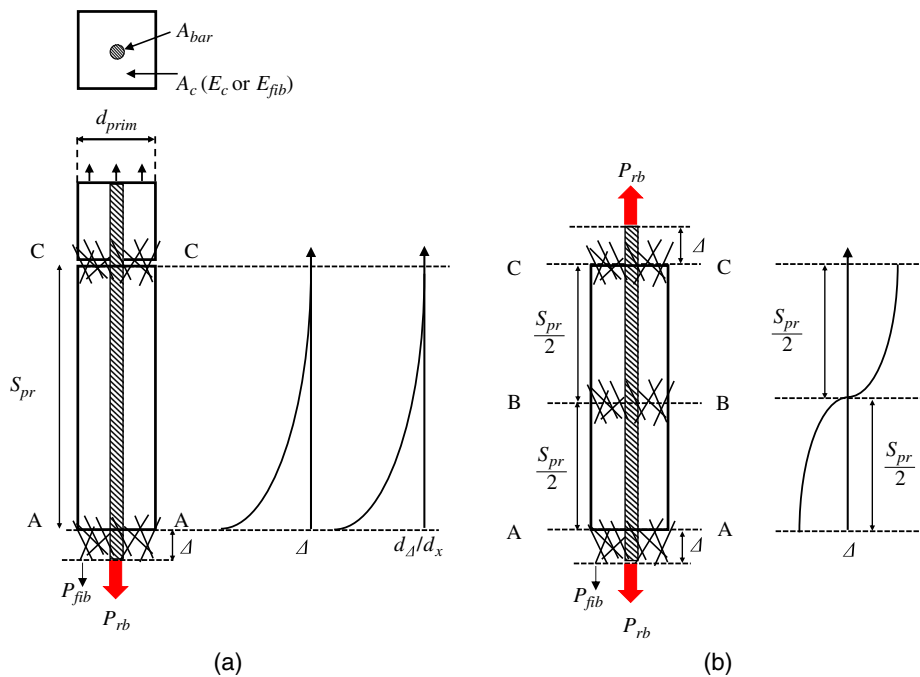


**Fig. 3.** Partial-interaction tension-stiffening mechanisms: (a) tension stiffening with a single crack; and (b) tension stiffening with multiple cracks.

tensile crack at Section AA, both residual tensile force in fibers ( $P_{fib}$ ) and force in tensile rebar ( $P_{rb}$ ) resist the widening of the initial crack. The slip distribution shown in Fig. 3(a) indicates that the maximum slip ( $\Delta$ ) occurred at the initial crack in Section AA and gradually decreased along the PI region until it reaches zero, and hence it results in a transfer of stress from the reinforcement to concrete through the bond.

Furthermore, the full interaction boundary conditions are defined when both distribution of  $\Delta$  and  $d_{\Delta}/d_x$  tend to zero at the same location, which in turn determines the crack spacing ( $S_{pr}$ ) and the force-slip ( $P_{rb}-\Delta$ ) relationship.

The partial-interaction tension-stiffening numerical mechanism for multiple cracks as reported in previous studies (Mohamed Ali et al. 2008; Shukri et al. 2016; Visintin and Oehlers 2018) is illustrated in Fig. 3(b). For modeling the case of multiple cracks using the shooting method, its boundary condition is defined as the distribution of  $\Delta$  reaching zero at the location of  $S_{pr}/2$  from the initial crack. This hence redefines the  $P_{rb}-\Delta$  response at the hinge section for generating the  $M-\theta$  relationships of the columns.

As presented in Fig. 4, the concrete prism is divided into multiple segments with a very short element length ( $L_e$ ) to determine the variation in reinforcement slip and the distribution of strain in the reinforcement and concrete. Following that, slip ( $\Delta_1$ ) was imposed as the initial value for the slip ( $\Delta$ ) with the maximum value of  $W_{cr}/2$ , which is the half of the maximum crack length

(Visintin and Oehlers 2018). The corresponding force in UHPFRC due to fiber bridging effect is identified as  $P_{fib}$ , which is derived from the relationship between tensile stress ( $\sigma_r$ ) and the half crack width ( $W_{cr}/2$ ).

As presented in Figs. 4 and 5, the force of the tensile reinforcement at the crack face ( $P_{rb}$ ) is initially guessed as the average of the low boundary ( $P_{rl}$ ) and high boundary ( $P_{ru}$ ), and the corresponding strain in the reinforcement ( $\varepsilon_{b1}$ ) and concrete ( $\varepsilon_{c1}$ ) can be obtained, as presented in Fig. 5. Hence, the slip strain of the first concrete segment ( $(d_{\Delta}/d_x)_1$ ) which is the algebraic difference of the strain magnitudes between the reinforcement and concrete ( $\varepsilon_{b1} - \varepsilon_{c1}$ ) is determined. The corresponding differential slip ( $\delta\Delta_1$ ) between concrete and reinforcement in Segment 1 is obtained by integrating the slip strain ( $(d_{\Delta}/d_x)_1$ ) along the segmental length ( $L_e$ ). The bond force in the first element ( $B_1$ ) can be calculated from the known bond-slip ( $\tau-\Delta$ ) properties and contact perimeter ( $L_{per}$ ) of the rebar. This procedure is repeated for Element 2 with the tensile force in reinforcement determined as  $P_{rb} - B_1$ , and the force in concrete determined as  $P_c + B_1$ . The slip of the tensile reinforcement at the second segment ( $\Delta_2$ ) is obtained by subtracting  $\delta\Delta_1$  from the initial slip ( $\Delta_1$ ), and the corresponding bond force ( $B_2$ ) in Element 2 can therefore be determined, as shown in Fig. 4.

A flowchart is given in Fig. 5 to show the details of applying this shooting method to obtain the  $P_{rb}-\Delta_1$  relationship, and additional information on this shooting method has been given by Visintin and

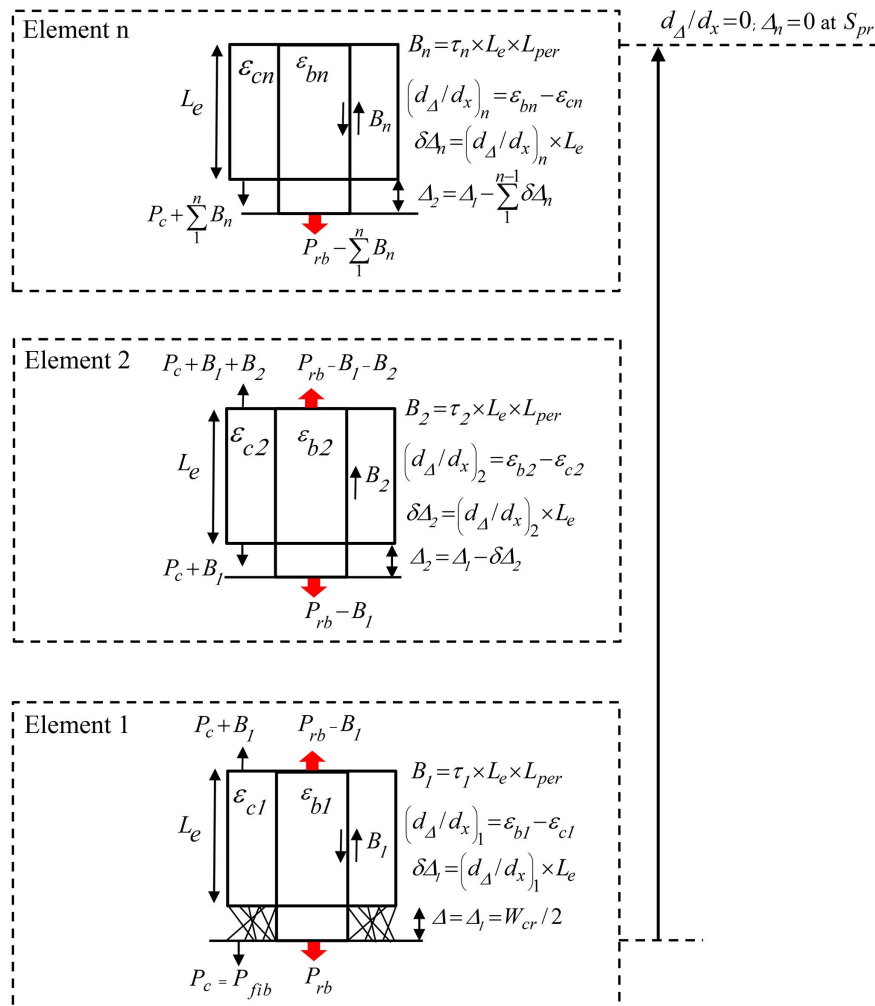


Fig. 4. Shooting method for tension-stiffening numerical analysis.

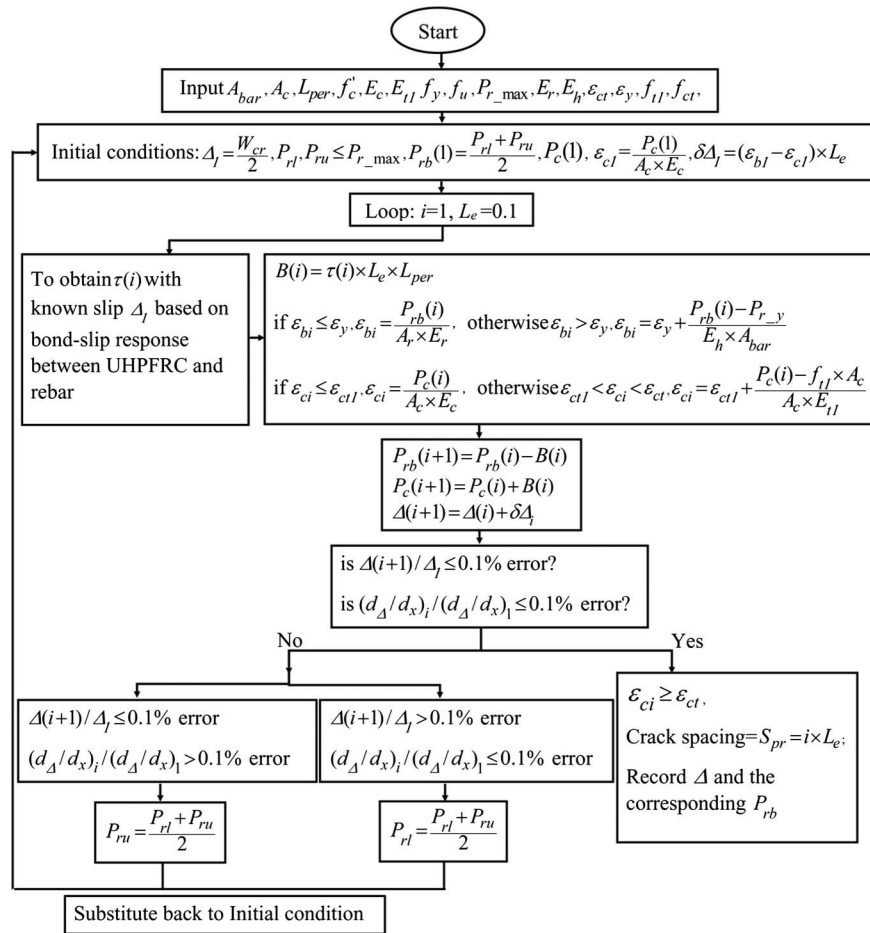


Fig. 5. Modeling procedure to determine the  $P_{rb}$ - $\Delta$  relationship.

Oehlers (2018). This analysis can then be repeated successively for subsequent elements to yield the  $P_{rb}$  needed to produce a given slip ( $\Delta_i$ ) until the full-interaction boundary conditions are satisfied, where both slip ( $\Delta$ ) and slip strain ( $d_\Delta/d_x$ ) values in the segment tend to zero. Consequently, this defines the minimum distance from the initial crack face to the primary cracks that may form, namely initial crack spacing ( $S_{pr}$ ). Similarly, the same shooting method was applied to conduct the PI tension-stiffening analysis for the case of the multiple cracking, and one boundary condition, where the slip ( $\Delta$ ) equals zero at the location of  $S_{pr}/2$  from the initial crack, is required.

### PI Concrete Softening

When the compressive strain in conventional concrete exceeds the strain corresponding to the peak stress, concrete starts crushing, and a sliding wedge starts to form in the PI compression region. It is known that the compressive stress-strain ( $\sigma$ - $\epsilon$ ) relationship for plain concrete contains two branches, namely an ascending branch up to the peak strength that depends entirely on the material deformations and a descending branch associated with PI sliding along the concrete to the concrete interface of the softening wedge (Zhang et al. 2014). A generic size-dependent  $\sigma$ - $\epsilon$  relationship based on the results of standard cylinder tests was proposed by Chen et al. (2014), which encompassed the ascending branch dependent on the length of the specimens and the descending branch dominated by the shear friction mechanism along the sliding wedge. This approach, which has been successfully applied to conventional concrete

(Chen et al. 2014) and has been further extended to steel-fiber concrete (FRC) by Visintin and Oehlers (2018), accommodating the wedge-restrained by fibers in a flexural analysis, is therefore applied in the segmental analysis of current study to derive the stress in the PI sliding wedge

$$\epsilon_{def} = (\epsilon_{test} - \epsilon_{mat}) \frac{200}{L_{def}} + \epsilon_{mat} \quad (1)$$

where  $\epsilon_{mat}$  = material strain corresponding to the strain at peak stress;  $\epsilon_{test}$  = total strain based on standard compression test using a 200-mm cylinder; and  $L_{def}$  = deformation length, which is also a half of the cracking space ( $S_{pr}/2$ ) determined from the partial-interaction (PI) tension-stiffening mechanism (mm).

### Load-Deflection Relationship

Having FI, PI tension-stiffening, and PI concrete-softening mechanisms integrated, sectional internal moment corresponding to varying  $\theta$  can be calculated, and hence the completed  $M$ - $\theta$  relationship of individual short UHPFRC column can be determined. Excluding the secondary moment effect due to buckling in simulating the load-midheight deflection ( $P$ - $\delta_{mid}$ ) relationship of the deflected column depicted in Fig. 6(a), the distributions of the flexural moment and curvature along the half column are presented in Figs. 6(b and c), respectively.

Moment distribution along the half of the column is constant without considering the second moment effects, whereas the distribution of curvature is nonlinear at the hinge region due to the

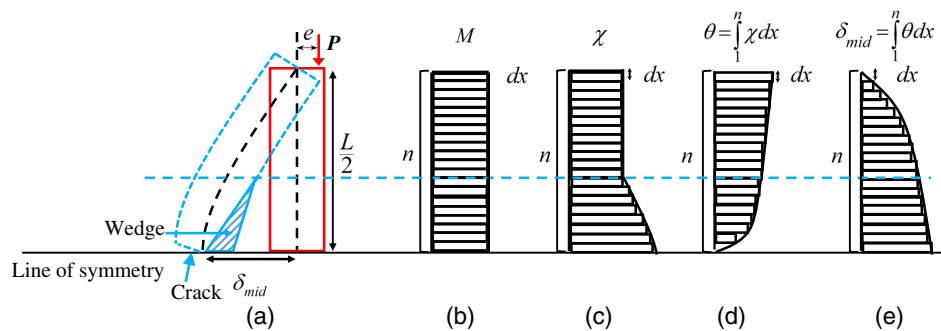


**Fig. 6.** Schematic diagram for deriving lateral deflection of the short UHPFRC column: (a) deflected short UHPFRC column; (b) moment distribution for the column; (c) curvature distribution for the column; (d) rotation distribution for the column; and (e) lateral deflection distribution for the column.

extra rotation induced by concrete softening (Visintin et al. 2013). Subsequently, the distribution of rotation along the column shown in Fig. 6(d) is obtained by integrating the curvature ( $\chi$ ) from the middle height of the column ( $L/2$ ) to the top of the column. Similarly, having obtained the  $M$ - $\theta$  relationship of the short column, it is a matter of integrating the distribution of rotation from the middle height of the column to the top of the column to determine the lateral deflection  $\delta_{mid}$  as shown in Fig. 6(e).

## Finite-Element Modeling

Detailed three-dimensional (3D) finite-element models are developed to predict the behaviors of concentrically and eccentrically loaded short UHPFRC columns. The FE models are first applied for the simulation of column specimens tested in this study, and the experimental results are utilized to validate the numerical results predicted by the FE models. This has demonstrated the very good performance of the numerical model. With this confidence, the FE model is adopted to produce additional results for different eccentricities. A beam under three-point bending is also modeled because such a specimen is tested to get the pure bending capacity of the specimen (with no axial load), which needed for completing the load-moment interaction diagram.

In order to have a reliable model of these structures, well-regarded commercially available finite-element code ABAQUS is used in this study. The concrete is modeled with 3D hexahedral solid elements having eight nodes (C3D8R), where the element formulation is based on the reduced integration technique. The steel reinforcements are modeled with truss elements in 3D space with two nodes (T3D2). The steel reinforcements (truss elements) are embedded within the concrete (solid elements) that imposed a perfect bonding between these two materials. However, a slip between them is expected in reality, which is incorporated indirectly through the tension-stiffening feature of the CDP model, which is the most advanced material model provided by ABAQUS for simulating normal-strength concrete. Thus, this model may not provide reliable results if it is applied directly without any adjustment to UHPFRC, as experienced by Singh et al. (2016, 2017). Based on that, the problem is addressed by adjusting some parameters such as biaxial ratio and dilation angle. The essential technical details of the CDP model are provided in the following section. For the steel reinforcements, the elastoplastic material model with steel hardening and softening is employed.

Fig. 7 shows the FE model of one of the four column specimens and a beam specimen. Steel caps consisting of a rectangular flat plate (length = 500 mm, breadth = 350 mm, and thickness = 65 mm) and square ring (length = 165 mm and thickness = 45 mm)

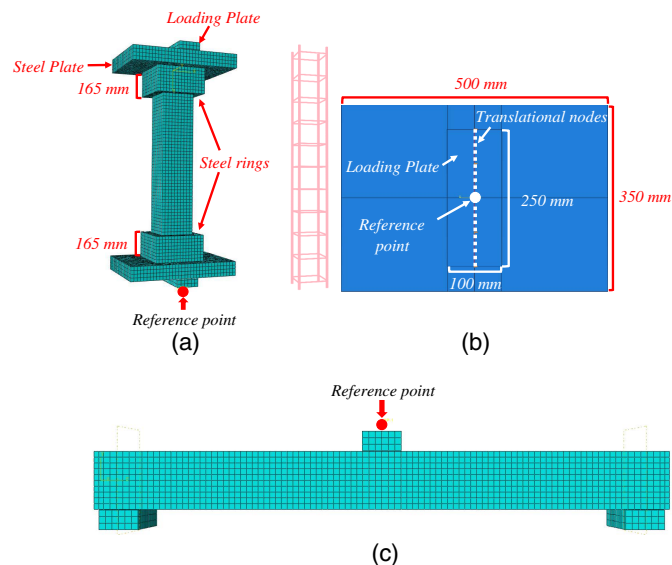


**Fig. 7.** FE simulations: (a) UHPFRC concentrically and eccentrically loaded short column; (b) details for steel cap, steel loading plate, and reference point; and (c) UHPFRC beam with three-point bending setup.

used at the two ends of a column are modeled with 3D elements (C3D8R) using an elastoplastic material model, as shown in Figs. 7(a and b). This is similarly followed for the two additional steel plates (length = 250 mm; breadth = 100 mm and thickness = 50 mm) used at the two ends of the columns for the application of loading. The breadth of the loading plate (100 mm) is aligned with the length of the steel cap (500 mm). All translational displacements of the nodes laying on the 250-mm-long central line at the top surface of the upper loading plate are restrained, as shown in Fig. 7(b). This is similarly applied to the lower loading plate at its lower surface except the vertical displacement to allow vertical upward movement.

The vertical displacement of these nodes having a single value is imposed and increased gradually at a steady rate (0.15 mm/min) using a reference point along with multipoint coupling constrain to load the column in the form of displacement control. The preceding procedure is applicable for the concentrically loaded case, and the positions of these restraining and loading lines are simply moved from the central line for the eccentrically loaded scenarios. The contact between the steel cap and the column is ensured by using the surface to surface contact (standard) algorithm provided by ABAQUS where a hard contact is provided for the normal displacement and sliding contact for the tangential displacements with a



friction coefficient of 0.1. A tie contact is used to connect the loading plate with the steel cap.

Three loading plates used for the beam have the same size as the loading plate used for the columns, where the length of these plates (250 mm) is oriented along the breadth of the beam. The same surface-to-surface contact (standard) is used between the beam and loading plates. The displacements of the 250-mm long central line nodes at the bottom surface of the two supporting plate are fully restrained. Vertically downward displacement of the central loading plate having a single value is imposed and increased gradually at a steady rate (0.15 mm/min) using a reference point along with multipoint coupling constrain to load the beam. A convergence study for the mesh size was conducted to assure a stable converged solution, and it was found that an element size of 15 mm is adequate, which is consistently used in all cases, as shown in Figs. 7(a–c).

### Concrete Damage Plasticity Model

In this study, the inelastic responses of concrete material in the CDP model is represented by a plasticity-based continuum damage model that encompassed the elastoplastic responses under tension and compression, and this model is in conjunction with inputted scalar/isotropic damage parameters. Two equivalent plastic strains obtained from the elastoplastic responses are associated with failure mechanism under compression and tension and hence govern the envelope of the yield surface (Lubliner et al. 1989). To this end, the uniaxial ( $\sigma$ - $\varepsilon$ ) responses of concrete in compression or tension are required to either represent the formation of microcracks in tension or characterize the plastic response in compression. In order to have a nonassociated flow rule, a plastic potential is used to accommodate with the yield function, and five additional parameters are required to determine the yield function and plastic potential

$$F = \frac{1}{1-\alpha} (\bar{q} - 3\alpha\bar{p} + \beta(\bar{\varepsilon}^{pl})\langle\hat{\sigma}_{\max}\rangle - \gamma\langle-\hat{\sigma}_{\max}\rangle) - \bar{\sigma}_c(\bar{\varepsilon}^{pl}) \leq 0 \quad (2)$$

$$G = \sqrt{(\xi\sigma_{t0} \tan \varphi)^2 + \bar{q}^2} - \bar{p} \tan \varphi \quad (3)$$

$$\alpha = \frac{\sigma_{bo} - \sigma_{co}}{2\sigma_{bo} - \sigma_{co}}; \quad 0 \leq \alpha \leq 0.5 \quad (4)$$

$$\beta(\bar{\varepsilon}^{pl}) = \frac{\bar{\sigma}_c(\bar{\varepsilon}^{pl})}{\bar{\sigma}_t(\bar{\varepsilon}^{pl})} (1 - \alpha) - (1 + \alpha) \quad (5)$$

$$\gamma = \frac{3(1 - k_c)}{2k_c - 1} \quad (6)$$

where  $\alpha$  and  $\gamma$  = material dependent constants;  $\bar{q}$  = effective von Mises equivalent stress;  $\bar{p}$  = hydrostatic pressure based on effective stresses;  $\hat{\sigma}_{\max}$  = maximum principal effective stress;  $\bar{\sigma}_c(\bar{\varepsilon}^{pl})$  and  $\bar{\sigma}_t(\bar{\varepsilon}^{pl})$  = functions of equivalent plastic strain  $\bar{\varepsilon}^{pl}$ , representing effective cohesive stresses under compressive and tensile stresses;  $G$  = flow potential, which follows a Drucker Prager hyperbolic function;  $\xi$  = potential eccentricity parameter for describing the rate of the function approaches the asymptote;  $\sigma_{t0}$  = uniaxial tensile stress; and  $\varphi$  = dilation angle obtained from the measurement from the  $p$ - $q$  plane under high confining pressure.

To characterize the shape of the yield surface, two critical parameters are required: (1)  $\sigma_{bo}/\sigma_{co}$  ratio of the initial biaxial compressive strength and initial uniaxial compressive strength, and (2) parameter  $k_c$ , which is the ratio between the distances from the hydrostatic axis to tensile and compressive meridians. In this study, the value of  $\sigma_{bo}/\sigma_{co}$  is taken as 1.05 for UHPFRC instead of the 1.16 that is usually taken for normal-strength concrete (Singh et al. 2017). Similarly, the value of the dilation angle  $\varphi$  is taken as  $35^\circ$  (Singh et al. 2016) for UHPFRC instead of  $30^\circ$ , which is normally applied for conventional concrete.

As presented in Fig. 8, completed uniaxial  $\sigma$ - $\varepsilon$  curves of conventional concrete are generated from cylinder compression and direct tensile tests, and both inelastic strain ( $\varepsilon_c^{in}$ ) and cracking strain ( $\varepsilon_t^{ck}$ ) are determined by subtracting the elastic components ( $\varepsilon_{0c}^{el}$  and  $\varepsilon_t^{el}$ ) from the total strain ( $\varepsilon_c$  and  $\varepsilon_t$ ), respectively

$$\varepsilon_c^{in} = \varepsilon_c - \varepsilon_{0c}^{el} = \varepsilon_c - \sigma_c/E_0 \quad (7)$$

$$\varepsilon_t^{ck} = \varepsilon_t - \varepsilon_t^{el} = \varepsilon_t - \sigma_t/E_0 \quad (8)$$

where  $E_0$  = undamaged elastic modulus of concrete. With this, the aforementioned equivalent plastic strains ( $\bar{\varepsilon}_c^{pl}$  and  $\bar{\varepsilon}_t^{pl}$ ) determining the failure mechanism of the yield function can be derived as follows:

$$\bar{\varepsilon}_c^{pl} = \varepsilon_c^{in} - \frac{d_c}{(1-d_c)} \frac{\sigma_c}{E_0} \quad (9)$$

$$\bar{\varepsilon}_t^{pl} = \varepsilon_t^{ck} - \frac{d_t}{(1-d_t)} \frac{\sigma_t}{E_0} \quad (10)$$

Damage parameters ( $d_c$  and  $d_t$ ) are utilized to characterize the level of degradation in the material stiffness, ranging from 0 to 1 for

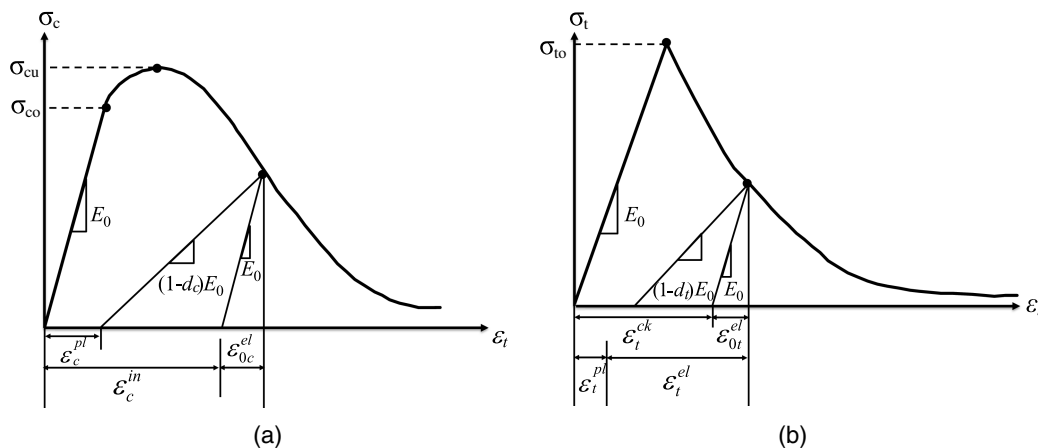


Fig. 8. Definition of (a) compressive behavior; and (b) tension stiffening.

describing undamaged and fully damaged states, respectively. The damage parameters are determined utilizing the concepts of Bertel and Mark (2006) and Mahmud et al (2013) as follows:

$$d_c = 1 - \left[ \frac{\frac{\sigma_c}{E_0}}{0.2e_c^{in} + \frac{\sigma_c}{E_0}} \right] \quad (11)$$

$$d_t = 1 - \frac{\sigma_t}{f_t} \quad (12)$$

## Comparison between Theoretical Model and Test Results

### Introduction of Experimental Program

As shown in Fig. 9(a), there are four reinforced UHPFRC columns with a square cross section of 150 × 150 mm and 900 mm in height, and all columns are reinforced by four longitudinal steel reinforcements with a diameter of 16 mm and yield stress of 500 MPa. A clean concrete cover of 20 mm measured from edge of reinforcements to edge of columns was applied to all cross sections. Transverse reinforcements with a diameter of 6 mm were placed in the

columns with a constant stirrup spacing of 85 mm. One column was subjected to pure axial load, and the three other columns were subjected to eccentric loads with eccentricities of 35, 50, or 80 mm, respectively. Besides that, a UHPFRC member was cast as a beam with the same cross section and stirrup arrangement as those of the companion columns but a longer span of 1,350 mm, as shown in Fig. 9(b). This UHPFRC beam was tested under a simply supported condition and further subjected to three-point flexural bending induced by the concentrated point load at the midspan of the beam.

All UHPFRC columns were tested in the lab of the University of Adelaide using a universal testing machine (Amsler, Schaffhouse, Switzerland) with a maximum capacity of 5,000 kN, and the UHPFRC beam was tested using an Avery universal testing machine with a capacity of 1,000 kN. For both concentrically and eccentrically loaded columns, the local contraction and elongation of the column were measured by linear variable differential transducers (i.e., LVDT-1 and LVDT-3, respectively), and the global displacements of the short columns were captured by LVDT-2 and LVDT-4. Additionally, lateral displacements at the middle region including the middle height of the column and 200 mm above and below the midheight were measured by LVDTs 5–7.

The experimental setup of beam is exhibited in Fig. 9(b), in which LVDTs 1–3 were used to measure the deflection at the

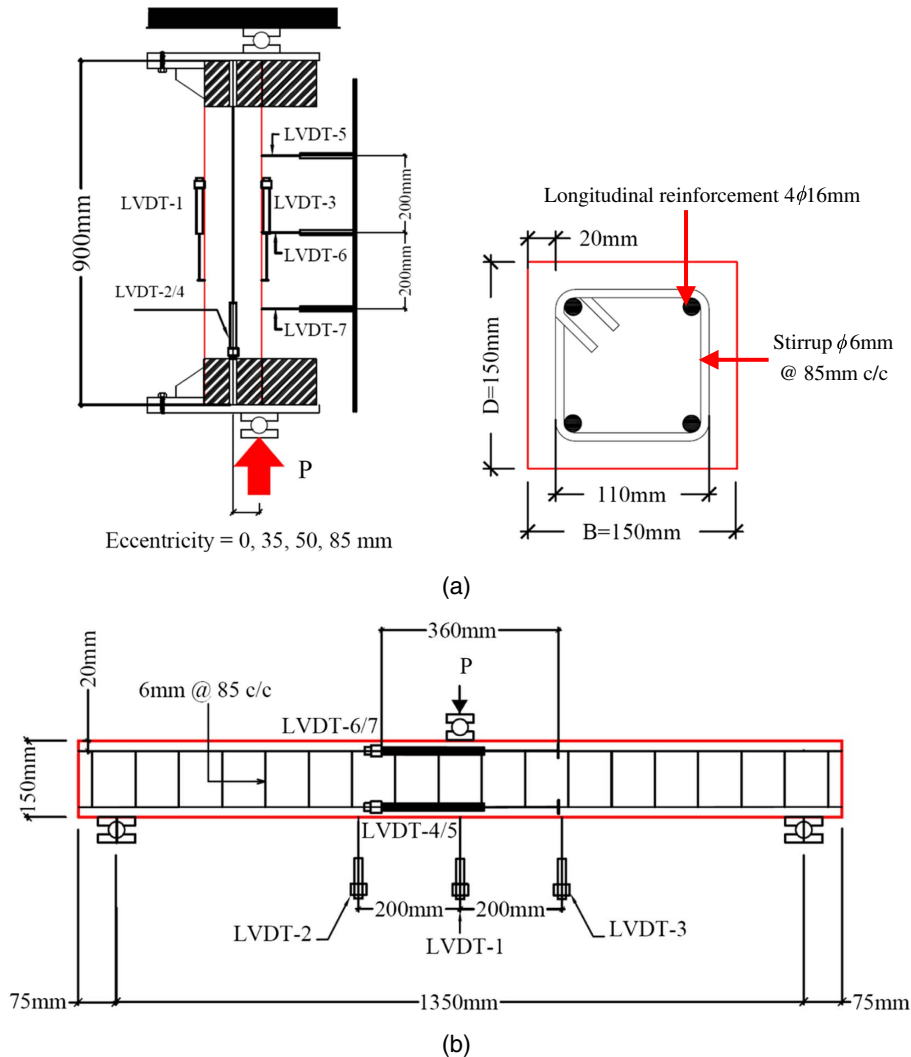


**Fig. 9.** Instrumentation setup and member geometry details: (a) concentrically and eccentrically loaded column; and (b) three-point flexural bending tests performed on UHPFRC beam.

middle span of the beam, and LVDTs 4 and 5 were used to measure the tensile crack opening at tensile surface of the beam. LVDTs 6 and 7 were placed close to the upper surface of the beam and used to measure the contractions due to the hinge rotation.

### Fundamental Material Properties

#### Unconfined and Confined Compressive Stress-Strain Relationships of UHPFRC

Material constitutive relationships can be represented using the material model presented in this section, which is used as input for both numerical approaches. The compressive stress-strain relationship of UHPFRC can be reproduced using the model developed by Singh et al. (2017) to cooperate with the numerical modeling. As can be seen in Fig. 10(a), there is high agreement between the experimental result and modeling result. For improving the accuracy of the model, the confining effects on the core concrete inside the stirrups were considered, and an active confinement model for

high-strength concrete established by Razvi and Saatcioglu (1999) validated using the UHPFRC experimental results was directly applied to represent its stress-strain relationship.

In testing the behavior of UHPFRC under triaxial load, compression tests were conducted on UHPFRC cylinders with a diameter of 62.5 mm and height of 120 mm. Uniform lateral confinement stress of  $f_l = 4.5$  MPa was acting on all cylinders via a Hoek cell to reproduce the confinement pressure induced by the transverse reinforcements. Fig. 10(b) shows the comparisons between experimental and model results and indicates the good prediction of triaxial behavior of the UHPFRC using the model. Parameters of the confined UHPFRC calculated by using the Razvi and Saatcioglu (1999) model are presented in Table 1.

#### Tensile Characterizations of UHPFRC

Tensile characterization of UHPFRC, including its stress-strain relationship prior to cracking, strain hardening, and postpeak stress-crack opening relationship, are defined using Eq. (13), which was established based on the idealized modeling approach with three

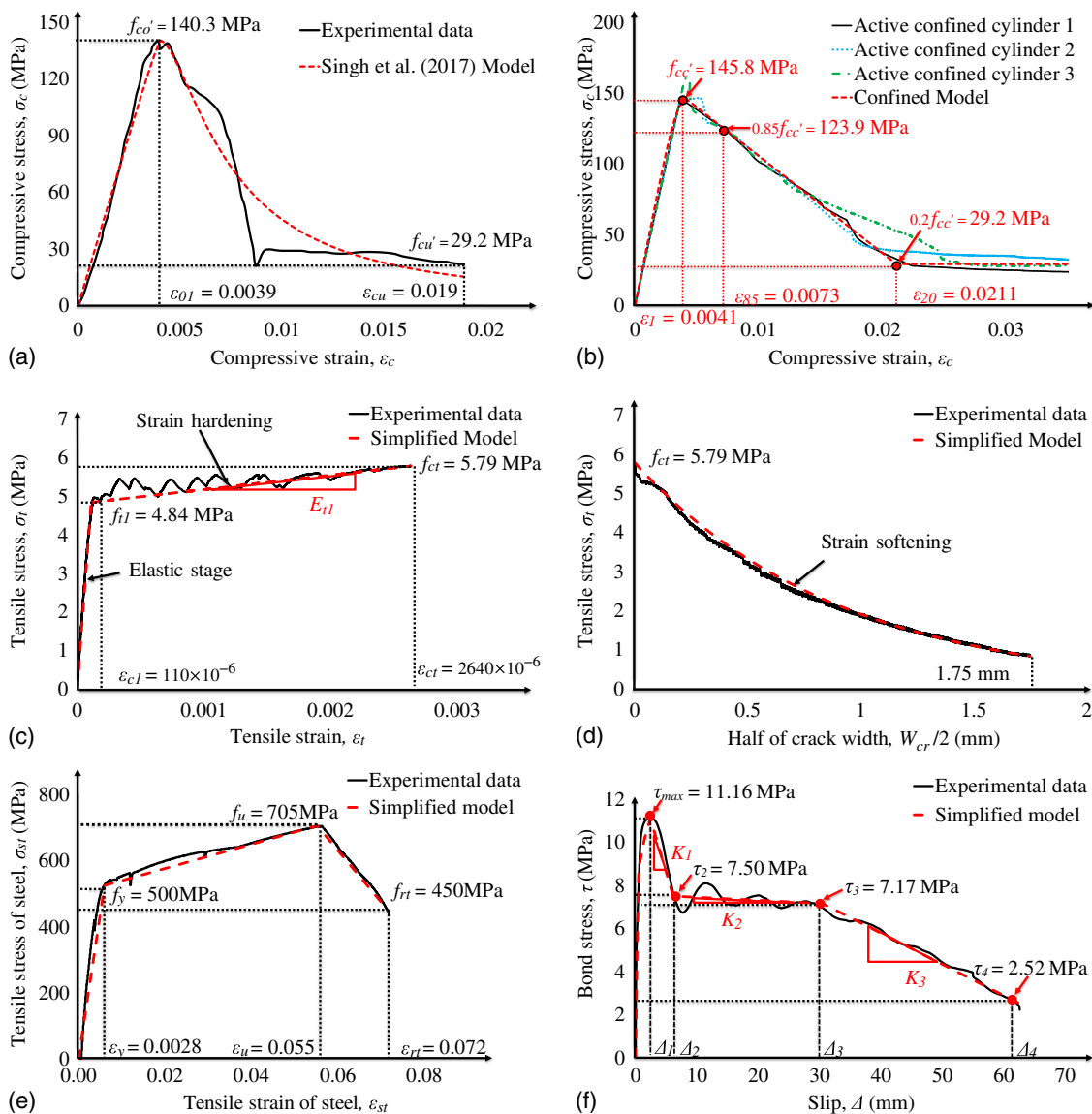


**Fig. 10.** Material properties of UHPFRC: (a) compressive stress-strain responses for unconfined UHPFRC; (b) compressive stress-strain response for confined UHPFRC with lateral confining pressure of 4.5 MPa; (c) tensile characterizations of UHPFRC; (d) tensile stress and crack opening response; (e) tensile stress-strain response for steel reinforcement; and (f) proposed bond-slip model between UHPFRC and reinforcement.

**Table 1.** Summary of parameters of confined UHPFRC calculated using Razvi's model from Razvi and Saatcioglu (1999)

Parameter	Value
Given material properties	
$f'_{co}$ (MPa)	140.3
$s$ (mm)	85.0
$b_c$ (mm)	98.0
$d_s$ (mm)	6.0
$q$	2.0
$\alpha$	90.0
$s_l$ (mm)	82.0
Coefficients and lateral confined pressure	
$k_2$	0.176
$\rho_c$	0.007
$f'_s$ (MPa)	663.4
$f'_l$ (MPa)	4.504
$f'_{le}$ (MPa)	.0793
$k_1$	6.970
$f'_{cc}$ (MPa)	145.8
Ductility of confined concrete and descending branch	
$\varepsilon_1$	0.0041
$\varepsilon_{01}$	0.0039
$k_3$	0.2852
$\varepsilon_{085}$	0.0052
$k_4$	1.3268
$\varepsilon_{85}$	0.0073
$K$	0.0394

different phases as proposed by Wille et al. (2014) and simplified based on experimental tested results reported in Singh et al. (2015), as presented in Figs. 10(c and d)

$$\sigma_t = \begin{cases} E_{ct}\varepsilon_{ct} & (0 \leq \varepsilon_{ct} \leq \varepsilon_{cc}) \\ f_{t1} + E_{t1}(\varepsilon_{ct} - \varepsilon_{t1}) & (\varepsilon_{cc} \leq \varepsilon_{ct} \leq \varepsilon_{soft}) \\ \alpha_1 e^{-\beta_1(W_{cr}/2)} & (W_{cr}/2 \leq \varepsilon_{ct} \leq \varepsilon_{soft}) \end{cases} \quad (13)$$

where  $\sigma_t$  = tensile stress (MPa);  $\varepsilon_{ct}$  = total tensile strain;  $E_{ct}$  = elastic modulus of UHPFRC of 44,000 MPa;  $\varepsilon_{cc}$  = strain prior to strain hardening ( $\varepsilon_{cc} = 110 \times 10^{-6}$ );  $f_{t1}$  = maximum tensile stress of UHPFRC within elastic range ( $f_{t1} = 4.84$  MPa);  $E_{t1}$  = modulus for the tensile strain hardening stage ( $E_{t1} = 373.67$  MPa);  $\varepsilon_{soft}$  = strain corresponding to the peak stress of 5.79 MPa prior the crack opening stage ( $\varepsilon_{soft} = 2,640 \times 10^{-6}$ ); and  $\alpha_1$  and  $\beta_1$  = constant coefficients of descending curve ( $\alpha_1 = 5.794$  and  $\beta_1 = -1.098$ ).

### Local Bond-Slip ( $\tau/\delta$ ) Relationship

The experimentally generated material characteristic of steel reinforcements used for the local slip-bond test and subsequently a simplified stress-strain relationship in both numerical models are presented in Fig. 10(e). The local bond-slip ( $\tau-\Delta$ ) relationship is required as a fundamental input for the shooting method when calculating the crack spacing and modeling the tension-stiffening behavior in a concrete prism, and the experimental local bond-slip ( $\tau-\Delta$ ) relationship was obtained from the direct pullout tests conducted by University of Adelaide. For the direct pullout tests, steel rebar having the same diameter and material properties as the longitudinal reinforcements used in the UHPFRC columns was embedded in a block of UHPFRC concrete with an embedment depth of 240 mm. Displacements of the reinforcing bar at the top and bottom of the specimen were recorded along with the corresponding force by the Avery machine. As presented in Fig. 10(f), a polyline local  $\tau-\Delta$  relationship was defined using the general expressions in Eqs. (14) and (15)

$$\tau_{max} = \alpha_2 \sqrt{f'_c} \quad (14)$$

$$\sigma_t = \begin{cases} \tau_{max} \left( \frac{\Delta}{\Delta_1} \right)^{\beta_2} & (0 \leq \Delta \leq \Delta_1) \\ k_1 \Delta + b_1 & (\Delta_1 \leq \Delta \leq \Delta_2) \\ k_2 \Delta + b_2 & (\Delta_2 \leq \Delta \leq \Delta_3) \\ k_3 \Delta + b_3 & (\Delta_3 \leq \Delta \leq \Delta_4) \end{cases} \quad (15)$$

where  $\tau_{max}$  = peak bond stress (MPa);  $\delta_1$  = corresponding local slip of the peak bond stress;  $\alpha_2$  and  $\beta_2$  = empirical coefficients fitting the experimental result, with  $\alpha_2 = 0.91$  and  $\beta_2 = 0.2$  for UHPC with a steel fiber content of 2.25%;  $k_1$ ,  $k_2$ , and  $k_3$ , and  $b_1$ ,  $b_2$ , and  $b_3$  = slopes and y-intersections, respectively, for describing linear descending bond-slip ( $\tau-\Delta$ ) relationship after peak load, in which  $k_1 = -0.97$ ,  $k_2 = -0.01$ ,  $k_3 = -0.15$ ,  $b_1 = 13.47$ ,  $b_2 = 7.56$ , and  $b_3 = 11.50$ ;  $\Delta_1$ ,  $\Delta_2$ ,  $\Delta_3$ , and  $\Delta_4$  = slips within different stages of the bond-slip ( $\tau/\delta$ ) relationship, where  $\Delta_1 = 2.4$  mm,  $\Delta_2 = 6.16$  mm,  $\Delta_3 = 30.00$  mm, and  $\Delta_4 = 62.65$  mm.

## Validation of Numerical Model and Finite Element Modeling (FEM) Simulation

### Load-Deflection Relationships

Load-axial deflection ( $P-\delta_{axial}$ ) relationships of the concentrically loaded columns obtained from experiments, numerical, and FE models are presented in Fig. 11(a), and load-midheight deflection ( $P-\delta_{mid}$ ) relationships of eccentrically loaded columns generated from both experiments and models are shown in Figs. 11(b–g). For the beam subjected to three-point bending, the load-midspan deflection ( $P-\delta_{mid}$ ) relationships can be observed in Fig. 11(h). It is worth highlighting that the numerical model and FE model well-predict the  $P-\delta_{axial}$  and  $P-\delta_{mid}$  relationships of UHPFRC short columns subjected to eccentricity of 0, 35, 50, and 85 mm.

Figs. 11(b, d, and g) present the numerical-model and FE-model predicted  $P-\delta_{mid}$  relationships of UHPC columns subjected to load eccentricities of 20, 45, and 100 mm, in which these eccentricities were not studied experimentally but their effects on  $P-\delta_{mid}$  relationships of UHPFRC short columns were numerically investigated and helped to complete the load-moment interaction envelope presented subsequently.

For the UHPFRC beam shown in Fig. 11(h), the proposed PI-based model provides an appropriate prediction for the load-midspan deflection ( $P-\delta_{mid}$ ) relationship, and it slightly underestimates the load for the simply supported beam at the postpeak stage. This could be attributed to the edge effect of friction and bond stress between steel fibers and concrete along the concrete wedge sliding planes in reality, where the friction provided residual force along the concrete softening zone, and fibers prevented crack propagation and hence restrained the rotation and middle-span displacement at the hinge region.

Experimental, numerical, and finite element modeling (FEM) results pertaining to the peak load and corresponding deflections, including  $\delta_{axial}$  and  $\delta_{mid}$ , are summarized in Table 2, and the errors of predictions regarding the peak load ( $P_p$ ) are less than 9%. The results presented in Fig. 11 and Table 2 show the good correlations between the PI-based numerical model and FE simulation, which indicates the applicability and accuracy of the proposed numerical and FE models for predicting the  $P-\delta_{mid}$  relationships of short UHPFRC columns. In order to show the generic nature of the proposed mechanics-based model and FEM model, additional experimental results from a different experiment were adopted as

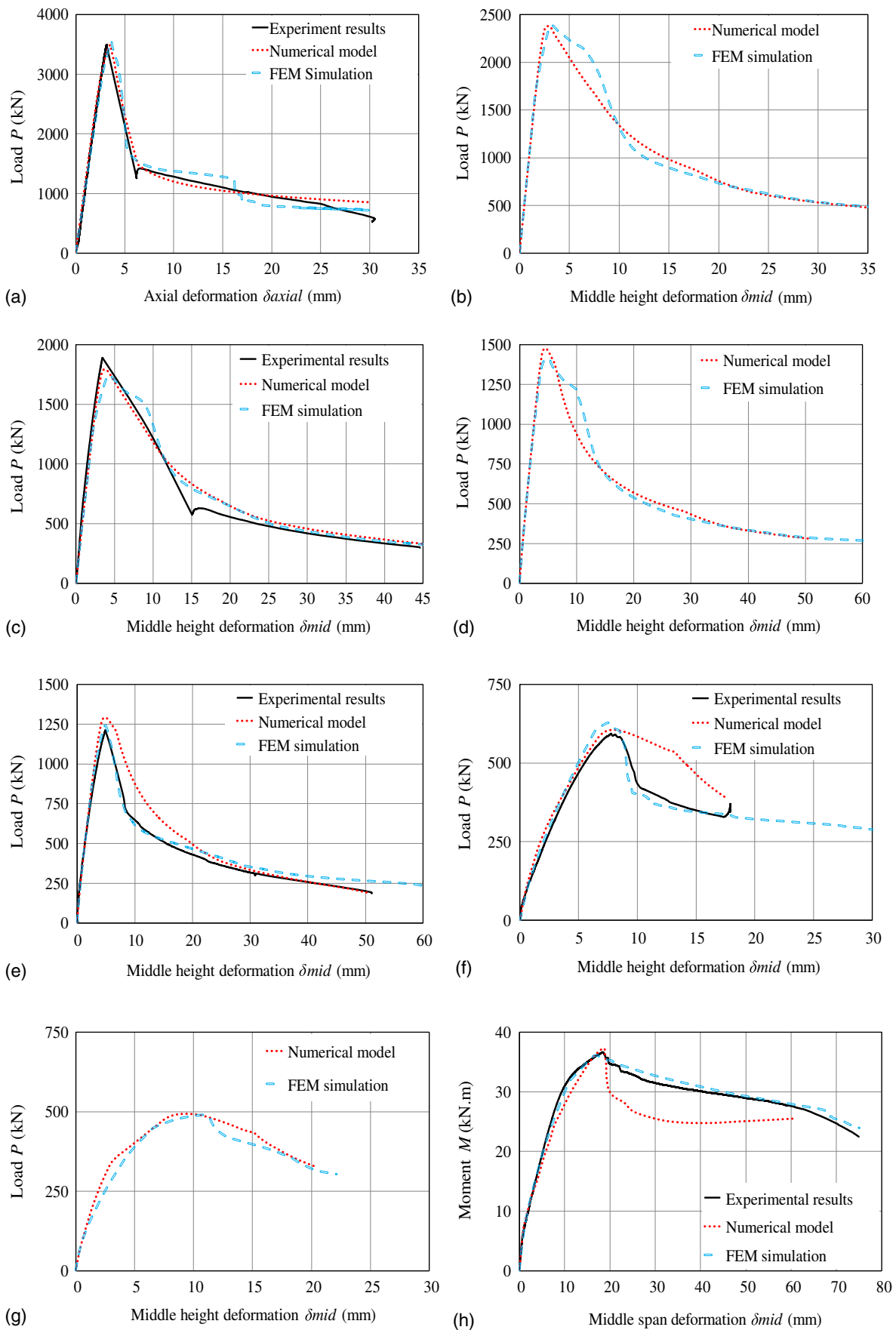


**Fig. 11.** Comparisons of experimental results with analytical and numerical models for UHPFRC columns loaded with different eccentricities: (a) concentrated; (b) eccentricity = 20 mm; (c) eccentricity = 35 mm; (d) eccentricity = 45 mm; (e) eccentricity = 50 mm; (f) eccentricity = 85 mm; (g) eccentricity = 100 mm; and (h) UHPFRC beam.

**Table 2.** Comparisons among of experimental, numerical, and numerical simulation results

Eccentricity (mm)	Experimental		Numerical		FEM	
	$P_p$ (kN)	$\delta_p$ (mm)	$P_p$ (kN)	$\delta_p$ (mm)	$P_p$ (kN)	$\delta_p$ (mm)
0	3,490.86	3.16	3,489.66	3.53	3,541.48	3.59
20	—	—	2,378.36	3.04	2,369.43	3.02
35	1,890.16	3.43	1,793.87	3.75	1,735.83	4.05
45	—	—	1,476.10	4.56	1,409.58	5.18
50	1,212.72	4.87	1,292.52	4.86	1,241.23	4.93
85	593.91	7.77	605.50	8.00	627.82	7.55
100	—	—	493.10	9.32	489.73	10.8
Pure bending	108.57	18.32	110.51	18.54	106.99	17.00

benchmarks for them, in which the experimental program was reported in detail by Steven and Empelmann (2014) and the corresponding results are illustrated in Fig. 12.

### Verification of Proposed Load-Moment Interaction Diagram

Integrating results of the numerical models for short UHPFRC columns loaded with eccentricities from 0 to 100 mm and the UHPFRC beam, a complete load-moment ( $P$ - $M$ ) interaction envelope was plotted in conjunction with actual the experimental results, as presented in Fig. 13. The comparisons shown in the figure suggest a good agreement between experimental and theoretical results because the experimental results of the columns loaded with eccentricities of 0 and 85 mm and the pure bending case closely match with the curve developed numerically. Although the model well-simulates the axial load of the columns loaded with eccentricities of 35 and 50 mm, it slightly underestimates and overestimates the flexural moments, respectively, as shown in Fig. 13.

A potential explanation for the differences between the numerical and experimental results is that the fiber distributions and density in the column specimens were slightly different from those of the material tested specimens, and this also influence the load-carrying capacities ( $P_p$ ) of the short columns due to fiber bridging effects, and hence increases the difference at the moment ( $M$ ) when using  $P_p$  to multiply the constant eccentricities. Further comparisons of the bending moment of short columns revealed that eccentricity of 45 mm led to the largest moment acting on the short UHPFRC columns, and it can be deduced that the loading eccentricity for the columns caused the balance failure of the column ranges from 35 to 45 mm.

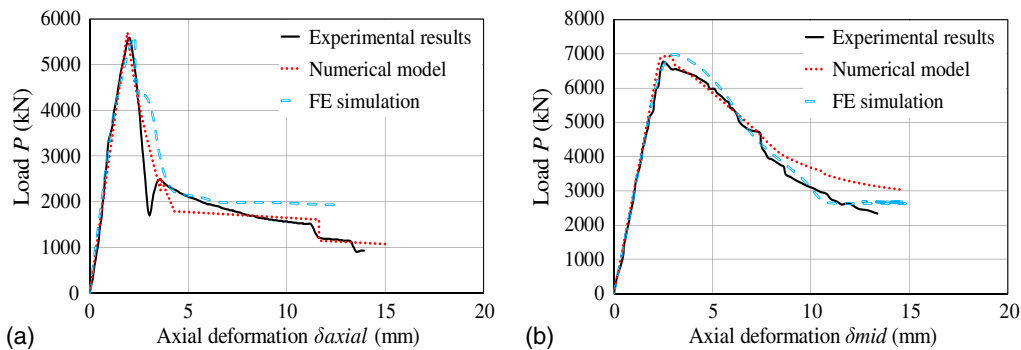


**Fig. 12.** Comparisons of experimental results with analytical and numerical models for UHPFRC columns conducted by Steven and Empelmann (2014): (a) Column S3; and (b) Column SE2.

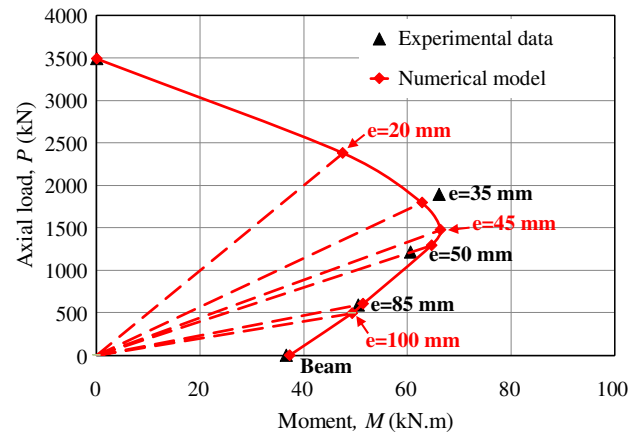


**Fig. 13.** Load-moment interaction diagram for UHPFRC short columns.

### Failure Modes

The failure modes of all column specimens are presented in Figs. 14(a–g). Having obtained the compressive damage parameters calculated using Eqs. (11) and (12) and inputted these values into the CDP model, the compressive damage pattern for a UHPFRC column under concentric load is determined by the FE model, as shown in Fig. 14(a). A maximum compressive damage level of 98.33% has been observed in the middle region of the column, and this observation indicates that the UHPFRC column under concentric load failed predominately by concrete spalling at the surface induced by concrete softening of the UHPFRC. Similar failure patterns of UHPFRC columns subjected to concentric loads have been reported in previous studies (Hosinih et al. 2015; Shin et al. 2017).

Using the compressive and tensile damage parameters inputted in the FE models, compressive and tensile damage patterns for eccentrically loaded columns are exhibited in Figs. 14(b–g). As shown in Figs. 14(b, d, and f), significant concrete softening under compression was observed in the compressive damage patterns of eccentrically loaded columns with eccentricities of 35, 50, and 85 mm. Additionally, comparisons of compressive damage patterns and maximum damage levels reveal that the compressive damage level decreased with an increase in loading eccentricity, for instance, the wedge length for columns ( $e = 35, 50,$  and  $85$  mm) are approximately 360, 315, and 165 mm, respectively.

Tensile damage patterns for eccentrically loaded columns are presented in Figs. 14(c, e, and g), and small flexural tensile cracks

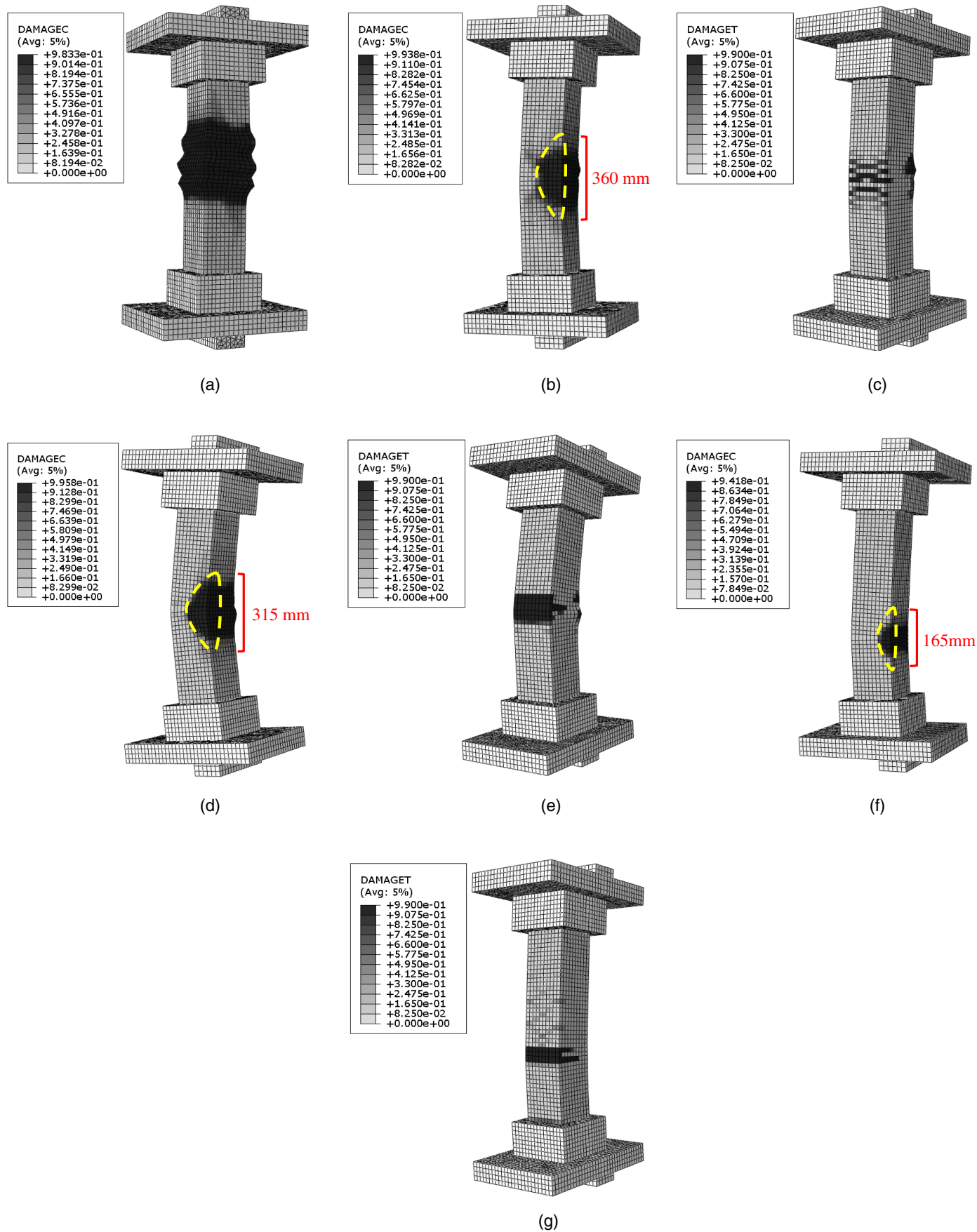


**Fig. 14.** FEM simulation results: (a) compressive damage pattern for  $e = 35$  mm; (b) compressive damage pattern for  $e = 35$  mm; (c) tensile damage pattern for  $e = 35$  mm; (d) compressive damage pattern for  $e = 50$  mm; (e) tensile damage pattern for  $e = 50$  mm; (f) compressive damage pattern for  $e = 85$  mm; and (g) tensile damage pattern for  $e = 85$  mm.

can be observed in Fig. 14(c) on the tensile face of the column, which is loaded with an eccentricity of 35 mm. With increases in eccentricity, more prominent tensile flexural cracks can be observed at the middle height of the columns with loading eccentricities of 50 and 85 mm. The aforementioned phenomenon suggests that flexural failure governs the overall failure of UHPFRC short columns over the compressive failure when the load eccentricity increases.

## Conclusions

In this study, a PI-based numerical model as well as FE models were developed to simulate the behaviors of short UHPFRC columns subjected to concentric and eccentric loads together with a simply supported beam, and the following conclusions can be made:

- Both PI-based and FEM models can be applied confidently to simulate  $P$ - $\delta_{axial}$  and  $P$ - $\delta_{mid}$  relationships for short UHPFRC columns and beams, respectively.
- To analyze UHPFRC columns using these models, only the fundamental material properties of concrete and reinforcements are required to predict the  $P$ - $\delta_{midheight}$  relationships of eccentrically loaded columns without resorting to costly and time-consuming structural tests on UHPFRC columns.
- The proposed  $P$ - $M$  interaction envelopes generated in this study accurately predict the behaviors of short columns loaded with various eccentricities, and this highlights the reliability of the numerical models in simulating the behaviors of eccentrically loaded UHPFRC columns. Therefore, it can serve as the basis for further research and design of UHPFRC columns.
- FE simulations successfully reproduced the damage patterns of UHPFRC members under different loading conditions. Comparisons of these simulated damage patterns indicated that the compressive damage level of short UHPFRC columns decreases with an increase in loading eccentricity.

## Acknowledgments

The authors would like to extend their sincere gratitude to Dr. Phillip Visintin for his valuable advises on PI models used for this study. The authors would also like to extend their gratitude to Douglas, Fairweather, Jolly, Sedev, and Reid, who conducted the active-confined cylinder and direct pullout tests presented in this paper.

## Notation

The following symbols are used in this paper:

- $A_{bar}$  = area of one longitudinal reinforcement;
- $A_c$  = area of the surrounding prism at the partial-interaction region;
- $B_n$  = bond force in the  $n$ th element;
- $B_1$  = bond force in the first element;
- $B_2$  = bond force in the second element;
- $b_1$  = empirical coefficient for the bond-slip relationship in Stage 2;
- $b_2$  = empirical coefficient for bond-slip relationship in Stage 3;
- $b_3$  = empirical coefficient for the bond-slip relationship in Stage 4;
- $d_c$  = compressive damage parameter defined in Eq. (11);
- $d_t$  = tensile damage parameter defined in Eq. (12);

- $d_{\Delta}/d_x$  = slip strain between the tensile reinforcement and surrounding concrete;
- $(d_{\Delta}/d_x)_n$  = slip strain between the tensile reinforcement and surrounding concrete in the  $n$ th element;
- $(d_{\Delta}/d_x)_1$  = slip strain between the tensile reinforcement and surrounding concrete in the first element;
- $(d_{\Delta}/d_x)_2$  = slip strain between the tensile reinforcement and surrounding concrete in the second element;
- $E_c$  = Young's modulus of UHPFRC;
- $E_{ct}$  = elastic modulus of UHPFRC =  $E_c$ ;
- $E_{fib}$  = Young's modulus of steel fiber;
- $E_h$  = modulus of steel hardening;
- $E_r$  = Young's modulus of the steel reinforcement;
- $E_{t1}$  = modulus of tensile hardening of UHPFRC;
- $E_0$  = undamaged elastic modulus of concrete, which is also  $E_c$ ;
- $f'_c$  = ultimate compressive strength of UHPFRC obtained from standard cylinder tests;
- $f_{ct}$  = ultimate tensile strength of UHPFRC;
- $f_{t1}$  = maximum tensile stress of UHPFRC before tensile hardening;
- $f_u$  = maximum strength of the steel reinforcement;
- $f_y$  = yield stress of steel reinforcements;
- $G$  = flow potential;
- $k_1$  = slope of bond-slip relationship in the second stage;
- $k_2$  = slope of bond-slip relationship in the third stage;
- $k_3$  = slope of bond-slip relationship in the fourth stage;
- $L_{def}$  = deformation length, which is also a half of the crack spacing ( $S_{pr}$ );
- $L_e$  = element length for each segment;
- $L_{per}$  = contact perimeter of tensile reinforcement;
- $L_w$  = width of compression wedge;
- $P_c$  = force in surrounding concrete;
- $P_{cc}$  = sectional compressive force from UHPFRC;
- $P_{ct}$  = sectional tensile force from UHPFRC;
- $P_{fib}$  = force owing to fiber bridging effect in UHPFRC after cracking;
- $P_{rb}$  = sectional force in reinforcements placed at the left;
- $P_{rl}$  = lower boundary of initial guess for the force in tensile reinforcement;
- $P_{rt}$  = sectional force in reinforcements placed at the right;
- $P_{ru}$  = upper boundary of initial guess for the force in tensile reinforcement;
- $P_{r-max}$  = maximum force of the steel reinforcement;
- $P_{r-y}$  = tensile force of the steel reinforcement reaches yield stress;
- $\bar{p}$  = hydrostatic pressure based on effective stresses;
- $\bar{q}$  = effective von Mises equivalent stress;
- $S_{pr}$  = crack spacing between primary cack and initial crack;
- $W_{cr}/2$  = crack width at the initial crack;
- $\alpha$  = material dependent constant in Eq. (4);
- $\alpha_1$  = constant coefficient of descending curve of concrete under tension;
- $\alpha_2$  = empirical coefficient fitting the experimental result of bond tests;
- $\beta_1$  = constant coefficient of descending curve of concrete under tension;
- $\beta_2$  = empirical coefficient fitting the experimental result of bond tests;



$\gamma$  = material dependent constant in Eq. (6);  
 $\Delta$  = relative slip between the tensile reinforcement and surrounding concrete;

$\Delta_n$  = relative slip between tensile reinforcement and surrounding concrete in the  $n$ th element;

$\Delta_1$  = relative slip between tensile reinforcement and surrounding concrete in the first element;

$\Delta_2$  = relative slip between tensile reinforcement and surrounding concrete in the second element;

$\delta\Delta_1$  = differential slip between the tensile reinforcement and surrounding concrete in the first element;

$\delta\Delta_2$  = differential slip between the tensile reinforcement and surrounding concrete in the second element;

$\varepsilon_{bn}$  = strain of the tensile reinforcement in the  $n$ th element;

$\varepsilon_{b1}$  = strain of the tensile reinforcement in the first element;

$\varepsilon_{b2}$  = strain of the tensile reinforcement in the second element;

$\varepsilon_c$  = total compressive strain in concrete;

$\varepsilon_{0c}^{el}$  = elastic compressive strain corresponding to the yield stress of the concrete;

$\varepsilon_c^{in}$  = inelastic strain;

$\varepsilon_{cc}$  = strain prior strain hardening;

$\varepsilon_{cn}$  = strain of the concrete in the  $n$ th element;

$\varepsilon_{ct}$  = corresponding tensile strain of UHPFRC at the ultimate tensile strength;

$\varepsilon_{c1}$  = strain of the concrete in the first element;

$\varepsilon_{c2}$  = strain of the concrete in the second element;

$\varepsilon_{def}$  = strain in deformed region;

$\varepsilon_{mat}$  = material strain corresponding to the strain at the peak stress;

$\varepsilon_{pk}$  = strain corresponding to peak stress of UHPFRC;

$\varepsilon_{r1}$  = strain in reinforcements placed at the left;

$\varepsilon_{r2}$  = strain in reinforcements placed at the right;

$\varepsilon_{soft}$  = strain corresponding to the peak stress;

$\varepsilon_t$  = total tensile strain in concrete;

$\varepsilon_t^{ck}$  = cracking strain;

$\varepsilon_t^{el}$  = elastic tensile strain corresponding to the yield stress of the concrete;

$\varepsilon_{test}$  = total strain based on standard cylinder test using a 200-mm-tall cylinder;

$\varepsilon_y$  = yield strain of steel;

$\tilde{\varepsilon}^{pl}$  = equivalent plastic strain;

$\tilde{\varepsilon}_c^{pl}$  = plastic strains in compression;

$\tilde{\varepsilon}_t^{pl}$  = plastic strains in tension;

$\xi$  = potential eccentricity parameter for describing the rate at which the function approaches the asymptote;

$\sigma_{cc}$  = compressive stress in UHPFRC;

$\sigma_{ct}$  = tensile stress in UHPFRC;

$\sigma_{r1}$  = stress in reinforcements placed at the left;

$\sigma_{r2}$  = stress in reinforcements placed at the right;

$\sigma_{t0}$  = uniaxial tensile stress;

$\bar{\sigma}_c(\tilde{\varepsilon}^{pl})$  = effective cohesive stress under compression corresponding to each equivalent plastic strain;

$\bar{\sigma}_t(\tilde{\varepsilon}^{pl})$  = effective cohesive stress under tension corresponding to each equivalent plastic strain;

$\hat{\sigma}_{max}$  = maximum principal effective stress;

$\tau_n$  = bond stress in the  $n$ th element;

$\tau_1$  = bond stress in the first element;

$\tau_2$  = bond stress in the second element; and

$\varphi$  = dilation angle obtained from the measurement from the  $p$ - $q$  plane under high confining pressure.

## References

- Baby, F., P. Marchand, and F. Toutlemonde. 2014. "Shear behavior of ultra-high performance fiber-reinforced concrete beams. I: Experimental investigation." *J. Struct. Eng.* 140 (5): 04013111. [https://doi.org/10.1061/\(ASCE\)ST.1943-541X.0000907](https://doi.org/10.1061/(ASCE)ST.1943-541X.0000907).
- Birtel, V., and P. Mark. 2006. "Parameterized finite element modelling of RC beam shear failure." In *Proc., Abaqus User's Conf.*, 95–107. Palo Alto, CA: ABAQUS.
- Chen, Y., P. Visintin, D. J. Oehlers, and U. Alengaram. 2014. "Size-dependent stress-strain model for unconfined concrete." *J. Struct. Eng.* 140 (4): 04013088. [https://doi.org/10.1061/\(ASCE\)ST.1943-541X.0000869](https://doi.org/10.1061/(ASCE)ST.1943-541X.0000869).
- Dagenais, M. A., and B. Massicotte. 2017. "Cyclic behavior of lap splices strengthened with ultrahigh performance fiber-reinforced concrete." *J. Struct. Eng.* 143 (2): 4016163. [https://doi.org/10.1061/\(ASCE\)ST.1943-541X.0001652](https://doi.org/10.1061/(ASCE)ST.1943-541X.0001652).
- Hosinih, M. M., H. Aoude, W. D. Cook, and D. Mitchell. 2015. "Behaviours of ultra-high performance fiber reinforced concrete columns under pure axial loading." *Eng. Struct.* 99 (Sep): 388–401. <https://doi.org/10.1016/j.engstruct.2015.05.009>.
- Lubliner, J., J. Oliver, S. Oller, and E. Onate. 1989. "A plastic-damage model for concrete." *Int. J. Solids Struct.* 25 (3): 299–326. [https://doi.org/10.1016/0020-7683\(89\)90050-4](https://doi.org/10.1016/0020-7683(89)90050-4).
- Mahmud, G. H., Z. Yang, and A. M. T. Hassan. 2013. "Experimental and numerical studies of size effects of ultra high performance steel fibre reinforced concrete (UHPFRC) beams." *Constr. Build. Mater.* 48 (Nov): 1027–1034. <https://doi.org/10.1016/j.conbuildmat.2013.07.061>.
- Mohamed Ali, M. S., D. J. Oehlers, and M. C. Griffith. 2008. "Simulation of plastic hinges in FRP-plated RC beams." *J. Compos. Constr.* 12 (6): 617–625. [https://doi.org/10.1061/\(ASCE\)1090-0268\(2008\)12:6\(617\)](https://doi.org/10.1061/(ASCE)1090-0268(2008)12:6(617)).
- Razvi, S., and M. Saatcioglu. 1999. "Confinement model for high-strength concrete." *J. Struct. Eng.* 125 (3): 281–289. [https://doi.org/10.1061/\(ASCE\)0733-9445\(1999\)125:3\(281\)](https://doi.org/10.1061/(ASCE)0733-9445(1999)125:3(281)).
- Shin, H. O., K. H. Min, and D. Mitchell. 2017. "Confinement of ultra-high-performance fiber reinforced concrete columns." *Compos. Struct.* 176 (Sep): 124–142. <https://doi.org/10.1016/j.compstruct.2017.05.022>.
- Shin, H. O., K. H. Min, and D. Mitchell. 2018. "Uniaxial behavior of circular ultra-high-performance fiber-reinforced concrete columns confined by spiral reinforcement." *Constr. Build. Mater.* 168 (Apr): 379–393. <https://doi.org/10.1016/j.conbuildmat.2018.02.073>.
- Shukri, A. A., P. Visintin, D. J. Oehlers, and M. Z. Jumaat. 2016. "Mechanics model for simulating RC hinges under reversed cyclic loading." *Materials* 9 (4): 305. <https://doi.org/10.3390/ma9040305>.
- Singh, M., M. S. Mohamed Ali, and A. H. Sheikh. 2015. "Structural behaviour of ultra-high performance fibre reinforced concrete columns subjected to eccentric loading." In *Proc., IABSE Conf.—Structural Engineering: Providing Solutions to Global Challenges*. Zürich, Switzerland: International Association for Bridge and Structural Engineering.
- Singh, M., M. S. Mohamed Ali, A. H. Sheikh, M. C. Griffith, and P. Visintin. 2016. "Structural behaviour of ultra high performance fibre reinforced concrete beams with steel and polymer bar reinforcement." In *Proc., 11th fib Int. PhD Symp. in Civil Engineering*. Lausanne, Switzerland: CEB-Fib.
- Singh, M., A. H. Sheikh, M. S. Mohamed Ali, P. Visintin, and M. C. Griffith. 2017. "Experimental and numerical study of the flexural behaviour of ultra-high performance reinforced concrete beams." *Constr. Build. Mater.* 138 (May): 12–25. <https://doi.org/10.1016/j.conbuildmat.2017.02.002>.
- Steven, G., and M. Empelmann. 2014. "UHPFRC-columns with high-strength longitudinal reinforcement." *Beton-Stahlbetonbau* 109: 344–354. <https://doi.org/10.1002/best.201300090>.
- Sturm, A. B., P. Visintin, D. J. Oehlers, and R. Seracino. 2018. "Time-dependent tension-stiffening mechanics of fiber-reinforced and ultra-high-performance fiber-reinforced concrete." *J. Struct. Eng.*

- 144 (8): 04018122. [https://doi.org/10.1061/\(ASCE\)ST.1943-541X.0002107](https://doi.org/10.1061/(ASCE)ST.1943-541X.0002107).
- Visintin, P., and D. J. Oehlers. 2018. "Fundamental mechanics that govern the flexural behavior of reinforced concrete beams with fibre-reinforced concrete." *Adv. Struct. Eng.* 21 (7): 1088–1102. <https://doi.org/10.1177/1369433217739705>.
- Visintin, P., D. J. Oehlers, M. Haskett, and C. Wu. 2013. "Mechanics-based hinge analysis for reinforced concrete columns." *J. Struct. Eng.* 139 (11): 1973–1980. [https://doi.org/10.1061/\(ASCE\)ST.1943-541X.0000761](https://doi.org/10.1061/(ASCE)ST.1943-541X.0000761).
- Visintin, P., A. B. Sturm, M. S. Mohamed Ali, and D. J. Oehlers. 2018b. "Blending macro- and micro-fibres to enhance the serviceability behaviour of UHPFRC." *Aust. J. Civ. Eng.* 16 (2): 106–121.
- Visintin, P., A. B. Sturm, and D. J. Oehlers. 2018a. "Long and short term serviceability behavior of reinforced concrete beams: Mechanics models for deflections and crack widths." *Struct. Concr.* 19 (2): 489–507. <https://doi.org/10.1002/suco.201700022>.
- Wille, K., S. El-Tawil, and A. E. Naaman. 2014. "Properties of strain hardening ultra-high performance fibre reinforced concrete (UHP-FRC) under direct tensile loading." *Cem. Concr. Compos.* 48 (Apr): 53–66. <https://doi.org/10.1016/j.cemconcomp.2013.12.015>.
- Xie, T., M. S. Mohamed Ali, P. Visintin, D. J. Oehlers, and A. H. Sheikh. 2018. "Partial interaction model of flexural behavior of PVA fiber-reinforced concrete beams with GFRP bars." *J. Compos. Constr.* 22 (5): 04018043. [https://doi.org/10.1061/\(ASCE\)CC.1943-5614.0000878](https://doi.org/10.1061/(ASCE)CC.1943-5614.0000878).
- Yoo, D. Y., and N. Banthia. 2016. "Mechanical properties of ultra-high-performance fiber-reinforced concrete: A review." *Cem. Concr. Compos.* 73: 267–280. <https://doi.org/10.1016/j.cemconcomp.2016.08.001>.
- Yoo, D. Y., and Y. S. Yoon. 2016. "A review on structural behavior, design, and application of ultra-high-performance fiber-reinforced concrete." *Int. J. Concr. Struct. Mater.* 10 (2): 125–142. <https://doi.org/10.1007/s40069-016-0143-x>.
- Zhang, T., P. Visintin, D. J. Oehlers, and M. C. Griffith. 2014. "Presliding shear failure in prestressed RC beams. I: Partial-interaction mechanism." *J. Struct. Eng.* 140 (10): 04014069. [https://doi.org/10.1061/\(ASCE\)ST.1943-541X.0000988](https://doi.org/10.1061/(ASCE)ST.1943-541X.0000988).